Realization of Topological and Unconventional Superconducting Behavior in Low-Dimensional Quantum Many-Body Systems

Von der Fakultät für Mathematik, Informatik und Naturwissenschaften der RWTH Aachen University zur Erlangung des akademischen Grades einer Doktorin der Naturwissenschaften genehmigte Dissertation

vorgelegt von

Clara Stephanie Weber, M. Sc.

aus

Köln

Berichter:	Prof. Dr. rer. nat. Dante M. Kennes Prof. Dr. phil. Herbert Schoeller
Tag der mündlichen Prüfung:	10.12.2024

Diese Dissertation ist auf den Internetseiten der Universitätsbibliothek verfügbar.

Abstract

In this thesis, emergent phenomena in low-dimensional (one or two-dimensional) systems and possible mechanisms behind them are investigated. Here, we focus on topological properties, as well as unconventional superconductivity.

Following the introduction of the methods and formalisms used in this thesis, which are exact diagonalization, density matrix renormalization group, Green's functions and generalized Bardeen-Cooper-Schrieffer theory, multiple physical systems with exotic properties are investigated.
First, we study a subclass of second-order topological insulators in two dimensions. The chosen subclass is supersymmetric for an applied Aharanov-Bohm flux of half a flux quantum through the system's center. The present supersymmetry leads to a fully two-fold degenerate spectrum and is, in combination with a chiral symmetry, responsible for the protection of zero-dimensional topological bound states at zero energy. At the example of the Bernevig-Hughes-Zhang model, the spectrum as well as the zero energy bound states are examined in great detail on a Corbino disk.
After the investigation of this non-interacting topological system, we concentrate on an interacting system and study superconductors with multiple competing orders on the level of mean-field approximations. Here, we examine under which conditions a subleading order can be metastable. Only if the subleading order is metastable, it can be targeted by employing a light pulse. Thereby, under certain conditions, a conventional superconductor can be driven into an unconventional superconductor via light switching. Interestingly, we observe that the phase difference between the multiple orders can be crucial for the question of metastability. Moreover, we find that real valuead pairing (such as $p_{x,y}$) is in general unstable, while topological chiral instabilities (e.g. p_x+ip_y) can be subleading metastable orders.
Hereafter, a second mechanism leading to unconventional superconductivity, based on strong electronic couplings, is investigated. Here, we study a weakly- and a strongly-interacting layer coupled and combined into a hetero bilayer structure. This leads to an effective attractive interaction yielding Cooper pairs mostly present in the nearly-metallic layer. In the strong coupling regime, the appearance of electronic pairs is explained using a single rung and the superconducting behavior is found to be intertwined with magnetic ordering. Using numerical methods, we investigate both, the superconducting and the magnetic ordering which continue to exist beyond the strong coupling regime. Remarkably, some parts of the phase diagram do not show uniform pairing but instead a pair density wave is formed here.
Finally, possible systems that can possess the needed strong correlations are discussed in more detail. Here, we focus on systems with a partially filled flat band but disregard possible electronic correlations. We study the behavior of the Ruderman-Kittel-Kasuya-Yosida interaction, which describes indirect couplings of impurity spins, in one dimension. The Ruderman-Kittel-Kasuya-Yosida interaction is usually calculated using a perturbative expression. This approach cannot be employed in flat band systems due to the vanishing band width, making an exact treatment necessary. Indeed, we find that the standard approach does not cover the results if at least one of the impurities is directly coupled to the eigenstates of the flat band. Additionally, the decay of the Ruderman-Kittel-Kasuya-Yosida coupling in real space depends on the band structure of the system. In systems with a flat band isolated by a band gap, an exponential decay occurs, while systems, where other bands cross the flat band, have a Ruderman-Kittel-Kasuya-Yosida interaction with an algebraic powerlaw decay (in the limit of large distances).

Deutsche Zusammenfassung

In dieser Dissertation werden emergente Phänomene in niedrigdimensionalen (ein- oder zweidimensionalen) Systemen und mögliche dahinterliegende Mechanismen untersucht. Dabei fokussieren wir uns auf topologische Eigenschaften sowie unkonventionelle Supraleitung.

Im Anschluss an die Einführung der in dieser Arbeit verwendeten Methoden und Formalismen, welche exakte Diagonalisierung, Dichte-Matrix Renormalisierungsgruppe, Greensche Funktionen und generalisierte Bardeen-Cooper-Schrieffer Theorie sind, werden mehrere physikalische Systeme mit exotischen Eigenschaften untersucht.
Zunächst betrachten wir eine Unterklasse von topologischen Isolatoren zweiter Ordnung in zwei Dimensionen. Die gewählte Unterklasse ist supersymmetrisch für einen angelegten Aharanov-Bohm Fluss von einem halben Flussquant durch das Systemzentrum. Die vorhandene Supersymmetrie führt zu einem vollständig zweifach entarteten Spektrum und ist, gemeinsam mit einer chiralen Symmetrie, für den Schutz der topologisch gebundenen Zustände bei Nullenergie verantwortlich. Am Beispiel des Bernevig-Hughes-Zhang Models werden das Spektrum sowie die gebundenen Nullenergie-Zustände auf einer Corbino-Scheibe detailliert begutachtet.
Nach der Untersuchung dieses nicht-interagierenden topologischen Systems konzentrieren wir uns auf ein interagierendes System und studieren Supraleiter mit mehreren konkurrierenden Ordnungen auf dem Level von Molekularfeldtheorie-Approximationen. Dabei prüfen wir, unter welchen Bedingungen eine untergeordnete Ordnung metastabil sein kann. Nur wenn die untergeordnete Ordnung metastabil ist, kann sie durch die Anwendung eines Lichtpulses anvisiert werden. Dadurch kann unter bestimmten Vorraussetzungen ein konventioneller Supraleiter mittels Lichtschaltung in einen unkonventionellen Supraleiter getrieben werden. Interessanterweise finden wir, dass die Phasendifferenz zwischen den verschiedenen Ordnungen ausschlaggebend für die Frage der Metastabilität sein kann. Außerdem finden wir, dass reell-wertige Paarung (wie $p_{x,y}$) im Generellen unstabil ist, während topologische chirale Instabilitäten (z.B. p_x+ip_y) untergeordnete metastabile Ordnungen sein können.
Danach wird ein zweiter Mechanismus untersucht, der zu unkonventioneller Supraleitung führt und auf starken elektronischen Kopplungen basiert. Dabei studieren wir eine schwach und eine stark wechselwirkendende Lage, die gekoppelt sind und zu einer Heterobilagenstruktur kombinert werden. Dies führt zu einer effektiven attraktiven Wechselwirkung, welche Cooper Paare hervorbringt, die überwiegend in der fast metallischen Lage präsent sind. In dem Regime starker Interaktionen wird das Auftreten von Elektronenpaaren anhand einer einzelnen Sprosse erklärt und es zeigt sich, dass das supraleitende Verhalten mit magnetischer Ordnung verflochten ist. Mithilfe numerischer Methoden untersuchen wir sowohl die supraleitende, als auch die magnetische Ordnung, welche auch außerhalb des Regimes starker Wechselwirkung existieren. Bemerkenswerterweise zeigen einige Teile des Phasendiagramms keine gleichmäßige Supraleitung, sondern stattdessen wird eine Paardichtewelle geformt.
Schließlich werden mögliche Systeme, die die benötigten starken Wechselwirkungen besitzen können, ausführlicher diskutiert. Dabei fokussieren wir uns auf Systeme mit einem teilweise gefüllten flachen Band, aber ignorieren mögliche elektronische Wechselwirkungen. Wir untersuchen das Verhalten der Ruderman-Kittel-Kasuya-Yosida Wechselwirkung, die indirekte Kopplungen von magnetischen Störstellen beschreibt, in einer Dimension. Die Ruderman-Kittel-Kasuya-Yosida Wechselwirkung wird normalerweise durch einen perturbativen Ausdruck berechnet. Dieser Ansatz kann aufgrund der verschwindenden Bandbreite nicht für Flachbandsysteme genutzt werden, wodurch eine exakte Betrachtung nötig ist. In der Tat finden wir, dass der Standardansatz die Resultate

nicht abdeckt, wenn mindestens eine der Störstellen direkt an die Eigenzustände des flachen Bandes gekoppelt ist. Außerdem hängt der Abfall der Ruderman-Kittel-Kasuya-Yosida Kopplung im Realraum von der Bandstruktur des Systems ab. In Systemen mit einem durch eine Bandlücke isoliertem flachen Band tritt ein exponentieller Abfall auf, während Systeme, bei denen andere Bänder das flache Band kreuzen, eine Ruderman-Kittel-Kasuya-Yosida Wechselwirkung mit einen algebraischen Potenzgesetz-Abfall (im Grenzfall großer Distanzen) haben.

Contents

Abstract **III**

Deutsche Zusammenfassung **V**

I Introduction **1**

1 Motivation **3**
1.1 Topology . . . 3
1.2 Superconductivity . . . 5

2 Outline **9**

II Methods **11**

3 Exact Diagonalization **13**
3.1 Non-Interacting Systems . . . 13
3.1.1 Lattice Models . . . 13
3.1.2 Continuum Models . . . 14
3.2 Interacting Systems . . . 15

4 Density Matrix Renormalization Group **17**
4.1 Matrix Product States . . . 17
4.1.1 Singular Value Decomposition . . . 18
4.1.2 Matrix Product State of an Arbitrary Quantum State . . . 18
4.1.3 Graphical Representation . . . 21
4.1.4 Γ-Λ Notation . . . 21
4.2 Matrix Product Operators and Observables . . . 23
4.2.1 Decomposing an Arbitrary Operator . . . 23
4.2.2 Applying an MPO to an MPS . . . 25
4.2.3 Calculation of Expectation Values . . . 25
4.3 Ground State Search . . . 26
4.4 Infinite System Size . . . 28
4.5 Entanglement . . . 29
4.6 Extrapolation of Correlations to Infinite Bond Dimension . . . 29

5 Green's Functions **33**
5.1 Real Time Single-Particle Green's Functions for Many-Body Systems . . . 33
5.1.1 Transformation to General Basis . . . 35
5.1.2 Translation-Invariant Systems . . . 35
5.1.3 Frequency Dependent Green's Functions . . . 36
5.1.4 Free Electron System . . . 36
5.1.5 Green's Functions as General Correlation Functions . . . 37
5.2 Matsubara Green's Functions . . . 37

5.2.1 Green's Functions of Imaginary Frequency . . . 38
5.2.2 Connection to Advanced and Retarded Green's Functions . . . 39
5.2.3 Self-Energy and Dyson Equation . . . 39
5.3 Keldysh Formalism . . . 40
5.3.1 Contour Ordered Green's Functions and Keldysh Rotation . . . 40
5.3.2 The Self-Energy and the Dyson Equation . . . 42
5.3.3 Keldysh Equations of Motion . . . 42
5.3.4 Wide-Band Limit . . . 43
5.4 Green's Functions for Block-Tridiagonal Hamiltonians . . . 43
5.4.1 Inversion algorithm . . . 45

6 Generalized BCS Theory 47
6.1 Mean-Field Theory . . . 47
6.2 Standard BCS Theory . . . 48
6.2.1 Gap Equation . . . 48
6.2.2 Bogoliubov Transformation . . . 49
6.2.3 Nambu Formalism . . . 49
6.2.4 Nambu Green's Functions . . . 50
6.3 Generalization . . . 50
6.3.1 Gap Equation . . . 51
6.3.2 Form Factor Decomposition . . . 52
6.3.3 Efficient Solution of the Gap Equation . . . 52
6.4 Time Evolution of Order Parameters . . . 54
6.5 Special Case with no Spin Structure needed . . . 55
6.5.1 BdG Hamiltonian and Gap Equation . . . 56
6.5.2 Free Energy . . . 58
6.5.3 Time Evolution . . . 58

III Questions 61

7 Topological Zero Energy States Protected by Supersymmetry 63
7.1 Considered Models . . . 64
7.1.1 Symmetries . . . 65
7.1.2 Supersymmetry . . . 65
7.1.3 Bernevig-Hughes-Zhang Model . . . 66
7.1.4 Tight-Binding Version . . . 68
7.2 Corbino Disk . . . 69
7.2.1 Zero Zeeman Field . . . 69
7.2.2 Finite Zeeman Field . . . 73
7.2.3 Zero Energy Bound States . . . 76
7.3 Infinite System with a Hole . . . 82
7.4 Applications . . . 83
7.5 Conclusion & Outlook . . . 83

8 Metastability of Subleading Superconducting Orders 85
8.1 Real Value Pairing for General One-Band Models . . . 86
8.2 Square Lattice Model . . . 89
8.2.1 Real Order Parameters . . . 90
8.2.2 Stability Criterion . . . 91
8.2.3 Numerical Determination of Stability . . . 97
8.2.4 Chiral Order Parameters . . . 99
8.2.5 Doping away from Half-Filling . . . 100
8.3 Driving of One-Band Models . . . 102
8.4 Multi-Band Models . . . 103
8.4.1 Stability Analysis . . . 103

8.4.2 Coupling of Different Parities . . . 104
8.5 Same Spin Pairing . . . 105
8.6 Conclusion & Outlook . . . 106

9 Unconventional Superconductivity in Bilayer Heterostructures 109
9.1 Model . . . 110
9.2 Strong Coupling Regime: Investigation of a Single Rung . . . 111
9.3 Parent State: Magnetic Ordering . . . 113
9.3.1 Phase Separation Regime . . . 115
9.3.2 Magnetic Phase Diagrams . . . 117
9.4 Evidences for Superconductivity . . . 118
9.4.1 Pair Binding Energy . . . 119
9.4.2 Pair Correlation Function . . . 119
9.4.3 Computation of an Order Parameter . . . 124
9.4.4 Combining Various Evidences . . . 126
9.5 Conclusion & Outlook . . . 128

10 RKKY Interaction for Flat-Band Systems in One Dimension 129
10.1 RKKY Interaction . . . 130
10.1.1 Standard RKKY Expression . . . 131
10.1.2 RKKY Interaction in Flat Bands . . . 132
10.2 Flat-Band Models . . . 132
10.2.1 Stub Lattice . . . 133
10.2.2 Diamond Lattice . . . 134
10.3 Effective Calculation of the RKKY coupling . . . 136
10.3.1 Decoupling of Spin Sectors . . . 136
10.3.2 Calculation using Green's Functions . . . 136
10.4 Results . . . 140
10.4.1 Stub Lattice . . . 140
10.4.2 Diamond Lattice . . . 142
10.4.3 Transition from Stub to Diamond Lattice . . . 144
10.5 Conclusion & Outlook . . . 146

IV Conclusion & Outlook 149

11 Conclusion 151

12 Outlook 153

V Appendices 155

A Analytical Expression for the Optimization of Solving the Gap Equation 157

B Perturbative Result for the Derivative of Gap Function 159

C Matrix Products for Derivations of Eqs. (6.82)-(6.88) **161**

D Rotation of Matrix with Different Eigenvalues 163

E Pair Correlation Function in Momentum Space: Failure of Convergence of Results Obtained Based on the Tail 165

F Matsubara Green's Function in Flat Band Systems 167
F.1 Stub Lattice . . . 167
F.2 Diamond Lattice . . . 170

List of Acronyms **173**

Bibliography **175**

Publications and Preprints **195**

Acknowledgment **197**

Eidesstattliche Erklärung **199**

Part I

Introduction

Chapter 1

Motivation

In condensed matter physics, emergent phenomena is usually associated with collective behavior which cannot be described by regarding the individual parts of a system [1–3]. Instead, the system has to be considered as its whole. The concept of emergence in the context of condensed matter physics is often based on the discussion by Anderson in his famous article 'More is different' from 1972 [4] and plays a central role in condensed matter physics [5, 6]. Emergent behavior includes, for example, topology, superconductivity and magnetism [1, 5, 7], which can also interplay and compete with each other [8]. In condensed matter systems, emergent phenomena often arise due to strong correlations [5, 8]. Nevertheless, there are topological phases (e.g. topological insulators) that do not need strong interactions and can even exist in non-interacting systems [5, 9].

In the remainder of this work, we concentrate on the phenomena of topology and (unconventional) superconductivity, which are analyzed in low-dimensional (one- and two-dimensional) systems. In the following, it is briefly introduced why these topics are of specific interest.

1.1 Topology

Topology is a concept that physicists have adapted from mathematics. Here, topology is about geometric objects and their properties staying invariant under continuous (or *smooth*) transformations [10–13]. Objects which can be deformed into each other using these continuous transformations are called topologically equivalent [12] and they possess the same topological invariants, which are properties staying invariant under such continuous transformations (or under homeomorphisms to be presice, see Ref. [12] for details). Therefore, topological invariants can be used for the classification of objects.
Possible applications to physics might not seem very obvious at first sight, but topology allows us to classify condensed matter systems in the same manner. Using topological invariants, topological phases can be defined, which are beyond the scope of the standard approach of Landau [14], which classifies phases based on spontaneously broken symmetries [15]. Importantly, topological properties are rather robust since they cannot be changed by smooth and small changes including various types of disorder [10, 15–18].

Topological Phases

One of the most prominent examples of materials with topological properties are topological insulators, which behave similar to ordinary insulators and have a band gap making the material's bulk insulating. However, topological insulators have gapless states localized at the edge or surface of the system. The existence of edge/surface states can be understood due to the topological index that can only change at a gap closing point. Since the trivial vacuum and the non-trivial topological insulator meet at the boundary, the gap has to close locally and gapless edge/surface modes arise [16, 19, 20]. One example of topological insulators are time-reversal symmetric $\mathbb{Z}_2$ topological insulators, which are sometimes only called topological insulators [15, 20]. Here, the topological states are protected by time reversal symmetry and lead to a conductance along the edges/surfaces

[9, 15, 20]. Another example are two-dimensional Chern insulators [9, 16, 21, 22] characterized by a topological invariant integer called Chern number. These systems are not time-reversal symmetric and they show a quantized Hall conductance due to the states at the system's boundary. Interestingly, clear evidences for topological insulators have also been found experimentally [15, 20].
Another interesting topological class is given by topological superconductors [23–26]. Here, the gapless states arising at the boundary are realized by Majorana fermions [10, 25], which are their own anti-particles [23–27]. One example of a topological superconductor are two-dimensional chiral superconductors (such as $p+ip$ superconductor), where chiral Majorana edge modes occur [28, 29]. Interestingly, some topological superconductors can host Majorana bound states at zero energy, which are therefore also known as Majorana zero modes. Those can, for example, appear at the ends of the one-dimensional Kitaev chain [23, 30, 31] or at zero dimensional vortices in two-dimensional chiral p-wave superconductors [15, 28, 29]. Interestingly, Majorana zero modes are non-Abelian anyons with the necessary properties for the realization of a topological quantum computer [15, 23, 25, 27, 32], which is introduced below. Unfortunately, the existence of these Majorana modes is experimentally extremely difficult to prove due to the obstacle of finding experimental signatures, which can unambiguously be associated with Majorana modes [23, 33]. Therefore, the observation of Majarona states in experiments remains an open question [26].
These are only some prominent examples of topological phases. The variety of topological phases goes well beyond those [34], including Floquet topological insulators [35, 36], topological semimetals [37, 38] or in general quantum Hall phases of various kinds [22, 34, 39, 40].

Topology and Symmetries

Topological properties are closely connected to the symmetries of the system. The present symmetries can, for example, be responsible for protecting the existence of topological zero energy states in a one-dimensional system [41] or the gapless states of a topological insulator as mentioned above [9, 15, 20]. Additionally, systems have been classified into certain topology classes using their symmetries and spatial dimensions [42–45]. This classification is called the periodic table of topological insulators and superconductors and includes only Hamiltonians on a single-particle level [46] (non-interacting or mean-field, which is introduced in Section 6.1). The periodic table is based on chiral, time-reversal and particle-hole symmetry and assigns the space of possible topological invariants in each dimension. These can either be 0 (no topological character), $\mathbb{Z}_2$ (only zero and one), $\mathbb{Z}$ (all integers) or $2\mathbb{Z}$ (all even integers).

Higher Order Topology

Within the last decade, higher order topological phases, such as higher order topological insulators and superconductors have emerged to a new field of topological condensed matter physics [47–57]. While the usual first order topological insulators of dimension D host gapless edge or surface states of dimension $D-1$, gapless states of a smaller dimension arise in higher order topological insulators. Here, the topologically protected states have a spatial dimension of $D-m$ ($m \leq D$) for a topological insulator of order m [50, 51, 53]. For example, a second-order topological insulator hosts zero-dimensional corner states in two and one-dimensional hinge states in three spatial dimensions. To this end, the edge states at higher dimensional surfaces need to be gapped in addition to the bulk states [47, 49, 50, 52, 55, 56]. The concept of higher order superconductors (on the level of effective single-particle Hamiltonians) works analogously leading to Majorana corner and hinge modes [50, 58–63].
Although the field of higher order topological phases is still young and emerging, higher order topology has been realized and studied experimentally as well [64–69].

As already mentioned above, topological properties are tightly connected to the system's symmetries. Nevertheless, there are symmetries which have so far been beyond the focus of condensed matter physics, although they still might lead to a topological character. In this thesis, higher order topological insulators with such a symmetry (supersymmetry) are considered.

Applications

Potential applications of topological properties of quantum systems are versatile [70] and include the broad field of spintronics [10, 15, 71, 72], as well as the improvement of numerous electrical and magnetic devices [73]. Here, the properties of the surface states in topological insulators can be exploited.
Most prominently, topological properties are a key feature in the perspective of building a quantum computer, or more precisely a topological quantum computer [74]. Here, robust topological properties, to be precise the manipulation of anyons [74, 75], can be employed. This allows to circumvent one of the main problems of quantum computing, which is the protection of the quantum information from outside noise [74–77].
In contrast to classical computers, which rely on classical bits that can only be in two states called '0' and '1', quantum computers are built from qubits that can be in any superposition of both [77–79]. Their existence would allow to solve problems beyond the reach of classical computers and provide a significant speed-up for some already solvable problems [76, 77, 79].
Unfortunately, so far quantum computers with only a very limited amount of qubits have been realized, recently exceeding 1000 qubits [80, 81]. However, these non-topological qubits are not sufficiently protected from noise and multiple physical qubits (typically a few hundreds or more) would need to be combined to build a single logical qubit [79, 80, 82]. Therefore, the applicability is restricted to very specific problems and the realization of a large scale quantum computer remains an open question.

1.2 Superconductivity

In general, superconductivity refers to the phenomena of zero electrical resistance in certain materials at low temperatures in combination with the expulsion of magnetic fields known as Meissner effect. Interestingly, the resistance does not approach zero continuously but instead it shows an abrupt drop at a certain temperature, which is called critical temperature or transition temperature.

Historical Overview

Superconductivity was first discovered in 1911 by the Dutch physicist Heike Kamerlingh Onnes, who observed a sudden disappearance of the electrical resistance of mercury at 4.2K [83]. This event marks the starting point of the fascination for superconductivity by generations of physicists. Later on, the Meissner effect was discovered [84], which describes the expulsion of a magnetic field. Above a certain magnetic field strength, the field cannot be expelled anymore and one either finds that the superconducting properties disappear (Type I, or above the upper critical field for Type II) or that a mixed state with a penetrating magnetic field is formed (Type II, between the lower and upper critical field) [85].
After a few decades, theoretical explanations were established. The first ones to describe the zero resistance as well as the Meissner effect were Fritz and Heinz London, who developed the classical London equations in 1935 [86]. These equations can be found through modifying the well-known Maxwell equations by adding two further equations [87]. In 1950, Ginzburg and Landau introduced another phenomenological theory [88]. They introduced an order parameter Ψ allowing for the description of the free energy landscape in orders of Ψ and its gradient $\nabla\Psi$ [87].
A microscopic theory explaining the appearance of superconductivity was developed by Bardeen, Cooper and Schrieffer, therefore called BCS theory [89, 90]. They showed, that a system becomes superconducting, when the electrons form bound pairs, which are referred to as Cooper pairs and which can form a condensate due to their bosonic character [91]. These pairs form as a consequence of an effective attraction between the electrons which arise due to vibrations of the ionic lattice, called phonons. In this scenario, the phonons are also called *pairing glue*, since they are responsible for *gluing* the electrons together. Although BCS theory is only a mean-field theory, it has been extremely successful in describing numerous conventional superconductors. Moreover, generalizations of the BCS theory have been established allowing for a description of certain types of unconventional superconductors.

Unconventional Superconductivity

More recently, the condensed matter research has also focused on unconventional superconductors. The expression *unconventional superconductivity* is used in different contexts, not allowing for a unique definition of this term, although different definitions have a substantial overlap. Most importantly, all of them have in common, that any form of unconventional superconductivity cannot be explained by the standard BCS theory.
First of all, the most common definition refers to superconductivity which is not mediated by phonons, but arises from a different pairing glue, such as spin fluctuations [92].
Another prevalent definition of unconventional superconductivity is based on the underlying pairing symmetry of the system. Here, conventional superconductors are superconductors with a standard and most symmetric (singlet) s-wave pairing, while unconventional superconductors have a less symmetric order parameter, such as p-wave, d-wave or f-wave pairing [91, 93, 94].
Both of the aforementioned definitions are strongly correlated, have a significant overlap and are therefore often used nearly equivalently [94]. Usually, phonon-electron interactions lead to standard s-wave pairing, meaning that other or additional pairing mechanisms are needed for the achievement of different pairing symmetries [91]. Within this thesis, we consider unconventional superconductivity under both of the aforementioned definitions. Therefore, any superconductor either being driven by other mechanisms than conventional electron-phonon coupling or not showing conventional s-wave pairing symmetries is classified as an unconventional superconductor.
Unconventional superconductivity has been found experimentally in a variety of different systems, such as heavy fermion compounds, cuprates, iron based materials and organic compounds [91, 92, 94]. Nevertheless, theorists have not been capable of finding a unified theory explaining the unconventional superconductivity for all of these subgroups [92]. For some classes, such as cuprates, the underlying mechanism is still under debate [94–96], explaining the ongoing research on these materials.

High Temperature Superconductivity

Unconventional superconductors are of significant interest since some of them have a much higher transition temperature than typical conventional superconductors and are therefore considered to be high-temperature superconductors [97, 98]. For conventional superconductors, it was believed that the critical temperature is always below 30 K until the discovery of MgB_2 [99] with a transition temperature of 39 K in 2001 [97]. MgB_2 can be considered as a high-temperature superconductor as well [98] showing that high-temperature superconductors do not have to be unconventional. Some high-temperature superconductors even have a critical temperature above 77 Kelvin, the boiling temperature of liquid nitrogen, which is sometimes even used as the definition of high-temperature superconductivity (see e.g. [100]).
This means, that these high temperature superconductors can be established by cooling with liquid nitrogen, which is an immense advantage over the necessity of liquid helium [98]. Besides from some interesting properties of several subclasses, e.g. Majoranas in topological superconductors, this is the main reason for the gigantic interest in unconventional superconductors.
A further investigation of (unconventional) superconductivity could lead to the discovery of superconductors with higher critical temperatures with the ultimate goal being the realization of a room-temperature superconductor, allowing to exploit the advantages of superconductors without any cooling.

Since possible mechanisms for the realization of unconventional superconductors are still under debate, two feasible approaches are theoretically investigated in this thesis. On the one hand, we discuss the possibility of inducing unconventional superconductivity with a light pulse and on the other hand, a superconductor in a bilayer hetero structure from purely repulsive electron-electron interactions is presented.

Applications

Superconductivity has not only been in the centre of condensed matter research due to these astonishing properties, but also due to the numerous possible applications in various sectors of our

every-day life.
Up to now, superconducting materials are mainly used, when large magnetic fields need to be employed. These can be realized using superconducting magnets, where a huge electric current is sent through a superconducting material resulting in a perpendicular magnetic field. In contrast to standard electro-magnets, superconducting magnets can generate much larger magnetic fields since an enormous electric current can be applied without any loss of energy. Such superconducting magnets can, for example, be used in so called superconducting *maglev* trains [101] or in magnetic resonance imaging (MRI) [102].
In addition to the superconducting magnets, superconductors can be used in superconducting quantum interference devices (SQUIDs), which allow for ultra-sensitive magnetic measurements. They are built from a ring of superconductors with small breaks inbetween called Josephson junctions [103].
Moreover, superconductors could be used in the future for the realization of the aforementioned quantum computers. Here, superconducting qubits based on Josephson junctions can be employed [104].
These are only a few of a vast number of applications of superconducting materials. For a more detailed listing of possible applications and extensive explanations, the reader is referred to Refs. [98, 102, 103, 105–107].

Chapter 2

Outline

The remainder of this thesis is organized as follows: In a first part, Chapters 3-6, the methods used for this thesis are introduced. First, the exact diagonalization method is presented allowing for the exact solution of non-interacting as well as interacting quantum systems.
After that, the density matrix renormalization group is discussed. In contrast to exact diagonalization, the density matrix renormalization group is not restricted to a few sites in typical interacting (one-dimensional) systems.
Furthermore, the Green's function formalism is introduced, which is used for both systems in and out of equilibrium within this thesis. After introducing the formalism for both of these cases, it is shown how to efficiently calculate Green's functions for block-tridiagonal Hamiltonians in equilibrium.
Finally, the generalized Bardeen–Cooper–Schrieffer theory is presented. This method can describe superconductivity including general, unconventional pairing functions on a mean-field level. It is also shown how dynamics can be described within this approach.

In a second part, results obtained with these methods are shown, allowing to answer several questions of interest. First, in Chapter 7, non-interacting models with topological properties are considered. Here, a typical group of two-dimensional second order topological insulators with an applied Aharanov-Bohm flux of half a flux quantum are shown to have a supersymmetric structure, meaning that all eigenstates are degenerate. The supersymmetric form of the model, in combination with a chiral symmetry, is revealed to protect the zero dimensional topological zero energy bound states.
Subsequently, we focus on topological phenomena in presence of interactions in Chapter 8. Here, a possibility for the realization of chiral topological insulators is introduced. Although topological superconducting orders are usually not the system's ground state, it turns out that they correspond to prototypical subleading instabilities with ideal properties to be targeted with a light pulse. Within this chapter, the stability of general subleading superconducting at higher energies is discussed in detail.
Furthermore, a second mechanism for the realization of unconventional superconductivity is introduced in Chapter 9. Here, a strong coupling mechanism promoting superconductivity from purely repulsive electronic interactions is established in hetero bilayer structure. This approach is investigated numerically, using a quasi one-dimensional variant of the system, which allows for a study even beyond the strong coupling regime. Magnetic correlations are analyzed in addition to superconducting properties.
After this, in Chapter 10, we consider a class of systems which typically show strong correlations, flat-band systems. These could be a prototypical example of systems allowing for a realization of the mechanism introduced in the previous chapter. However, only flat-band systems in one dimension without electronic correlations are investigated, where the appearance of the Ruderman-Kittel-Kasuya-Yosida interaction is studied, which describes the indirect coupling of two magnetic impurities via the itinerant electrons. Due to the vanishing of the band width, the impurities cannot be treated with the perturbative standard approach for the Ruderman-Kittel-Kasuya-Yosida interaction and a more careful analysis is necessary.

Finally, in Chapters 11 and 12, the results of this thesis are summarized and possible directions for the future are discussed.

In this thesis, units with $\hbar = k_B = 1$ are employed.

Part II

Methods

Chapter 3

Exact Diagonalization

We start by introducing a very basic and straightforward method that can be used to study quantum systems, the exact diagonalization (ED). Here, the system's Hamiltonian is translated to a matrix which is then diagonalized to find eigenstates and eigenvalues of the Hamiltonian. In this thesis, we use the term 'exact diagonalization' for the diagonalization of the Hamiltonian matrix both for interacting and non-interacting systems. Moreover, the term exact diagonalization is usually not only used for the full diagonalization of the matrix but also refers to more advanced methods like the Lanczos method (see e.g. Ref. [108]). In this thesis, we use the term 'diagonalize' as a general term including such advanced approaches and do not specify the exact method.

In this chapter, we first briefly recapitulate how ED can be performed for non-interacting lattice models. We then discuss the continuum case with the focus on a disk geometry. Here, we define the needed basis function and show how to project the Hamiltonian onto this basis. Finally, we quickly outline the difference for ED in interacting systems. Since this method is well-known and only rarely used in this thesis, we refrain from showing a detailed introduction and refer the reader to Ref. [108, 109] for more details.

3.1 Non-Interacting Systems

First, we consider non-interacting models and discuss how to solve them with ED. Here, the Hamiltonian can be projected onto a set of single-particle states to obtain a matrix that can be diagonalized. In a many-body ground state with N fermions, the N eigenstates with the lowest energy are then occupied.

3.1.1 Lattice Models

For non-interacting lattice models, ED is straightforward since the Hamiltonian can be projected onto the site-local functions. We still summarize this technique since the continuum case introduced below is easier to understand when comparing it to the lattice case. A non-interacting lattice Hamiltonian in first quantization is simply given by

$$H = \sum_{i,j} \mathcal{H}_{i,j} \, |i\rangle \langle j| \; . \tag{3.1}$$

Here, $|i\rangle$ denotes the state corresponding to the local site i. Moreover, the set of local states $\{|i\rangle\}$ is a complete orthonormal basis. The eigenstates of the Hamiltonian can simply be obtained by diagonalizing the matrix $\mathcal{H}$ with elements $\mathcal{H}_{ij} = \langle i \,|\, H \,|\, j \rangle$.
Additional degrees of freedoms, such as orbitals or spins, can be included in this formalism by substituting i with a double index (i, α), where i denotes the site and α the orbital/spin index. This leads to the general parametrization $H = \sum_{(i,\alpha),(j,\beta)} \mathcal{H}_{(i,\alpha),(j,\beta)} \, |i, \alpha\rangle \langle j, \beta|$.

3.1.2 Continuum Models

For continuum models, the employment of ED requires identifying a good set of basis functions $|\psi_i\rangle$ first. We assume that the basis functions are orthonormal with respect to the scalar product [110]

$$\langle \psi_i \,|\, \psi_j \rangle = \int_V d\mathbf{x}\, \psi_i^*(\mathbf{x}) \psi_j(\mathbf{x}) = \delta_{i,j}\,. \tag{3.2}$$

Additionally, the basis functions need to reflect the boundary conditions given by the system's geometry. The continuous Hamiltonian can then be translated to the matrix

$$\mathcal{H}_{ij} = \langle \psi_i \,|\, H \,|\, \psi_j \rangle = \int_V d\mathbf{x}\, \psi_i^*(\mathbf{x})\, H\, \psi_j(\mathbf{x}) \tag{3.3}$$

in the space of basis functions. Here, we used the symbol H also for the real space representation of the Hamiltonian H. For convenience, this notation is used in the entire thesis. It is crucial to mention that the basis of a continuous system contains an infinite number of basis functions. Since it is impossible to diagonalize a general infinite matrix, the Hamiltonian matrix needs to be truncated and only a finite number of basis states are taken into account. Consequently, one has to ensure that the results are converged in the considered number of basis functions.

Basis Functions of a Disk

The algorithm presented below was used in Ref. [111] (see Chapter 7 for details) and thus, parts of the introduction below are based on this reference. Note that I only implemented the algorithm; basis functions and matrix elements were provided by Dr. Mikhail Pletyukhov.

In the following, we consider a disk of finite radius $R_>$. In this case, it is the natural choice to describe the system in polar coordinates. We begin by making the ansatz that the basis functions can be separated in angular and radial direction. Since all solutions have to be periodic in φ with a periodicity of 2π, we use complex exponentials as basis functions in the radial direction and define

$$\psi_{l\beta}(r,\varphi) = u_{l\beta}(r)\, \frac{1}{\sqrt{2\pi}} e^{il\varphi}\,. \tag{3.4}$$

Here, $l \in \mathbb{Z}$ and $\beta \in \mathbb{N}$ numerates the functions in angular and radial direction, respectively.
There are certain boundary conditions that the radial basis functions $u_{l\beta}$ should respect. On the one hand, the $\psi_{l,\beta}$ need to be well defined at $r = 0$. On the other hand, the wave function has to vanish at the system's boundary at $r = R_>$. Therefore, the radial basis functions must fulfill

$$u_{l\beta}(0) = 0 \text{ for } l \neq 0\,, \quad u_{l\beta}(R) = 0. \tag{3.5}$$

In agreement with the boundary conditions (3.5) and orthonormality equation (3.2), we choose basis functions of form [111]

$$u_{l\beta}(r) = \frac{\sqrt{2}}{R_>}\, \frac{J_{|l|}\left(z_{|l|,\beta}\, \dfrac{r}{R_>}\right)}{|J_{|l|+1}(z_{|l|,\beta})|}\,. \tag{3.6}$$

Here, $J_\nu(z)$ is the Bessel function of the first kind and we denoted the positive zeros of the Bessel function with $z_{\nu\beta}$. They are defined using $J_\nu(z_{\nu,\beta}) = 0$ with $0 < z_{\nu,1} < z_{\nu,2} < \dots$. We check that these functions indeed fulfill the orthonormality conditions

$$\begin{aligned}
\langle l', \beta' \,|\, l, \beta \rangle &= \int_0^{R_>} r\, dr \int_0^{2\pi} d\varphi\, \psi_{l'\beta'}(r,\varphi)^*\, \psi_{l\beta}(r,\varphi) \\
&= \frac{1}{2\pi} \int_0^{R_>} r\, dr \int_0^{2\pi} d\varphi\, e^{i(l-l')\varphi}\, u_{l'\beta'}(r,\varphi)^*\, u_{l\beta}(r,\varphi)
\end{aligned}$$

$$= \delta_{l,l'} \frac{2}{R_>^2 \, |J_{|l|+1}(z_{|l|,\beta})| \, |J_{|l|+1}(z_{|l|,\beta'})|} \underbrace{\int_0^{R_>} dr \, r \, J_{|l|}\left(z_{|l|,\beta} \frac{r}{R_>}\right) J_{|l|}\left(z_{|l|,\beta'} \frac{r}{R_>}\right)}_{= \frac{R_>^2}{2} \delta_{\beta,\beta'} \left[J_{|l|+1}(z_{|l|,\beta})\right]^2 \text{ (see e.g. Ref. [112])}}$$

$$= \delta_{l,l'} \delta_{\beta,\beta'} \, . \tag{3.7}$$

Moreover, it is well known that both functions (radial part and angular part) are complete sets of basis functions since they are used for the complex Fourier transform [113] and Fourier-Bessel transform [112], respectively. Therefore, their combination (3.4) has to be a complete basis set as well and thus, it can be used as a basis for the disk. Furthermore, it is well known, that the chosen functions are the eigenfunctions of the Laplacian on a disk (see e.g. Ref. [114, 115] for the case of a unit disk). Therefore, the kinetic energy operator $H_{\text{kin}} = \mathbf{p}_K^2/2m = \Delta/2m$ is conveniently already diagonal in this basis.

In the following, we consider the same disk but we add an infinitely small hole in the center with $R_< = 0$, and apply a magnetic flux of $\Phi = 2\pi f$ with $f \in [0, 2\pi)$ through the hole. We still decompose the eigenfunctions according to Eq. (3.4), but the boundary conditions are different. All eigenfunctions for finite f have to be zero for $r = 0$ and they no longer have to be analytic in this point since $r = 0$ acts as a second boundary of the system. We therefore choose a different basis [111]

$$u_{l\beta}(r) = \frac{\sqrt{2}}{R} \frac{J_{|l+f|}(z_{|l+f|,\beta} \, r/R)}{|J_{|l+f|+1}(z_{|l+f|,\beta})|} \, . \tag{3.8}$$

We note that we retrieve the original basis functions (3.6) for $f = 0$, which is expected since the hole is essentially non-existent at vanishing flux. The orthonormality and completeness of the basis for finite f can be shown analogously to $f = 0$.

Interestingly, the chosen basis functions are eigenfunctions of the kinetic energy for all values of f. The corresponding operator $H_{\text{kin}} = \frac{\mathbf{p}_K^2}{2m}$ with a real space representation of

$$H_{\text{kin}} = \frac{\mathbf{p}_K^2}{2m} = \frac{1}{2m} \left[-\frac{1}{r} \partial_r r \partial_r + \frac{1}{r^2} (i\partial_\varphi - f)^2 \right] , \tag{3.9}$$

is therefore already diagonal within this choice and we find

$$H_{\text{kin}} \, \psi_{l\beta}(r, \varphi) = \epsilon_{l\beta} \, \psi_{l\beta}(r, \varphi) \text{ with } \epsilon_{l\beta} = \frac{z_{|l+f|,\beta}^2}{2m R_>^2} \, . \tag{3.10}$$

As mentioned above, it is necessary to properly truncate the Hamiltonian. We use cutoffs of N_L and N_Z and only take states with

$$-N_L + 1 \leq l \leq N_L \text{ and } \beta \leq N_Z \tag{3.11}$$

into account. This means that strongly varying parts of the Hamiltonian are neglected, which usually give irrelevant contributions to the low-energy states that we are interested in. Of course, convergence in these cutoffs needs to be ensured for all results. For the results shown in this thesis, it was sufficient to use cutoffs $N_L = 10$ and $N_Z = 150$.
Additional degrees of freedom can be taken into account by enlarging the corresponding basis analogous to the case of lattice models.

3.2 Interacting Systems

For interacting systems (see Refs. [108, 109] for more details as mentioned above), the Hamiltonian has to be projected onto many-particle states instead of single-particle states. After identifying the many-particle basis $|\psi_i\rangle$, one calculates the matrix $\mathcal{H}$ with matrix elements

$$\mathcal{H}_{ij} = \langle \psi_i \, | \, H \, | \, \psi_j \rangle \, , \tag{3.12}$$

(see e.g. [109]) and diagonalizes it in the same manner as for non-interacting systems.
The main disadvantage is that the matrix dimensions do not scale linearly with the system size, but exponentially. Consequently, it is helpful to identify symmetries of the Hamiltonian, such as translational invariance and conservation of spin. Exploiting these, the Hamiltonian can be brought into a block-diagonal form, where the blocks describe the symmetry sectors and can be solved individually [108]. This affects the matrix dimensions and can reduce the numerical effort of ED.
Compensating for this enormous cost, ED has the major advantage that it can resolve the whole spectrum, which is beyond the capabilities of most other methods for correlated systems. Nevertheless, it is helpful to introduce different approaches since ED is usually limited to a few sites (for lattice models) due to the aforementioned reasons. Therefore, we discuss the density matrix renormalization group in the following, which usually allows for the study of larger system sizes, especially in one dimension.

Chapter 4

Density Matrix Renormalization Group

In the following, the density matrix renormalization group (DMRG) is briefly outlined. Interacting systems are in general difficult to study, since the number of coefficients grows exponentially with system size. Therefore, the straight-forward ED approach, introduced in the last chapter, can only be used to simulate a few sites. Consequently, it is necessary to come up with different, more involved methods. The DMRG is an efficient tool to study ground states (or in general low-energy states) of low-dimensional interacting quantum systems by significantly reducing the number of parameters since it does not consider the full Hilbert space [116]. Importantly, one needs to verify that the state obtained by DMRG is converged with the amount of parameters taken into account.

First, matrix product states are introduced, which turn out to be the natural language for DMRG simulations. After this, we briefly discuss matrix product operators, which are the operator version of matrix product states. We explore, how matrix product operators can be applied to matrix product states and how expectation values can be calculated. The algorithm employed in this thesis, which is the iterative ground state search, is presented afterwards. For additional algorithms, such as time evolutions via time evolved block decimation (TEBD), the reader is referred to Ref. [117]. After discussing the ground state search for finite system sizes, we then discuss how the presented technique can be transferred to infinite systems. Moreover, we briefly discuss how entanglement dictates the success of DMRG and we see when DMRG is expected to fail. Finally, it is explained, how extrapolations to infinite bond dimension (infinite matrices) are performed within this thesis. The majority of this chapter (Sections 4.1-4.5) mainly follows Ref. [117] with additional influence from Refs. [118, 119]. The figures are also strongly based on these references. Within this thesis, we use the TeNPy library [120] for any DMRG calculations.

4.1 Matrix Product States

Although DMRG was originally formulated differently [121, 122], it turns out that matrix product states (MPSs) are the natural environment to perform DMRG calculations. Therefore, MPSs are introduced first and it is shown how any quantum state can be written in this form.

The crucial problem of many-body systems is the scaling of parameters with the system size. Imagining a system of L sites with a local Hilbert space of dimension d, the total number of states is given by d^L. This means that number of coefficients scales exponentially with the system size. In contrast to this, one can construct MPSs that scale only linearly with the system size at a fixed so-called “(maximal) bond dimension". This is a great advantage and makes calculations of larger system sizes possible. The main idea is to decompose the state into a product of matrices. The dimensions of these matrices are called bond dimensions. Interestingly, MPSs are exact representations of arbitrary quantum states up to the error due to matrix truncations.

4.1.1 Singular Value Decomposition

The main tool needed to write an arbitrary quantum state as an MPS is the singular value decoposition (SVD). An SVD decomposes an arbitrary matrix M (with dimensions $N_A \times N_B$) into

$$M = USV^\dagger \,. \tag{4.1}$$

Here, the matrices U (of dimension $N_A \times \min(N_A, N_B)$), S (of dimension $\min(N_A, N_B) \times \min(N_A, N_B)$) and $V^\dagger$ (of dimension $\min(N_A, N_B) \times N_B$) have the following beneficial attributes:
U and $V^\dagger$ both fulfill $U^\dagger U = I$ and $V^\dagger V = I$, respectively, which will turn out to be helpful for the calculation of overlaps and expectation values.
The matrix S is a diagonal matrix with non-negative entries s_i. These values are called singular values justifying the name of the decomposition. We can choose them to be sorted in descending order $s_1 \geq s_2 \geq \ldots \geq s_r > 0$, where r denotes the rank of the matrix, given by the number of nonzero singular values.

As previously stated, we will usually need to truncate the matrices in order to control the dimensions of the MPS and to make it suitable for calculations. A great property of the SVD is that it makes the optimal truncation apparent.
Let us assume we have a new diagonal matrix S' with diagonal entries $s_1 \geq s_2 \geq \ldots \geq s_{r'} > 0$ and $r' < r$. In other words, the last $r - r'$ singular values have been set to zero in comparison to the original matrix S. The new decomposed matrix $M' = US'V^\dagger$ is then known to be the best approximation with rank r' of M (in the Frobenius norm $||M||^2 = \sum_{i,j} |M_{ij}|^2$). This means that the optimal way to truncate our matrix is to neglect the smallest $r - r'$ singular values. In the actual calculation, only the first r' columns of U and the first r' rows of $V^\dagger$ need to be taken into account for the truncated matrix, which leads to a reduction of the matrix dimension and therefore the number of parameter.

4.1.2 Matrix Product State of an Arbitrary Quantum State

Any possible quantum state can be written in the form

$$|\psi\rangle = \sum_{\{\sigma_i\}} c_{\sigma_1,\ldots,\sigma_L} |\sigma_1, ..., \sigma_L\rangle \;, \tag{4.2}$$

where L is the systems size and σ_i denotes the physical index of the local Hilbert space with dimension d. The coefficient tensor $c_{\sigma_1,\ldots,\sigma_L}$ has dimension d^L, which means that number of coefficients grow exponentially with the system size. We will see that the number of coefficients of a (truncated) MPS scale only linearly with the systems size.
We now decompose the coefficient tensor into a product of matrices by employing SVDs repeatedly. To this end, we first reshape the tensor into a matrix Ψ and then apply an SVD in order to separate the first physical index from all the others:

$$\begin{aligned} c_{\sigma_1,\ldots,\sigma_L} = \Psi_{\sigma_1,(\sigma_2,\ldots,\sigma_L)} &= \sum_{a_1=1}^{r_1} U_{\sigma_1,a_1} S_{a_1,a_1} \left(V^\dagger\right)_{a_1,(\sigma_2,\ldots,\sigma_L)} = \sum_{a_1=1}^{r_1} U_{\sigma_1,a_1} c_{a_1,\sigma_2,\ldots,\sigma_L} \\ &= \sum_{a_1=1}^{r_1} A^{\sigma_1}_{a_1} c_{a_1,\sigma_2,\ldots,\sigma_L} \;, \end{aligned} \tag{4.3}$$

where we have multiplied $S_{a_1,a_1} \left(V^\dagger\right)_{a_1,(\sigma_2,\ldots,\sigma_L)} = c_{a_1,\sigma_2,\ldots,\sigma_L}$ and reshaped $U_{\sigma_1,a_1} = A^{\sigma_1}_{a_1}$. We end up in a similar situation and can perform the same steps with the new tensor $c_{a_1,\sigma_2,\ldots,\sigma_L}$:

$$\begin{aligned} c_{\sigma_1,\ldots,\sigma_L} = \sum_{a_1=1}^{r_1} A^{\sigma_1}_{a_1} c_{a_1,\sigma_2,\ldots,\sigma_L} &= \sum_{a_1=1}^{r_1} A^{\sigma_1}_{a_1} \Psi_{(a_1,\sigma_2),(\sigma_2,\ldots,\sigma_L)} \\ = \sum_{a_1=1}^{r_1} \sum_{a_2=1}^{r_2} A^{\sigma_1}_{a_1} U_{(a_1,\sigma_2),a_2} S_{a_2,a_2} \left(V^\dagger\right)_{a_2,(\sigma_3,\ldots,\sigma_L)} &= \sum_{a_1=1}^{r_1} \sum_{a_2=2}^{r_2} A^{\sigma_1}_{a_1} A^{\sigma_2}_{a_1,a_2} c_{a_2,\sigma_3,\ldots,\sigma_L} \end{aligned} \tag{4.4}$$

with $S_{a_2,a_2}\left(V^\dagger\right)_{a_2,(\sigma_3,\ldots,\sigma_L)} = c_{a_2,\sigma_3,\ldots,\sigma_L}$ and $U_{(a_1,\sigma_2),a_2} = A^{\sigma_2}_{a_1,a_2}$.
Continuing with this process, one ends up with the multiplication of matrices

$$\begin{aligned} c_{\sigma_1,\ldots,\sigma_L} &= \sum_{\{a_i\}} A^{\sigma_1}_{a_1} A^{\sigma_2}_{a_1,a_2} \cdots A^{\sigma_2}_{a_{L-2},a_{L-1}} A^{\sigma_L}_{a_{L-1}} \\ &= A^{\sigma_1} \cdot A^{\sigma_2} \cdot \ldots \cdot A^{\sigma_{L-1}} \cdot A^{\sigma_L} \end{aligned} \tag{4.5}$$

and the final MPS form of the quantum state

$$|\psi\rangle = \sum_{\{\sigma_i\}} A^{\sigma_1} \cdot A^{\sigma_2} \cdot \ldots \cdot A^{\sigma_{L-1}} \cdot A^{\sigma_L} |\sigma_1, \ldots, \sigma_L\rangle \ . \tag{4.6}$$

In this chapter, we explicitly denote the matrix products with a dot to distinguish the two notations shown in Eq. (4.5). However, we refrain from showing these explicit dots in the rest of this thesis. The matrices A^{σ_i} (with fixed σ_i) will in general have dimensions $(1\times d)$, $(d\times d^2)$, ..., $(d^{L/2-1}\times d^{L/2})$, $(d^{L/2}\times d^{L/2-1})$, ..., $(d^2\times d)$, $(d\times 1)$ assuming an even system size L. Of course, this still leads to exponential number of parameters since there is no loss of information. Only if the matrices are truncated to a maximal bond dimension, the number of coefficients scales linearly with the system size, since we need L tensors for the MPS.

Left-Canonical Form

Remembering the feature $U^\dagger U = I$ of the SVD, one can find that the current choice of tensors leads to an interesting property. One can find

$$\begin{aligned} \delta_{a_\ell,a'_\ell} &= \sum_{a_{\ell-1},\sigma_\ell} \left(U^\dagger\right)_{a_\ell,(a_{\ell-1},\sigma_\ell)} U_{(a_{\ell-1},\sigma_\ell),a'_\ell} = \sum_{a_{\ell-1}\sigma_\ell} \left(A^{\sigma_\ell\dagger}\right)_{a_\ell,a_{\ell-1}} A^{\sigma_\ell}_{a_{\ell-1},a'_\ell} \\ &= \sum_{\sigma_\ell} \left(A^{\sigma_\ell\dagger} A^{\sigma_\ell}\right)_{a_\ell,a'_\ell} \end{aligned} \tag{4.7}$$

and therefore, the A-tensors fulfill

$$\sum_{\sigma_l} A^{\sigma_l\dagger} A^{\sigma_l} = I \tag{4.8}$$

and are called left-normalized. When introducing matrix product operators, we will note how this feature simplifies many calculations.
An MPS consisting of only left normalized tensors, is called left-canonical. Nevertheless, this choice is not unique and there is a certain gauge freedom in the MPS representation.

Right-Canonical Form

One can also construct a right-canonical MPS by separating the physical indices from the right. This leads to

$$\begin{aligned} c_{\sigma_1,\ldots,\sigma_L} = \Psi_{(\sigma_1,\ldots,\sigma_{L-1}),\sigma_L} &= \sum_{a_{L-1}=1}^{r_{L-1}} U_{(\sigma_1,\ldots,\sigma_{L-1}),a_{L-1}} S_{a_{L-1},a_{L-1}} \left(V^\dagger\right)_{a_{L-1},\sigma_L} \\ &= \sum_{a_{L-1}=1}^{r_{L-1}} c_{\sigma_1,\ldots,\sigma_{L-1},a_{L-1}} B^{\sigma_L}_{a_{L-1}} = \ldots = \sum_{\{a_i\}} B^{\sigma_1}_{a_1} B^{\sigma_2}_{a_1,a_2} \cdots B^{\sigma_{L-1}}_{a_{L-2},a_{L-1}} B^{\sigma_L}_{a_{L-1}}. \end{aligned} \tag{4.9}$$

in the same manner as shown for the left-canonical form. Here, we defined $B^{\sigma_L}_{a_{L-1}} = \left(V^\dagger\right)_{a_{L-1},\sigma_L}$ and $U_{(\sigma_1,\ldots,\sigma_{L-1}),a_{L-1}} S_{a_{L-1},a_{L-1}} = c_{\sigma_1,\ldots,\sigma_{L-1},a_{L-1}}$, which corresponds to a reshaping of $V^\dagger$, as well as a multiplication of U and S and a reshaping afterwards.
The MPS can be written as

$$|\psi\rangle = \sum_{\{\sigma_i\}} B^{\sigma_1} \cdot B^{\sigma_2} \cdot \ldots \cdot B^{\sigma_{L-1}} \cdot B^{\sigma_L} |\sigma_1, \ldots, \sigma_L\rangle \ , \tag{4.10}$$

where the B-tensors fulfill

$$\sum_{\sigma_l} B^{\sigma_l} B^{\sigma_l \dagger} = I \tag{4.11}$$

due to $V^\dagger V = I$ and are called right-normalized.

Mixed-Canonical Form

Finally, it is also possible to combine both representations and use a mixed-canonical form. Here, one starts by decomposing the state e.g. from the left and stops after the state has been decomposed until site ℓ. The current form of the coefficient tensor is then given by

$$c_{\sigma_1,\ldots,\sigma_L} = \sum_{\{a_i\},\, i=1,\ldots,\ell} A^{\sigma_1}_{a_1} A^{\sigma_2}_{a_1,a_2} \cdots A^{\sigma_\ell}_{a_{\ell-1},a_\ell} S_{a_t,a_\ell} \left(V^\dagger\right)_{a_\ell,(\sigma_{\ell+1},\ldots,\sigma_L)} . \tag{4.12}$$

We now reshape $\left(V^\dagger\right)_{a_\ell,(\sigma_{\ell+1},\ldots,\sigma_L)}$ and start decomposing it from the right. This leads to

$$\begin{aligned}
\left(V^\dagger\right)_{a_\ell,(\sigma_{\ell+1},\ldots,\sigma_L)} &= \Psi_{(a_\ell,\sigma_{\ell+1},\ldots,\sigma_{L-1}),\sigma_L} = \sum_{a_{L-1}=1}^{r_{L-1}} U_{(a_\ell,\sigma_{\ell+1},\ldots,\sigma_{L-1}),a_{L-1}} S_{a_{L-1},a_{L-1}} \left(V^\dagger\right)_{a_{L-1},\sigma_L} \\
&= \sum_{a_{L-1}=1}^{r_{L-1}} \Psi_{(a_\ell,\sigma_{\ell+1},\ldots,\sigma_{L-2}),(a_{L-1},\sigma_{L-1})} B^{\sigma_L}_{a_{L-1}} \\
&= \ldots = \sum_{\{a_i;\, i>\ell\}} U_{(a_\ell,\sigma_{\ell+1}),a_{\ell+1}} S_{a_{\ell+1},a_{\ell+1}} B^{\sigma_{\ell+2}}_{a_{\ell+1},a_{\ell+2}} \cdots B^{\sigma_L}_{a_{L-1}} \\
&= \sum_{\{a_i;\, i>\ell\}} B^{\sigma_{\ell+1}}_{a_\ell,a_{\ell+1}} \cdots B^{\sigma_L}_{a_{L-1}} ,
\end{aligned} \tag{4.13}$$

where $U_{(a_\ell,\sigma_{\ell+1}),a_{\ell+1}}$ and $S_{a_{\ell+1},a_{\ell+1}}$ were multiplied and reshaped to $B^{\sigma_{\ell+1}}_{a_\ell,a_{\ell+1}}$. Here, we exploited that this tensor has to be right-normalized due to the properties of $V^\dagger$ from the SVD:

$$\begin{aligned}
\delta_{a_\ell,a'_\ell} &= \sum_{\{\sigma_i;\, i>L\}} \left(V^\dagger\right)_{a_\ell,(\sigma_{l+1},\ldots,\sigma_L)} V_{(\sigma_{\ell+1}\ldots\sigma_L),a'_\ell} \\
&= \left[\sum_{\{\sigma_i;\, i>L\}} B^{\sigma_{\ell+1}} \cdot \ldots \cdot B^{\sigma_L} \cdot B^{\sigma_L \dagger} \cdot \ldots \cdot B^{\sigma_{\ell+1}\dagger} \right]_{a_\ell,a'_\ell} \\
&= \left[\sum_{\sigma_{\ell+1}} B^{\sigma_{\ell+1}} \cdot \ldots \cdot \underbrace{\left(\sum_{\sigma_L} B^{\sigma_L} \cdot B^{\sigma_L \dagger} \right)}_{I} \cdot \ldots \cdot B^{\sigma_{\ell+1}\dagger} \right]_{a_\ell,a'_\ell} \\
&= \left[\sum_{\sigma_{\ell+1}} B^{\sigma_{\ell+1}} \cdot \ldots \cdot \underbrace{\left(\sum_{\sigma_{L-1}} B^{\sigma_{L-1}} \cdot B^{\sigma_{L-1}\dagger} \right)}_{I} \cdot \ldots \cdot B^{\sigma_{\ell+1}\dagger} \right]_{a_\ell,a'_\ell} \\
&= \ldots = \left[\sum_{\sigma_{\ell+1}} B^{\sigma_{\ell+1}} B^{\sigma_{\ell+1}\dagger} \right]_{a_\ell,a'_\ell} .
\end{aligned} \tag{4.14}$$

The coefficient tensor and the MPS can therefore be written as

$$\begin{aligned}
c_{\sigma_1,\ldots,\sigma_L} &= \sum_{\{a_i\}} A^{\sigma_1}_{a_1} \cdots A^{\sigma_\ell}_{a_{\ell-1},a_\ell} S_{a_\ell,a_\ell} B^{\sigma_{\ell+1}}_{a_\ell,a_{\ell+1}} \cdots B^{\sigma_L}_{a_L} \\
&= A^{\sigma_1} \cdot \ldots \cdot A^{\sigma_\ell} S B^{\sigma_{\ell+1}} \cdot \ldots \cdot B^{\sigma_L} ,
\end{aligned} \tag{4.15}$$

$$|\psi\rangle = \sum_{\{\sigma_i\}} A^{\sigma_1} \cdot \ldots \cdot A^{\sigma_\ell} \cdot S \cdot B^{\sigma_{\ell+1}} \cdot \ldots \cdot B^{\sigma_L} |\sigma_1, \ldots, \sigma_L\rangle \ , \tag{4.16}$$

which is called the mixed-canonical form. Here, an additional tensor S appears on the bond between the A and B tensors.

Let us now bring the state into a slightly different notation by multiplying $A^{\sigma_l} \cdot S = M^{\sigma_l}$. The MPS then has the form

$$|\psi\rangle = \sum_{\{\sigma_i\}} A^{\sigma_1} \cdot \ldots \cdot A^{\sigma_{\ell-1}} \cdot M^{\sigma_\ell} \cdot B^{\sigma_{\ell+1}} \cdot \ldots \cdot B^{\sigma_L} |\sigma_1, \ldots, \sigma_L\rangle \ , \tag{4.17}$$

where the tensor M is the only tensor which is neither right- nor left-normalized. Although this form looks slightly different since there is no tensor on any bonds, this representation is still called mixed-canonical. It is possible to move the unnormalized tensor M with an SVD, which will be beneficial in the ground state search algorithm. To this end, we first contract the product $A^{\sigma_{\ell-1}} M^{\sigma_\ell}$ into a new tensor Ψ and perform an SVD afterwards. We find

$$\begin{aligned}
c_{\sigma_1,\ldots,\sigma_L} &= \sum_{\{a_i\}} A^{\sigma_1}_{a_1} \cdots A^{\sigma_{\ell-2}}_{a_{\ell-3},a_{\ell-2}} A^{\sigma_{\ell-1}}_{a_{\ell-2},a_{\ell-1}} M^{\sigma_\ell}_{a_{\ell-1},a_\ell} B^{\sigma_{\ell+1}}_{a_\ell,a_{\ell+1}} \cdots B^{\sigma_L}_{a_{L-1}} \\
&= \sum_{\{a_i;\, i\neq\ell-1\}} A^{\sigma_1}_{a_1} \cdots A^{\sigma_{\ell-2}}_{a_{\ell-3},a_{\ell-2}} \Psi_{(a_{\ell-2},\sigma_{\ell-1}),(a_\ell,\sigma_\ell)} B^{\sigma_{\ell+1}}_{a_\ell,a_{\ell+1}} \cdots B^{\sigma_L}_{a_{L-1}} \\
&= \sum_{\{a_i\}} A^{\sigma_1}_{a_1} \cdots A^{\sigma_{\ell-2}}_{a_{\ell-3},a_{\ell-2}} U_{(a_{\ell-2},\sigma_{\ell-1}),a_{\ell-1}} S_{a_{\ell-1},a_{\ell-1}} \left(V^\dagger\right)_{a_{\ell-1},(a_\ell,\sigma_\ell)} B^{\sigma_{\ell+1}}_{a_\ell,a_{\ell+1}} \cdots B^{\sigma_L}_{a_{L-1}} \\
&= \sum_{\{a_i\}} A^{\sigma_1}_{a_1} \cdots A^{\sigma_{\ell-2}}_{a_{\ell-3},a_{\ell-2}} M^{\sigma_{\ell-1}}_{a_{\ell-2},a_{\ell-1}} B^{\sigma_\ell}_{a_{\ell-1},a_\ell} B^{\sigma_{\ell+1}}_{a_\ell,a_{\ell+1}} \cdots B^{\sigma_L}_{a_{L-1}} \ ,
\end{aligned} \tag{4.18}$$

where we contracted $U_{(a_{\ell-2},\sigma_{\ell-1}),a_{\ell-1}} S_{a_{\ell-1},a_{\ell-1}} = M^{\sigma_{\ell-1}}_{a_{\ell-2},a_{\ell-1}}$ and reshaped $\left(V^\dagger\right)_{a_{\ell-1},(a_\ell,\sigma_\ell)}$ to the right normalized tensor $B^{\sigma_\ell}_{a_{\ell-1},a_\ell}$. To move the unnormalized tensor to the right instead, one merely needs to follow the steps above in reverse order.

4.1.3 Graphical Representation

For any kind of tensor networks, of which MPS is a one dimensional example, a graphical representation is commonly used. In Fig. 4.1 it is displayed how the the representation of a state changes from the fully connected coefficient tensor to an MPS representation by decomposing it (a) from the left and (b) from the right. We start with the fully connected tensor which is denoted as a black rounded bar with vertical lines at its top denoting the physical indices. Then, we decompose it into a single site tensor, denoted by a blue filled circle on the left (right), with the remaining connected tensor on the other sites. The contraction of the two tensors gets indicated by a small line. The procedure is repeated until every tensor contains only a single physical index.
It is also possible to represent a state in the mixed-canonical form (4.16) graphically. In this case, one needs to change the graphical representation due to the additional tensor on the bond between A and B matrices. We denote this tensor using a diamond as shown in Fig. 4.2. Nonetheless, the graphical representation of a state in the mixed-canonical form (4.17) with no bond tensor does not differ from the left- or right-canonical form shown at the bottom of Fig. 4.1.
We will also use a graphical representation for matrix product operators, making this notation feasible for the description of all operations within the language of MPSs.

4.1.4 Γ-Λ Notation

Before moving from MPSs to matrix product operators, the Γ-Λ notation [123] is introduced. In contrast to the right- and left-canonical form, there are additional matrices present on each bond. This representation is called $\Gamma - \Lambda$ notation since the site and bond tensors are called Γ and Λ, respectively. We can derive this form by starting with the usual SVD (as in the decomposition of the left-canonical form). We reshape $U_{\sigma_1,a_1} = A^{\sigma_1}_{a_1} = \Gamma^{\sigma_1}_{a_1}$, rename $S_{a_1,a_1} = \Lambda^{[1]}_{a_1,a_1}$ and find

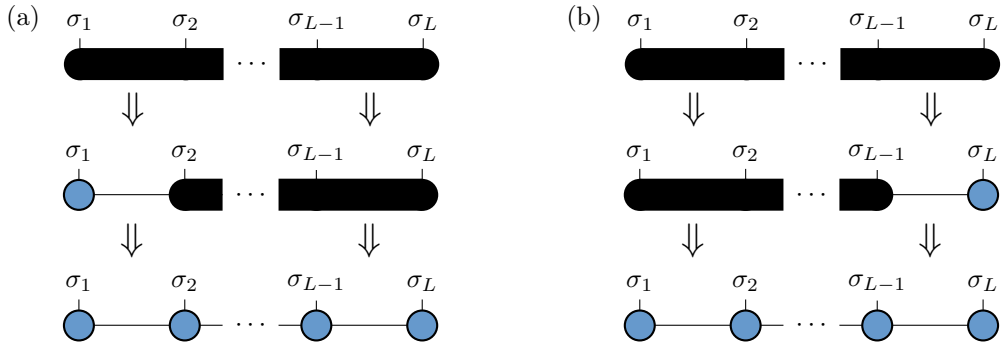

Figure 4.1: Iterative decomposition of an arbitrary quantum state into an MPS starting from the (a) left and (b) right. The fully connected coefficient tensor is denoted by a black box. One physical index after another gets separated by an SVD. The local tensor are shown by blue circles. The final state is in the (a) left-canonical and (b) right-canonical form, respectively.

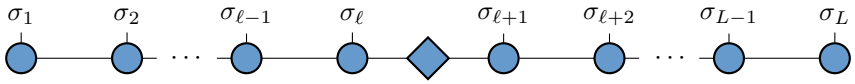

Figure 4.2: Mixed-canonical form of an MPS. In comparison to the left- and right-canonical form, there is an additional tensor on one of the bonds (see Eq. (4.16)), which is denoted by a blue diamond.

$$\begin{aligned} c_{\sigma_1,\ldots,\sigma_L} &= \Psi_{\sigma_1,(\sigma_2,\ldots,\sigma_L)} = \sum_{a_1} U_{\sigma_1,a_1} S_{a_1,a_1} \left(V^\dagger\right)_{a_1,(\sigma_2,\ldots,\sigma_L)} \\ &= \sum_{a_1} A^{\sigma_1}_{a_1} \Lambda^{[1]}_{a_1,a_1} \left(V^\dagger\right)_{a_1,(\sigma_2,\ldots,\sigma_L)} = \sum_{a_1} \Gamma^{\sigma_1}_{a_1} \Psi_{(a_1,\sigma_2),(\sigma_3,\ldots,\sigma_L)} \,. \end{aligned} \tag{4.19}$$

In contrast to the former decompositions, the matrix $\Lambda^{[1]}$ is reused below. In an numerical implementation, it therefore needs to be stored before contracting it with $V^\dagger$. Performing the next SVD leads to

$$\begin{aligned} c_{\sigma_1,\ldots,\sigma_L} &= \sum_{a_1} \Gamma^{\sigma_1}_{a_1} \Psi_{(a_1,\sigma_2),(\sigma_3,\ldots,\sigma_L)} = \sum_{a_1,a_2} \Gamma^{\sigma_1}_{a_1} U^{\sigma_2}_{(\sigma_2,a_1),a_2} S^{[2]}_{a_2,a_2} \left(V^\dagger\right)_{a_2,(\sigma_3,\ldots,\sigma_L)} \\ &= \sum_{a_1,a_2} \Gamma^{\sigma_1}_{a_1} A^{\sigma_2}_{a_1,a_2} \Lambda^{[2]}_{a_2,a_2} \left(V^\dagger\right)_{a_2,(\sigma_3,\ldots,\sigma_L)} = \sum_{a_1,a_2} \Gamma^{\sigma_1}_{a_1} A^{\sigma_2}_{a_1,a_2} \Psi_{(a_2,\sigma_3),(\sigma_4,\ldots,\sigma_L)} \,. \end{aligned} \tag{4.20}$$

Again, we reshaped U into A and renamed S into $\Lambda^{[2]}$. Now we get to the crucial point of this decomposition. Reusing the $\Lambda^{[1]}$ matrix we define

$$\Gamma^{\sigma_2}_{a_1,a_2} = \left(\Lambda^{[1]}_{a_1,a_1}\right)^{-1} A^{\sigma_2}_{a_1,a_2} \tag{4.21}$$

and decompose $A^{\sigma_2}_{a_1,a_2} = \Lambda^{[1]}_{a_1,a_1} \Gamma^{\sigma_2}_{a_1,a_2}$. We note that all $\Lambda^{[i]}$ are invertible after the truncation of all inessential singular values $s_i = 0$. This leads to

$$c_{\sigma_1,\ldots,\sigma_L} = \sum_{a_1,a_2} \Gamma^{\sigma_1}_{a_1} \Lambda^{[1]}_{a_1,a_1} \Gamma^{\sigma_2}_{a_1,a_2} \Psi_{(a_2,\sigma_3),(\sigma_4,\ldots,\sigma_L)} \,. \tag{4.22}$$

Repeating this procedure until the whole state is decomposed ends in

$$c_{\sigma_1,\ldots,\sigma_L} = \sum_{\{a_i\}} \Gamma^{\sigma_1}_{a_1} \Lambda^{[1]}_{a_1,a_1} \Gamma^{\sigma_2}_{a_1,a_2} \Lambda^{[2]}_{a_2,a_2} \cdots \Lambda^{[L-1]}_{a_{L-1},a_{L-1}} \Gamma^{\sigma_L}_{a_{L-1}} = \Gamma^{\sigma_1} \cdot \Lambda^{[1]} \cdot \Gamma^{\sigma_2} \cdot \Lambda^{[2]} \cdot \ldots \cdot \Lambda^{[L-1]} \cdot \Gamma^{\sigma_L} \tag{4.23}$$

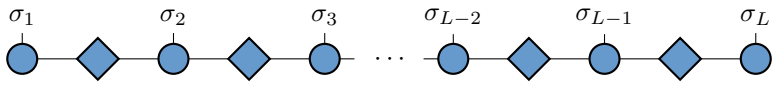

Figure 4.3: $\Gamma - \Lambda$ form of an MPS with tensors on the sites (Γ) and on the bonds (Λ). The Γ and Λ tensors are represented by blue circles and diamonds, respectively.

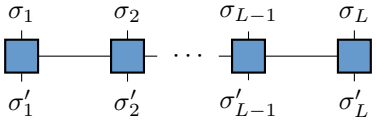

Figure 4.4: Matrix product operator with two physical indices (one incoming and one outgoing) on all sites. The W tensors of the operator are denoted by blue squares.

and the MPS can be written as

$$|\psi\rangle = \sum_{\{\sigma_i\}} \Gamma^{\sigma_1} \cdot \Lambda^{[1]} \cdot \Gamma^{\sigma_2} \cdot \Lambda^{[2]} \cdot \ldots \cdot \Lambda^{[L-1]} \cdot \Gamma^{\sigma_L} |\sigma_1, \ldots, \sigma_L\rangle \ . \tag{4.24}$$

One can easily change from the $\Gamma - \Lambda$ notation to left- or right-canonical form by contracting each site tensor with one bond tensor. To this end, we need to identify

$$A^{\sigma_\ell}_{a_{\ell-1},a_\ell} = \Lambda^{[\ell-1]}_{a_{\ell-1},a_{\ell-1}} \Gamma^{\sigma_\ell}_{a_{l-1},a_\ell}, \qquad B^{\sigma_\ell}_{a_{\ell-1},a_\ell} = \Gamma^{\sigma_\ell}_{a_{\ell-1},a_\ell} \Lambda^{[\ell]}_{a_\ell,a_\ell} \tag{4.25}$$

with $\Lambda^{[0]}_{a_0,a_0} = \Lambda^{[L]}_{a_L,a_L} = 1$. For the graphical representation shown in Fig. 4.3, the additional matrices get denoted by diamonds on the bonds, as in the case of the mixed-canonical form.

4.2 Matrix Product Operators and Observables

In the following matrix product operators (MPOs), the operator counterpart of MPSs, are introduced. After the detailed introduction to MPSs, there is only a short explanation about the decomposition of MPOs, since it is analogous to the one of MPSs. Following the demonstration of the decomposition by employing an example, the proper way to multiply states and operators as well as the calculation of expectation values in the MPS and MPO language are presented.

4.2.1 Decomposing an Arbitrary Operator

Any arbitrary operator can be written as

$$O = \sum_{\{\sigma_i\},\{\sigma'_i\}} c_{(\sigma_1,\sigma'_1),\ldots,(\sigma_L,\sigma'_L)} |\sigma_1, \ldots, \sigma_L\rangle \langle\sigma'_1, \ldots, \sigma'_L| \ . \tag{4.26}$$

Treating the double index $(\sigma_\ell, \sigma'_\ell)$ in the same way as the single index σ_ℓ of a state, the operator can be decomposed analogously. The MPO representation is then given by

$$\begin{aligned} O &= \sum_{\{\sigma_i\},\{\sigma'_i\}} \sum_{\{b_i\}} W^{\sigma_1,\sigma'_1}_{b_1} W^{\sigma_2,\sigma'_2}_{b_1,b_2} \cdots W^{\sigma_{L-1},\sigma'_{L-1}}_{b_{L-2},b_{L-1}} W^{\sigma_L,\sigma'_L}_{b_{L-1}} |\sigma_1, \ldots, \sigma_L\rangle \langle\sigma'_1, \ldots, \sigma'_L| \\ &= \sum_{\{\sigma_i\},\{\sigma'_i\}} W^{\sigma_1\sigma'_1} \cdot W^{\sigma_2\sigma'_2} \cdot \ldots \cdot W^{\sigma_{L-1}\sigma'_{L-1}} \cdot W^{\sigma_L\sigma'_L} |\sigma_1, \ldots, \sigma_L\rangle \langle\sigma'_1, \ldots, \sigma'_L| \ , \end{aligned} \tag{4.27}$$

which can be graphically represented as shown in Fig. 4.4. In contrast to an MPS, the single tensors of the MPO are denoted using blue squares that have two physical indices, one incoming and one outgoing corresponding to bra and ket, respectively.

Decomposition of an Example Hamiltonian

Instead of employing the brute-force method described above, we use an example Hamiltonian to show how the composition for these operators can be done in a more intuitive way below, also leading to a rather compact MPO representation. In contrast to Eq. (4.27), we include the ket and bra into the tensors and obtain

$$H = W^{[1]} \cdot W^{[2]} \cdot \ldots \cdot W^{[L-1]} \cdot W^{[L]} \tag{4.28}$$

with the matrices $W^{[i]}$ containing operators. In the following, we consider the example Hamiltonian

$$H = \sum_{i=1}^{L-1} \frac{J}{2} S_i^+ S_{i+1}^- + \frac{J}{2} S_i^- S_{i+1}^+ + J^z S_i^z S_{i+1}^z - h \sum_i S_i^z \,. \tag{4.29}$$

The Hamiltonian is written in a short notation for actual tensor products with identities on all unmentioned sites. The expanded form of any operator product is given by a "tensor string"

$$O_i P_j = I \otimes \ldots \otimes I \otimes \underbrace{O}_{\text{site } i} \otimes I \otimes \ldots \otimes I \otimes \underbrace{P}_{\text{site } j} \otimes I \otimes \ldots \otimes I \,. \tag{4.30}$$

For the decomposition of H, we start from the right end of the possible tensor strings and move bond by bond to the left. At each bond, there are 5 possible situations for the tensor strings that we need to take into account:

1 There is an already completed term to the right hand side of the current bond. In this case, there have to be only identities to the left. Therefore, the next operator to apply has to be I transitioning $1 \to 1$.

2, 3, 4 There is a "started" but not completed interaction term to the right. In this example, it could be an S^z (2), S^+ (3) or S^- (4) just to the right of the current bond. This immediately sets the next operator that needs to be applied and we transform $2, 3, 4 \to 1$ by applying S^z, S^- or S^+, respectively.

5 There are only identity terms to the right of the current bond. In this case, the next operator can be any of the operators being either a local term or the very right of an interaction term, as well as the identity. One can therefore apply $-hS^z$ ($5 \to 1$), S^z ($5 \to 2$), S^- ($5 \to 3$), S^+ ($5 \to 4$) or I ($5 \to 5$).

This leads to the local tensor ($i \neq 1, L$)

$$W^{[i]} = \begin{pmatrix} I & J^z S^z & \frac{J}{2} S^+ & \frac{J}{2} S^- & -hS^z \\ 0 & 0 & 0 & 0 & S^z \\ 0 & 0 & 0 & 0 & S^- \\ 0 & 0 & 0 & 0 & S^+ \\ 0 & 0 & 0 & 0 & I \end{pmatrix} . \tag{4.31}$$

Furthermore, the string is evidently in situation 1 on the very left, and situation 5 on the very right. Therefore, the first and last tensors are given by the first line and last column, respectively:

$$W^{[1]} = \begin{pmatrix} I & J^z S^z & \frac{J}{2} S^+ & \frac{J}{2} S^- & -hS^z \end{pmatrix} , \quad W^{[L]} = \begin{pmatrix} hS^z \\ S^z \\ S^- \\ S^+ \\ I \end{pmatrix} . \tag{4.32}$$

If the Hamiltonian contains longer ranged terms, e.g. next-nearest-neighbor interactions, one can employ the same decomposition idea by introducing additional intermediate states (see Ref. [117] for details).

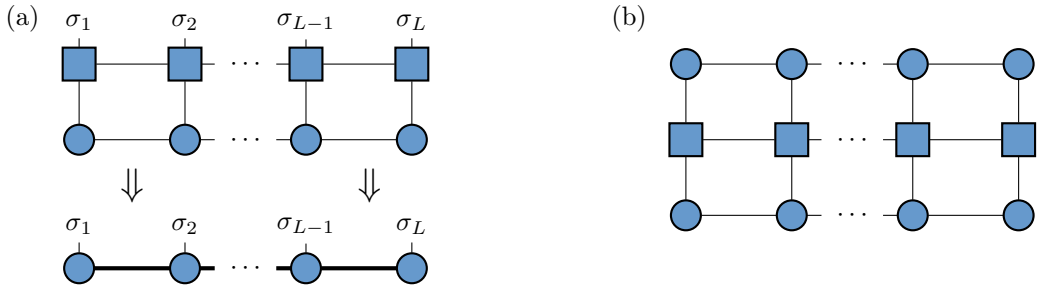

Figure 4.5: (a) Multiplication of an MPO and an MPS. The resulting MPS has bond dimensions given by the product of the bond dimensions of the MPO and the original MPS. (b) Network of tensors representing the expectation value of an MPO.

4.2.2 Applying an MPO to an MPS

After this short introduction to MPOs, we want to understand, how an MPO can be applied to an MPS. The multiplication leads to a new MPS

$$\begin{aligned} O|\psi\rangle &= \sum_{\{\sigma_i\},\{\sigma_i'\}} \left(\sum_{\{b_i\}} W_{b_1}^{\sigma_1,\sigma_1'} W_{b_1,b_2}^{\sigma_2,\sigma_2'} \cdots W_{b_{L-2},b_{L-1}}^{\sigma_{L-1},\sigma_{L-1}'} W_{b_{L-1}}^{\sigma_L,\sigma_L'} \right) \\ &\qquad \left(\sum_{\{a_i\}} M_{a_1}^{\sigma_1'} M_{a_1,a_2}^{\sigma_2'} \cdots M_{a_{L-2},a_{L-1}}^{\sigma_{L-1}'} M_{a_{L-1}}^{\sigma_L'} \right) |\sigma_1, \cdots, \sigma_L\rangle \\ &= \sum_{\{\sigma_i\}} \sum_{\{(b_i,a_i)\}} N_{(a_1,b_1)}^{\sigma_1} N_{(b_1,a_1),(b_2,a_2)}^{\sigma_2} \cdots N_{(b_{L-2},a_{L-2}),b_{L-1},a_{L-1})}^{\sigma_{L-1}} N_{(b_{L-1},a_{L-1})}^{\sigma_L} |\sigma_1, \ldots, \sigma_L\rangle \\ &= \sum_{\{\sigma_i\}} N^{\sigma_1} \cdot N^{\sigma_2} \cdot \ldots \cdot N^{\sigma_{L-1}} \cdot N^{\sigma_L} |\sigma_1, \ldots, \sigma_L\rangle \end{aligned} \tag{4.33}$$

with tensors $N_{(b_{i-1},a_{i-1}),(b_i,a_i)}^{\sigma_i} = \sum_{\sigma_i'} W_{b_{i-1}b_i}^{\sigma_i\sigma_i'} M_{a_{i-1}a_i}^{\sigma_i'}$. We note, that the bond dimensions of this MPS is given by the multiplication of the bond dimensions of O and $|\psi\rangle$. The process is depicted in Fig.4.5(a), where the contraction lines of the new MPS are thicker due to the enhanced bond dimensions.

4.2.3 Calculation of Expectation Values

Finally, we want to have a quick look at expectation values, which can be written as

$$\langle\psi \,|\, O \,|\, \psi\rangle = \sum_{\{\sigma_i,\sigma_i'\}} \sum_{\{a_i,b_i,a_i'\}} \left(M_{1,a_1}^{\sigma_1 *} W_{1,b_1}^{\sigma_1,\sigma_1'} M_{1,a_1'}^{\sigma_1'} \right) \cdots \left(M_{a_{L-1},1}^{\sigma_L *} W_{b_{L-1},1}^{\sigma_L,\sigma_L'} M_{a_{L-1}',1}^{\sigma_L'} \right) . \tag{4.34}$$

We can represent this expression with a network consisting of state and operator tensors shown in Fig. 4.5(b). The expectation value can then be calculated by contracting the whole network. There are several observables for which the network can be significantly simplified using an appropriate choice of tensors. Let us first consider a local operator O_j acting only on site j. If we choose the MPS to be in the mixed-canonical form (4.17), with the non-normalized tensor M on site j, the parts of the network located to the left and to the right of site j collapse to the identity, respectively, due to the normalization properties of the matrices. This leads to a simplified network as shown in Fig. 4.6(a).
Similarly, the calculation of a correlation function $\langle\psi \,|\, O_i P_j \,|\, \psi\rangle$ of local operators O_i and P_j (acting on sites i and j, respectively) can be simplified as shown in Fig. 4.6(b). Here, the unnormalized M tensor needs to be placed on or between the sites i and j, where the local operators are applied. In this case, the network can be simplified to a contraction of the tensors on and between sites i and j.

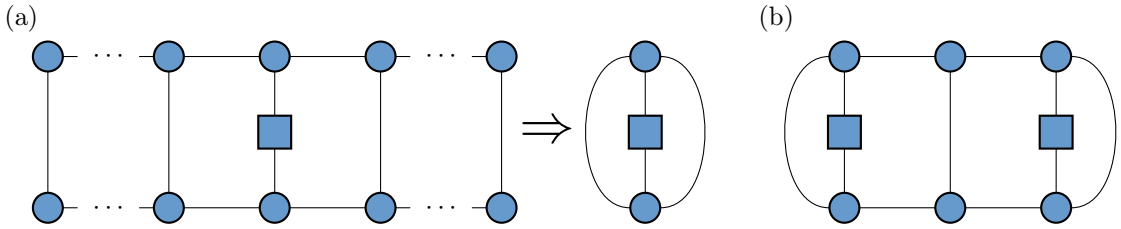

Figure 4.6: Simplification of the expectation values of (a) local operators and (b) the correlation of local operators when choosing an appropriate form for the MPS. Everything to the left and right of the operators simplifies to the identity.

4.3 Ground State Search

When searching for the system's ground state, one needs to find the state with the minimal energy, meaning that we need to minimize

$$\langle\psi\,|\,H\,|\,\psi\rangle \;\text{ with }\; \langle\psi\,|\,\psi\rangle = 1\,. \tag{4.35}$$

In other words, we need to minimize the expectation value of H with an equation constraint. This can be solved using the the well-known method of Lagrange multipliers (see e.g. Ref. [124]), which tells us that we need to extremize

$$\langle\psi\,|\,H\,|\,\psi\rangle - \lambda\left(\langle\psi\,|\,\psi\rangle - 1\right)\,, \tag{4.36}$$

whose graphical representation is shown in Fig. 4.7. We assume the state to be in the mixed-canonical form (4.17) and find

$$\langle\psi\mid\psi\rangle = \sum_{\sigma_\ell}\sum_{a_{\ell-1}a_\ell}\sum_{a'_{\ell-1}a'_\ell}\Psi^A_{a_{\ell-1},a'_{\ell-1}}M^{\sigma_\ell *}_{a_{\ell-1},a_\ell}M^{\sigma_\ell}_{a'_{\ell-1},a'_\ell}\Psi^B_{a_\ell,a'_\ell} = \sum_{\sigma_\ell}\sum_{a_{\ell-1}a_\ell}\sum_{a_{\ell-1}a'_\ell}M^{\sigma_\ell *}_{a_{\ell-1},a_\ell}M^{\sigma_\ell}_{a_{\ell-1},a_\ell}\,, \tag{4.37}$$

where we used

$$\Psi^A_{a_{\ell-1},a'_{\ell-1}} = \sum_{\{\sigma_i;\,i<\ell\}}\left(A^{\sigma_{\ell-1}\dagger}\cdot\ldots\cdot A^{\sigma_1\dagger}\cdot A^{\sigma_1}\cdot\ldots\cdot A^{\sigma_{\ell-1}}\right)_{a_{\ell-1},a'_{\ell-1}} = \delta_{a_{\ell-1},a_{\ell-1}}\,, \tag{4.38}$$

$$\Psi^B_{a_\ell,a'_\ell} = \sum_{\{\sigma_i;\,i>\ell\}}\left(B^{\sigma_{\ell+1}}\cdot\ldots\cdot B^{\sigma_L}\cdot B^{\sigma_L\dagger}\cdot\ldots\cdot B^{\sigma_{\ell+1}\dagger}\right)_{a'_\ell,a_\ell} = \delta_{a_\ell,a'_\ell}\,. \tag{4.39}$$

The expectation value can be written as

$$\langle\psi|H|\psi\rangle = \sum_{\sigma_\ell,\sigma'_\ell}\sum_{a'_{\ell-1},a'_\ell}\sum_{a_{\ell-1},a_\ell}\sum_{b_{\ell-1},b_\ell}L^{a_{\ell-1},a'_{\ell-1}}_{b_{\ell-1}}W^{\sigma_\ell,\sigma'_\ell}_{b_{\ell-1},b_\ell}R^{a_\ell,a'_\ell}_{b_\ell}M^{\sigma_\ell *}_{a_{\ell-1},a_\ell}M^{\sigma'_\ell}_{a'_{\ell-1},a'_\ell}\,, \tag{4.40}$$

where all tensors to the left and right of M and M^* were grouped to blocks

$$L^{a_{\ell-1},a'_{\ell-1}}_{b_{\ell-1}} = \sum_{\{a_i,b_i,a'_i;i<\ell-1\}}\left(\sum_{\sigma_1\sigma'_1}A^{\sigma_1 *}_{1,a_1}W^{\sigma_1,\sigma'_1}_{1,b_1}A^{\sigma'_1}_{1,a'_1}\right)\cdots\left(\sum_{\sigma_{\ell-1}\sigma'_{\ell-1}}A^{\sigma_{\ell-1}*}_{a_{\ell-2},a_{\ell-1}}W^{\sigma_{\ell-1},\sigma'_{\ell-1}}_{b_{\ell-2},b_{\ell-1}}A^{\sigma'_{\ell-1}}_{a'_{\ell-2},a'_{\ell-1}}\right), \tag{4.41}$$

$$R^{a_\ell,a'_\ell}_{b_\ell} = \sum_{\{a_i,b_i,a'_i;i>\ell\}}\left(\sum_{\sigma_{\ell+1}\sigma'_{\ell+1}}B^{\sigma_{\ell+1}*}_{a_\ell,a_{\ell+1}}W^{\sigma_{\ell+1},\sigma'_{\ell+1}}_{b_\ell,b_{\ell+1}}B^{\sigma'_{\ell+1}}_{a'_\ell,a'_{\ell+1}}\right)\cdots\left(\sum_{\sigma_L\sigma'_L}B^{\sigma_L *}_{a_{L-1},1}W^{\sigma_L,\sigma'_L}_{b_{L-1},1}B^{\sigma'_L}_{a'_{L-1},1}\right). \tag{4.42}$$

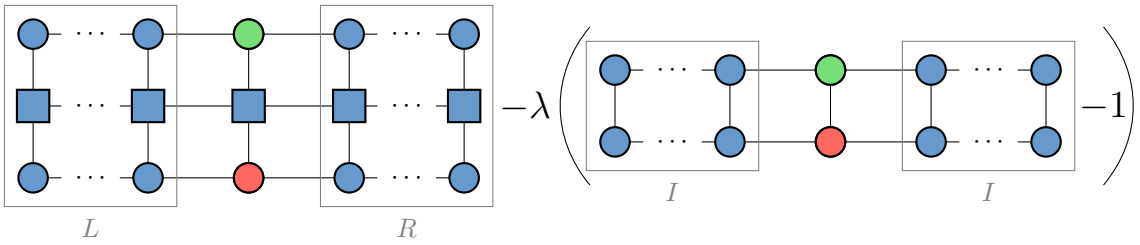

Figure 4.7: Expression $\langle\psi\,|\,H\,|\,\psi\rangle - \lambda\,(\langle\psi\,|\,\psi\rangle - 1)$, that needs to be minimized during the ground state search. We assume the state to be in the mixed-canonical form (4.17) with green/red being the unnormalized tensor of bra and ket, respectively. In $\langle\psi\,|\,H\,|\,\psi\rangle$ we group everything to the left and right of these into blocks L and R. In the $\langle\psi\,|\,\psi\rangle$ term, everything to the left and right of these tensors simplifies to the identity.

We first consider only the elements $M^{\sigma_\ell}_{a_{\ell-1},a_\ell}$ as variables. Since we want to extremize Eq. (4.36), we differentiate it with respect to $M^{\sigma_\ell *}_{a_{\ell-1},a_\ell}$ and set the result equal to zero. We end up with the simple eigenvalue problem

$$\sum_{\sigma'_\ell}\sum_{a'_{\ell-1}a'_\ell}\sum_{b_{\ell-1},b_\ell} L^{a_{\ell-1},a'_{\ell-1}}_{b_{\ell-1}} W^{\sigma_\ell,\sigma'_\ell}_{b_{\ell-1},b_\ell} R^{a_\ell,a'_\ell}_{b_\ell} M^{\sigma'_\ell}_{a'_{\ell-1},a'_\ell} - \lambda M^{\sigma'_\ell}_{a'_{\ell-1},a'_\ell} = 0 \tag{4.43}$$

which is shown in Fig. 4.8. We solve this equation for the $M^{\sigma_\ell}_{a_{\ell-1},a_\ell}$ with the lowest eigenvalue λ. The new $M^{\sigma_\ell}_{a_{\ell-1},a_\ell}$ is then the optimal tensor and we update the MPS accordingly. Its eigenvalue λ is the new approximation for the ground state energy.
Since we only minimized the expression (4.36) according to $M^{\sigma_\ell}_{a_{\ell-1},a_\ell}$, the other tensors are not optimized. We therefore find the system's ground state by sweeping through the system and optimizing one site after another until convergence is achieved. During the sweeping procedure one employs SVDs to move the to-be-updated M tensor to the right and to the left as shown in Eq. (4.18). Throughout this process one also saves and updates the expressions for R and L to avoid the repeated contraction of the whole network.
The full algorithm then involves the following steps:

1. We start from a right-canonical state and calculate the R blocks for all possible positions of the to-be-updated tensor.
2. We then optimize the tensor on the very left site.
3. We move to the second site by applying an SVD, calculate the L expression and save it for the upcoming left sweep. Additionally, we use the already saved expression for R.
4. We repeat this procedure and sweep to the right until the very right site is optimized.
5. Then we sweep left using the saved L expressions and calculate, as well as save, R at each step.
6. We keep sweeping through the system until the state is converged. Convergence can be verified in multiple ways. In the implementation used for this thesis, the combination of the energy $\langle\psi\,|\,H\,|\,\psi\rangle$ and the entropy is considered. Another common option is to investigate the variance $\langle\psi\,|\,H^2\,|\,\psi\rangle - \langle\psi\,|\,H\,|\,\psi\rangle^2$.

With the algorithm described above, it is not unlikely to get stuck in local energy minima instead of reaching the global minimum. There are several workarounds for this. First, one can use a two-site algorithm instead of the one-site version introduced above. In this case, two sites get optimized at the same time. Additionally one can use a so-called mixer, where the reduced density matrix gets slightly perturbed for a first part of the sweeping procedure. For the remainder of this thesis, both of these methods are employed in all calculations.

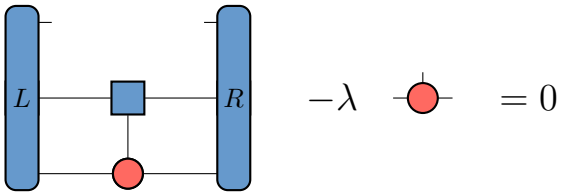

Figure 4.8: Eigenvalue that needs to be solved during the update step. We optimize the red tensor and take λ as the new energy guess. This procedure needs to be repeated for all states until convergence is achieved.

In order to make the DMRG algorithm as efficient as possible, it is very important that symmetries are implemented and exploited. This provides not only an immense speed up but it also allows finding the ground state of a certain symmetry sector.
For this thesis, we only exploit additive and Abelian quantum numbers. In the following, we consider the example of the magnetization m. If the magnetization is conserved, only matrix elements of the MPS fulfilling

$$m\left(|a_{l-1}\rangle\right) + m\left(|\sigma_l\rangle\right) = m\left(|a_l\rangle\right) \,, \tag{4.44}$$

can be non-zero (see Ref. [117] for details), where we chose the $|\sigma_i\rangle$ and $|a_i\rangle$ as eigenstates of the magnetization. The total magnetization of the MPS can then be fixed by setting the difference of the magnetization between the dummy indices on the right and the left of the MPS to the total magnetization. A condition similar to Eq. (4.44) can also be found for MPOs as explained in Ref. [117].

4.4 Infinite System Size

The algorithm for the ground state search described above is only valid for finite systems. Nevertheless, it is possible to generalize this approach to infinite system sizes, which is then called iDMRG. Below, it is briefly presented how the algorithm works in the case of an infinite chain. For more details, the reader is again referred to Ref. [117].
For the ground state search of the infinite system, we use the same local optimization procedure as for the finite size algorithm. The only crucial difference is that, instead of sweeping through the chain, we insert new sites in the center of the chain, which will then grow until convergence is achieved.
As a starting point, a chain with two sites (with physical indices σ_1^A, σ_1^B) is used. The ground state can be written as

$$|\psi_1\rangle = \sum_{\sigma_1^A,\,\sigma_1^B} \Psi^{\sigma_1^A,\sigma_1^B} \left|\sigma_1^A,\sigma_1^B\right\rangle = \sum_{\sigma_1^A,\,\sigma_1^B} A^{\sigma_1^A} \cdot \Lambda^{[1]} \cdot B^{\sigma_1^B} \left|\sigma_1^A,\sigma_1^B\right\rangle \,, \tag{4.45}$$

where we used an SVD to get to the mixed-canonical form and denoted the S matrix as $\Lambda^{[1]}$ in this case. As a next step we insert two additional states in the center of the chain, leading to

$$\sum_{\sigma_1^A,\,\sigma_1^B} A^{\sigma_1^A} \cdot \Psi^{\sigma_2^A,\sigma_2^B} \cdot B^{\sigma_1^B} \left|\sigma_1^A,\sigma_2^A,\sigma_2^B,\sigma_1^B\right\rangle \,. \tag{4.46}$$

We optimize $\Psi^{\sigma_2^A\sigma_2^B}$ with respect to the Hamiltonian of a four site chain. Finally, another SVD is performed and we end up in the mixed-canonical form of a four site chain

$$|\psi_2\rangle = \sum_{\sigma_1^A,\sigma_2^A,\sigma_2^B,\sigma_1^B} A^{\sigma_1^A} \cdot A^{\sigma_2^A} \cdot \Lambda^{[2]} \cdot B^{\sigma_2^B} \cdot B^{\sigma_1^B} \left|\sigma_1^A,\sigma_2^A,\sigma_2^B,\sigma_1^B\right\rangle \,. \tag{4.47}$$

We continue to insert new sites and find a state of

$$|\psi_\ell\rangle = \sum_{\{\sigma_i^{\mathrm{A}}\},\,\{\sigma_i^{\mathrm{B}}\}} A^{\sigma_1^{\mathrm{A}}} \cdot \ldots \cdot A^{\sigma_\ell^{\mathrm{A}}} \cdot \Lambda^{[\ell]} \cdot B^{\sigma_\ell^{\mathrm{B}}} \cdot \ldots \cdot B^{\sigma_1^{\mathrm{B}}} \left|\sigma_1^{\mathrm{A}},\ldots,\sigma_\ell^{\mathrm{A}},\sigma_\ell^{\mathrm{B}},\ldots,\sigma_1^{\mathrm{B}}\right\rangle \tag{4.48}$$

$$= \sum_{\{\sigma_i^{\mathrm{A}}\},\{\sigma_i^{\mathrm{B}}\}} \Gamma^{\sigma_1^A} \cdot \ldots \cdot \Lambda^{[\ell-1]} \cdot \Gamma^{\sigma_\ell^A} \cdot \Lambda^{[\ell]} \cdot \Gamma^{\sigma_\ell^B} \cdot \Lambda^{[\ell-1]} \cdot \ldots \cdot \Gamma^{\sigma_1^B} \left|\sigma_1^{\mathrm{A}}, \ldots, \sigma_\ell^{\mathrm{A}}, \sigma_\ell^{\mathrm{B}}, \ldots, \sigma_1^{\mathrm{B}}\right\rangle \tag{4.49}$$

after the ℓ-th step. Here, the state was translated to the $\Gamma - \Lambda$ notation using (4.25). The chain growing is stopped, once the unit cell in the center

$$\Lambda^{[\ell-1]} \cdot \Gamma^{\sigma_\ell^A} \cdot \Lambda^{[\ell]} \cdot \Gamma^{\sigma_\ell^B} = A^{\sigma_\ell^A} \cdot \Lambda^{[\ell]} \cdot B^{\sigma_\ell^B} \cdot \left(\Lambda^{[\ell-1]}\right)^{-1} \tag{4.50}$$

is converged. The ground state of the infinite chain is given by an infinite repetition of this unit cell.

4.5 Entanglement

So far, tensor network methods, such as DMRG, seem to be the perfect tool to investigate many-body systems. Before finishing this chapter, the main weakness of these methods are briefly discussed. We will see that DMRG is a great tool to study certain kinds of interacting systems, while it is obliged to fail for other types.
We consider the entanglement entropy of a bipartite quantum state $|\psi\rangle = \sum_{i,j} \Psi_{i,j} |i\rangle_A \otimes |j\rangle_B$. The reduced density matrices of both parts are given by $\rho_A = \Psi \cdot \Psi^\dagger$ and $\rho_B = \Psi^\dagger \cdot \Psi$, respectively. The entanglement entropy can be written as

$$S_{A|B} = -\operatorname{Tr}\left[\rho_A \log_2 \rho_A\right] = -\sum_a w_a \log_2 w_a \tag{4.51}$$

with w_a being the eigenvalues of the reduced density matrix. For a gapped system with short-range interactions, this entanglement entropy scales as

$$S \propto L^{D-1}\,, \tag{4.52}$$

which is known as the area law. This shows that the entanglement entropy does not scale with the system size in one dimension. Let us now make a hand-wavy argument how this connects to the algorithms described above. When assuming a bipartite state with χ-dimensional Hilbert spaces for A and B, respectively, the maximal entanglement entropy is given by $S = \log_2 \chi$. For a bipartite state with an entanglement entropy S, we therefore need a state with (bond) dimension $\chi = 2^S$ to accurately describe the actual state. Since, in one dimension, the entanglement entropy does not scale with L, this means that χ stays more or less constant with the system size. In other words, when increasing the system size, the bond dimension does not need to be significantly enhanced, making DMRG well suited for gapped one-dimensional systems.
For critical, gapless systems, the entanglement entropy does not scale according to the area law (4.52). In this case, the entanglement scales as $S \propto L \log_2 L$ and does not stay constant when increasing the system size. Therefore, convergence is very hard to achieve for critical systems. In this case, one is usually restricted to much smaller system sizes. The area law (4.52) is also the reason why tensor networks work well in one dimensional systems, while failing already for relatively small system sizes in higher dimensions.

4.6 Extrapolation of Correlations to Infinite Bond Dimension

This section is based on Ref. [125] (see Chapter 9 for details), where the results were already published.

Finally, we discuss a method to circumvent convergence problems in the case of a strong entanglement due to the absence of a gap. To this end, we consider the case of a quasi long-ranged correlation function that decays algebraically with a power law. For the observation of long ranged correlations, it is essential to investigate those on a large scale. Therefore, we examine them in an infinite system using iDMRG (Section 4.4). As already in the last section, the entanglement scales

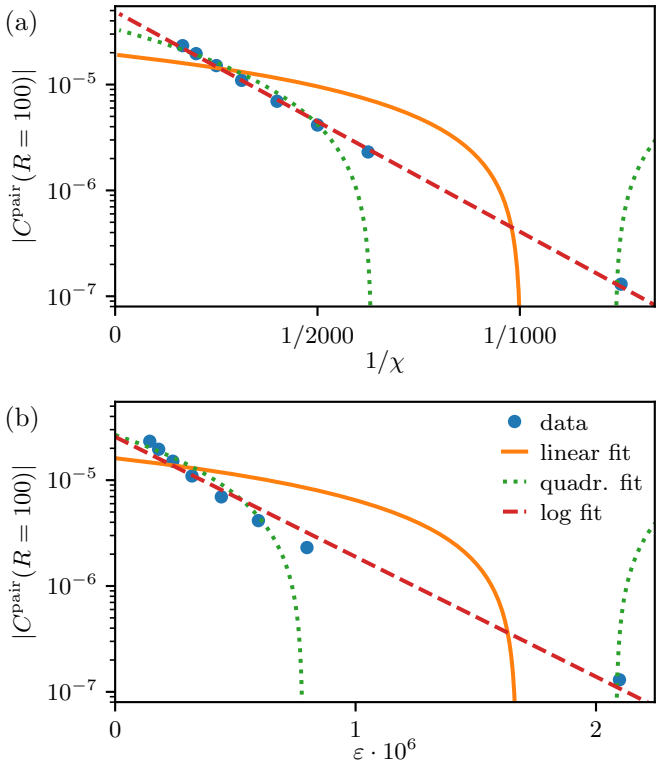

Figure 4.9: Possible fitting procedures for the extrapolation of the pair correlation function (9.18) to infinite bond dimension. The data is plotted as a function of (a) the inverse bond dimension $1/\chi$ and (b) maximal truncation error ε. A linear, a quadratic and a logarithmic fit are shown in dependence on the same parameters. The most successful description can be found using the logarithmic fit in dependence on the inverse bond dimension. Here, the obtained fit provides more accurate results than any other fit either as a function of the inverse bond dimension or as a function of the maximal truncation error. This method is therefore used for the determination of correlation functions at infinite bond dimension. The used Hamiltonian is given by Eq. (9.3) with parameters $t_A = t_B = 0.25$, $J = 3.0$, $U' = 0.4$, $U_d = 1.0$, $U_c = 0.0$ and $t_\perp = t_\perp^{\max}$. Here, the pair correlation function is shown for a distance of $R = 100$ since a good extrapolation is more important for large distances where the results are less converged.

logarithmically with the system size in gapless systems. This already indicates, that an infinite bond dimension is needed for an accurate description. The failure of finite bond dimension can be understood in more detail by regarding the structure of MPSs. Any MPS with finite bond dimension automatically has a finite correlation length [117] and is therefore incapable of describing a power law correlation. Instead, the MPS approximate the critical correlation with a sum of exponential functions which will always fail at too large distances.

For the purpose of obtaining accurate results, it is therefore often unavoidable that the needed correlation functions are extrapolated to infinite bond dimension. Typically, extrapolations are done by describing the data as a function of variance, truncation error or inverse bond dimension [126, 127] and by fitting a corresponding function. Nevertheless, it is still under debate how the result for infinite bond dimension can be found in an optimal way leading to a variety of proposals and many methods used for different models and observables [126–131]. Therefore, we compare the fitting results of multiple functions in dependence on different variables in order to provide the best possible data for the analysis.

Here, the model examined in Chapter 9 is used and various possible extrapolations for the pair correlation function are provided for an infinite system. The used Hamiltonian as well as the definition of the correlation function are postponed to Chapter 9 (Eqs. (9.3) and (9.18)). The exact definitions are not yet required since this section only deals with the extrapolation to infinite

bond dimension.
In Fig. 4.9 the pair correlation function of a typical parameter set within the superconducting regime, where a quasi long ranged behavior is expected, is shown for different bond dimensions in dependence on (a) inverse bond dimension $1/\chi$ and (b) maximal truncation errors ε. A further analysis in comparison to the variance is left for future research since the computation of variances for infinite MPSs is more involved. We use a rather large distance $R = 100$ to identify the optimal method since the results for small distances are already converged for moderate bond dimensions, meaning that the exact procedure is significantly more important at larger values. We then fit various functions to the data in dependence on (a) $1/\chi$ or (b) ε. The y-intercept provides the extrapolated value at infinite bond dimension or equivalently at zero maximal truncation error. Here, in Fig. 4.9, the results for a linear fit $y = ax + b$, a quadratic fit $y = ax^2 + bx + c$ and a logarithmic fit $log(y) = ax + b$ are shown. We note that in both panels, the linear and quadratic fit does not suitably describe the data and that the logarithmic fit is the best option. We observe that the fit performed as a function of the inverse bond dimension is even more accurate. In summary, the logarithmic fit in dependence on the inverse bond dimension turned out to be ideal in our analysis. We therefore use this procedure for the extrapolation of correlation functions to infinite bond dimension within this thesis.
We note that we have only compared the different techniques for the pair correlation function from Chapter 9 which is connected to the superconducting behavior. Within this thesis, the same technique is also used for extrapolating magnetic correlation functions to infinite bond dimension (also Chapter 9). Nevertheless, it is theoretically possible that different extrapolation procedures are ideal for different correlation functions.

Chapter 5

Green's Functions

In this chapter the concept of Green's functions is introduced, which is employed both for systems in and out of equilibrium in this thesis. Originally, the term Green's function referred to a powerful method for solving ordinary and partial differential equation [132]. Such a type of Green's functions can, for example, be used for solving the single-particle Schrödinger equation. For more details on the general concept of Green's functions as an approach to solve ordinary and partial differential equations as well as the application to the single-particle Schrödinger equation, the reader is referred to Ref. [132].
A different type of Green's functions can be defined for many-particle systems. Here, the term Green's function is often used as a short-hand notation for the single-particle Green's functions but it can also refer to general correlation functions. In the following, we concentrate on Green's functions of many-particle systems, introduce both of these definitions and discuss various different Green's functions that can be defined.

In the remainder of this chapter, we first introduce the concept of Green's functions for systems in equilibrium. Here, Green's functions in real and imaginary time are discussed. By employing a Fourier transform, Green's functions in real and imaginary frequency are presented as well. After that, we turn to the non-equilibrium case and we introduce the Keldysh formalism which allows for a simple description of systems out of equilibrium. In addition to the definition of Green's functions based on the Keldysh contour, we briefly discuss the Keldysh equations of motions and the wide band limit. Finally, an algorithm is introduced which makes it possible to speed up the calculation of Green's functions for a non-interacting system in equilibrium as long as the Hamiltonian can be written in a block-tridiagonal form. This allows for an efficient computation of observables which are connected to the Green's function, such as the energy or the occupation.

The Green's function algorithm is well known and there are several textbooks and lecture notes with detailed introductions, including Refs. [132–138]. In the following, only a brief overview is given and the reader is referred to one of these references for more detailed explanations.
Note that the majority of Sections 5.1 and 5.2 is strongly based on Ref. [132] and that Section 5.3.1 is mostly based on Ref. [134] with an additional influence from Refs. [118, 138]. However, these references are also used in other sections and additional references are employed for all sections.

Within this chapter, we consider the system within the grand canonical ensemble and directly include the term $-\mu N$ with μ being the chemical potential and N being the total particle number operator into the Hamiltonian ($H \to H - \mu N$).

5.1 Real Time Single-Particle Green's Functions for Many-Body Systems

In the following, we define the single-particle Green's functions of many-particle systems. Here, we see that *the* Green's function does not exist. Instead, multiple Green's functions are defined in

the literature, with numerous connections between them.

The Green's functions can be obtained for fermions and bosons simultaneously. Any differences that occur are only due to a possible sign change. In these cases, both signs are shown with the upper sign for bosons and the lower sign for fermions as it has e.g. been done in Refs. [132, 136, 137]. For example, it is well known that bosons and fermions obey the (anti-)commutation relations

$$[\Psi_{\sigma_1}(\mathbf{r}_1), \Psi^\dagger_{\sigma_2}(\mathbf{r}_2)]_- = \delta(\mathbf{r}_1 - \mathbf{r}_2)\delta_{\sigma_1,\sigma_2}\,, \qquad [\Psi_{\sigma_1}(\mathbf{r}_1), \Psi^\dagger_{\sigma_2}(\mathbf{r}_2)]_+ = \delta(\mathbf{r}_1 - \mathbf{r}_2)\delta_{\sigma_1,\sigma_2}\,, \tag{5.1}$$

respectively, with $\Psi_\sigma(\mathbf{r})^{(\dagger)}$ being the annihilation (creation) operator of a particle with spin σ at position $\mathbf{r}$ and the (anti-)commutator

$$[A, B]_+ = [A, B] = AB + BA\,, \qquad [A, B]_- = \{A, B\} = AB - BA\,. \tag{5.2}$$

This can be summarized to [136]

$$[\Psi_{\sigma_1}(\mathbf{r}_1), \Psi^\dagger_{\sigma_2}(\mathbf{r}_2)]_\mp = \delta(\mathbf{r}_1 - \mathbf{r}_2)\delta_{\sigma_1,\sigma_2} \tag{5.3}$$

within our notations. As a first single-particle Green's function, we can define the retarded Green's function

$$G^R\left(\mathbf{r}\sigma t, \mathbf{r}'\sigma' t'\right) = -i\theta\left(t - t'\right)\left\langle \left[\Psi_\sigma(\mathbf{r}t), \Psi^\dagger_{\sigma'}\left(\mathbf{r}'t'\right)\right]_\mp \right\rangle . \tag{5.4}$$

Here and in the remainder of this chapter, an operator $A(t)$ refers to the operator within the Heisenberg picture. Additionally, the operator $\Psi_\sigma(\mathbf{r}t)^{(\dagger)}$ refers to the annihilation (creation) operator for a particle of spin σ at position $\mathbf{r}$ and time t. As already mentioned above, there are multiple single-particle Green's functions for many-body systems. Analogously, the advanced Green's function can be defined as

$$G^A\left(\mathbf{r}\sigma t, \mathbf{r}'\sigma' t'\right) = i\theta\left(t' - t\right)\left\langle \left[\Psi_\sigma(\mathbf{r}t), \Psi^\dagger_{\sigma'}\left(\mathbf{r}'t'\right)\right]_\mp \right\rangle . \tag{5.5}$$

Moreover, there are the lesser Green's function

$$G^<\left(\mathbf{r}\sigma t, \mathbf{r}'\sigma' t'\right) = -i(\pm 1)\left\langle \Psi^\dagger_{\sigma'}\left(\mathbf{r}'t'\right)\Psi_\sigma(\mathbf{r}t)\right\rangle \tag{5.6}$$

and similarly the greater Green's function

$$G^>\left(\mathbf{r}\sigma t, \mathbf{r}'\sigma' t'\right) = -i\left\langle \Psi_\sigma(\mathbf{r}t)\Psi^\dagger_{\sigma'}\left(\mathbf{r}'t'\right)\right\rangle . \tag{5.7}$$

Interestingly, it is possible to connect these single-particle Green's functions via

$$G^R\left(\mathbf{r}\sigma t, \mathbf{r}'\sigma' t'\right) = \theta\left(t - t'\right)\left[G^>\left(\mathbf{r}\sigma t, \mathbf{r}'\sigma' t'\right) - G^<\left(\mathbf{r}\sigma t, \mathbf{r}'\sigma' t'\right)\right] \tag{5.8}$$

$$G^A\left(\mathbf{r}\sigma t, \mathbf{r}'\sigma' t'\right) = \theta\left(t' - t\right)\left[G^<\left(\mathbf{r}\sigma t, \mathbf{r}'\sigma' t'\right) - G^>\left(\mathbf{r}\sigma t, \mathbf{r}'\sigma' t'\right)\right] \tag{5.9}$$

We can further define the time-ordered Green's function (for the introduction of (anti-) time ordered and Keldysh Green's function, we follow Ref. [134])

$$G^T\left(\mathbf{r}\sigma t, \mathbf{r}'\sigma' t'\right) = -i\left\langle T\left(\psi_\sigma(\mathbf{r}t)\psi^\dagger_{\sigma'}\left(\mathbf{r}'t'\right)\right)\right\rangle \tag{5.10}$$

with the time-ordering operator

$$T\left[A\left(t_1\right)B\left(t_2\right)\right] = \begin{cases} A\left(t_1\right)B\left(t_2\right) & \text{for} \quad t_1 > t_2 \\ \mp B\left(t_2\right)A\left(t_1\right) & \text{for} \quad t_2 > t_1 \end{cases} . \tag{5.11}$$

Analogously, we obtain the anti-time-ordered Green's function

$$G^{\tilde{T}}\left(\mathbf{r}\sigma t, \mathbf{r}'\sigma' t'\right) = -i\left\langle \tilde{T}\left(\psi_\sigma(\mathbf{r}t)\psi^\dagger_{\sigma'}\left(\mathbf{r}'t'\right)\right)\right\rangle \tag{5.12}$$

with the anti-time-ordering operator

$$\tilde{T}\left[A\left(t_1\right)B\left(t_2\right)\right]=\begin{cases} A\left(t_1\right)B\left(t_2\right) & \text{for} \quad t_2>t_1 \\ \mp B\left(t_2\right)A\left(t_1\right) & \text{for} \quad t_1>t_2 \end{cases} \tag{5.13}$$

bringing the operators in the opposite order compared to the time-ordering operator. We note that the (anti-)time-ordered Green's functions can be connected to the lesser and greater Green's function via

$$G^T\left(\mathbf{r}\sigma t,\mathbf{r}'\sigma' t'\right)=\theta\left(t-t'\right)G^>\left(\mathbf{r}\sigma t,\mathbf{r}'\sigma' t'\right)+\theta\left(t'-t\right)G^<\left(\mathbf{r}\sigma t,\mathbf{r}'\sigma' t'\right)\,, \tag{5.14}$$

$$G^{\tilde{T}}\left(\mathbf{r}\sigma t,\mathbf{r}'\sigma' t'\right)=\theta\left(t-t'\right)G^<\left(\mathbf{r}\sigma t,\mathbf{r}'\sigma' t'\right)+\theta\left(t'-t\right)G^>\left(\mathbf{r}\sigma t,\mathbf{r}'\sigma' t'\right)\,. \tag{5.15}$$

Finally, we can define the Keldysh Green's function [134]

$$G^K\left(\mathbf{r}\sigma t,\mathbf{r}'\sigma' t'\right)=-i\left\langle\left[\psi_\sigma(\mathbf{r}t),\psi^\dagger_{\sigma'}\left(\mathbf{r}'t'\right)\right]_\pm\right\rangle=G^>\left(\mathbf{r}\sigma t,\mathbf{r}'\sigma' t'\right)+G^<\left(\mathbf{r}\sigma t,\mathbf{r}'\sigma' t'\right)\,. \tag{5.16}$$

At this point, the introduced Green's functions seem like a huge set of unorganized functions. However, not all Green's functions that we have introduced are independent of each other as one might assume due to various connections between them. Later on in this chapter, we find out how to properly organize them into matrices within the Keldysh formalism and which Green's functions are actually independent.

5.1.1 Transformation to General Basis

So far, we have only defined the Green's functions in the real space basis. Nevertheless, Green's functions can naturally be defined and transformed in an arbitrary basis. Let us therefore consider a general discrete basis $|\psi_\nu\rangle$ with

$$[a_{\nu,\sigma},a^\dagger_{\nu',\sigma'}]_\mp=\delta_{\nu\nu'}\delta_{\sigma\sigma'}\,,\quad [a_{\nu,\sigma},a_{\nu',\sigma'}]_\mp=0\,,\quad [a^\dagger_{\nu,\sigma},a^\dagger_{\nu',\sigma'}]_\mp=0\,. \tag{5.17}$$

Here, $a^{(\dagger)}_{\nu,\sigma}$ denotes the annihilation (creation) operator for a particle with spin σ in state $|\psi_\nu\rangle$. The retarded Green's function is then defined as

$$G^R\left(\nu\sigma t,\nu'\sigma' t'\right)=-i\theta\left(t-t'\right)\left\langle\left[a_{\nu,\sigma}(t),a^\dagger_{\nu',\sigma'}\left(t'\right)\right]_\mp\right\rangle\,. \tag{5.18}$$

The other Green's functions can be treated analogously by replacing $\Psi_\sigma(\mathbf{r},t)$ and $\Psi^\dagger_{\sigma'}(\mathbf{r}',t')$ with $a_{\nu,\sigma}(t)$ and $a^\dagger_{\nu',\sigma'}(t')$, respectively. Greens functions of different bases can also be transformed into each other. We find for example

$$G^X\left(\mathbf{r}\sigma t,\mathbf{r}'\sigma' t'\right)=\sum_{\nu\nu'}\langle\mathbf{r}\mid\psi_\nu\rangle\,G^X\left(\nu\sigma t,\nu'\sigma' t'\right)\langle\psi'_\nu\mid\mathbf{r}'\rangle \tag{5.19}$$

with $X=R,A,<,>,T,\tilde{T},K$ for the conversion from the basis $|\psi_\nu\rangle$ to the real space basis.

5.1.2 Translation-Invariant Systems

In the following, we want to treat translation-invariant systems. Here, the Green's functions only depend on the position difference $\mathbf{r}-\mathbf{r}'$. We can understand, how this simplifies the form of the single-particle Green's functions by treating the retarded Green's function as an example. Again, the other Green's functions have analogous properties and can be treated in the same way.
In translation-invariant systems, it usually is helpful to describe the system in the momentum space basis $|\mathbf{k}\rangle$ since the momentum is a good quantum number. We note in the following that, in this case, the Green's functions become diagonal in $\mathbf{k}$. We can rewrite the real space Green's function

$$G^R\left(\mathbf{r}\sigma t,\mathbf{r}'\sigma' t'\right)=G^R\left(\mathbf{r}-\mathbf{r}',\sigma t,\sigma' t'\right)=\frac{1}{\mathcal{V}}\sum_{\mathbf{k}\mathbf{k}'}e^{i\mathbf{k}\cdot\mathbf{r}}G^R\left(\mathbf{k}\sigma t,\mathbf{k}'\sigma' t'\right)e^{-i\mathbf{k}'\cdot\mathbf{r}'}$$

$$= \frac{1}{\mathcal{V}} \sum_{\mathbf{k}\mathbf{k}'} e^{i\mathbf{k}\cdot\left(\mathbf{r}-\mathbf{r}'\right)} G^R\left(\mathbf{k}\sigma t, \mathbf{k}'\sigma' t'\right) e^{i\left(\mathbf{k}-\mathbf{k}'\right)\cdot\mathbf{r}'} , \tag{5.20}$$

where $\mathcal{V}$ denotes the volume. We have already argued that the Green's function can only depend on $\mathbf{r}-\mathbf{r}'$ and not on $\mathbf{r}$ or $\mathbf{r}'$ explicitly. We therefore automatically find $G^R\left(\mathbf{k}\sigma t, \mathbf{k}'\sigma' t'\right) = 0$ for $\mathbf{k} \neq \mathbf{k}'$. This leads to the result that the momentum space Green's function is given by

$$G^R\left(\mathbf{k}\sigma t, \mathbf{k}'\sigma' t'\right) = \delta_{\mathbf{k},\mathbf{k}'} G^R\left(\mathbf{k}, \sigma t, \sigma' t'\right) \quad \text{with} \quad G^R\left(\mathbf{k}, \sigma t, \sigma' t'\right) = -i\theta\left(t-t'\right) \left\langle \left[a_{\mathbf{k}\sigma}(t), a^\dagger_{\mathbf{k}\sigma'}\left(t'\right) \right]_\mp \right\rangle . \tag{5.21}$$

and the real space Green's function is given by its Fourier transform

$$G^R\left(\mathbf{r}-\mathbf{r}', \sigma t, \sigma' t'\right) = \frac{1}{\mathcal{V}} \sum_{\mathbf{k}} e^{i\mathbf{k}\cdot\left(\mathbf{r}-\mathbf{r}'\right)} G^R\left(\mathbf{k}, \sigma t, \sigma' t'\right) . \tag{5.22}$$

5.1.3 Frequency Dependent Green's Functions

Similarly to the case of spatial translational invariance shown above, time-translational invariance can be treated as well. To this end, we consider systems in its thermal equilibrium, in which case the Green's functions are only a function of the time difference $t-t'$ (denoted with t below) [134]. We can then transform the Green's functions into frequency space by applying a Fourier transform. Here, one has to be careful that the Fourier transform converges properly. To this end, we need to add a convergence factor. For the retarded Green's function, this can be done by replacing $\omega \to \omega + i\eta$, while for the advanced Green's function, we have to replace $\omega \to \omega - i\eta$. We then find

$$G^{R/A}(\nu, \nu', \omega) = \int_{-\infty}^{\infty} dt e^{i\omega t} e^{\mp\eta t} G^{R/A}(\nu, \nu', t) . \tag{5.23}$$

For an arbitrary Green's function from above, the needed Fourier transform is given by [136, 137]

$$G^X(\nu, \nu', \omega) = \int_{-\infty}^{\infty} dt e^{i\omega|t|} e^{\mp\eta t} G^X(\nu, \nu', t) . \tag{5.24}$$

This yields for the lesser Green's function [137]

$$G^<(\nu, \nu', \omega) = \pm n_{F/B}(\omega) \left[G^R(\nu, \nu', \omega) - G^A(\nu, \nu', \omega) \right] , \tag{5.25}$$

where $n_{F/B}(\omega)$ denotes the Fermi-/Bose-function, which used for this thesis. For the results of the other Green's functions, the reader is referred to Ref. [137].

5.1.4 Free Electron System

In the following, we consider the free electron example and compute the advanced and retarded Green's functions explicitly. We regard a translation-invariant system, which is always diagonal in the momentum space basis. Moreover, we consider our system to conserve the spin and define an Hamiltonian of

$$H = \sum_{\mathbf{k}\sigma} \xi_{\mathbf{k}\sigma} c^\dagger_{\mathbf{k}\sigma} c_{\mathbf{k}\sigma} . \tag{5.26}$$

Since the system is not only translationally invariant, but diagonal in spin σ as well, the Green's function has to be diagonal in spin and momentum. We can therefore write

$$G^X\left(\mathbf{k}\sigma t, \mathbf{k}'\sigma' t'\right) = \delta_{\mathbf{k},\mathbf{k}'} \delta_{\sigma,\sigma'} G^X\left(\mathbf{k}, \sigma, t-t'\right) \tag{5.27}$$

for $X = R, A, <, >, T, \tilde{T}, K$, where we exploited that the Green's function can only depend on $t-t'$. The retarded Green's function is then given by

$$G^R\left(\mathbf{k}\sigma, t-t'\right) = -i\theta\left(t-t'\right) \left\langle \left[c_{\mathbf{k}\sigma}(t-t'), c^\dagger_{\mathbf{k}\sigma} \right]_+ \right\rangle = -i\theta\left(t-t'\right) \left\langle \left[c_{\mathbf{k}\sigma}, c^\dagger_{\mathbf{k}\sigma} \right]_+ \right\rangle e^{-i\xi_k\left(t-t'\right)}$$

$$= -i\theta\left(t-t'\right)e^{-i\xi_k\left(t-t'\right)} \tag{5.28}$$

Remarkably, this result coincides with the retarded Green's function of the single-particle Schrödinger equation in the eigenbasis (see e.g. Ref. [132]). We thus conclude that the single-particle Green's functions are closely connected to the Green's functions of the single-particle Schrödinger equation, which thus justifies the name 'Green's functions'. Furthermore, we find analogously for the advanced Green's function

$$G^A\left(\mathbf{k}\sigma, t-t'\right) = i\theta\left(t'-t\right)\left\langle\left[c_{\mathbf{k}\sigma}(t-t'), c^\dagger_{\mathbf{k}\sigma}\right]_+\right\rangle = i\theta\left(t'-t\right)e^{-i\xi_k\left(t-t'\right)} \tag{5.29}$$

which agrees with the advanced Green's function from the one-particle Schrödinger equation as well (in the eigenbasis, see e.g. Ref. [132]).

Based on these results, we can also calculate the frequency dependent retarded and advanced Green's functions for the free electron system. For the retarded Green's function, we find

$$G^R(\mathbf{k}\sigma,\omega) = -i\int_{-\infty}^{\infty} dt\,\theta\left(t-t'\right)e^{i\omega\left(t-t'\right)}e^{-i\xi_{\mathbf{k}}\left(t-t'\right)-\eta\left(t-t'\right)} = \frac{1}{\omega-\xi_{\mathbf{k}}+i\eta}\,, \tag{5.30}$$

where we are still in the eigenbasis of the system. More general, we can write [137]

$$G^R(\nu,\nu',\omega) = G^R_{\nu,\nu'}(i\omega) = \left[\frac{1}{\omega+i0^+-\mathcal{H}}\right]_{\nu,\nu'} \tag{5.31}$$

for an arbitrary basis. In contrast to Subsection 5.1.1, a possible spin index is included in this basis. For the advanced Green's function, we can analogously find [137]

$$G^A(\nu,\nu',\omega) = G^A_{\nu,\nu'}(\omega) = \left[\frac{1}{\omega-i0^+-\mathcal{H}}\right]_{\nu,\nu'}\,. \tag{5.32}$$

5.1.5 Green's Functions as General Correlation Functions

So far, we have only considered the single-particle Green's functions of a many body system. When referring to a Green's function within this thesis, usually these single-particle Green's functions are meant. Nevertheless, the term Green's function can also denote a general correlation function that can be obtained by replacing the annihilation and creation operators with general operators A and B. For example, the general retarded Green's function is then given by

$$C^R_{AB}\left(t,t'\right) = -i\theta\left(t-t'\right)\left\langle\left[A(t), B\left(t'\right)\right]_\mp\right\rangle\,. \tag{5.33}$$

In the following, we use this general notation in order to introduce the Green's function in imaginary time. The usual single-particle Green's functions can always be found by replacing $A(t)\to\psi_\sigma(\mathbf{r}t)$, $a_{\nu,\sigma}(t)$ and $B(t')\to\psi^\dagger_{\sigma'}(\mathbf{r}',t')$, $a^\dagger_{\nu',\sigma'}(t')$.

5.2 Matsubara Green's Functions

In the previous parts of this chapter, we have always defined Green's functions in real time. In this section, we introduce the imaginary time Green's function, which is also known as the Matsubara Green's function. At first sight, this seems to be exotic since we have no intuition for imaginary times. The imaginary time space does not have a physical interpretation but should be seen as an theoretical approach, which simplifies the calculation of Green's functions, especially in the case of interacting systems, where Green's functions are often computed using Feynman diagrams within the framework of perturbation theory. Unfortunately, this is beyond the scope of this thesis and the reader is referred to Ref. [132] for more details on diagrammatic techniques. Within this section, we assume that the system is in equilibrium and is described by a time-independent Hamiltonian.

The imaginary time picture simply can be found by replacing $it \to \tau$ with the real time t and the imaginary time τ. For a generic operator A with no explicit time dependence, this leads, for example, to a time evolution of $A(\tau) = e^{\tau H} A e^{-\tau H}$. The Matsubara Green's function is defined as

$$C_{AB}(\tau, \tau') \coloneqq -\langle T_\tau [A(\tau) B(\tau')] \rangle \tag{5.34}$$

with T_τ being the time ordering operator in imaginary time with analogous properties as the one in real time defined by Eq. (5.13). We further note that the Matsubara Green's function only depends on the time difference $\tau - \tau'$:

$$\begin{aligned} C_{AB}(\tau, \tau') &= -\frac{1}{Z} \operatorname{Tr}\left[e^{-\beta H} e^{\tau H} A e^{-\tau H} e^{\tau' H} B e^{-\tau' H}\right] = -\frac{1}{Z} \operatorname{Tr}\left[e^{-\beta H} e^{(\tau-\tau')H} A e^{-(\tau-\tau')H} B\right] \\ &= C_{AB}(\tau - \tau') \end{aligned} \tag{5.35}$$

Here, $\beta = 1/k_B T$ is the inverse temperature with the temperature T and the Boltzmann constant k_B (set to $k_B = 1$ in this thesis). Moreover, $Z = \sum_n e^{-\beta E_n}$ denotes the system's partition function and we have used that $e^{-\beta H}$ and $e^{-\tau H}$ commute with each other as well as the invariance of the trace under cyclic permutations. The Matsubara Green's function is only well defined for $-\beta < \tau - \tau' < \beta$ since the expression might diverge outside this regime (see Ref. [132] for details). Therefore, we restrict the Matsubara Green's function to this interval.

5.2.1 Green's Functions of Imaginary Frequency

Green's functions can not only be defined for imaginary time, but also for imaginary frequencies. In the following, we thus investigate the frequency dependent Matsubara Green's function, which can be obtained by a Fourier transform, similarly as its counterparts in real times. Since the imaginary time Green's function is only defined on the interval $-\beta < \tau < \beta$, we assume periodic boundary conditions and apply a Fourier transform on that regime. This leads to the definition

$$C_{AB}(n) \coloneqq \frac{1}{2} \int_\beta^\beta d\tau e^{i\pi n \tau \beta} C_{AB}(\tau)\,. \tag{5.36}$$

The corresponding back transform is given by

$$C_{AB}(\tau) = \frac{1}{\beta} \sum_{n=-\infty}^{\infty} e^{-i\pi n \tau \beta} C_{AB}(n)\,. \tag{5.37}$$

We evaluate $C_{AB}(n)$ in more detail by exploiting that the time-dependent Matsubara Green's function is even (bosonic operators) or odd (fermionic operators) with respect to $\tau = 0$. To prove this, we assume $\tau < 0$ (and automatically $\tau + \beta > 0$) and obtain

$$\begin{aligned} C_{AB}(\tau + \beta) &= \frac{-1}{Z} \operatorname{Tr}\left[e^{\beta H} e^{(\tau+\beta)H} A e^{-(\tau+\beta)H} B\right] = \frac{-1}{Z} \operatorname{Tr}\left[e^{\tau H} A e^{-\tau H} e^{\beta H} B\right] \\ &= \frac{-1}{Z} \operatorname{Tr}\left[e^{\beta H} B e^{\tau H} A e^{-\tau H}\right] = \pm \frac{-1}{Z} \operatorname{Tr}\left[e^{\beta H} T_\tau (A(\tau) B)\right] = \pm C_{AB}(\tau). \end{aligned} \tag{5.38}$$

Inserting this into Eq.(5.36) leads to

$$C_{AB}(n) = \frac{1}{2}\left(1 \pm e^{-i\pi n}\right) \int_0^\beta d\tau e^{i\pi n \tau \beta} C_{AB}(\tau) \tag{5.39}$$

showing that $C_{AB}(n)$ is only finite for even n in the case of bosons and odd n in the case of fermions. The Matsubara Green's function in frequency space is therefore given by

$$C_{AB}(i\omega_n) = \int_0^\beta d\tau e^{i\omega_n \tau} C_{AB}(\tau) \tag{5.40}$$

with discrete Matsubara frequencies

$$\omega_n = \frac{2n\pi}{\beta} \text{ for bosons } , \quad \omega_n = \frac{(2n+1)\pi}{\beta} \text{ for fermions.} \tag{5.41}$$

5.2.2 Connection to Advanced and Retarded Green's Functions

As mentioned above, imaginary times and frequencies have no physical meaning and should rather be seen as a computational trick. In the following, we compare the different frequency dependent Green's functions and find, in equilibrium, that the retarded and advanced Green's functions can be obtained from the Matsubara Green's function rather easily. This allows to going to the physical real time spaces and makes the application of imaginary times so useful.
We can show the connection with the so called Lehman representation. Here, we explicitly calculate the correlation functions using a decomposition within the eigenstates of the system. For the Matsubara Green's function we obtain

$$\begin{aligned} C_{AB}\left(i\omega_n\right) &= \int_0^\beta d\tau e^{i\omega_n\tau} C_{AB}(\tau) = \int_0^\beta d\tau e^{i\omega_n\tau} \left\langle A(\tau)B\right\rangle \\ &= \int_0^\beta d\tau e^{i\omega_n\tau} \frac{-1}{Z} \sum_{nn'} e^{-\beta E_n} \left\langle n|A|n'\right\rangle \left\langle n'|B|n\right\rangle e^{\tau(E_n - E_{n'})} \\ &= \frac{-1}{Z} \sum_{nn'} e^{-\beta E_n} \frac{\left\langle n|A|n'\right\rangle \left\langle n'|B|n\right\rangle}{i\omega_n + E_n - E_{n'}} \left(e^{i\omega\beta} e^{\beta(E_n - E_{n'})} - 1\right) \\ &= \frac{1}{Z} \sum_{nn'} \frac{\left\langle n|A|n'\right\rangle \left\langle n'|B|n\right\rangle}{i\omega_n + E_n - E_{n'}} \left(e^{-\beta E_n} \mp e^{-\beta E_{n'}}\right) . \end{aligned} \tag{5.42}$$

The Lehman representations of the retarded and advanced Green's functions can be computed analogously and is given by [132, 136]

$$C^R_{AB}(\omega) = \frac{1}{Z} \sum_{nn'} \frac{\left\langle n|A|n'\right\rangle \left\langle n'|B|n\right\rangle}{\omega + E_n - E_{n'} + i0^+} \left(e^{-\beta E_n} \mp e^{-\beta E_{n'}}\right) , \tag{5.43}$$

$$C^A_{AB}(\omega) = \frac{1}{Z} \sum_{nn'} \frac{\left\langle n|A|n'\right\rangle \left\langle n'|B|n\right\rangle}{\omega + E_n - E_{n'} - i0^+} \left(e^{-\beta E_n} \mp e^{-\beta E_{n'}}\right) . \tag{5.44}$$

We refrain from showing the explicit calculation here and refer to Ref. [132] for details. We can compare the Lehman representations of the different correlation functions and note that we recover the retarded Green's function via

$$C^R_{AB}(\omega) = C_{AB}\left(i\omega_n \to \omega + i0^+\right) . \tag{5.45}$$

Similarly, one can obtain the advanced Green's function from the Matsubara Green's function via

$$C^A_{AB}(\omega) = C_{AB}\left(i\omega_n \to \omega - i0^+\right) . \tag{5.46}$$

Therefore, one often finds the expressions $C_{AB}(\omega \pm i0^+)$ (G for the single-particle version) for the retarded and advanced Green's functions as well.
Using connections (5.45) and (5.46), we can immediately see from Eqs. (5.31) and (5.32), that the Matsubara single-particle Green's function of a non-interacting system is given by

$$G(\nu, i\omega_n) = \frac{1}{i\omega_n - \xi_\nu} . \tag{5.47}$$

in the system's eigenbasis and

$$G(\nu, \nu', i\omega_n) = G_{\nu,\nu'}(i\omega_n) = \left[\frac{1}{i\omega_n - \mathcal{H}}\right]_{\nu,\nu'} \tag{5.48}$$

within a general basis set [137].

5.2.3 Self-Energy and Dyson Equation

We noticed above, that the Matsubara Green's function of a non-interacting system has the simple form of Eq. (5.48). Nevertheless, this is not possible for other systems, where any kind of couplings

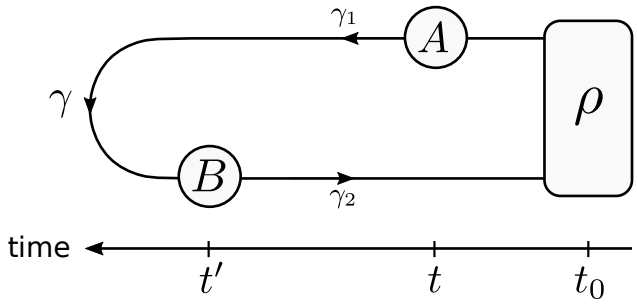

Figure 5.1: Keldysh contour γ needed for the definition of the contour ordered Greens function (5.51). The contour goes from t_0 to infinity and back to t_0. The operators occurring in the Green's function can appear on the upper (γ_1) or lower branch (γ_2). The density matrix operator ρ can be placed placed either at the beginning or at the end of the ordering. The operators on the contour are included as it was done in Ref. [118, 138].

are present. In this case, it is, however, possible to write the Matsubara Green's function in such a compact form using the so-called self-energy Σ. The total Green's function is then given by [137]

$$G(\nu, \nu', i\omega_n) = G_{\nu,\nu'}(i\omega_n) = \left[\frac{1}{i\omega_n - \mathcal{H} - \Sigma(i\omega_n)}\right]_{\nu,\nu'}. \tag{5.49}$$

Therefore, the full Green's function is connected to the Green's function of the free system $G_0(i\omega_n) = \left[\frac{1}{i\omega_n - \mathcal{H}}\right]$ via the famous Dyson Equation

$$G(i\omega_n) = G_0(i\omega_n) + G_0(i\omega_n)\Sigma(i\omega_n)G(i\omega_n). \tag{5.50}$$

The self-energy can usually be computed using the single-particle irreducible diagrams. However, diagrammatic techniques are beyond the scope of this thesis and we refer to Ref. [132] for a detailed introduction.
For the case of the real-time Green's functions introduced above, a similar Dyson equation can be found, which is introduced in the following chapter, where non-equilibrium Green's functions are discussed.

5.3 Keldysh Formalism

In the following, we consider the case where our system is out of equilibrium. In this case, the real-time Green's functions defined above depend on both times t and t' and not only on their difference. In order to be able to deal with those kinds of systems, the Keldysh formalism is introduced, which turns out to be a method that can treat non-equalibrium Green's functions in a very simple way. This formalism is named after L. V. Keldysh, who established this method in Ref. [139].

5.3.1 Contour Ordered Green's Functions and Keldysh Rotation

For the analysis of Green's functions for systems out of equilibrium, we introduce the so-called Keldysh contour, which is shown in Fig. 5.1. The contour starts at t_0, goes to infinty and back to t_0 with multiple operators occuring on the contour. It consists of two different branches: The upper part evolves along the time-axis and the lower part propagates in the counter-direction. We denote the Keldysh contour with γ and define the two branches as γ_1 (upper branch, forward direction) and γ_2 (lower branch, backward direction).
Based on this contour, we can define a contour ordered Green's function, which is given by

$$C^C_{AB}(\tilde{t}, \tilde{t}') = -i \operatorname{Tr}\left[\rho(t_0) T_\gamma \left(A(\tilde{t})B(\tilde{t}')\right)\right] = -i \left\langle T_\gamma \left(A(\tilde{t})B(\tilde{t}')\right)\right\rangle \tag{5.51}$$

for general operators A and B with the contour variables $\tilde{t}$, which contains the time t and the contour index denoting the branch of the contour, where the operator is placed. Moreover, $\rho(t_0) = e^{-\beta H(t_0)} / \operatorname{Tr}\left[e^{-\beta H(t_0)}\right]$ and T_γ denotes the contour ordering operator with

$$T_\gamma \left[A\left(\tilde{t}_1\right) B\left(\tilde{t}_2\right)\right] = \begin{cases} A\left(\tilde{t}_1\right) B\left(\tilde{t}_2\right) & \text{for} \quad \tilde{t}_1 \overset{\gamma}{>} \tilde{t}_2 \\ \mp B\left(\tilde{t}_2\right) A\left(\tilde{t}_1\right) & \text{for} \quad \tilde{t}_2 \overset{\gamma}{>} \tilde{t}_1 \end{cases} . \tag{5.52}$$

Here, the contour ordering symbol $\overset{\gamma}{\lessgtr}$ indicates whether $\tilde{t}_1$ appears before ($\tilde{t}_1 \overset{\gamma}{<} \tilde{t}_2$) or after $\tilde{t}_2$ ($\tilde{t}_1 \overset{\gamma}{>} \tilde{t}_2$) along the Keldysh contour shown in Fig. 5.1.
For the contour ordered single-particle Green's function we thus obtain

$$G^C(\mathbf{r}\sigma\tilde{t}, \mathbf{r}'\sigma'\tilde{t}') = -i \operatorname{Tr}\left[\rho(t_0) T_\gamma \left(\Psi_\sigma(\mathbf{r}\tilde{t}) \Psi_\sigma^\dagger(\mathbf{r}'\tilde{t}')\right)\right] = -i \left\langle T_\gamma \left(\Psi_\sigma(\mathbf{r}\tilde{t}) \Psi_\sigma^\dagger(\mathbf{r}'\tilde{t}')\right)\right\rangle . \tag{5.53}$$

or

$$G^C(\nu\sigma\tilde{t}, \nu'\sigma'\tilde{t}') = -i \operatorname{Tr}\left[\rho(t_0) T_\gamma \left(a_{\nu\sigma}(\tilde{t}) a_{\nu'\sigma'}^\dagger(t')\right)\right] = -i \left\langle T_\gamma \left(a_{\nu\sigma}(\tilde{t}) a_{\nu'\sigma'}^\dagger(\tilde{t}')\right)\right\rangle . \tag{5.54}$$

within an arbitrary basis from Subsection 5.1.1. Often, all needed indices are grouped into a multi-index $1 = (\nu, \sigma, t')$, which leads to the short-hand notation

$$G^C(1, 1') = -i \left\langle T_\gamma \left(a(1) a^\dagger(1')\right)\right\rangle . \tag{5.55}$$

Based on the contour ordering formalism, it is quite natural to define four different Green's functions depending on the position of the operators (upper or lower contour for both of them). Instead of a single contour ordered Green's function, this leads to the matrix

$$\begin{pmatrix} G^{11} & G^{12} \\ G^{21} & G^{22} \end{pmatrix} \tag{5.56}$$

where the Keldysh indices (first index for A and second for B) indicate whether the corresponding operator is placed on the upper (1) or lower (2) branch of the Keldysh contour. This matrix can now be considered as a single Green's function with twice as many degrees of freedom as in the equilibrium case. Based on this matrix notation, a Dyson equation is introduced below, with which it is now straight-forward to include additional couplings in this formalism. However, a more detailed explanation showing why this formalism is well suited for the inclusion of interactions is beyond the scope of this brief introduction and the reader is referred to the literature.
Moreover, based on the definition of the Green's functions introduced in Subsection 5.1 as well as the contour ordered Green's function, we can identify the different component of the matrix with

$$G^{11} = G^T, \quad G^{12} = G^<, \quad G^{21} = G^>, \quad G^{22} = G^{\tilde{T}} . \tag{5.57}$$

Although there are four different Green's functions defined on the Keldysh contour, it turns out that only three of them are independent. This can be seen by rotating the matrix in Keldysh space. We therefore define the rotation matrices

$$L = \frac{1}{\sqrt{2}}(1 - i\sigma^y)\sigma^z = \frac{1}{\sqrt{2}} \begin{pmatrix} 1 & 1 \\ 1 & -1 \end{pmatrix} \text{ and } R = \frac{1}{\sqrt{2}}(1 - i\sigma^y)^\dagger = \frac{1}{\sqrt{2}} \begin{pmatrix} 1 & 1 \\ -1 & 1 \end{pmatrix} \tag{5.58}$$

with the Pauli matrices σ^i. This leads to the rotated Keldysh Green's functions in the RAK-basis

$$\hat{G} = \begin{pmatrix} G^{\mathrm{R}} & G^{\mathrm{K}} \\ 0 & G^{\mathrm{A}} \end{pmatrix} = L \begin{pmatrix} G^T & G^< \\ G^> & G^{\tilde{T}} \end{pmatrix} R , \tag{5.59}$$

where we identified the advanced, retarded and Keldysh Green's functions from above.
In this thesis, we stick to the RAK-basis and therefore, we have defined $\hat{G}$ and $\hat{\Sigma}$ in this basis, which is used in the following.

5.3.2 The Self-Energy and the Dyson Equation

As already mentioned above, a simple Dyson equation allowing for additional couplings can also be found in the non-equilibrium case. The Dyson equation in its most general form can be written as (notation adapted from the contour ordered case in Ref. [135] and from above)

$$\hat{G}(1,2) = \hat{G}_0(1,2) + \int d3 \int d4\, \hat{G}_0(1,3)\hat{\Sigma}(3,4)\hat{G}(4,2)\,, \tag{5.60}$$

where the indices are multi-indices including all necessary components including the Keldysh index indicating the position within the matrix (5.59). This form is completely general and can be used both for frequency and time dependent Green's functions and for an arbitrary basis of the individual G^X. In the short-hand notation with matrix multiplications, the Dyson equation reads [134]

$$\hat{G} = \hat{G}_0 + \hat{G}_0\hat{\Sigma}\hat{G}\,, \tag{5.61}$$

The self energy $\hat{\Sigma}$ can be written as

$$\hat{\Sigma} = \begin{pmatrix} \Sigma^{\mathrm{R}} & \Sigma^{\mathrm{K}} \\ 0 & \Sigma^{\mathrm{A}} \end{pmatrix}. \tag{5.62}$$

5.3.3 Keldysh Equations of Motion

For the derivation of the Keldysh equations of motions, a slightly different notation (compared to the ones employed above) is used. Here, we only show the time indices and all additional indices are included implicitly by assuming that $\hat{G}$ and $\hat{\Sigma}$ are still matrices containing all other indices. Using this notation, the Dyson equation from above is given by

$$\hat{G}(t,t') = \hat{G}_0(t,t') + \int dt_1 \int dt_2\, \hat{G}_0(t,t_1)\hat{\Sigma}(t_1,t_2)\hat{G}(t_2,t')\,. \tag{5.63}$$

In the next step we are interested in finding the equations of motion for these Green's functions. To this end, we apply the operator $[i\partial_t - \mathcal{H}(t)]$ to Eq. (5.63), where $\mathcal{H}$ is the Hamiltonian matrix leading to $\hat{G}_0$ (see e.g. Ref. [140]). Therefore, it fulfills the differential equations [141]

$$[i\partial_t - \mathcal{H}(t)]G_0^X(t,t') = \delta(t-t') \text{ for } X = R, A\,, \quad [i\partial_t - \mathcal{H}(t)]G_0^X(t,t') = 0 \text{ for } X = <, >\,. \tag{5.64}$$

Exploiting Eq. (5.16), we can summarize this in the short-hand notation

$$[i\partial_t - \mathcal{H}(t)]\hat{G}_0 = \delta(t-t')\,. \tag{5.65}$$

This leads to the following differential equation for $\hat{G}$:

$$[i\partial_t - \mathcal{H}(t)]\hat{G}(t,t') = [i\partial_t - \mathcal{H}(t)]\hat{G}_0(t,t') + \int dt_1 \int dt_2 [i\partial_t - \mathcal{H}(t)]\hat{G}_0(t,t_1)\hat{\Sigma}(t_1,t_2)\hat{G}(t_2,t') \tag{5.66}$$

$$= \delta(t-t') + \int dt_1 \int dt_2 \delta(t-t_1)\hat{\Sigma}(t_1,t_2)\hat{G}(t_2,t') \tag{5.67}$$

$$= \delta(t-t') + \int dt_2 \hat{\Sigma}(t,t_2)\hat{G}(t_2,t') \tag{5.68}$$

The derivative with respect to t' can be computed analogously. This leads to the Keldysh equations of motion. For $t \neq t'$ and in momentum space using a translation-invariant system, they read

$$i\partial_t \hat{G}_{\mathbf{k}}(t,t') = \mathcal{H}_{\mathbf{k}}(t)\hat{G}_{\mathbf{k}}(t,t') + \int d\tau \hat{\Sigma}_{\mathbf{k}}(t,\tau)\hat{G}_{\mathbf{k}}(\tau,t')\,, \tag{5.69}$$

$$-i\partial_{t'} \hat{G}_{\mathbf{k}}(t,t') = \hat{G}_{\mathbf{k}}(t,t')\,\mathcal{H}_{\mathbf{k}}(t') + \int d\tau \hat{G}_{\mathbf{k}}(t,\tau)\hat{\Sigma}_{\mathbf{k}}(\tau,t')\,. \tag{5.70}$$

Here, we use the short-hand notation $\hat{G}_{\mathbf{k}}(t,t') = \hat{G}(\mathbf{k},t,t')$, which can also be used for the individual Green's functions. For convenience, this notation is employed in this thesis for any time-dependent calculations.

5.3.4 Wide-Band Limit

One possible source for a self-energy is the coupling to a fermionic bath. In this thesis, we use the wide-band limit, where the spectral density of the bath is assumed to be constant. This can be done since we are not interested in effects due to specific details of the band structure of the fermionic bath [142]. In the following, we only briefly discuss how the wide band limit simplifies some of the equations that were introduced above. For a more detailed introduction of the wide band limit, the reader is referred to Refs. [135, 142, 143].
The self-energy can then be simplified significantly, leading to [144]

$$\begin{aligned}\hat{\Sigma}_{\mathbf{k}}(t,t') &= \int \frac{d\Omega}{2\pi} e^{-i\Omega(t-t')} \begin{bmatrix} -i\Gamma & -2i\Gamma \tanh\left(\frac{\beta\Omega}{2}\right) \\ & i\Gamma \end{bmatrix} \\ &= \begin{bmatrix} -i\Gamma\delta(t-t') & -2\Gamma\left[\beta \sinh\left(\frac{\pi(t-t')}{\beta}\right)\right]^{-1} \\ & i\Gamma\delta(t-t') \end{bmatrix} . \end{aligned} \tag{5.71}$$

Inserting this into equations (5.69) and (5.70), we obtain very simple equations of motions as shown in Ref. [144]. For the retarded Green's function we find

$$i\partial_t G^R_{\mathbf{k}}(t,t') = \mathcal{H}_{\mathbf{k}}(t) G^R_{\mathbf{k}}(t,t') + \int_{t'}^{t} d\tau \Sigma^R(t,\tau) G^R_{\mathbf{k}}(\tau,t') \tag{5.72}$$

$$= \left[\mathcal{H}_{\mathbf{k}}(t) - i\Gamma\right] G^R_{\mathbf{k}}(t,t') \tag{5.73}$$

and for the Keldysh Green's function we find

$$\partial_t G^K_{\mathbf{k}}(t,t') = -i\left[\mathcal{H}_{\mathbf{k}}(t) - i\Gamma\right] G^K_{\mathbf{k}}(t,t') - i\int_{-\infty}^{t'} d\tau \Sigma^K(t,\tau) G^A_{\mathbf{k}}(\tau,t') \tag{5.74}$$

$$\partial_{t'} G^K_{\mathbf{k}}(t,t') = +iG^K_{\mathbf{k}}(t,t')\left[\mathcal{H}_{\mathbf{k}}(t') + i\Gamma\right] + i\int_{-\infty}^{t} d\tau G^R_{\mathbf{k}}(t,\tau)\Sigma^K(\tau,t') . \tag{5.75}$$

The other equations of motions can also be simplified but their simplified versions are not shown explicitly since they are not needed for the remainder of this thesis.
Moreover, the wide band limit also simplifies the frequency dependent Green's functions in equilibrium. In case of the advanced and retarded Green's functions, one finds

$$G^R_{\nu,\nu'}(\omega) = \left[\frac{1}{(\omega + i\Gamma) - \mathcal{H}}\right]_{\nu\nu'} , \quad G^A_{\nu,\nu'}(\omega) = \left[\frac{1}{(\omega - i\Gamma) - \mathcal{H}}\right]_{\nu\nu'} \tag{5.76}$$

by using Eq. (5.71) and performing a Fourier transform.

5.4 Green's Functions for Block-Tridiagonal Hamiltonians

This section is based on Ref. [145] (see Chapter 10 for details), where the algorithm was presented in the same form.

In this section, we introduce an efficient method to compute the Green's functions of block-tridiagonal Hamiltonians. Many typical condensed matter systems have the needed block-tridiagonal Hamiltonian, such as non-interacting few-nearest-neighbor models, where only sites being k-nearest-neighbors with finite and optimally small k are connected. Additionally, a vast amount of observables can be connected to Green's functions, suggesting that the algorithm can be employed for many applications.

The most simple example of systems with suitable Hamiltonians are non-interacting nearest-neighbor models in one dimension. Here, the Hamiltonian is not only of block-tridiagonal, but even of tridiagonal form. For longer ranged models, an artificial unit cell has to be introduced, such that only nearest-neighbor unit cells are connected due to the terms of the Hamiltonian. In

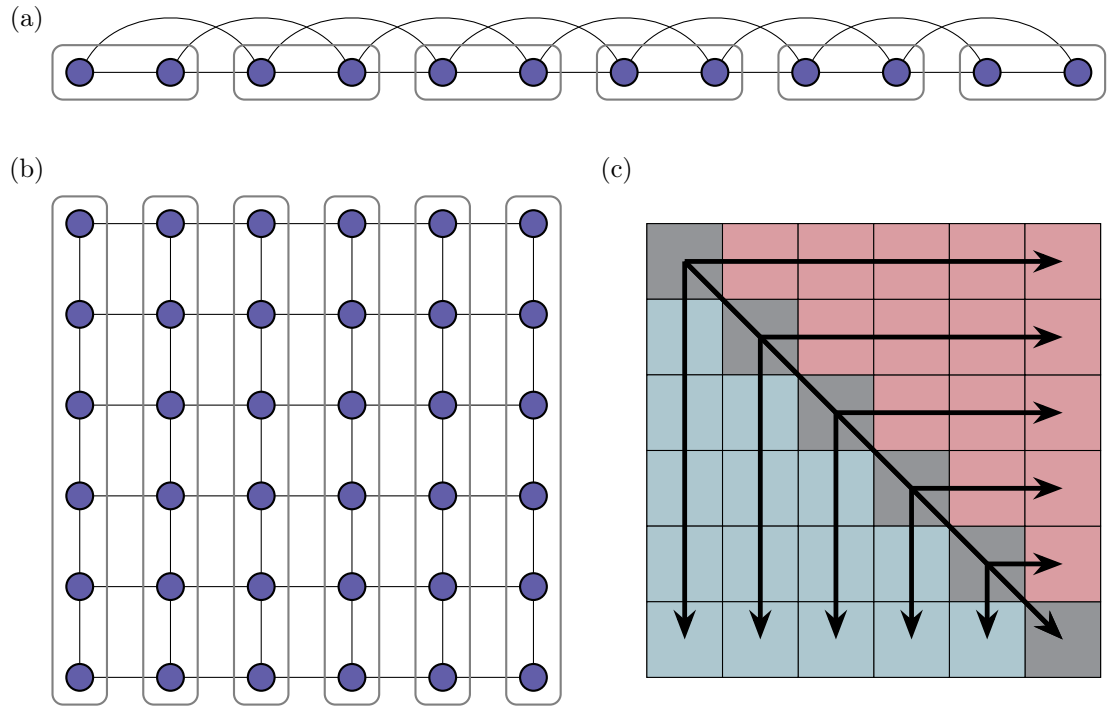

Figure 5.2: (a) Chain with nearest-neighbor and next-nearest-neighbor hopping. The gray boxes show the artificial unit cells that give rise to the block-structure of the matrix. In these unit cells, the matrix is block-tridiagonal. (b) Two dimensional square lattice model with nearest-neighbor hopping. Each column belongs to an artificial unit cell. Equivalently, it would be possible to chose the rows as unit cells. Since only nearest-neighbor unit cells are connected, the Hamiltonian has a block-tridiagonal form as well. (c) Recursion scheme of the inversion algorithm, where G_{11} is the starting point. The diagonal, marked in gray, is computed using Eq. (5.87). The upper (red) and lower (blue) triangle can be found exploiting Eqs. (5.88) and (5.89), respectively.

this case, each of the unit cells belong to a block of the Hamiltonian, which is then given in a block-tridiagonal structure. As an example, the artificial unit cells for a next-nearest-neighbor model are shown in Fig. 5.2(a) as gray boxes. Of course, it is possible that the artificial unit cell agrees with the physical unit cell of the system, but this is not necessary.

It also possible to find a block-tridiagonal structure in higher-dimensional systems. Let us e.g. consider a non-interacting two-dimensional system on a square lattice with only nearest neighbor hopping as shown in Fig. 5.2(b). In this case, we can introduce an artificial unit cell containing a column (or alternaternively a row) of sites as denoted by the gray boxes. Since only neighboring columns are connected, this leads to a block-tridiagonal structure, where the size of the blocks are given by the size of the Hilbert space of a single column.

The proper definition of the according unit cells is straightforward and well known. It has for example been shown in a similar way in Refs. [146, 147].

For Hamiltonians with a block-tridiagonal structure, there are ways to optimize the calculation of Green's functions, or in other words, efficient computation methods for the inversion of specific block-tridiagonal matrices exist [146–152], which we want to discuss in the following. Here, we mainly follow the presentation of Refs. [148], where an algorithm was introduced for translation-invariant block-tridiagonal Hamiltonians. We generalize their notation to the case of block-tridiagonal Hamiltonians without translation invariance by merging the algorithm with the one of Ref. [153], where the same method was shown for tridiagonal Hamiltonians. Impressively, the computation time of this method scales linearly with the number of blocks if only a few columns, rows or diagonals are needed. This is a significant speed-up since a standard diagonalization typically scales cubic with the size of the matrix. In one-dimension, this leads to a linear scaling with

the system size as the block sizes are constant. In higher dimensions, we note that the block size of the systems scales with the system size (assuming e.g. an $L \times L$ square lattice). Therefore, the algorithm is less efficient in this case although still leading to a significant speed-up.
The extraordinary scaling of this method relies on the fact that it is not necessary to calculate all elements of the Green's functions. But even if the complete Green's function is needed, we find a quadratic scaling with the number of blocks, which is still better than the typical scaling of standard methods which do not exploit the block-tridiagonal structure.

5.4.1 Inversion algorithm

We now discuss the explicit algorithm for an efficient calculation of the Green's function for a block-tridiagonal Hamiltonian. As already mentioned above, we therefore employ the presentation of Ref. [148] for translation-invariant block-tridiagonal Hamiltonians and of Ref. [153] for tridiagonal Hamiltonians without translational invariance and generalize it to the case of block-tridiagonal Hamiltonians without translational invariance. The retarded, advanced and Matsubara Green's functions can be written as

$$G = [x - \mathcal{H}]^{-1} = A^{-1} \tag{5.77}$$

with x being a complex number. Given that $\mathcal{H}$ is of block-tridiagonal form, A has to be of such form as well. In the following, we assume that we only deal with hermitian Hamiltonians. This leads to the fact that the matrix, that needs to be inverted, can always be written in the form

$$A = \begin{pmatrix} a_1 & b_1 & & & & \\ b_1^\dagger & a_2 & b_2 & & & \\ & b_2^\dagger & a_3 & b_3 & & \\ & & b_3^\dagger & a_4 & \ddots & \\ & & & \ddots & \ddots & b_{N-1} \\ & & & & b_{N-1}^\dagger & a_N \end{pmatrix}, \tag{5.78}$$

with blocks a_i, b_i, and $b_i^\dagger$, and N being the number of artificial unit cells or diagonal blocks.
In the next step, we employ a UDL-decomposition and find $A = UDL$ with a block-diagonal matrix D consisting of blocks D_i with $i \in 1 \dots N$ and

$$U = \begin{pmatrix} 1 & U_1 & & & \\ & 1 & U_2 & & \\ & & \ddots & \ddots & \\ & & & \ddots & U_{N-1} \\ & & & & 1 \end{pmatrix}, \quad L = \begin{pmatrix} 1 & & & & \\ L_1 & 1 & & & \\ & L_2 & \ddots & & \\ & & \ddots & \ddots & \\ & & & L_{N-1} & 1 \end{pmatrix}. \tag{5.79}$$

We note that D_i, U_i and L_i are still blocks with the same size as the original blocks of A. These blocks can be found recursively by starting from $i = N$, where we find

$$D_N = a_N\,, \tag{5.80}$$

We can then calculate U_i, L_i and D_i recursively from D_{i+1}

$$U_i = b_i D_{i+1}^{-1} \tag{5.81}$$

$$L_i = D_{i+1}^{-1} b_i^\dagger \tag{5.82}$$

$$\begin{aligned} D_i &= a_i - U_i b_i^\dagger \\ &= a_i - b_i D_{i+1}^{-1} b_i^\dagger \end{aligned} \tag{5.83}$$

until all blocks are known.

The inverse of A can then be found by calculating the inverse of the matrix product UDL, which is given by $G = A^{-1} = L^{-1}D^{-1}U^{-1}$. Consequently, it is necessary to compute the inverses of D, U and L, which are given by

$$D^{-1} = \begin{pmatrix} D_1^{-1} & & & \\ & D_2^{-1} & & \\ & & \ddots & \\ & & & D_N^{-1} \end{pmatrix}, \quad U^{-1} = \begin{pmatrix} 1 & -U_1 & U_1U_2 & \cdots & (-1)^{N-1}U_1\cdots U_{N-1} \\ & 1 & -U_2 & \ddots & \vdots \\ & & \ddots & \ddots & U_{N-2}U_{N-1} \\ & & & \ddots & -U_{N-1} \\ & & & & 1 \end{pmatrix}, \tag{5.84}$$

$$L^{-1} = \begin{pmatrix} 1 & & & & \\ -L_1 & \ddots & & & \\ L_2L_1 & \ddots & \ddots & & \\ \vdots & \ddots & -L_{N-2} & 1 & \\ (-1)^{N-1}L_{N-1}\dots L_1 & \dots & L_{N-1}L_{N-2} & -L_{N-1} & 1 \end{pmatrix}. \tag{5.85}$$

The special structure of D^{-1}, U^{-1} and L^{-1} allows finding the entries of G using a recursion relation as well. For the diagonal blocks, we find

$$G_{1,1} = D_1^{-1}\,, \tag{5.86}$$

$$\begin{aligned} G_{i+1,i+1} &= D_{i+1}^{-1} + L_i G_{i,i} U_i \\ &= D_{i+1}^{-1} + D_{i+1}^{-1} b_i^\dagger G_{i,i} b_i D_{i+1}^{-1}\,. \end{aligned} \tag{5.87}$$

The calculation of the diagonal blocks of G will therefore only scale linearly with the number of blocks. In one dimension the scaling is therefore linear in system size which is a huge speed up compared to the cubic scaling of a standard full diagonalization of the matrix.
For the off-diagonal blocks of the inverse matrix a recursion relation can be constructed as well. One finds for $j \geq i$

$$G_{i,j+1} = -G_{i,j}U_j\,, \tag{5.88}$$

$$G_{j+1,i} = -L_j G_{j,i}\,, \tag{5.89}$$

which allows the calculation of all elements of the Green's function. Here, Eqs. (5.88) and (5.89) can be used to compute the upper and lower triangle of G, respectively, by starting from the diagonal blocks that have been calculated before. The complete recursive procedure needed for the computation of the full inverse is shown in Fig. 5.2(c), where the upper and lower diagonals are marked in red and blue, respectively, and the recursion directions are denoted by arrows.
In the cases where not only the diagonal blocks are needed (but also off-diagonal blocks), the algorithm still allows for a significant speed-up. Remarkably, if only a few rows, columns or off-diagonals are needed, the runtime is still linear in system size. In this thesis, this algorithm is used to employ systems with a size of up to the order of 10^5 unit cells for a unit cell size of $n = 3$.

Chapter 6

Generalized BCS Theory

In this chapter, a generalization of the famous Bardeen-Cooper-Schrieefer (BSC) theory is introduced. The BCS theory was invented by J. Baardeen, L.N. Cooper and J.R. Schrieffer in 1957 [89, 90]. This theory explains superconductivity by an effective attractive interaction between electrons that leads to the formation of bound states of two electrons, which are called Cooper-pairs. Here, the effective interaction arises due to phonons that couple to the electrons of the system and it is treated on a mean-field level. In BCS theory, a very simple form of an attractive interaction is considered, leading to a standard s-wave superconductor.
However, generalized BCS approaches with BCS-like Hamiltonians, which can describe general momentum-dependent pairing interactions, multi-band models and superconducting gaps with an additional spin structure, have been established and employed to solve more general superconducting models on a mean-field level (see e.g. Refs. [31, 60, 91, 144, 154–162]). Therefore, generalizations of the standard theory allow for the description of unconventional pairing orders, which we exploit in this thesis.

In the remainder of this chapter, we first briefly review the idea of mean-field theory. After this, the BCS theory is presented. We then introduce a generalization of the BCS theory to models with both multiple bands and superconducting gaps with an additional spin structure. Here, it is also discussed how to decompose the gap into different form factors and how to solve the gap equation efficiently. Moreover, a set of differential equations is derived which allows for the calculation of the time evolution of order parameters. Finally, it is shown, how the approach simplifies if it is not necessary to take a spin structure for the gap into account. Here, simplified equations are shown for both, stationary equilibrium solutions and time evolutions. Furthermore, it is discussed how to compute the free energy within this simplified case.

Significant parts of this chapter are based on Refs. [91, 132, 144, 163].

6.1 Mean-Field Theory

Before discussing the standard and generalized BCS theory, the mean-field theory approach, on which BCS is based, is briefly reviewed. For a more detailed introduction, the reader is referred to Ref. [132] on which most of this introduction is based.
The main idea of mean-field theory is to replace interactions with a single particle picture by using a mean-field that includes the effect of all other particles. In this way, many-body Hamiltonians can be traced back to single-particle Hamiltonians which then need to be solved self-consistently.

The concept of mean-field theory can be understood by considering the generic Hamiltonian

$$H_{AB} = AB\,, \tag{6.1}$$

with general operators A and B. The corresponding mean-field Hamiltonian is then given by

$$H_{AB}^{\mathrm{MF}} = A\,\langle B\rangle + \langle A\rangle\,B - \langle A\rangle\,\langle B\rangle\ , \tag{6.2}$$

showing that we consider the operator A in the presence of the mean-field coming from B and the other way around, as well as an additional term including only the expectation values of both. In the mean-field approximation, only the term $(A-\langle A\rangle)(B-\langle B\rangle)$ is neglected. This term is assumed to be small since it is quadratic in fluctuations.
In case of electronic interactions, we usually deal with terms of the form of $c_q^\dagger c_r^\dagger c_s c_t$ with $c_q^{(\dagger)}$ denoting the annihilation (creation) operator for an electron in state $|q\rangle$. In this case, two operators need to get contracted to form the mean-field parameter. For superconducting instabilities we then contract $\langle cc\rangle$ and $\langle c^\dagger c^\dagger\rangle$, which leads to

$$c_q^\dagger c_r^\dagger c_s c_t \approx \langle c_q^\dagger c_r^\dagger\rangle c_s c_t + c_q^\dagger c_r^\dagger \langle c_s c_t\rangle - \langle c_q^\dagger c_r^\dagger\rangle \langle c_s c_t\rangle \ . \tag{6.3}$$

One could also contract different operators that belong to different instabilities treated in the Hartree Fock theory (see e.g. Ref. [132]). Since we are only interested in the superconducting instabilities, we ignore all other (Wick) contractions in the following.

6.2 Standard BCS Theory

We start by recapitulating the BCS theory (here also denoted as standard BCS theory to distinguish it from the generalizations), which is introduced in detail in a variety of different textbooks. Possible examples are Refs. [91, 132, 134, 163–165] and the reader is referred to one of these for more details. For the introduction of BCS theory, we directly consider the presence of an effective attractive interaction between the electrons in the following, which is assumed to be phonon-mediated.

6.2.1 Gap Equation

In the first part of this section, the gap equation is derived, which is the self-consistency equation being the basis of standard BCS theory. This part is mainly based on Ref. [91].
We consider a Hamiltonian of form

$$\begin{aligned} H &= H_0 + H_{\text{int}} && (6.4)\\ &= \sum_{\mathbf{k},\sigma} \xi_{\mathbf{k}} c_{\mathbf{k}\sigma}^\dagger c_{\mathbf{k}\sigma} + g \sum_{\mathbf{k},\mathbf{k}',\mathbf{q}} c_{\mathbf{k}+\mathbf{q},\uparrow}^\dagger c_{\mathbf{k}'-\mathbf{q},\downarrow}^\dagger c_{\mathbf{k}'\downarrow} c_{\mathbf{k}\uparrow}\,, && (6.5)\end{aligned}$$

with $c_{\mathbf{k},\sigma}^{(\dagger)}$ being the annihilation (creation) operator of an electron at momentum $\mathbf{k}$ and spin σ. Here, we assumed that the non-interacting part H_0 is diagonal in momentum k and independent of spin σ, as well as a momentum-independent effective attractive interaction $g<0$ (g is assumed to scale anti-proportional to the volume or to the number of $\mathbf{k}$-points) yielding a model with a very simple structure. In real space, the momentum-independent interaction leads to a local interaction $\propto g\delta(\mathbf{r}-\mathbf{r}')$. Within this chapter, the grand-canonical ensemble is used. Here, we assume that the chemical potential μ is already included in $\xi_{\mathbf{k}} = \epsilon_{\mathbf{k}} - \mu$, where $\epsilon_{\mathbf{k}}$ denotes the single particle energies.
The model gets simplified even further by only considering a vanishing total momentum of the interacting particles $\mathbf{k}+\mathbf{k}'$, which is the only part that needs to be included for the BCS theory. We therefore treat only the $\mathbf{k}+\mathbf{k}'=\mathbf{0}$ case in the following and thus, we can rewrite [1]

$$H = \sum_{\mathbf{k},\sigma} \xi_{\mathbf{k}} c_{\mathbf{k}\sigma}^\dagger c_{\mathbf{k}\sigma} + g \sum_{\mathbf{k},\mathbf{k}'} c_{\mathbf{k},\uparrow}^\dagger c_{-\mathbf{k},\downarrow}^\dagger c_{-\mathbf{k}'\downarrow} c_{\mathbf{k}'\uparrow}\,. \tag{6.6}$$

We now treat this model with a mean-field approach and concentrate on the mean-field terms

$$b_{\mathbf{k}} = \langle c_{-\mathbf{k},\downarrow} c_{\mathbf{k},\uparrow}\rangle \tag{6.7}$$

[1] Note that in other references, see e.g. [132], the sum of the interacting part is often restricted to momenta around the Fermi surface.

which correspond to the superconducting instability. Other possible contractions are not considered since they belong to different instabilities that we are not interested in. This leads to the mean-field Hamiltonian

$$H^{\mathrm{MF}} = \sum_{\mathbf{k},\sigma} \xi_{\mathbf{k}} c^\dagger_{\mathbf{k}\sigma} c_{\mathbf{k}\sigma} + g \sum_{\mathbf{k},\mathbf{k}'} \left(b^*_{\mathbf{k}'} c_{-\mathbf{k}\downarrow} c_{\mathbf{k}\uparrow} + b_{\mathbf{k}'} c^\dagger_{\mathbf{k}\uparrow} c^\dagger_{-\mathbf{k}\downarrow} - b^*_{\mathbf{k}} b_{\mathbf{k}'} \right) \tag{6.8}$$

$$= \sum_{\mathbf{k},\sigma} \xi_{\mathbf{k}} c^\dagger_{\mathbf{k}\sigma} c_{\mathbf{k}\sigma} - \sum_{\mathbf{k}} \left(\Delta^* c_{-\mathbf{k}\downarrow} c_{\mathbf{k}\uparrow} + \Delta c^\dagger_{\mathbf{k}\uparrow} c^\dagger_{-\mathbf{k}\downarrow} \right) - \frac{|\Delta|^2}{g} , \tag{6.9}$$

where we defined the superconducting gap

$$\Delta = -g \sum_{\mathbf{k}} b_{\mathbf{k}} = -g \sum_{\mathbf{k}} \langle c_{-\mathbf{k},\downarrow} c_{\mathbf{k},\uparrow} \rangle \tag{6.10}$$

in the last step. Eq. (6.10) is known as the gap equation that needs to be solved self-consistently. A finite gap cannot exist for arbitrary high temperatures. Therefore, there is a critical temperature where a phase transition between a superconducting and a non-superconducting state occurs. The critical temperature can thus be defined by the lowest temperature with a vanishing gap.

6.2.2 Bogoliubov Transformation

The mean-field Hamiltonian (6.9) is now quadratic and can therefore be diagonalized in a single-particle picture as it is shown in this subsection, which is mainly based on Ref. [91]. Nevertheless, annihilation and creation operators, or in other words particles and holes, get mixed in the diagonalization since there are terms containing only creation or only annihilation operators. We therefore perform the Bogolyubov transformation

$$c_{\mathbf{k}\uparrow} = u^*_{\mathbf{k}} \gamma_{\mathbf{k}1} + v_{\mathbf{k}} \gamma^\dagger_{\mathbf{k}2} , \quad c_{-\mathbf{k}\downarrow} = -v^*_{\mathbf{k}} \gamma_{\mathbf{k}1} + u_{\mathbf{k}} \gamma^\dagger_{\mathbf{k}2} \tag{6.11}$$

with $|u_{\mathbf{k}}|^2 + |v_{\mathbf{k}}|^2 = 1$ for proper normalization and (anti-)commutation relations. $\gamma^{(\dagger)}_{\mathbf{k},i}$ thereby denotes the annihilation and creation operators of electron like ($i = 1$) and hole like ($i = 2$) quasiparticles.
With the choice of [132]

$$|u_{\mathbf{k}}|^2 = \frac{1}{2} \left(1 + \frac{\xi_{\mathbf{k}}}{E_{\mathbf{k}}} \right) , \quad |v_{\mathbf{k}}|^2 = \frac{1}{2} \left(1 - \frac{\xi_{\mathbf{k}}}{E_{\mathbf{k}}} \right) \tag{6.12}$$

the mean-field Hamiltonian gets diagonal and we find

$$H^{\mathrm{MF}} = \sum_{\mathbf{k}} E_{\mathbf{k}} \left(\gamma^\dagger_{\mathbf{k}1} \gamma_{\mathbf{k}1} + \gamma^\dagger_{\mathbf{k}2} \gamma_{\mathbf{k}2} \right) + \sum_{\mathbf{k}} \left[\xi_{\mathbf{k}} - E_{\mathbf{k}} + \Delta b_{\mathbf{k}} \right] \tag{6.13}$$

with the quasiparticle energy

$$E_{\mathbf{k}} = \sqrt{\xi^2_{\mathbf{k}} + |\Delta|^2} . \tag{6.14}$$

6.2.3 Nambu Formalism

In this subsection, we rewrite the mean-field Hamiltonian from above by introducing the Nambu formalism. Therefore, we define the Nambu spinor (see e.g. Ref. [132, 163])

$$\boldsymbol{\psi}_{\mathbf{k}} = \begin{pmatrix} c_{\mathbf{k},\uparrow} \\ c^\dagger_{-\mathbf{k},\downarrow} \end{pmatrix} , \quad \boldsymbol{\psi}^\dagger_{\mathbf{k}} = \begin{pmatrix} c^\dagger_{\mathbf{k},\uparrow}, c_{-\mathbf{k},\downarrow} \end{pmatrix} \tag{6.15}$$

with anti-commutation relations

$$\{ \psi_{\mathbf{k},i}, \psi_{\mathbf{k}',j} \} = \left\{ \psi^\dagger_{\mathbf{k},i}, \psi^\dagger_{\mathbf{k}',j} \right\} = 0 , \quad \left\{ \psi_{\mathbf{k},i}, \psi^\dagger_{\mathbf{k}',j} \right\} = \delta_{\mathbf{k},\mathbf{k}'} \delta_{i,j} . \tag{6.16}$$

With these Nambu vectors, the mean-field Hamiltonian (6.9) can be rewritten as (see e.g. Ref. [163])

$$H^{\mathrm{MF}} = \sum_{\mathbf{k}} \boldsymbol{\psi}_{\mathbf{k}}^{\dagger} \begin{pmatrix} \xi_{\mathbf{k}} & \Delta \\ \Delta^{*} & -\xi_{-\mathbf{k}} \end{pmatrix} \boldsymbol{\psi}_{\mathbf{k}} + C = \sum_{\mathbf{k}} \boldsymbol{\psi}_{\mathbf{k}}^{\dagger} \mathcal{H}_{\mathrm{BCS}}(\mathbf{k}) \boldsymbol{\psi}_{\mathbf{k}} + C \tag{6.17}$$

with

$$C = \sum_{\mathbf{k}} \xi_{\mathbf{k}} - \frac{|\Delta|^2}{g} \,. \tag{6.18}$$

6.2.4 Nambu Green's Functions

We cannot only rewrite the Hamiltonian in the Nambu basis, but we can also use this basis to define Green's functions of the superconducting system, which we do in the following mainly based on Ref. [132, 163].
We therefore define the normal Green's function

$$\mathcal{G}_{\sigma\sigma}(\mathbf{k}, \Delta\tau = \tau_2 - \tau_1) = -\left\langle T_\tau c_{\mathbf{k}\sigma}(\tau_2) c_{\mathbf{k}\sigma}^{\dagger}(\tau_1) \right\rangle \tag{6.19}$$

and the analomous Green's function

$$\mathcal{F}_{\downarrow\uparrow}(\mathbf{k}, \Delta\tau = \tau_2 - \tau_1) = -\left\langle T_\tau c_{-\mathbf{k}\downarrow}^{\dagger}(\tau_2) c_{\mathbf{k}\uparrow}^{\dagger}(\tau_1) \right\rangle \tag{6.20}$$

in imaginary time. The Nambu Green's function in imaginary time of the BCS Hamiltonian, which is given by

$$G_{i,j}(\mathbf{k}, \Delta\tau = \tau_2 - \tau_1) = -\left\langle T_\tau \psi_{\mathbf{k},i}(\tau_2) \psi_{\mathbf{k},j}^{\dagger}(\tau_1) \right\rangle \,, \tag{6.21}$$

can then be written as

$$\begin{aligned} G(\mathbf{k}, \Delta\tau) &= \begin{pmatrix} \mathcal{G}_{\uparrow,\uparrow}(\mathbf{k}, \Delta\tau) & \left[\mathcal{F}_{\downarrow\uparrow}(\mathbf{k}, \Delta\tau)\right]^{*} \\ \mathcal{F}_{\downarrow\uparrow}(\mathbf{k}, \Delta\tau) & \mathcal{G}_{\downarrow,\downarrow}(-\mathbf{k}, -\Delta\tau) \end{pmatrix} \\ &= \frac{1}{\beta} \sum_{i\omega_n} e^{-i\omega_n \tau} G(\mathbf{k}, i\omega_n) = \frac{1}{\beta} \sum_{i\omega_n} e^{-i\omega_n \tau} \frac{1}{i\omega_n - \mathcal{H}_{\mathrm{BCS}}(\mathbf{k})}. \end{aligned} \tag{6.22}$$

Here, we ignored the additional term K and used the connection of Green's functions in imaginary time and imaginary frequency from the last chapter.
We insert these relations and compute the matrix inverse to obtain the final result of

$$\begin{aligned} \Delta &= -g \left\langle c_{-\mathbf{k},\downarrow} c_{\mathbf{k},\uparrow} \right\rangle = -g \sum_{\mathbf{k}} G_{1,2}\left(\mathbf{k}, \Delta\tau = 0^{+}\right) = -g \sum_{\mathbf{k}} \left[\mathcal{F}_{\downarrow\uparrow}\left(\mathbf{k}, \Delta\tau = 0^{+}\right)\right]^{*} \\ &= -g \sum_{\mathbf{k}} \frac{1}{\beta} \sum_{i\omega_n} \frac{-\Delta e^{-i\omega_n 0^{+}}}{(i\omega_n)^2 - (\xi_{\mathbf{k}}^2 + |\Delta|^2)} \end{aligned} \tag{6.23}$$

for the gap equation. In the same manner, we can also write the gap equation in terms of the Nambu lesser Green's function

$$G_{i,j}^{<}(k, \Delta t = t_2 - t_1) = i \left\langle \psi_{\mathbf{k},j}^{\dagger}(t_1) \psi_{\mathbf{k},i}(t_2) \right\rangle \,, \tag{6.24}$$

which leads to

$$\Delta = -g \sum_{\mathbf{k}} \frac{1}{i} G_{1,2}^{<}\left(\mathbf{k}, \Delta t = 0\right) \,. \tag{6.25}$$

6.3 Generalization

We now turn to a more generalized version of this formalism and see how to derive a gap equation in that case. To this end, we assume a pairing gap, which can have a momentum dependence, a spin index, as well as an orbital index as it was used, for example, in Ref. [31, 60, 157, 158].

6.3.1 Gap Equation

In the following we derive the gap equation of this generalized theory. Here, we mainly follow Ref. [91] and generalize their spin index to a multi-index containing the spin and the orbital (in case of multiple orbitals). We start with a Hamiltonian of the general form

$$H = \sum_{\mathbf{k},a,b} h_{\mathbf{k}}^{a,b} c_{\mathbf{k},a}^\dagger c_{\mathbf{k},b} + \frac{1}{2N} \sum_{\mathbf{k},\mathbf{k}',a,b,a',b'} V_{\mathbf{k}',\mathbf{k}}^{a'b'ab} \, c_{\mathbf{k}',a'}^\dagger \, c_{-\mathbf{k}',b'}^\dagger \, c_{-\mathbf{k},b} \, c_{\mathbf{k},a} \tag{6.26}$$

with N being the number of $\mathbf{k}$-points taken into account and a, b being the multi-indices containing spin and orbital degrees of freedom.
Using mean-field theory, we approximate the quartic term with multiple quadratic terms and arrive at the expression

$$\begin{aligned}
H^{\mathrm{MF}} =& \sum_{\mathbf{k},ab} h_{\mathbf{k}}^{a,b} c_{\mathbf{k},a}^\dagger c_{\mathbf{k},b} + \frac{1}{2N} \sum_{\mathbf{k}\mathbf{k}',aba'b'} V_{\mathbf{k}',\mathbf{k}}^{a'b'ab} \Big(\Big\langle c_{\mathbf{k}',a'}^\dagger c_{-\mathbf{k}',b'}^\dagger \Big\rangle \, c_{-\mathbf{k},b} c_{\mathbf{k},a} \\
& + c_{\mathbf{k}',a'}^\dagger c_{-\mathbf{k}',b'}^\dagger \, \langle c_{-\mathbf{k},b} c_{\mathbf{k},a} \rangle - \Big\langle c_{\mathbf{k}',a'}^\dagger c_{-\mathbf{k}',b'}^\dagger \Big\rangle \, \langle c_{-\mathbf{k},b} c_{\mathbf{k},a} \rangle \Big) \\
=& \frac{1}{2} \Bigg[\sum_{\mathbf{k},ab} \Big(h_{\mathbf{k}}^{a,b} c_{\mathbf{k},a}^\dagger c_{\mathbf{k},b} - h_{-\mathbf{k}}^{b,a} c_{-\mathbf{k},a} c_{-\mathbf{k},b}^\dagger \Big) \\
& + \frac{1}{N} \sum_{\mathbf{k},ab} \left(\sum_{\mathbf{k}',a'b'} V_{\mathbf{k}',\mathbf{k}}^{a'b'ab} \Big\langle c_{\mathbf{k}',a'}^\dagger c_{-\mathbf{k}',b'}^\dagger \Big\rangle \right) c_{-\mathbf{k},b} c_{\mathbf{k},a} \\
& + \frac{1}{N} \sum_{\mathbf{k},ab} \left(\sum_{\mathbf{k}',a'b'} V_{\mathbf{k},\mathbf{k}'}^{aba'b'} \Big\langle c_{-\mathbf{k}',b'} c_{\mathbf{k}',a'} \Big\rangle \right) c_{\mathbf{k},a}^\dagger c_{-\mathbf{k},b}^\dagger \Bigg] + K \\
=& \frac{1}{2} \sum_{\mathbf{k}} \boldsymbol{\psi}_{\mathbf{k}}^\dagger \begin{pmatrix} h_{\mathbf{k}} & \Delta_{\mathbf{k}} \\ \Delta_{\mathbf{k}}^\dagger & h_{-\mathbf{k}}^* \end{pmatrix} \boldsymbol{\psi}_{\mathbf{k}} + K
\end{aligned} \tag{6.27}$$

with the Nambu vector $\boldsymbol{\psi}_{\mathbf{k}} = \left[c_{\mathbf{k},\uparrow}, c_{\mathbf{k},\downarrow}, c_{-\mathbf{k},\uparrow}^\dagger, c_{-\mathbf{k},\downarrow}^\dagger \right]^T$. Here, $c_{\mathbf{k},\sigma}^{(\dagger)} = \left[c_{\mathbf{k},A,\sigma}^{(\dagger)}, c_{\mathbf{k},B,\sigma}^{(\dagger)}, \cdots \right]^T$ is still a vector containing all orbital indices. Moreover, we defined the superconducting gap

$$\Delta_{\mathbf{k}}^{ab} = \frac{1}{N} \sum_{\mathbf{k}',a'b'} V_{\mathbf{k},\mathbf{k}'}^{aba'b'} \, \langle c_{-\mathbf{k}',b'} \, c_{\mathbf{k}',a'} \rangle \tag{6.28}$$

and the energy shift

$$K = -\frac{1}{2N} \sum_{\mathbf{k}\mathbf{k}',aba'b'} V_{\mathbf{k}',\mathbf{k}}^{a'b'ab} \Big\langle c_{\mathbf{k}',a'}^\dagger c_{-\mathbf{k}',b'}^\dagger \Big\rangle \Big\langle c_{-\mathbf{k},b} c_{\mathbf{k},a} \Big\rangle + \frac{1}{2} \sum_{\mathbf{k}} \operatorname{Tr} h_{\mathbf{k}} \,, \tag{6.29}$$

where we used the trace $\operatorname{Tr} h_{\mathbf{k}} = \sum_a h_{\mathbf{k}}^{aa}$. Eq. (6.28) is the gap equation of the mean-field Hamiltonian (6.27), that needs to be solved self-consistently. Numerically, this can be done iteratively as it is discussed in detail below.
In this thesis, we denote the matrix

$$\mathcal{H}_{\mathrm{BdG}}(\mathbf{k}) = \begin{pmatrix} h_{\mathbf{k}} & \Delta_{\mathbf{k}} \\ \Delta_{\mathbf{k}}^\dagger & -h_{-\mathbf{k}}^* \end{pmatrix} , \tag{6.30}$$

which appears in the mean-field Hamiltonian, as Bogoliubov de Gennes (BdG) Hamiltonian in the following (as e.g. done Ref. [60]), although the BdG Hamiltonian sometimes also denotes the operator $H^{BdG} = 1/2 \sum_{\mathbf{k}} \boldsymbol{\psi}_{\mathbf{k}}^\dagger \mathcal{H}_{\mathrm{BdG}}(\mathbf{k}) \boldsymbol{\psi}_{\mathbf{k}}$ as in Ref. [31] . The factor $1/2$ in front of equation (6.27) arises due to artificial doubling of annihilation and creation operators. Every term in equation (6.27) occurs twice and needs therefore to be counted with a factor of $1/2$.

6.3.2 Form Factor Decomposition

It is possible to simplify the calculation of the superconducting gap by applying a form factor decomposition. Here, the interaction gets decomposed into a number of form factors belonging to the irreducible representations of point group of the underlying lattice. Form factor decompositions are, for example, often used for functional renormalization group approaches (see e.g. Ref. [166–168]). Moreover, form factor decompositions have also been applied for other works that treated superconductivity on mean-field level (see e.g. Ref. [144, 154], from where we adapt most of the notation used below). Moreover, the functions that we denote here as form factors are regularly also denoted as basis functions (see e.g. Ref. [155, 156]).
The form factor decomposition of the interaction tensor can be written as

$$V^{a'b',ab}_{\mathbf{k}',\mathbf{k}} = \sum_i v_i \left(f^{a'b'}_{i,\mathbf{k}'}\right)^* f^{ab}_{i,\mathbf{k}} \,, \tag{6.31}$$

which is basically a simple eigenvector decomposition of the matrix that arises when treating the mutli-indices $(\mathbf{k}, a, b)$ and $(\mathbf{k}', a', b')$ as a single index. The index i distinguishes the different form factors. Inserting this expression into the gap equation (6.10) leads to

$$\Delta^{ab}_{\mathbf{k}} = \frac{1}{N} \sum_i f^{ab}_{i,\mathbf{k}} \sum_{\mathbf{k}',a'b'} v_i \left(f^{a'b'}_{i,\mathbf{k}'}\right)^* \langle c_{-\mathbf{k}',b'}\, c_{\mathbf{k}',a'} \rangle \,. \tag{6.32}$$

showing that the gap equation can be decomposed into

$$\Delta^{ab}_{\mathbf{k}} = \sum_i f^{ab}_{i,\mathbf{k}} \Delta_i \quad \text{with} \quad \Delta_i = \frac{1}{N} \sum_{\mathbf{k}',a'b'} v_i \left(f^{a'b'}_{i,\mathbf{k}'}\right)^* \langle c_{-\mathbf{k}',b'}\, c_{\mathbf{k}',a'} \rangle \,. \tag{6.33}$$

The form factor decomposition thus allows for a direct computation of the gaps arising from the individual pairing channels corresponding to the different form factors. Moreover, an implementation of the gap equation in its decomposed form can lead to a significant speed-up when solving the gap equation self-consistently. When using its conventional form, the full $\Delta^{ab}_{\mathbf{k}}$ needs to be calculated in every iteration step. In contrast to that, only the gaps Δ_i are computed when using the form factor decomposed version. Thus, the number of elements that are calculated in every iteration step can be reduced by a factor of $\frac{\textit{number of k-points} \times \textit{number of orbital and spin combinations}^2}{\textit{number of form factors}}$.

We note, that we can also find a simple form for the additional term K, defined over Eq. (6.29), using the form factor decomposition. This leads to

$$\begin{aligned} K &= -\frac{1}{2N} \sum_{\mathbf{k}\mathbf{k}',aba'b'} \sum_i v_i \left(f^{a'b'}_{i,\mathbf{k}'}\right)^* f^{ab}_{i,\mathbf{k}} \left\langle c^\dagger_{\mathbf{k}',a'} c^\dagger_{-\mathbf{k}',b'} \right\rangle \left\langle c_{-\mathbf{k},b} c_{\mathbf{k},a} \right\rangle + \frac{1}{2} \sum_{\mathbf{k}} \operatorname{Tr} h_{\mathbf{k}} \\ &= -\frac{N}{2} \sum_i \frac{|\Delta_i|^2}{v_i} + \frac{1}{2} \sum_{\mathbf{k}} \operatorname{Tr} h_{\mathbf{k}} \,. \end{aligned} \tag{6.34}$$

In theory, arbitrary normalizations can be used for the form factors. A change of the normalization would simply lead to a different pairing strength v_i. However, we normalize the form factors in this thesis according to normalized eigenvectors and we therefore set

$$1 = \sum_{a,b} \frac{1}{\mathcal{V}} \int dk \, |f^{ab}_{i,\mathbf{k}}|^2 \,, \tag{6.35}$$

with $\mathcal{V}$ being the volume of the integral in momentum space. The result can be obtained by either using a single Brioullin Zone or by taking $\mathcal{V} \to \infty$.

6.3.3 Efficient Solution of the Gap Equation

Finding the solution of Eq. (6.33) can be optimized even further. The bottleneck of the individual iteration steps is the calculation of the expectation value $\langle c_{-\mathbf{k}',b'}\, c_{\mathbf{k}',a'} \rangle$. We can solve this expectation value numerically using

$$\langle c_{-\mathbf{k}',b'}\, c_{\mathbf{k}',a'} \rangle = \frac{1}{i} G^<_{(1,a'),(2,b')}(\mathbf{k}', \Delta t = 0) \,. \tag{6.36}$$

Here, $G^{<}_{(j,a),(i,b)}(\mathbf{k}, \Delta t)$ denotes the time-dependent lesser Green's function in the Nambu basis. For convenience, we here use the multi-index $(j,\ a)$ to describe the index of the Nambu basis with a describing both the orbital and spin sector as above and j being the Nambu index. In the following, we consider the wide band limit introduced in Subsection 5.3.4, in which case the lesser Green's function can be simplified to

$$\begin{aligned} G^{<}_{(j,a),(i,b)}(\mathbf{k}, \Delta t = 0) &= \int \frac{d\omega}{2\pi} G^{<}_{(j,a),(i,b)}(\mathbf{k}, \omega) \\ &= \frac{-1}{2\pi} \int d\omega\, n_F(\omega) \left[G^{\mathrm{R}}(\mathbf{k}, \omega) - G^{\mathrm{A}}(\mathbf{k}, \omega) \right]_{(j,a),(i,b)} \\ &= \frac{-1}{2\pi} \int d\omega\, n_F(\omega) \left[\frac{1}{(\omega + i\Gamma) - \mathcal{H}^{\mathrm{BdG}}(\mathbf{k})} - \frac{1}{(\omega - i\Gamma) - \mathcal{H}^{\mathrm{BdG}}(\mathbf{k})} \right]_{(j,a),(i,b)} . \end{aligned} \tag{6.37}$$

Nevertheless, this calculation is rather slow due to the integral that needs to be solved. We therefore aim for finding an analytical expression. For a 2×2-Hamiltonian in the Nambu basis, it is possible to rewrite the gap equation using the digamma function $\Psi(z)$ [169] and we want to find a similar solution for a BdG Hamiltonian of arbitrary size in the following. To this end, we translate the Hamiltonian into its diagonal form and compute the lesser Green's function in this basis. For each eigenvalue E, we can calculate

$$\begin{aligned} G^{<}(E, \Delta t = 0) =& \frac{-1}{2\pi} \int d\omega\, n_F(\omega) \left[\frac{1}{(\omega + i\Gamma) - E} - \frac{1}{(\omega - i\Gamma) - E} \right] \\ =& \frac{-1}{2\pi} \int d\omega \left(\frac{1}{2} - \frac{1}{2} \tanh\left(\frac{b\omega}{2} \right) \right) \frac{-2i\Gamma}{(\omega - E)^2 + \Gamma^2} . \end{aligned} \tag{6.38}$$

This integral can be solved by translating it into Matsubara space (details can be found in Appendix A), which allows us to arrive at the final expression

$$\begin{aligned} G^{<}(E, \Delta t = 0) =& \frac{i}{2} - \frac{i}{2} \left\{ \tanh\left(\frac{b}{2}(E + i\Gamma) \right) + \frac{2}{b} \frac{2i\Gamma}{\left(i\frac{\pi}{b} - E \right)^2 + \Gamma^2} \right. \\ & \left. + \frac{1}{i\pi} \left[\Psi\left(1 + \frac{1}{2} + \Gamma\frac{b}{2\pi} + iE\frac{b}{2\pi} \right) - \Psi\left(1 + \frac{1}{2} - \Gamma\frac{b}{2\pi} + iE\frac{b}{2\pi} \right) \right] \right\} \end{aligned} \tag{6.39}$$

for $\frac{1}{2} - \frac{\Gamma b}{2\pi} + i\frac{Eb}{2\pi} \neq -1, -2, -3, \ldots$. The needed expectation value can then be found by transforming the results back to the original basis, which leads to

$$\langle c_{-\mathbf{k}',b'}\, c_{\mathbf{k}',a'} \rangle = \frac{1}{i} \left[V \begin{pmatrix} G^{<}(E_{\mathbf{k}',1}, \Delta t = 0) & & \\ & G^{<}(E_{\mathbf{k}',2}, \Delta t = 0) & \\ & & \ddots \end{pmatrix} V^{\dagger} \right]_{(1,a'),(2,b')} \tag{6.40}$$

with V being the diagonalization matrix of $\mathcal{H}_{\mathrm{BdG}}(\mathbf{k})$ (with columns consisting of the eigenvectors). This results in an immense speed-up since no integral needs to be solved.

Moreover, it is desirable to find an algorithm for solving the gap equation that converges as fast as possible, meaning that only a minimal amount of iteration steps needs to be performed, and for all possible parameters (even in the limit of $\Delta_i \to 0$). The convergence can be improved by mixing the old and new gap function before applying the next iteration step to avoid too abrupt changes of the superconducting gap. The gap function concerning form factor i to insert in the next step is then given by

$$\Delta_i^{\mathrm{new}} = \Theta\, \Delta_i^{\mathrm{old}} + (1 - \Theta) \sum_{\mathbf{k}',a'b'} v_i \left(f_{i,\mathbf{k}'}^{a'b'} \right)^{*} \langle c_{-\mathbf{k}',b'}\, c_{\mathbf{k}',a'} \rangle^{\mathrm{old}} \tag{6.41}$$

with $\Theta \in [0,1]$ being an adjustable number to improve convergence and $\langle c_{-\mathbf{k}',b'}\, c_{\mathbf{k}',a'}\rangle^{\mathrm{old}}$ being the expectation value (6.36) when including Δ_i^{old}.

The optimized algorithm for solving the gap equation then runs as follows:

1. We take an initial guess $\Delta_i^{\mathrm{start}}$ for the gap functions of the individual form factors. Importantly, this guess should be varied to find all solutions of the gap equation including the ground state.
2. $\Delta_i^{\mathrm{start}}$ gets inserted into Eq. (6.41) as Δ_i^{old} leading to the new solution Δ_i^{new}. Here, the expectation value of the two annihilation operators is calculated via Eq. (6.40).
3. This procedure is repeated by treating Δ_i^{new} as the new Δ_i^{old}.
4. We keep iterating until the solution is converged. This can be checked by ensuring that $\sqrt{\sum_i \left(\Delta_i^{\mathrm{new}} - \Delta_i^{\mathrm{old}}\right)^2} \Big/ \sqrt{\sum_i \left(\Delta_i^{\mathrm{old}}\right)^2}$ is below a certain threshold. In this thesis we set a threshold of $10^{-10} - 10^{-6}$.

6.4 Time Evolution of Order Parameters

In the previous part of this chapter, we have only considered superconducting systems in equilibrium. In the following, we discuss, how to treat the time dependence of superconducting order parameters in generalized BCS theory. Therefore, we derive a self-consistent set of differential equations that can then be solved numerically.
In the following, we use the approach introduced in Ref. [144] and generalize it to the case where the order parameters may have an additional spin structure. This section is thus strongly based on Ref. [144].

In the following, we employ the Keldysh equations of motion derived above and use their simplified form from Subsection 5.3.4 since we consider the wide band limit. We apply the equations of motion for the Nambu basis and consider the BdG Hamiltonian from above, which is now time-dependent and thus given by

$$\mathcal{H}_{\mathbf{k}}^{\mathrm{BdG}}(t) = \begin{pmatrix} h_{\mathbf{k}}(t) & \Delta_{\mathbf{k}}(t) \\ \Delta_{\mathbf{k}}^{\dagger}(t) & -h_{-\mathbf{k}}^{*}(t) \end{pmatrix} . \tag{6.42}$$

We start by defining the equal time expectation values

$$N_{\mathbf{k}}^{mn}(t) = \left\langle \psi_{\mathbf{k}n}^{\dagger}(t)\psi_{\mathbf{k}m}(t) \right\rangle = -\frac{i}{2} G_{\mathbf{k},mn}^{K}(t,t) + \frac{1}{2} , \tag{6.43}$$

where $\psi_{\mathbf{k}n}$ denotes the n-th entry of the Nambu vector defined above. Here, we used the shorthand notation for the Green's function $G_{\mathbf{k}}^{X}(t,t') = G^{X}(\mathbf{k},t,t')$ that was already introduced in Subsection 5.3.3 for the time dependent calculations. The corresponding matrix $N_{\mathbf{k}}(t)$ can be written as a block matrix

$$N_{\mathbf{k}}(t) = \begin{pmatrix} n_{\mathbf{k}}(t) & f_{\mathbf{k}}(t) \\ f_{\mathbf{k}}^{\dagger}(t) & 1 - n_{-\mathbf{k}}^{*}(t) \end{pmatrix} \tag{6.44}$$

with

$$n_{\mathbf{k}}^{ab}(t) = \left\langle c_{\mathbf{k}b}^{\dagger}(t) c_{\mathbf{k}a}(t) \right\rangle , \quad f_{\mathbf{k}}^{ab}(t) = \langle c_{\mathbf{k}b}(t) c_{\mathbf{k}a}(t) \rangle . \tag{6.45}$$

Taking its derivative and inserting equations (5.74) and (5.75) leads to

$$\begin{aligned} \partial_t N_{\mathbf{k}}(t) &= -\frac{i}{2} \left(\partial_\tau + \partial_{\tau'}\right) G_{\mathbf{k}}^{K}(\tau,\tau') \Big|_{\tau=\tau'=t} \\ &= -i \left[\mathcal{H}_{\mathbf{k}}^{\mathrm{BdG}}(t), N_{\mathbf{k}}(t)\right] - \Gamma \left\{2N_{\mathbf{k}}(t) - 1 - I_{\mathbf{k}}^{K}(t)\right\} , \end{aligned} \tag{6.46}$$

where we defined the integral

$$\begin{aligned} I_{\mathbf{k}}^{K}(t) &= \frac{1}{2\Gamma}\int_{-\infty}^{t} d\tau \left[G_{\mathbf{k}}^{R}(t,\tau) + G_{\mathbf{k}}^{R}(t,\tau)^{\dagger}\right]\Sigma^{K}(\tau - t) \\ &= \frac{1}{2\Gamma}\int_{0}^{\infty} d\tau \left[G_{\mathbf{k}}^{R}(t,t-\tau) + G_{\mathbf{k}}^{R}(t,t-\tau)^{\dagger}\right]\Sigma^{K}(\tau)\,. \end{aligned} \tag{6.47}$$

with G^R being the retarded Nambu Green's function. The integral can also be written as a block matrix

$$I_{\mathbf{k}}^{K}(t) = \begin{pmatrix} I_{\mathbf{k}}^{G}(t) & I_{\mathbf{k}}^{D}(t) \\ (I_{\mathbf{k}}^{D}(t))^{\dagger} & -\left(I_{-\mathbf{k}}^{G}(t)\right)^{*} \end{pmatrix} \tag{6.48}$$

in Nambu space, where we defined

$$I_{\mathbf{k}}^{G}(t) = \frac{1}{2\Gamma}\int_{0}^{\infty} d\tau \left[\mathcal{G}_{\mathbf{k}}^{R}(t,t-\tau) + \mathcal{G}_{\mathbf{k}}^{R}(t,t-\tau)^{\dagger}\right]\Sigma^{K}(\tau), \tag{6.49}$$

$$I_{\mathbf{k}}^{D}(t) = \frac{1}{2\Gamma}\int_{0}^{\infty} d\tau \left[\mathcal{F}_{\mathbf{k}}^{R}(t,t-\tau) + \mathcal{F}_{\mathbf{k}}^{R}(t,t-\tau)^{T}\right]\Sigma^{K}(\tau) \tag{6.50}$$

using the normal and analomous retarded Green's functions

$$\mathcal{G}_{\mathbf{k},ab}^{R}(t,t') = G_{\mathbf{k},(1,a)(1,b)}^{R}(t,t') = -i\theta\left(t-t'\right)\left\langle\left[c_a(t), c_b^{\dagger}\left(t'\right)\right]_{+}\right\rangle, \tag{6.51}$$

$$\mathcal{F}_{\mathbf{k},ab}^{R}(t,t') = G_{\mathbf{k},(2,a)(1,b)}^{R}(t,t') = -i\theta\left(t-t'\right)\left\langle\left[c_a^{\dagger}(t), c_b^{\dagger}\left(t'\right)\right]_{+}\right\rangle, \tag{6.52}$$

respectively. In order to evolve the integral $I_{\mathbf{k}}^{K}$ in time, the time derivative of the retarded Green's function from Eq. (5.73) is employed.

We can now summarize all necessary ingredients obtained above to arrive at the closed set of differential equations, which can be solved numerically:

$$i\partial_t n_{\mathbf{k}}(t) = [h_{\mathbf{k}}(t), n_{\mathbf{k}}(t)] + \Delta_{\mathbf{k}}(t) f_{\mathbf{k}}^{\dagger}(t) - f_{\mathbf{k}}(t)\Delta_{\mathbf{k}}^{\dagger}(t) - i\Gamma\left(2n_{\mathbf{k}}(t) - 1 - I_{\mathbf{k}}^{G}(t)\right) \tag{6.53}$$

$$\begin{aligned} i\partial_t f_{\mathbf{k}}(t) &= h_{\mathbf{k}}(t) f_{\mathbf{k}}(t) + f_{\mathbf{k}}(t) h_{-\mathbf{k}}^{*}(t) - \Delta_{\mathbf{k}}(t)\left(n_{-\mathbf{k}}^{*}(t) - 1\right) - n_{\mathbf{k}}(t)\Delta_{\mathbf{k}}(t) \\ &\quad - i\Gamma\left(2f_{\mathbf{k}}(t) - I_{\mathbf{k}}^{D}(t)\right) \end{aligned} \tag{6.54}$$

$$\Delta_{\mathbf{k}}^{ab}(t) = \frac{1}{N}\sum_{\mathbf{k}',a',b'} V_{\mathbf{k},\mathbf{k}'}^{ab,a'b'} f_{\mathbf{k}'}^{a'b'}(t) \tag{6.55}$$

$$I_{\mathbf{k}}^{K}(t) = \frac{1}{2\Gamma}\int_{0}^{\infty} d\tau \left[G_{\mathbf{k}}^{R}(t,t-\tau) + G_{\mathbf{k}}^{R}(t,t-\tau)^{\dagger}\right]\Sigma^{K}(\tau) \tag{6.56}$$

$$= \begin{pmatrix} I_{\mathbf{k}}^{G}(t) & I_{\mathbf{k}}^{D}(t) \\ \left(I_{\mathbf{k}}^{D}(t)\right)^{\dagger} & -\left(I_{-\mathbf{k}}^{G}(t)\right)^{*} \end{pmatrix} \tag{6.57}$$

$$i\partial_t G_{\mathbf{k}}^{R}\left(t,t'\right) = \left(\mathcal{H}_{\mathbf{k}}(t) - i\Gamma\right) G_{\mathbf{k}}^{R}\left(t,t'\right)\,. \tag{6.58}$$

In the case of the presence of a light pulse, the electromagnetic field is included using the Peierls substitution, where we replace

$$h_{\pm\mathbf{k}} \to h_{\pm\mathbf{k}+\frac{e}{c}\mathbf{A}}\,, \tag{6.59}$$

where $\mathbf{A}$ denotes the vector potential and e and c are the electronic charge and light velocity, respectively.

6.5 Special Case with no Spin Structure needed

In the previous sections, we derived a generalization of BCS theory which allows for multiple orbitals and a possible spin structure of the superconducting gap. However, there are many cases,

where the generalization to a gap function with spin indices is not necessary. Therefore, we find in the following a simplification of the approach discussed above, which can be applied for models without same spin pairing and without a coupling of different spin sectors in the non-interacting part of the Hamiltonian. This leads to a multi-band generalization, which is usually found by directly generalizing the standard BCS theory to the multi-orbital case. However, we here derive the needed equations from the more general case introduced above, which allows us to compare both approaches for Hamiltonians, which can be treated using both methods.

6.5.1 BdG Hamiltonian and Gap Equation

As already mentioned, we assume in this section, that the different spin sectors are not coupled in the non-interacting part of the considered Hamiltonian. Thus, we can write

$$h_{\mathbf{k}}^{(\alpha\sigma),(\beta\sigma')} = h_{\mathbf{k},\sigma}^{\alpha,\beta}\delta_{\sigma\sigma'} \tag{6.60}$$

where the multi-indices a, b from above are now explicitly written as a combination of the orbital α/β and the spin σ/σ'. Moreover, we only consider opposite spin pairing and therefore, we only need to employ this part of the interaction, leading to

$$V_{\mathbf{k}',\mathbf{k}}^{(\alpha'\sigma_1)(\beta'\sigma_2),(\alpha\sigma_3)(\beta\sigma_4)} = 0 \text{ for } \sigma_1 = \sigma_2 \text{ or } \sigma_3 = \sigma_4\,. \tag{6.61}$$

These assumptions lead to the new full Hamiltonian

$$H = \sum_{\mathbf{k},\alpha,\beta,\sigma} h_{\mathbf{k},\sigma}^{\alpha,\beta} c_{\mathbf{k},\alpha,\sigma}^\dagger c_{\mathbf{k},\beta,\sigma} + \frac{1}{N}\sum_{\mathbf{k},\mathbf{k}',\alpha,\beta,\alpha',\beta'} \tilde{V}_{\mathbf{k}',\mathbf{k}}^{\alpha'\beta',\alpha\beta}\, c_{\mathbf{k}',\alpha',\uparrow}^\dagger\, c_{-\mathbf{k}',\beta',\downarrow}^\dagger\, c_{-\mathbf{k},\beta,\downarrow}\, c_{\mathbf{k},\alpha,\uparrow} \tag{6.62}$$

with

$$\begin{aligned}\tilde{V}_{\mathbf{k}',\mathbf{k}}^{\alpha'\beta',\alpha\beta} &= \frac{1}{2}\left(V_{\mathbf{k}',\mathbf{k}}^{(\alpha'\uparrow)(\beta'\downarrow),(\alpha\uparrow)(\beta\downarrow)} - V_{-\mathbf{k}',\mathbf{k}}^{(\beta'\downarrow)(\alpha'\uparrow),(\alpha\uparrow)(\beta\downarrow)} - V_{\mathbf{k}',-\mathbf{k}}^{(\alpha'\uparrow)(\beta'\downarrow),(\beta\downarrow)(\alpha\uparrow)} + V_{-\mathbf{k}',-\mathbf{k}}^{(\beta'\downarrow)(\alpha'\uparrow),(\beta\downarrow)(\alpha\uparrow)}\right)\\ &= 2\,V_{\mathbf{k}',\mathbf{k}}^{(\alpha'\uparrow)(\beta'\downarrow),(\alpha\uparrow)(\beta\downarrow)}\,,\end{aligned} \tag{6.63}$$

where we assumed that the tensor $V_{\mathbf{k}',\mathbf{k}}^{(\alpha'\uparrow)(\beta'\downarrow),(\alpha\uparrow)(\beta\downarrow)}$ is fully anti-symmetrized.
Equivalently to the calculation of the more general form above, we now approximate the Hamiltonian on a mean-field level, leading to

$$\begin{aligned}H^{\mathrm{MF}} = &\sum_{\mathbf{k},\alpha,\beta,\sigma} h_{\mathbf{k},\sigma}^{\alpha,\beta} c_{\mathbf{k},\alpha,\sigma}^\dagger c_{\mathbf{k},\beta,\sigma} + \frac{1}{N}\sum_{\mathbf{k},\mathbf{k}',\alpha,\beta,\alpha',\beta'} \tilde{V}_{\mathbf{k}',\mathbf{k}}^{\alpha'\beta',\alpha\beta}\left(\left\langle c_{\mathbf{k}',\alpha',\uparrow}^\dagger c_{-\mathbf{k}',\beta',\downarrow}^\dagger\right\rangle c_{-\mathbf{k},\beta,\downarrow} c_{\mathbf{k},\alpha,\uparrow}\right.\\ &\left. + c_{\mathbf{k}',\alpha',\uparrow}^\dagger c_{-\mathbf{k}',\beta',\downarrow}^\dagger \langle c_{-\mathbf{k},\beta,\downarrow} c_{\mathbf{k},\alpha,\uparrow}\rangle - \left\langle c_{\mathbf{k}',\alpha',\uparrow}^\dagger c_{-\mathbf{k}',\beta',\downarrow}^\dagger\right\rangle \langle c_{-\mathbf{k},\beta,\downarrow} c_{\mathbf{k},\alpha,\uparrow}\rangle\right)\\ = &\sum_{\mathbf{k}} \tilde{\boldsymbol{\psi}}_{\mathbf{k}}^\dagger \begin{pmatrix} h_{\mathbf{k},\uparrow} & \tilde{\Delta}_{\mathbf{k}} \\ \tilde{\Delta}_{\mathbf{k}}^\dagger & -h_{-\mathbf{k},\downarrow}^* \end{pmatrix} \tilde{\boldsymbol{\psi}}_{\mathbf{k}} + \tilde{K}\end{aligned} \tag{6.64}$$

with $\tilde{K} = -1/N\sum_{\mathbf{k},\mathbf{k}',\alpha,\beta,\alpha',\beta'} \tilde{V}_{\mathbf{k}',\mathbf{k}}^{\alpha'\beta',\alpha\beta}\left\langle c_{\mathbf{k}',\alpha',\uparrow}^\dagger c_{-\mathbf{k}',\beta',\downarrow}^\dagger\right\rangle \langle c_{-\mathbf{k},\beta,\downarrow} c_{\mathbf{k},\alpha,\uparrow}\rangle + \sum_{\mathbf{k}} \mathrm{Tr}\, h_{\mathbf{k},\downarrow}$ and the Nambu vector $\tilde{\boldsymbol{\psi}}_{\mathbf{k}} = \left[c_{\mathbf{k},\uparrow}, c_{-\mathbf{k},\downarrow}^\dagger\right]^T$. In this case, the BdG Hamiltonian is defined as

$$\tilde{\mathcal{H}}_{\mathrm{BdG}}(\mathbf{k}) = \begin{pmatrix} h_{\mathbf{k},\uparrow} & \tilde{\Delta}_{\mathbf{k}} \\ \tilde{\Delta}_{\mathbf{k}}^\dagger & -h_{-\mathbf{k},\downarrow}^* \end{pmatrix} \tag{6.65}$$

and the gap equation is given by

$$\tilde{\Delta}_{\mathbf{k}}^{\alpha\beta} = \frac{1}{N}\sum_{\mathbf{k}',\alpha'\beta'} \tilde{V}_{\mathbf{k},\mathbf{k}'}^{\alpha\beta,\alpha'\beta'} \langle c_{-\mathbf{k}',\beta',\downarrow}\, c_{\mathbf{k}',\alpha',\uparrow}\rangle\,. \tag{6.66}$$

This gap equation can also be found by directly generalizing Eq. (6.10) to a multi-band structure with a momentum dependent interaction. This form of a superconducting gap was for example used in Refs. [144, 154, 170].

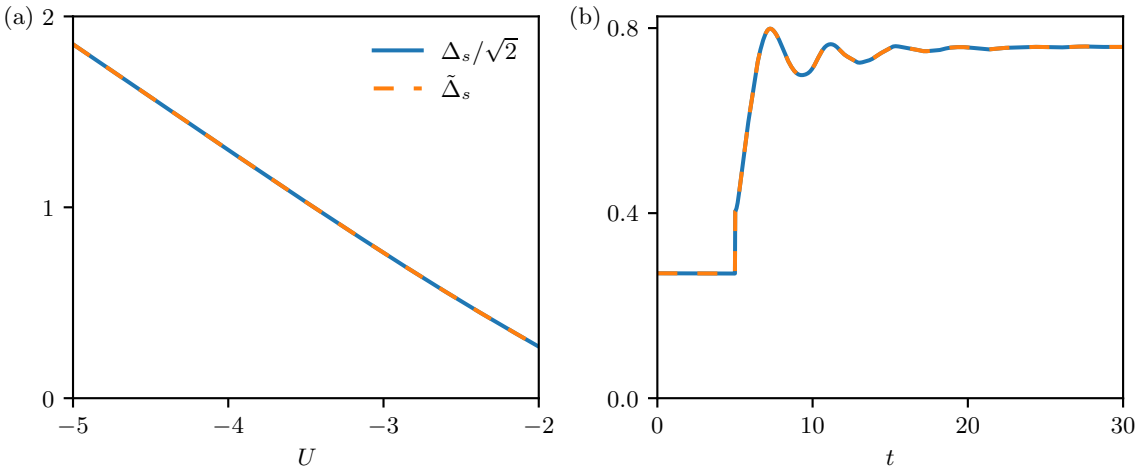

Figure 6.1: Comparison of the algorithms including and excluding same spin pairing for the square lattice model of Chapter 8 including only a s-wave instability ($U' = 0$). (a) Gap in the equilibrium position as a function of the local interaction U at $T = 0.05$, $\Gamma = 0.1$ and a system size of $N = 20 \times 20$. (b) Time evolution of the gap resulting from a quench from $U = -2$ to $U = -3$ at $t_0 = 5$ with $T = 0.05$, $\Gamma = 0.1$ and a system size of $N = 20 \times 20$. The results obtained with both algorithms perfectly agree up to the prefactor identified in Eq. (6.69).

The gap equation can still be solved efficiently using the trick that was introduced in Section 6.3.3, by exploiting $\langle c_{-\mathbf{k}',\beta',\downarrow} c_{\mathbf{k}',\alpha',\uparrow} \rangle = \frac{1}{i} \tilde{G}^{<}_{(1,\alpha'),(2,\beta')}(\mathbf{k}', \Delta t = 0)$. Moreover, a slightly adapted form factor decomposition can be employed with

$$\tilde{V}^{\alpha'\beta',\alpha\beta}_{\mathbf{k}',\mathbf{k}} = \sum_i \tilde{v}_i \left(\tilde{\not{f}}^{\alpha'\beta'}_{i,\mathbf{k}'} \right)^* \tilde{\not{f}}^{\alpha\beta}_{i,\mathbf{k}} , \tag{6.67}$$

which yields

$$\tilde{\Delta}^{\alpha\beta}_{\mathbf{k}} = \sum_i \tilde{\not{f}}^{\alpha\beta}_{i,\mathbf{k}} \tilde{\Delta}_i \quad \text{with} \quad \tilde{\Delta}_i = \frac{1}{N} \sum_{\mathbf{k}',\alpha'\beta'} \tilde{v}_i \left(\tilde{\not{f}}^{\alpha'\beta'}_{i,\mathbf{k}'} \right)^* \langle c_{-\mathbf{k}',\beta',\downarrow} c_{\mathbf{k}',\alpha',\uparrow} \rangle \ . \tag{6.68}$$

In this case, the normalization is set to $1 = \sum_{\alpha,\beta} \frac{1}{\mathcal{V}} \int dk \, |\tilde{\not{f}}^{\alpha\beta}_{i,\mathbf{k}}|^2$, which again corresponds to normalized eigenvectors.

For models, where the simplified approach from this section can be used, both methods need to be equivalent. However, the results can be connected by prefactors due to the different normalizations of the form factors.
The form factors are connected via $\tilde{\not{f}}^{\alpha\beta}_{i,\mathbf{k}} = \sqrt{2} \not{f}^{(\alpha,\uparrow),(\beta,\downarrow)}_{i,\mathbf{k}}$, which then leads to $\tilde{v}_i = v_i$. Nevertheless, a prefactor occurs for the gaps of the individual pairing channels. Here, we find the connection

$$\tilde{\Delta}_i = \Delta_i / \sqrt{2} \, . \tag{6.69}$$

In the following, we want to confirm the equivalence of both approaches as well as the relation Eq. (6.69) by explicitly calculating the gap using both methods. To this end, results for the square lattice model from Section 8.2 are shown in the presence of a local attractive Hubbard U leading to a single form factor, which represents s-wave order (see Section 8.2 for details). The definition of this model is postponed to Section 8.2 since we are not interested in the details of the corresponding model, but only in the comparison of both methods. The absolute value of the gap is shown for different local interaction U in Fig. 6.1(a). We find that the methods are indeed equivalent for the chosen model. Moreover, the results are connected by Eq. (6.69) as expected based on the shown calculation.

6.5.2 Free Energy

In this section, we discuss how to compute the free energy landscape for a BdG Hamiltonian. In this thesis, the free energy is only calculated for BdG Hamiltonians of form (6.65) and therefore, we refrain from discussing the free energy for BdG Hamiltonians of the more general form (6.30). Importantly, for the determination of the free energy, we always assume that there is no coupling to a fermionic bath and we therefore set $\Gamma = 0$.
The free energy is defined as

$$F = E - T \cdot S \tag{6.70}$$

with energy E, temperature T and entropy S. From Eq. (6.64), the energy can be calculated via

$$E = \sum_{\mathbf{k}} \sum_{i} E_{\mathbf{k},i}\, n_{\mathrm{F}}(E_{\mathbf{k},i}) + \tilde{K}\,, \tag{6.71}$$

where $E_{\mathbf{k},i}$ denotes the quasiparticle energies of the BdG Hamiltonian (6.65). Moreover, $\tilde{K}$ is the additional term from the Hamiltonian (6.64) as defined above. However, since we are only interested in comparing relative energies, we only need to consider the part of $\tilde{K}$ that depends on the superconducting gap. Therefore, the second term from $\tilde{K}$ is neglected and for the rest of this thesis, we use

$$\begin{aligned}\tilde{K} &= -\frac{1}{N} \sum_{\mathbf{k},\mathbf{k}',\alpha,\beta,\alpha',\beta'} \tilde{V}^{\alpha'\beta',\alpha\beta}_{\mathbf{k}',\mathbf{k}} \left\langle c^{\dagger}_{\mathbf{k}',\alpha'} c^{\dagger}_{-\mathbf{k}',\beta'} \right\rangle \langle c_{-\mathbf{k},\beta} c_{\mathbf{k},\alpha} \rangle \\ &= -N \sum_{i} \frac{|\tilde{\Delta}_i|^2}{\tilde{v}_i}\,,\end{aligned} \tag{6.72}$$

where we employed the form factor decomposition to simplify $\tilde{K}$ even further. The entropy is given by [171, 172]

$$S = -\sum_{\mathbf{k}} \sum_{i} \left\{ n_{\mathrm{F}}(E_{\mathbf{k},i}) \ln\left[n_{\mathrm{F}}(E_{\mathbf{k},i})\right] + \left[1 - n_{\mathrm{F}}(E_{\mathbf{k},i})\right] \ln\left[1 - n_{\mathrm{F}}(E_{\mathbf{k},i})\right] \right\}\,. \tag{6.73}$$

This leads to a free energy of

$$\begin{aligned}F =& \sum_{\mathbf{k}} \sum_{i} E_{\mathbf{k},i}\, n_{\mathrm{F}}(E_{\mathbf{k},i}) + \tilde{K} \\ &+ T \cdot \sum_{\mathbf{k}} \sum_{i} \left\{ n_{\mathrm{F}}(E_{\mathbf{k},i}) \ln\left[n_{\mathrm{F}}(E_{\mathbf{k},i})\right] + \left[1 - n_{\mathrm{F}}(E_{\mathbf{k},i})\right] \ln\left[1 - n_{\mathrm{F}}(E_{\mathbf{k},i})\right] \right\}\,,\end{aligned} \tag{6.74}$$

which can be calculated in dependence on the order parameters $\tilde{\Delta}_i$ since both the quasi-particle energies as well as $\tilde{K}$ still depend on the $\tilde{\Delta}_i$.
Using this equation, it is even possible to calculate the free energy for gap parameters that do not solve the gap equation allowing for the computation of a full free energy landscape. Here, the stationary points (minima, maxima and saddle points) correspond to the solutions of the gap equation. Furthermore, the state with the minimal free energy belongs to the system's ground state. However, this can only be exploited if the coupling Γ to the external fermionic bath is taken to zero, since, as already mentioned above, we can only compute the free energy in that case.

6.5.3 Time Evolution

In the following, we investigate how the differential equations for the time evolution simplify for the case of a BdG Hamiltonian of form (6.30), which is treated within this section. These equations of motion can also be obtained directly by repeating the calculation from above for the BdG Hamiltonian (6.30) as it was done in Ref. [144]. However, we here derive the equations of motions directly from the more general case treated above. This allows us to see that both approaches are connected and equivalent for a Hamiltonian without same spin pairing and with uncoupled spin

sectors in the non-interacting part. This leads to the same results that were obtained in Ref. [144], but in contrast to Ref. [144] we refrain form setting $n_{\mathbf{k},\uparrow} = n_{\mathbf{k},\downarrow}$.

Using the properties of the Hamiltonian, the matrices from the general case above can be written in the block form

$$h_{\mathbf{k}} = \begin{pmatrix} h_{\mathbf{k},\uparrow} & 0 \\ 0 & h_{\mathbf{k},\downarrow} \end{pmatrix}, n_{\mathbf{k}} = \begin{pmatrix} n_{\mathbf{k},\uparrow} & 0 \\ 0 & n_{\mathbf{k},\downarrow} \end{pmatrix}, f_{\mathbf{k}} = \begin{pmatrix} 0 & f_{\mathbf{k},1} \\ f_{\mathbf{k},2} & 0 \end{pmatrix}, \Delta_{\mathbf{k}} = \begin{pmatrix} 0 & \Delta_{\mathbf{k},1} \\ \Delta_{\mathbf{k},2} & 0 \end{pmatrix} \tag{6.75}$$

with

$$f_{\mathbf{k},1}^{\alpha\beta} = \langle c_{-\mathbf{k},\beta,\downarrow} c_{\mathbf{k},\alpha,\uparrow} \rangle = \tilde{f}_{\mathbf{k}}^{\alpha\beta}, \qquad f_{\mathbf{k},2}^{\alpha\beta} = \langle c_{-\mathbf{k},\beta,\uparrow} c_{\mathbf{k},\alpha,\downarrow} \rangle = -\tilde{f}_{-\mathbf{k}}^{\beta\alpha}, \tag{6.76}$$

$$\Delta_{\mathbf{k},1}^{\alpha\beta} = \frac{1}{N} \sum_{\mathbf{k}',\alpha'\beta'\sigma\sigma'} V_{\mathbf{k},\mathbf{k}'}^{(\alpha\uparrow)(\beta\downarrow),(\alpha'\sigma)(\beta'\sigma')} f_{\mathbf{k}'}^{(\alpha'\sigma)(\beta'\sigma')} = \frac{1}{N} \sum_{\mathbf{k}',\alpha'\beta'} \tilde{V}_{\mathbf{k},\mathbf{k}'}^{\alpha\beta,\alpha'\beta'} \tilde{f}_{\mathbf{k}'}^{\alpha'\beta'} = \tilde{\Delta}_{\mathbf{k}}^{\alpha\beta}, \tag{6.77}$$

$$\Delta_{\mathbf{k},2}^{\alpha\beta} = \frac{1}{N} \sum_{\mathbf{k}',\alpha'\beta'\sigma\sigma'} V_{\mathbf{k},\mathbf{k}'}^{(\alpha\downarrow)(\beta\uparrow),(\alpha'\sigma)(\beta'\sigma')} f_{\mathbf{k}'}^{(\alpha'\sigma)(\beta'\sigma')} = -\frac{1}{N} \sum_{\mathbf{k}',\alpha'\beta'} \tilde{V}_{-\mathbf{k},\mathbf{k}'}^{\beta\alpha,\alpha'\beta'} \tilde{f}_{\mathbf{k}'}^{\alpha'\beta'} = -\tilde{\Delta}_{-\mathbf{k}}^{\beta\alpha}. \tag{6.78}$$

Here, we identified the $\tilde{f}_{\mathbf{k}}$ with the off-diagonal blocks from the new equal time expectation value

$$\tilde{N}_{\mathbf{k}}(t) = \begin{pmatrix} n_{\mathbf{k},\uparrow}(t) & \tilde{f}_{\mathbf{k}}(t) \\ \tilde{f}_{\mathbf{k}}^{\dagger}(t) & 1 - n_{-\mathbf{k},\downarrow}^{*}(t) \end{pmatrix} \text{ with } \tilde{N}_{\mathbf{k}}^{mn}(t) = \left\langle \tilde{\psi}_{\mathbf{k}n}^{\dagger}(t) \tilde{\psi}_{\mathbf{k}m}(t) \right\rangle = -\frac{i}{2} \tilde{G}_{\mathbf{k},mn}^{K}(t,t) + \frac{1}{2}. \tag{6.79}$$

Furthermore, we define the collision integral for the new BdG Hamiltonian $\tilde{\mathcal{H}}_{\mathrm{BdG}}$ as

$$\tilde{I}_{\mathbf{k}}^{K}(t) = \frac{1}{2\Gamma} \int_0^{\infty} d\tau \left[\tilde{G}_{\mathbf{k}}^{R}(t, t-\tau) + \tilde{G}_{\mathbf{k}}^{R}(t, t-\tau)^{\dagger} \right] \Sigma^{K}(\tau) = \begin{pmatrix} \tilde{I}_{\mathbf{k}}^{G,1}(t) & \tilde{I}_{\mathbf{k}}^{D}(t) \\ \left(\tilde{I}_{\mathbf{k}}^{D}(t)\right)^{\dagger} & \tilde{I}_{\mathbf{k}}^{G,2}(t) \end{pmatrix}. \tag{6.80}$$

Here, the blocks are connected to those of the general form via

$$\tilde{I}_{\mathbf{k}}^{G,1} = \left[I_{\mathbf{k}}^{G}\right]_{\uparrow\uparrow}, \quad \tilde{I}_{\mathbf{k}}^{D} = \left[I_{\mathbf{k}}^{D}\right]_{\uparrow\downarrow}, \quad \tilde{I}_{\mathbf{k}}^{G,2} = -\left[I_{-\mathbf{k}}^{G}\right]_{\downarrow\downarrow}^{*}. \tag{6.81}$$

Inserting the matrices into Eqs. (6.53)-(6.58) leads to the following simplified equations (see Appendix C for needed the matrix products):

$$i\partial_t n_{\mathbf{k},\uparrow}(t) = [h_{\mathbf{k},\uparrow}(t), n_{\mathbf{k},\uparrow}(t)] + \tilde{\Delta}_{\mathbf{k}}(t) \tilde{f}_{\mathbf{k}}^{\dagger}(t) - \tilde{f}_{\mathbf{k}}(t) \tilde{\Delta}_{\mathbf{k}}^{\dagger}(t) - i\Gamma \left[2n_{\mathbf{k},\uparrow}(t) - 1 - \tilde{I}_{\mathbf{k}}^{G,1}(t) \right] \tag{6.82}$$

$$-i\partial_t n_{-\mathbf{k},\downarrow}^{*}(t) = \left[h_{-\mathbf{k},\downarrow}^{*}(t), n_{-\mathbf{k},\downarrow}^{*}(t)\right] + \tilde{\Delta}_{\mathbf{k}}^{\dagger}(t) \tilde{f}_{\mathbf{k}}(t) - \tilde{f}_{\mathbf{k}}^{\dagger}(t) \tilde{\Delta}_{\mathbf{k}}(t) + i\Gamma \left[2n_{-\mathbf{k},\downarrow}^{*}(t) - 1 + \tilde{I}_{\mathbf{k}}^{G,2}(t) \right] \tag{6.83}$$

$$\begin{aligned} i\partial_t \tilde{f}_{\mathbf{k}}(t) =& h_{\mathbf{k},\uparrow}(t) \tilde{f}_{\mathbf{k}}(t) + \tilde{f}_{\mathbf{k}}(t) h_{-\mathbf{k},\downarrow}^{*}(t) - \tilde{\Delta}_{\mathbf{k}}(t) \left(n_{-\mathbf{k},\downarrow}^{*}(t) - 1 \right) - n_{\mathbf{k},\uparrow}(t) \tilde{\Delta}_{\mathbf{k}}(t) \\ & - i\Gamma \left(2\tilde{f}_{\mathbf{k}}(t) - \tilde{I}_{\mathbf{k}}^{D}(t) \right) \end{aligned} \tag{6.84}$$

$$\tilde{\Delta}_{\mathbf{k}}^{\alpha\beta}(t) = \frac{1}{N} \sum_{\mathbf{k}'} \tilde{V}_{\mathbf{k},\mathbf{k}'}^{\alpha\beta,\alpha'\beta'} \tilde{f}_{\mathbf{k}'}^{\alpha'\beta'}(t) \tag{6.85}$$

$$\tilde{I}_{\mathbf{k}}^{K}(t) = \frac{1}{2\Gamma} \int_0^{\infty} d\tau \left[\tilde{G}_{\mathbf{k}}^{R}(t, t-\tau) + \tilde{G}_{\mathbf{k}}^{R}(t, t-\tau)^{\dagger} \right] \Sigma^{K}(\tau) \tag{6.86}$$

$$= \begin{bmatrix} \tilde{I}_{\mathbf{k}}^{G,1}(t) & \tilde{I}_{\mathbf{k}}^{D}(t) \\ \left(\tilde{I}_{\mathbf{k}}^{D}(t)\right)^{\dagger} & \tilde{I}_{\mathbf{k}}^{G,2}(t) \end{bmatrix} \tag{6.87}$$

$$i\partial_t \tilde{G}_{\mathbf{k}}^{R}(t,t') = \left(\tilde{\mathcal{H}}_{\mathbf{k}}(t) - i\Gamma \right) \tilde{G}_{\mathbf{k}}^{R}(t,t'). \tag{6.88}$$

As already mentioned above, the same results are found when following Ref. [144] using a BdG Hamiltonian of form (6.65), which was also considered there, without setting $n_{\mathbf{k},\uparrow} = n_{\mathbf{k},\downarrow}$.

Interestingly, in the case of a single-band model with $n_{\mathbf{k},\uparrow} = n_{-\mathbf{k},\downarrow}$ and $\tilde{I}^{G,1}_{\mathbf{k}} = -\left(\tilde{I}^{G,2}_{\mathbf{k}}\right)^*$ (ergo $\left[I^G_{\mathbf{k}}\right]_{\uparrow\uparrow} = \left[I^G_{-\mathbf{k}}\right]_{\downarrow\downarrow}$), we find $\partial_t n_{\mathbf{k},\uparrow} = \partial_t n_{-\mathbf{k},\downarrow}$ which can be exploited to simplify the approach even further.

For the time dependent calculations, we can once again compare the results of both approaches for the square lattice model from Section 8.2 in the presence of an s-wave instability. To this end, we perform a quench and show the results in Fig. 6.1(b). We note that the results again perfectly agree for both methods indicating that they are indeed equivalent for suitable models that can be described with the simplified BdG Hamiltonian (6.65).
In the remainder of this thesis, the additional tilde of the symbols in this section are not shown for convenience. In this thesis, all equations and results are usually shown within the notation of the simplified approach presented here, although the results can be obtained with both methods as shown above. Only in Section 8.5, where same spin pairing is considered, the notation of the general version from above (Sections 6.3 and 6.4) is used since the simplified approach cannot be applied.

Part III

Questions

Chapter 7

Topological Zero Energy States Protected by Supersymmetry

This chapter is based on the following publication, where the results were already published (except for the added Figs. 7.5, 7.7 and the lower two panels in Fig. 7.9(b)):
[111] C. S. Weber, M. Pletyukhov, Z. Hou, D. M. Kennes, J. Klinovaja, D. Loss, and H. Schoeller, "Second-order topology and supersymmetry in two-dimensional topological insulators", Phys. Rev. B **107**, 235402 (2023)
For this project, I implemented the code for the Corbino disk in continuum numerics using matrix elements calculated by Dr. Mikhail Pletyukhov. Additionally, I implemented a code for the tight binding model. I performed the continuum numerical simulations and partly the tight-binding numerical simulations. Furthermore, I contributed to the creation of the figures in the manuscript. Note that I only provided numerical results for this project. This means that all analytical insights (including the ones shown below) were not done by me but by Prof. Herbert Schoeller and Dr. Mikhail Pletyukhov. Moreover, the applications and the transfer to the case of a single hole discussed below are based on ideas from Prof. Herbert Schoeller.

In recent years, the theory of topological quantum condensed matter systems has evolved to one of the central topics in the research of the condensed matter community. As already mentioned in the introduction of this thesis (Chapter 1), topological properties are often related to the symmetries of the system. Most importantly, topological systems can host gapless modes or zero energy bound states which are symmetry-protected [9, 15, 20, 41].
Nevertheless, there are symmetries that might be responsible for the protection of topological zero energy bound states, which have not been in the focus of research so far. In this chapter, supersymmetry (SUSY) is introduced as an additional symmetry allowing for the protection of the topological bound states.

While SUSY plays only a minor role in the quantum condensed matter community, it is the basis of a famous theory in high energy physics. Here, the minimal supersymmetric extension of the standard model (as one of various supersymmetric extension) was established, where bosons and fermions are expected to appear as pairs in our universe, with each boson having a fermionic superpartner and vice versa (see e.g. Refs. [173, 174]; for a detailed review of the minimal supersymmetric extension of the standard model the reader is refered e.g. to Ref. [175]). This extension is able to explain physical phenomena beyond the well-established standard model, but unfortunately no experimental prove for the additional SUSY partners has been found [174]. More explicitly, a supersymmetric model contains a symmetry, called supersymmetry, represented by the operator U which maps fermions and bosons into each other via

$$U\,|\text{Fermion}\rangle = |\text{Boson}\rangle \tag{7.1}$$

and vice versa [173].
A similar concept of supersymmetric models can be used in nonrelativstic quantum mechanics [176–180], where the eigenstates of the system can be separated into fermionic and bosonic states,

which are connected by SUSY [180]. The states can be ordered into these fermionic and bosonic groups by classifying the states into subgroups with a positive/negative eigenvalue of the so-called Witten operator [180]. In a supersymmetric system this leads to a spectrum, where all eigenstates except for the vacuum are degenerate [179].
There is a variety of quantum condensed matter systems, where the presence of SUSY has been discussed [181–183], including some systems with topological properties [184–186].
Here, only a brief introduction to SUSY in quantum mechanics was provided and therefore, the reader is referred to Refs. [176–180] for a more detailed introduction.

Within this chapter, it will be shown that a significant subgroup of two-dimensional second order topological insulators (SOTIs) has a supersymmetric spectrum. As explained in the introduction, two-dimensional SOTIs are systems with zero dimensional bound states that we call corner states in the following, even in the case of a circular surface where no corners are present. First, the subgroup of SOTIs with the corresponding symmetries is introduced. Then we concentrate on the Bernevig-Hughes-Zhang (BHZ) Model, which falls into the subgroup of SOTIs having the necessary properties. This model is analyzed on a Corbino disk utilizing numerical methods, which are supported by analytical arguments taken from Ref. [111]. Here, we differentiate the cases of zero and finite Zeeman field since the Zeeman term is responsible for the second order mechanism yielding a gap in the edge state spectrum. Furthermore, based on the results for the Corbino disk, we discuss consequences for an infinite system with a hole. Finally, we briefly comment on possible applications.

7.1 Considered Models

We start by introducing the subclass of 2D-SOTI that we consider in this chapter. Although a specific model is employed for most of the studies, all 2D-SOTI in this subclass do have the needed supersymmetric structure.
For the definition of a whole subgroup of second-order topological insulators, general matrices Γ_i with $i = 0, \dots, d$ that fulfill the relations

$$\Gamma_i^2\,, \quad \Gamma_i\Gamma_j = -\Gamma_j\Gamma_i\,, \tag{7.2}$$

are often considered [187, 188]. With these matrices one can then define a Hamiltonian with a topological phase in a certain parameter regime [187, 188]. Moreover, an additional term is needed for the realization of a second-order topological insulator. To this end, we use an additional general matrix γ with the properties

$$\gamma^2 = 1\,, \quad \Gamma_0\gamma = -\gamma\Gamma_0\,, \quad \Gamma_{1,2}\,\gamma = \gamma\,\Gamma_{1,2}\,. \tag{7.3}$$

We consider a system including a kinetic energy term, a band inversion, a spin orbit coupling and a Zeeman term. We first introduce the chosen subgroup for the case where there is no magnetic flux in the system. Here, the general Hamiltonian is given by

$$H_0 = \Gamma_0 \left(\frac{\mathbf{p}^2}{2m^*} - \delta \right) + \lambda\, \mathbf{p}\cdot\mathbf{\Gamma} + E_Z\, \mathbf{b}\cdot\mathbf{\Gamma}\,\gamma \tag{7.4}$$

with $\mathbf{\Gamma} = (\Gamma_1, \Gamma_2)^T$, the effective mass m^*, the Zeeman energy E_Z, the spin-orbit coupling strength λ, the generalized inversion parameter δ, the two-dimensional momentum $\mathbf{p}$ and the arbitrary two-dimensional real and normalized vector $\mathbf{b}$. The index 0 indicates that there is zero magnetic flux. Units with $\hbar = 1$ are chosen here and in the remainder of this thesis as already mentioned above.
In the next step, we include a magnetic Aharanov-Bohm flux through the center of the system. To this end, we consider the presence of a hole at the origin. We write the magnetic flux $\Phi = f\Phi_0$ in units of the magnetic flux quantum $\Phi_0 = \dfrac{2\pi c}{e}$, resulting in an adjusted Hamiltonian of

$$H_f = e^{-if\varphi}\, H_0\, e^{if\varphi} = \Gamma_0 \left(\frac{1}{2m^*}\mathbf{p}_K^2 - \delta \right) + \lambda\, \mathbf{p}_K\cdot\mathbf{\Gamma} + E_Z\Gamma_2\gamma\,. \tag{7.5}$$

Here, $\mathbf{p}_K = \mathbf{p} + \frac{e}{c}\mathbf{A}$ denotes the canonical momentum, which includes the vector potential $\mathbf{A}$ (e denotes the electric charge and c the velocity of light). In this chapter, we restrict $f \in [0, 1)$ to due to periodicity in f.
Due to the spatial symmetries of model (7.4), we can fix the direction of $\mathbf{b}$, as well as the sign of λ without loss of generality. A rotation of $\mathbf{b}$ would only result in a rotation of the system, while changing the sign of λ would lead to an inversion. In this chapter, we stick to the choice of $\mathbf{b} = \mathbf{e}_y$ and $\lambda > 0$, leading to

$$H_f = \Gamma_0 \left(\frac{1}{2m^*} \mathbf{p}_K^2 - \delta \right) + \lambda \, \mathbf{p}_K \cdot \mathbf{\Gamma} + E_Z \Gamma_2 \gamma \,, \tag{7.6}$$

7.1.1 Symmetries

In the following, the symmetries of the subclass of 2D-SOTIs, defined by the Hamiltonian (7.6), are investigated. It is straightforward to find the chiral symmetry

$$S H_f S = -H_f \,, \quad S = S^\dagger = \Gamma_1 \Gamma_2 \gamma \,. \tag{7.7}$$

Additionally, the model obeys an inversion symmetry

$$\Pi H_f \Pi = H_f \,, \quad \Pi = \Pi^\dagger = P_{\mathbf{x}} \, \Gamma_0 \,, \tag{7.8}$$

with $P_{\mathbf{x}}$ being the spatial inversion transforming $\mathbf{x} \to -\mathbf{x}$. Finally, we find the mirror symmetry

$$U_f H_f U_f = H_f \,, \quad U_f = U_f^\dagger = e^{-if\varphi} \, P_\varphi \, \Gamma_0 \Gamma_2 \gamma \, e^{if\varphi} = e^{-i2f\varphi} \, P_\varphi \, \Gamma_0 \Gamma_2 \gamma \,. \tag{7.9}$$

for $f = 0$ and $f = 1/2$. Here, P_φ transforms the polar angle via $\varphi \to -\varphi$. For a finite system size, the shape of the system needs to respect the same symmetries.

7.1.2 Supersymmetry

We now study possible supersymmetric properties of the Hamiltonians under investigation [111]. In order to obtain a supersymmetric spectrum, all eigenstates need to appear in degenerate multiplets. Therefore, we consider the cases of $f = 0$ and $f = 1/2$, where we have found the additional U_f symmetry. We then regard an eigenstate $|\psi\rangle$ of the system. Since U_f is a present symmetry, the state $|\tilde{\psi}\rangle = U_f \, |\psi\rangle$ needs to be an eigenstate with the same energy. Nevertheless, there is still the possibility of the states $|\psi\rangle$ and $|\tilde{\psi}\rangle$ being linear dependent.
However, for a Aharonov-Bohm flux of half a flux quantum, $U_{1/2}$ anti-commutes with the inversion operator leading to

$$\langle\psi|\tilde{\psi}\rangle = \langle\psi|U_{1/2}|\psi\rangle = \langle\psi|\Pi \, U_{1/2} \, \Pi|\psi\rangle = -\langle\psi| \, U_{1/2} \, \Pi \, \Pi|\psi\rangle = -\langle\psi| \, U_{1/2}|\psi\rangle = -\langle\psi|\tilde{\psi}\rangle \,, \tag{7.10}$$

where we chose the eigenstate $|\psi\rangle$ as an eigenstate of the inversion, and therefore $\Pi \, |\psi\rangle = \pm \, |\psi\rangle$. Thus, the overlap of $|\psi\rangle$ and $|\tilde{\psi}\rangle$ vanishes, showing that these states are linearly independent, and consequently degenerate eigenstates. Since this conclusion follows for every eigenstate, the whole spectrum is degenerate, showing that the system is indeed supersymmetric at $f = 1/2$. Therefore, from now on, the operator $U_{1/2}$ will be called SUSY operator.
The supersymmetric properties of the considered topological insulators are the central ingredient for the findings within this chapter. At the SUSY point $f = 1/2$, the spectrum has to be at least twice degenerate. Therefore, pairs of zero energy states cannot split. Furthermore, due to the chiral symmetry introduced above, the energy of a single pair of zero energy states cannot be changed and has to remain at exactly zero energy. This indicates a topological protection of zero energy states due to the combination of SUSY and the chiral symmetry. In the case of multiple pairs at zero energy, the pairs can have an exponentially small energy due to overlaps between the different states. Nevertheless, for any odd number of pairs, there is in general at least one pair at exactly zero due to the alliance of SUSY and chiral symmetry.
The degeracy of SUSY partners is comparable with the degeneracy of time reversal partners in Kramers theorem, which can also lead to a protection of topological zero energy states by time reversal symmetry when including a chiral symmetery (explained in e.g. Ref. [49]).

7.1.3 Bernevig-Hughes-Zhang Model

As already mentioned above, we restrict ourselves to a specific model for the remainder of this chapter although the properties to be proven can be found in any model of the given subclass from Eq. (7.4). Therefore, we choose

$$\Gamma_0 = \eta_z \otimes \mathbb{1}_\sigma \,, \quad \mathbf{\Gamma} = \eta_x \otimes \boldsymbol{\sigma} \,, \quad \gamma = \eta_x \otimes \mathbb{1}_\sigma \,, \tag{7.11}$$

with η_i and σ_i both being Pauli matrices representing the conduction/valence band and the spin $\mathbf{S} = \frac{1}{2}\boldsymbol{\sigma}$, respectively. In the following, we use a short hand notation and write

$$\eta_i \otimes \mathbb{1}_\sigma = \eta_i \,, \quad \mathbb{1}_\eta \otimes \sigma_i = \sigma_i \,, \quad \eta_i \otimes \sigma_j = \eta_i \sigma_j \tag{7.12}$$

for conciseness. This leads to a two-dimensional Bernevig-Hughes-Zhang (BHZ) Hamiltonian including an in-plane Zeeman-term

$$H_f = e^{-if\varphi}\, H_0\, e^{if\varphi} = \eta_z \left(\frac{1}{2m^*} \mathbf{p}_K^2 - \delta \right) + \lambda\, \eta_x \mathbf{p}_K \cdot \boldsymbol{\sigma} + E_Z \sigma_y \,. \tag{7.13}$$

The BHZ-model has first been introduced by Bernevig, Hughes and Zhang in 2006 for the description of the quantum spin hall effect in HgTe quantum wells [189], but it has also been applied to other materials, including inverted InAs/GaSb/AlSb Type-II semiconductor quantum wells [190]. However, the matrices were here chosen slightly differently in comparison to the original version. For the obtained model (7.13), we note that the arising spin-orbit coupling term in Eq. (7.13) is a well-known Rashba spin-orbit coupling (see e.g. [191, 192] for detailed reviews) which is connected to its standard form by a straightforward spin rotation.

Symmetries

As the BHZ model is one element of the subgroup of 2D-SOTI, for which the symmetries in Subsection 7.1.1 were found, the BHZ-Hamiltonian has to obey these symmetries. Inserting the definitions from Eq. (7.11) leads to

$$S = \eta_x \sigma_x \sigma_y \,, \quad \Pi = P_{\mathbf{x}} \eta_z \,, \quad U_f = e^{-i2f\varphi} P_\varphi \eta_z \sigma_y \tag{7.14}$$

for the chiral, inversion and mirror (only for $f = 0, 1/2$) symmetries. Again, at half integer flux $f = 1/2$, the mirror symmetry $U_{1/2}$ is responsible for a supersymmetric spectrum.
Furthermore, for the BHZ model, we can reverse the Aharanov-Bohm flux by applying the time reversal symmetry transformation

$$H_{-f} = \eta_z \sigma_x H_f^* \eta_z \sigma_x \tag{7.15}$$

leading to a symmetric spectrum around $f = 0$ or in general $f = n$ with $n \in \mathbb{Z}$ when disregarding the chosen restriction of $f \in [0, 1)$. Automatically, the spectrum does also have to be symmetric around $f = n + 1/2$ (or just $f = 1/2$ within the chosen restriction).

Bulk Spectrum

The spectrum of the given model can be calculated analytically as shown in Ref. [111], which allows for a definition of possible topological phases. Since the surfaces do not matter for the bulk spectrum, the flux through the center cannot have any influence as well. Therefore, we set $f = 0$ in the following. To obtain the bulk spectrum, we use the momentum space basis and rewrite the Hamiltonian from Eq. (7.13) as $H_0 = \sum_{\mathbf{k}} |\mathbf{k}\rangle\, \mathcal{H}_{\mathbf{k}}\, \langle \mathbf{k}|$ with the matrix

$$\mathcal{H}_{\mathbf{k}} = \eta_z \left(\frac{1}{2m^*} \mathbf{k}^2 - \delta \right) + \lambda\, \eta_x \mathbf{k} \cdot \boldsymbol{\sigma} + E_Z \sigma_y \,. \tag{7.16}$$

The Hamiltonian's spectrum can then be found by squaring the matrix twice (see Ref. [111] for details), which results in a spectrum of

$$\epsilon_{\mathbf{k}}^{\alpha\beta} = \alpha \sqrt{ \left(\frac{k^2}{2m^*} - \delta \right)^2 + \lambda^2 k^2 + E_Z^2 + \beta 2 E_Z \sqrt{ \left(\frac{k^2}{2m^*} - \delta \right)^2 + \lambda^2 k^2 \cos^2\theta } } \,, \tag{7.17}$$

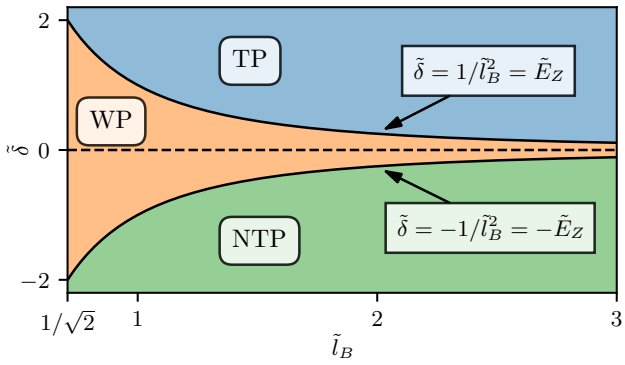

Figure 7.1: Phase diagram for our model for $\tilde{l}_B > 1/\sqrt{2}$ and $\tilde{\delta} < 2$. There are two gapped phases (topological (TP) and non-topological (NTP) phase), separated by a gapless Weyl phase (WP). The phase boundaries are given by the gap closing lines $\tilde{\delta} = \pm 1/\tilde{l}_B^2$. Since we only care about $\tilde{\delta} < 2$, the additional gap closing at $\tilde{\delta} = 1 + 1/(4\tilde{l}_B)$ for $\tilde{\delta} > 2$ is not shown. Figure taken from Ref. [111].

with $k = |\mathbf{k}|$, $k_y = k\cos\theta$ and $\alpha, \beta = \pm 1$. For convenience, the spectrum is converted into dimensionless units by rewriting all components in units of the spin orbit energy and wave vector

$$E_{\mathrm{so}} = \frac{k_{\mathrm{so}}^2}{2m^*} = \frac{1}{2} m^* \lambda^2 \,, \quad k_{\mathrm{so}} = \sqrt{2m^\star E_{\mathrm{so}}} = \lambda\, m^* \,. \tag{7.18}$$

This leads to a dimensionless spectrum of

$$\tilde{\epsilon}_{\tilde{\mathbf{k}}}^{\alpha\beta} = \frac{\epsilon_{\mathbf{k}}^{\alpha\beta}}{E_{\mathrm{so}}} = \alpha \sqrt{\left(\sqrt{(\tilde{k}^2 - \tilde{\delta})^2 + 4\tilde{k}^2\cos^2\theta} + \beta\tilde{E}_Z\right)^2 + 4\tilde{k}^2\sin^2\theta} \,, \tag{7.19}$$

where we have introduced dimensionless parameters $\tilde{A} = A/E_{\mathrm{so}}$ if A is an energy and $\tilde{\mathbf{k}} = \mathbf{k}/k_{\mathrm{so}}$ for any momentum $\mathbf{k}$. Further below, dimensionless units are also used for lengths. Here, the spin orbit wave length $a_{\mathrm{so}} = 1/k_{\mathrm{so}}$ is used, leading to renormalized lengths of $\tilde{r} = r/a_{\mathrm{so}}$.
From this dispersion relation, one can also extract the bulk gap as well as the gap closing points. We note that the minimal $|\tilde{\epsilon}|$ occurs for $\beta = -1$ and $\theta = 0$ (when assuming $E_Z \geq 0$). Due to the symmetry in α, we thus need to evaluate the minimum $\tilde{\Delta}_{\mathrm{bulk}} = \min_{\tilde{\mathbf{k}}} \tilde{\epsilon}_{\tilde{\mathbf{k}}}^{+1,-1}\big|_{\theta=0} = \left|\sqrt{(\tilde{k}^2 - \tilde{\delta})^2 + 4\tilde{k}^2} - \tilde{E}_Z\right|$ leading to a bulk gap of

$$\tilde{\Delta}_{\mathrm{bulk}} = \begin{cases} 2\sqrt{\tilde{\delta} - 1} - 1/\tilde{l}_B^2 & \text{for} \quad \tilde{\delta} > \max\{2, 1 + 1/(4\tilde{l}_B^4)\} \\ |\tilde{\delta}| - 1/\tilde{l}_B^2 & \text{for} \quad \tilde{\delta} < 2 \text{ and } |\tilde{\delta}| > 1/\tilde{l}_B^2 \\ 0 & \text{otherwise} \end{cases} , \tag{7.20}$$

where we defined $\tilde{l}_B = 1/\sqrt{\tilde{E}_Z}$. Furthermore, the gap closing lines are given by

$$\tilde{\delta} = \begin{cases} 1 + \frac{1}{4\tilde{l}_B^4} & \text{for } \tilde{\delta} > 2 \\ \pm\frac{1}{\tilde{l}_B^2} & \text{for } \tilde{\delta} < 2 \end{cases} , \tag{7.21}$$

which can be found by setting the first two cases in Eq. (7.20) to zero. Within this chapter, we only treat the system for $\tilde{\delta} < 2$ and $\tilde{l}_B > 1/\sqrt{2}$ (equivalent to $\tilde{E}_Z < 2$).
In Fig. 7.1, the phase diagram, obtained from these calculations, is schematically displayed. Since we investigate $\tilde{\delta} < 2$, only the phase boundaries at the gap closing lines $\tilde{\delta} = \pm 1/\tilde{l}_B^4$ are shown. There are two gapped phases for $|\tilde{\delta}| > E_Z$. Below, we find that one of the phases is topological (TP) leading to topological bound states within the gap, while the other phase turns out to be non-topological (NTP). In between those phases, there is a gapless phase that we call Weyl phase (WP) in the following. The gap closing points within the Weyl phase can be obtained by solving

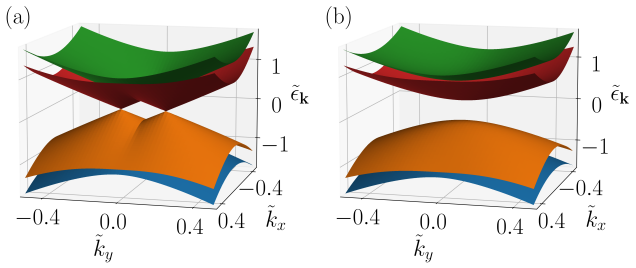

Figure 7.2: Dispersion for the different bands of our model in dimensionless parameters. $\tilde{\epsilon}_{\tilde{\mathbf{k}}}$ is shown in dependence of $\tilde{k}_{x,y}$. (a) The parameters ($\tilde{l}_B = 2$ and $\tilde{\delta} = 0$) are within the gapless Weyl phase, where the gap closes at the two Weyl points. (b) Here, the spectrum is shown for the gapped topological phase ($\tilde{l}_B = 2$ and $\tilde{\delta} = 1/2$). Figure taken from Ref. [111].

$\tilde{\epsilon}^{+1,-1}_{\tilde{\mathbf{k}}}\big|_{\theta=0} = 0$, which leads to the Weyl points $(0, \pm\tilde{k}_W)^T$ with $\tilde{k}_W = \sqrt{\tilde{\delta} - 2 + \sqrt{\tilde{E}_Z^2 + 4(1-\tilde{\delta})}}$. At the phase transition point, there is only a single Weyl point at $(0, 0)$, where the gap opens when entering the gapped phases.

In Fig. 7.2 the dispersion Eq. (7.19) of our model is presented for two exemplary parameters (a) in the Weyl phase and (b) in the topological phase.
In the Weyl phase, the gap closings at the two Weyl points are visible. In agreement with the analytical results presented above and taken from Ref. [111], the Weyl points appear on the y-axis and are symmetric around the origin. In the vicinity of the Weyl points, the spectrum forms cones with a linear dispersion.
As expected, the bulk spectrum of the topological phase is fully gapped. We further observe that the minimal gap appears at $\tilde{\mathbf{k}} = 0$, where the gap opens at the phase boundaries. The bulk spectrum in the non-topological phase is not distinguishable from the one of the topological phase and is therefore not shown here.

7.1.4 Tight-Binding Version

The Hamiltonian (7.13) can be analyzed for a disk in continuum by employing the continuum numerics as introduced in Section 3.1.2. It is possible to find an analytic expression for all matrix elements of the Hamiltonian matrix, which allows for a significant speedup. For the results from continuum numerics in this chapter, the matrix elements derived in Ref. [111] are used. We fix $\lambda = 1/m^* = 2$ and therefore $E_{\mathrm{so}} = k_{\mathrm{so}} = 1$, which is equivalent to applying dimensionless units.

Nevertheless, there are certain situations, where it is better to use a tight-binding approach and tolerate small discretization effects. For very large system sizes it is for example very hard to achieve convergence within the continuum. Additionally, it is cumbersome to find a good basis for a continuous system that has a more involved shape than a disk with an infinitely small hole (those shapes are beyond the scope of this thesis). Therefore, we set up a corresponding tight-binding Hamiltonian on a square lattice.
In order to find a tight-binding Hamiltonian, we replace

$$\mathbf{p}^2 \to \int_{1.\mathrm{B.Z}} d\mathbf{k} |\mathbf{k}\rangle\langle\mathbf{k}| \left\{ -\frac{2}{a^2} (\cos k_x + \cos k_y) + \frac{4}{a^2} \right\} , \tag{7.22}$$

$$\boldsymbol{\sigma} \cdot \mathbf{p} \to \int_{1.\mathrm{B.Z}} d\mathbf{k} |\mathbf{k}\rangle\langle\mathbf{k}| \frac{1}{a} (\sigma_x \sin k_x + \sigma_y \sin k_y) , \tag{7.23}$$

which is well justified in the low energy regime. Here, $|\mathbf{k}\rangle = |k_x\rangle \otimes |k_y\rangle$ denotes the state with momentum $\mathbf{k}$. The final tight-binding model in real space can then be found by simply inserting the Fourier transform $|k_{x,y}\rangle = \frac{1}{\sqrt{2\pi}} \sum_{n_{x,y}} e^{i k_{x,y} n_{x,y}} |n_{x,y}\rangle$ with $|\mathbf{n}\rangle = |n_x\rangle \otimes |n_y\rangle$ being the real space

state on site (n_x, n_y). This leads to the tight-binding Hamiltonian

$$H_0 = -t\eta_z \sum_{\mathbf{n}} \sum_{i=x,y} (|\mathbf{n}+\mathbf{e}_i\rangle\langle\mathbf{n}| + \text{h.c.}) + \frac{i\lambda}{2a}\eta_x \sum_{\mathbf{n}} \sum_{i=x,y} (\sigma_i|\mathbf{n}+\mathbf{e}_i\rangle\langle\mathbf{n}| - \text{h.c.}) + (4t-\delta)\eta_z + E_Z\sigma_y \tag{7.24}$$

with $t = 1/(2m^*a^2)$ and $|\mathbf{n}+\mathbf{e}_x\rangle = |n_x+1\rangle \otimes |n_y\rangle$. In order to avoid significant discretization effects, we choose the lattice spacing a in the same order as the spin-orbit length $a_{\text{so}} \sim 1/(\lambda m^*)$ since this is the smallest length scale for the case of strong spin-orbit interaction, which is in the focus of this chapter. This leads to a hopping of $t = 1/(2m^*a^2) \sim E_{\text{so}}$.
To arrive at dimensionless units, we thus set $t = a = 1$ and $\lambda = 1/m^* = 2$ for all tight binding calculations of this chapter.

If there is a magnetic flux in the center of the system, the Hamiltonian needs to be modified with $H_f = e^{-if\varphi}H_0e^{if\varphi}$ as discussed before. In the tight-binding description we can simply implement this by changing

$$|\mathbf{n}\rangle\langle\mathbf{m}| \to e^{-if\Delta\varphi_{\mathbf{n},\mathbf{m}}}|\mathbf{n}\rangle\langle\mathbf{m}| \tag{7.25}$$

with $\Delta\varphi_{\mathbf{n},\mathbf{m}} = (\varphi_{\mathbf{n}} - \varphi_{\mathbf{m}}) \bmod(2\pi)$. Here, $0 \leq \varphi_{\mathbf{n}} < 2\pi$ is the angle of site $|\mathbf{n}\rangle$ in polar coordinates. Assuming that there are no sites on the x-axis, $\bmod(2\pi)$ is chosen to be 2π (-2π), whenever considering a hopping at $x > 0$ with a sign change of $y < 0 \to y > 0$ $(y > 0 \to y < 0)$. For all other cases, the $\bmod(2\pi)$ contribution is given by zero. In other words, we ensure that $|\Delta\varphi_{\mathbf{n},\mathbf{m}}| < \pi$. This is necessary in order to accumulate the phase factor $e^{-i2\pi f}$ $(e^{i2\pi f})$ for every closed loop in the mathematical positive (negative) direction, which encloses the origin, where the magnetic flux is located.

7.2 Corbino Disk

In the following, we analyze the spectrum and the low energy states in the case of a Corbino disk, which has a circular shape of radius $R_>$ and a hole in its center around $(0,0)$ of radius $R_<$. The considered magnetic flux of $f\Phi_0$ is fully applied through the disk's hole. The investigated system is schematically depicted in Fig. 7.3, where the blue area shows the disk, while the light red part denotes the penetration of the flux. For the analysis of the Corbino disk, polar coordinates are applied.

7.2.1 Zero Zeeman Field

We begin with the study of the most simple case, where no Zeeman field is present in the system. In this case, there is no distinguished direction in the system and it is fully rotational invariant.

Numerical Results

First, the full spectrum is calculated numerically. Due to the large number of states needed for convergence of the complete edge state spectrum, we refrain from using the continuum numerics. Instead, we employ the tight-binding version despite the additional finite size effects arising from the limited number of sites and the slightly different Hamiltonian.
The resulting spectrum at zero Zeeman field for an exemplary parameter set from the topological phase is shown in Fig. 7.4 utilizing an outer radius of $\tilde{R}_> = R_>/a_{\text{so}} = 40$ and an inner radius $\tilde{R}_< = 0$. Here, the full spectrum within the bulk gap is shown in (a) and a zoom around $\tilde{\epsilon} = 0$ is displayed in (b).
In (a), we see that the bulk is gapped by the aforementioned gap calculated in Eq. (7.20). Within the gap, we find a *continuous* spectrum of edge states (although still being discrete due to the finite system size), which is not gapped due to the absence of a Zeeman term. This spectrum is symmetric around $f = 1/2$ due to the time reversal symmetry. All edge states cross at $f = 1/2$ since the system has to be degenerate at this point due to the aforementioned SUSY. We note that

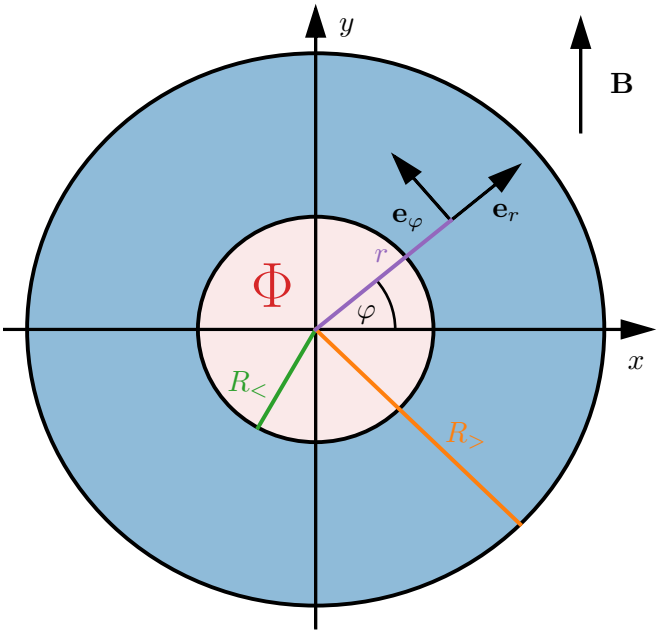

Figure 7.3: Corbino disk with a radius $R_>$ (orange) and a hole in its center of radius $R_<$ (green). For convenience, polar coordinates are employed in the remainder of this chapter. Through the center hole, a magnetic flux (shown in light red) is applied. Additionally, there is an in-plane magnetic field in the y-direction resulting in the presence of the Zeeman term in the Hamiltonian. Figure taken from Ref. [111].

most edge states seem to have a rather flat dispersion, while there are two additional states with a steep dispersion. They cross at zero and seem to disappear into the bulk for sufficiently large deviations from half integer flux. In contrast to all other states inside the gap, which appear at the outer boundary of the Corbino disk, those states are localized at the inner surface as shown below. We can investigate the spectrum of these states further by zooming into the energy spectrum around $\tilde{\epsilon} = 0$, which is shown in (b).
Here, it is visible that the edge states at the outer surface show a rather regular spacing, which is slightly larger than 0.04. Due to this spacing, we assign each of the pairs crossing at the SUSY point an integer number l, and denote their energy as $\tilde{\epsilon}_{l,\pm}$ with $\pm$ for an energy increasing/decreasing with the flux. Again, we can note the two center states crossing each other at $f = 1/2$ as well, due to the SUSY symmetry. The dispersion of these is extremely steep as mentioned above showing that those states are rather unstable against small flux deviations.

The spectrum for a configuration from the non-topological phase is shown in Fig. 7.5. Indeed, there are no edge states in the bulk gap in contrast to the spectrum of the topological phase presented in Fig. 7.4. This justifies the classification of the phases in Fig. 7.1, where we already indicated, which phase has a topological character.
We note that the size of the bulk gap in Fig. 7.5 agrees with the one found in Fig. 7.4. This was already expected from Eq. (7.20), where we observed that the gap in both gapped phases coincide if the same $\tilde{E}_Z$ (or equivalently $\tilde{l}_B$) and $|\tilde{\delta}|$ are employed.

Analytical Approximations

In the following, we gain a deeper understanding of the spectrum by using analytical calculations from Ref. [111]. The calculations are kept rather short and the reader is referred to Ref. [111] for a more detailed presentation (note that the notation is slightly different). For the analytical analysis of the Corbino disk, it is helpful to apply a few transformations to the Hamiltonian at half integer flux, which rotate the radial and angular components of spin onto fixed directions. We define the

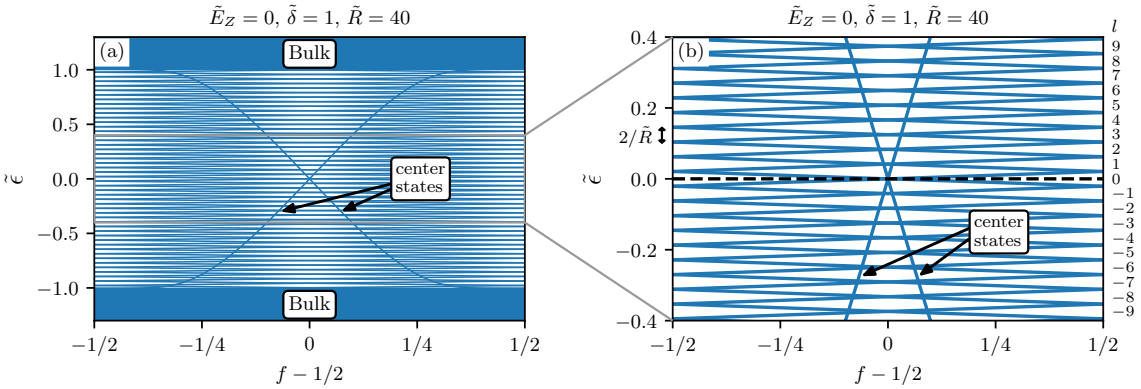

Figure 7.4: Spectrum $\tilde{\epsilon}$ in dimensionless units for $\tilde{E}_Z = 0$, $\tilde{\delta} = 1$, $\tilde{R}_> = 40$ and $\tilde{R}_< = 0$ using the tight-binding Hamiltonian introduced in Subsection 7.1.4 in dependence on the flux difference $f - 1/2$ to the SUSY point. (a) Overview of the spectrum. We find a bulk gap of roughly $|\tilde{\delta}|$ as expected from Eq. (7.20). Within the gap, there are numerous edge states as well as two center states. (b) Zoom into the low energy spectrum. We find no gap in the edge state spectrum. Instead, there are numerous edge states with a weak dispersion showing a roughly equidistant spectrum up to contrary slopes in the dispersion. Additionally, there is a pair of center states with a large dispersion. At the SUSY point $f = 1/2$, all states are degenerate. We label the pairs of edge states with integer numbers l. Figure taken from Ref. [111].

new Hamiltonian

$$\bar{H}_{1/2} = X^\dagger W^\dagger U^\dagger \sqrt{r}\, H_{1/2} \frac{1}{\sqrt{r}} U W X\,, \tag{7.26}$$

with $U = e^{-i\frac{1}{2}(1+\sigma_z)\varphi}$, $W = \frac{1}{2}(1+\eta_y) + \sigma_z \frac{1}{2}(1-\eta_y)$ and $X = \frac{1}{\sqrt{2}}(1 + i\eta_y)$. The additional $\sqrt{r}$-part is responsible for eliminating the Jacobian determinant in the norm, leading to a norm of $\int_{R_<}^{R_>} dr \int_0^{2\pi} d\varphi \sum_{\eta,\sigma=\pm1} |\bar{\psi}(r,\varphi,\eta,\sigma)|^2 = 1$ with σ, η being the spin and band index, respectively. This leads to a transformed Hamiltonian of

$$\begin{aligned}\bar{H}_{1/2}/E_{\mathrm{so}} =& \eta_x \left[\left(-\partial_{\tilde{r}}^2 - \tilde{\delta}\right)\sigma_z + 2i\partial_{\tilde{r}}\sigma_y\right] + \eta_x\left(-\frac{2}{\tilde{r}} i\partial_\varphi \sigma_x - \frac{1}{\tilde{r}^2}\partial_\varphi^2 \sigma_z + \frac{1}{\tilde{r}^2} i\partial_\varphi\right) \\ &+ \eta_y \frac{1}{\tilde{l}_B^2}\left(\sigma_x \sin\varphi + \sigma_y \cos\varphi\right)\,,\end{aligned} \tag{7.27}$$

in dimensionless units and in real space. Evidently, the symmetry operators have to be transformed in the same way, yielding

$$\bar{S} = -\eta_z\,, \quad \bar{\Pi} = -P_{\mathbf{x}}\eta_x\,, \quad \bar{U}_{1/2} = P_\varphi \eta_z \sigma_x\,. \tag{7.28}$$

In the following, possible topological localized bound states are investigated. To this end, we assume the two boundaries to be sufficiently separated with $\Delta\tilde{R} = \tilde{R}_> - \tilde{R}_< \gg 1$, allowing for an independent study of both. This specifically means that we neglect an exponential splitting of energies that can occur due to the hybridization of edge states placed at different boundaries.
Due to the rotational invariance, the z-component of the angular momentum is a good quantum number and we can decompose the Hamiltonian into blocks $\bar{H}_{1/2,\ell}$ each belonging to a quantum number ℓ of the angular momentum. In this way, we have already solved the angular part of the eigenfunctions, which is given by $\frac{1}{\sqrt{2\pi}} e^{i\ell\varphi}$. For each quantum number ℓ, we then find a Hamiltonian of

$$\bar{H}_{1/2,\ell}/E_{\mathrm{so}} = \eta_x \tilde{h}_\ell \quad \text{with} \quad \tilde{h}_\ell = (-\partial_{\tilde{r}}^2 - \tilde{\delta})\sigma_z + 2i\partial_{\tilde{r}}\sigma_y + \frac{2\ell}{\tilde{r}}\sigma_x + \frac{\ell^2}{\tilde{r}^2}\sigma_z - \frac{\ell}{\tilde{r}^2}\,, \tag{7.29}$$

which needs to be solved to obtain the radial part of the eigenfunctions. In the more general case of an arbitrary hole flux, the quantum numbers ℓ, which have been integers so far, need to be replaced by $\nu = \ell + f - 1/2$.

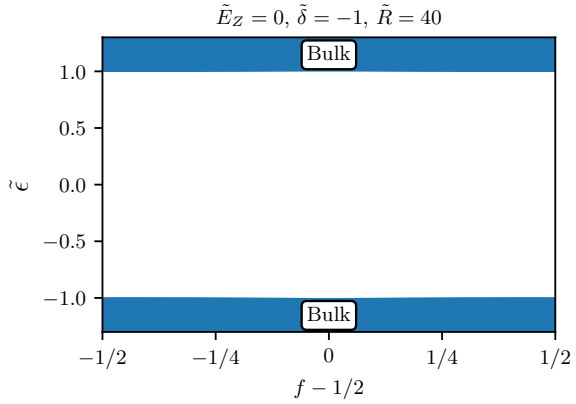

Figure 7.5: Spectrum $\tilde{\epsilon}$ in dimensionless units for $\tilde{E}_Z = 0$, $\tilde{\delta} = -1$, $\tilde{R}_> = 40$ and $\tilde{R}_< = 0$ using the tight-binding Hamiltonian introduced in Subsection 7.1.4 in dependence on the flux difference $f-1/2$ to the SUSY point. We find a bulk gap of approximately $|\tilde{\delta}| = 1$ as expected from Eq. (7.20). Within the gap there are not states present, showing that the phase is non-topological.

The most crucial point is to rewrite the Hamiltonian $\tilde{h}_\nu$ by employing the ladder operators $\Gamma_\nu^{(\dagger)}$ of the Hankel functions of first kind $H^{(1)}_{\nu\pm1/2}$ (see e.g. Ref. [193] for an introduction on Hankel functions), which are defined via $\Gamma_\nu\sqrt{\tilde{r}}H^{(1)}_{\nu+1/2}(\tilde{k}\tilde{r}) = \tilde{k}\sqrt{\tilde{r}}H^{(1)}_{\nu-1/2}(\tilde{k}\tilde{r})$ and $\Gamma_\nu^\dagger\sqrt{\tilde{r}}H^{(1)}_{\nu-1/2}(\tilde{k}\tilde{r}) = \tilde{k}\sqrt{\tilde{r}}H^{(1)}_{\nu+1/2}(\tilde{k}\tilde{r})$. Identifying these operators with $\Gamma_\nu^{(\dagger)} = (-)\partial_{\tilde{r}} + \nu/\tilde{r}$, the Hamiltonian can be rewritten as

$$\tilde{h}_\nu = \begin{pmatrix} \Gamma_\nu\Gamma_\nu^\dagger - \tilde{\delta} & 2\Gamma_\nu \\ 2\Gamma_\nu^\dagger & -(\Gamma_\nu^\dagger\Gamma_\nu - \tilde{\delta}) \end{pmatrix} \tag{7.30}$$

in the σ_z-basis. The eigenvalue equation $\tilde{h}_\nu\,\mathbf{\Phi}^{\text{bulk}}_{\tilde{k}\nu} = \tilde{\epsilon}\,\mathbf{\Phi}^{\text{bulk}}_{\tilde{k}\nu}$ can then be solved using

$$\tilde{\epsilon}_{\tilde{k}}^2 = (\tilde{k}^2 - \tilde{\delta})^2 + 4\tilde{k}^2\,, \quad \mathbf{\Phi}^{\text{bulk}}_{\tilde{k}\nu}(\tilde{r}) = \sqrt{\tilde{k}\tilde{r}}\begin{pmatrix} a_{\tilde{k}}H^{(1)}_{\nu-1/2}(\tilde{k}\tilde{r}) \\ H^{(1)}_{\nu+1/2}(\tilde{k}\tilde{r}) \end{pmatrix} \text{ with } a_{\tilde{k}} = \frac{\tilde{k}^2 - \tilde{\delta} + \tilde{\epsilon}_{\tilde{k}}}{2\tilde{k}}\,. \tag{7.31}$$

For a given energy, there are then four momenta in the complex plane (neglecting bifurcation points, where multiple solutions coincide) solving the equation for $\tilde{\epsilon}$. These momenta can be separated into groups of two momenta with $\text{Im}\tilde{k}_{1/2} \geq 0$ and $\text{Im}\tilde{k}_{3/4} \leq 0$, which can be used for establishing the topological bound states. Since we are interested in edge states, that decay far away from the boundary, only $\tilde{k}_{1/2}$ ($\tilde{k}_{3/4}$) can contribute to the states at the inner (outer) surface. The entire edge states are then constructed by a linear combination of the $\mathbf{\Phi}^{\text{bulk}}_{\tilde{k}_\alpha\nu}$ with $\alpha = 1,2\,(3,4)$, which respects the fact that the state has to vanish at the boundary. This leads to the boundary condition

$$a_{\tilde{k}_\alpha}\frac{H^{(1)}_{\nu-1/2}(\tilde{k}_\alpha\tilde{R})}{H^{(1)}_{\nu+1/2}(\tilde{k}_\alpha\tilde{R})} = a_{\tilde{k}_\beta}\frac{H^{(1)}_{\nu-1/2}(\tilde{k}_\beta\tilde{R})}{H^{(1)}_{\nu+1/2}(\tilde{k}_\beta\tilde{R})}\,, \tag{7.32}$$

with $\alpha,\beta = 1,2\ (3,4)$ and $\tilde{R} = \tilde{R}_<\ (\tilde{R}_>)$ at the inner (outer) edge of the Corbino disk.

At the outer surface, the condition (7.32) needs to be solved with $\tilde{R}_> \gg 1$. Inserting the asymptotic behavior of the Hankel functions as well as the definition of $a_{\tilde{k}}$ and the values of $\tilde{k}_{3/4}$, leads to an implicit equation of

$$\tilde{\epsilon}_\nu^> = \frac{\nu}{\tilde{R}_>}\sqrt{2\left(2 - \tilde{\delta} + \sqrt{\tilde{\delta}^2 - (\tilde{\epsilon}_\nu^>)^2}\right)} - \tilde{\delta} + \sqrt{\tilde{\delta}^2 - (\tilde{\epsilon}_\nu^>)^2} \tag{7.33}$$

for the energy. We only find solutions within the gap for $\tilde{\delta} > 0$ (inside the topological phase), which agrees perfectly with the numerical results shown above. Furthermore, the solution can easily be

solved in linear order in $1/\tilde{R}_>$. Here, the additional $\tilde{\epsilon}_\nu$ on the right-hand side gets neglected and we find

$$\tilde{\epsilon}_\nu^> = \frac{2\nu}{\tilde{R}_>} + \mathcal{O}\left(\frac{1}{\tilde{R}_>^2}\right). \tag{7.34}$$

Thus, the spacing between the edge states is expected to be given by $2/\tilde{R}_> = 0.05$ in Fig. 7.4, which is close to the value obtained by the numerical calculations. Due to the additional η_x in the full Hamiltonian (7.29), we can then find edge states with the energy $\pm\tilde{\epsilon}_\nu^>$, which are the helical edge modes already known to exist in the quantum spin Hall phase of the BHZ model [189]. This allows us to identify these results with the energies shown in Fig. 7.4 via

$$\tilde{\epsilon}_{l,\pm}(f) = \pm\tilde{\epsilon}^>_{\pm\ell+f-1/2}\,. \tag{7.35}$$

At the inner surface, we remain at the opposite limit $\tilde{R}_< \ll 1$. For small enough radii, only the edge state for $\ell = 0$ remains in the gap, while the other ones are pushed into the bulk. For the $\ell = 0$ state, one can again replace the ratio of the Hankel functions with an asymptotic function and expand for small ν, leading to

$$\tilde{\epsilon}_\nu^< \approx \tilde{\delta} + \tilde{k}_1\tilde{k}_2 + 2\,\frac{\tilde{k}_1+\tilde{k}_2}{\tilde{k}_1-\tilde{k}_2}\tilde{k}_1\tilde{k}_2\left(\ln\tilde{k}_1 - \ln\tilde{k}_2\right)\nu\,. \tag{7.36}$$

In the case of $\nu = 0$ or $f = 1/2$, this leads to $\tilde{\epsilon}_0 = \tilde{\delta} - \sqrt{\tilde{\delta}^2 - \tilde{\epsilon}_0^2}$, when inserting the values for the momenta $\tilde{k}_{1/2}$. Thus, the only valid solution within the gap is given by $\tilde{\epsilon}_0 = 0$. In linear order in ν, the energy dispersion can therefore be found by inserting $\tilde{k}_{1/2}(\tilde{\epsilon} = 0)$, leading to

$$\tilde{\epsilon}_\nu^< = -\frac{4\tilde{\delta}\nu}{\sqrt{|\tilde{\delta}-1|}}\begin{cases}\arctan\sqrt{\tilde{\delta}-1} & \text{for} \quad \tilde{\delta} > 1\\ \frac{1}{2}\ln\frac{1+\sqrt{\tilde{\delta}-1}}{1-\sqrt{\tilde{\delta}-1}} & \text{for} \quad 0 < \tilde{\delta} < 1\end{cases} + \mathcal{O}(\nu^2)\,. \tag{7.37}$$

Since $\tilde{\delta} = 1$ was used for the numerical studies of zero Zeeman field shown in Fig. 7.4, we calculate this limit and arrive at

$$\lim_{\tilde{\delta}\to 1}\tilde{\epsilon}^<_{\ell=0}(f) = 4\left(f - \frac{1}{2}\right). \tag{7.38}$$

This is in extraordinary agreement with the slope of the center states energies that we notice in Fig. 7.4(b) from the numerical results.

7.2.2 Finite Zeeman Field

Alltough, we have already seen interesting features due to the SUSY structure of our model, we are further interested in analyzing the behavior in the presence of a Zeeman term. In this case, the Zeeman term operates as the opener of the surface gap allowing for a second order mechanism to introduce second-order bound states in the system (discussed for various systems in e.g. Refs. [50, 194–196]). As already mentioned above, those states are also called corner states in the following, although there are no explicit corners present in the Corbino disk.
Within this subsection, we focus on the case of a small Zeeman field with $\tilde{l}_B^2 \gg 1$ or $\tilde{E}_Z \ll 1$.

Numerical Results

We start by calculating the spectrum numerically in the tight binding model for different Zeeman fields within the topological phase. The results are shown in Fig. 7.6, where the spectrum is once again symmetric around $f = 1/2$ and degenerate at the SUSY point $f = 1/2$.
Nevertheless, there are also qualitative differences to the results of zero Zeeman field shown in Fig. 7.4. In both cases of finite Zeeman field, the *continuum* of edge states only appears outside

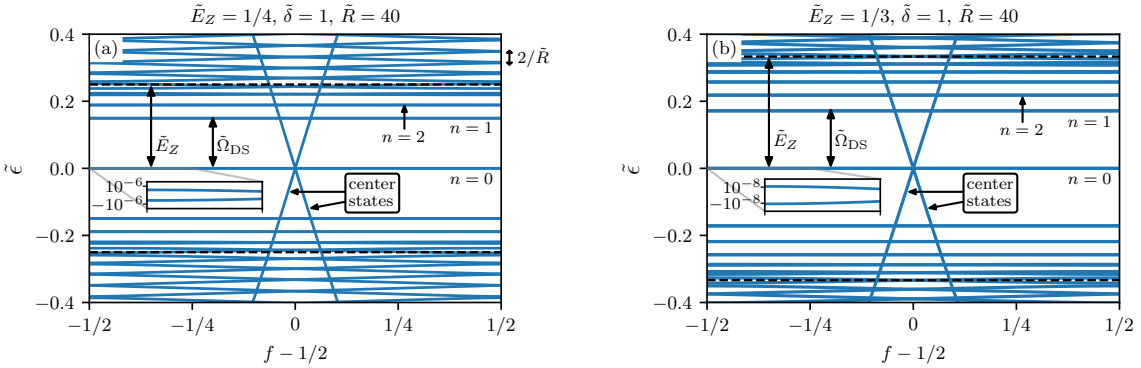

Figure 7.6: Spectrum $\tilde{\epsilon}$ in dimensionless units for small Zeeman fields (a) $\tilde{E}_Z = 1/4$ and (b) $\tilde{E}_Z = 1/4$. In contrast to the results at zero Zeeman field (see Fig. 7.4), there is a surface gap, where only a few localized bound states are present. The size of this gap is given by approximately $\tilde{E}_Z$. The pairs of corner states within the surface gap are labelled with $n = 1, \ldots, N_B$ with N_B being the number of pairs, which increases for larger Zeeman fields. The energy of the first pair with nonzero energy is denoted with $\tilde{\Omega}_{\mathrm{DS}}$. Furthermore, we note two center states with a significantly stronger dispersion that we have already found in Fig. 7.4 for the case of no Zeeman field. In the zoom, it is exemplarily shown for the states labelled with $n = 0$, that they do not have an energy of exactly zero, but instead a finite exponentially small splitting due to finite size effects if we are not at the SUSY point $f = 1/2$, where all states are degenerate. Figure taken from Ref. [111].

of a gap, which is called surface gap in the following. Interestingly, the size of the surface gap is approximately given by the Zeeman energy $\tilde{E}_Z$.

Within the surface gap, additional discrete states appear. Those states are localized in the angular direction and are therefore corner states. First, there are again two center states with an extremely steep dispersion. Although the behavior of the edge states at the outer surface has significantly changed, we note that the dispersion of the center states seems to be unchanged compared to the zero Zeeman field case in Fig. 7.4.

Furthermore, we find a few additional states with an extraordinary flat dispersion. On the scale shown here, the states seem to be perfectly flat although actually having an exponential splitting. Exemplary, a zoom into the zero energy states is depicted in the insets showing that the maximal splitting is given by approximately 10^{-6} for $\tilde{E}_Z = 1/4$ and 10^{-8} for $\tilde{E}_Z = 1/3$. This splitting disappears at the SUSY point, where all states are exactly degenerate (up to a minuscule spitting due to the hibridization with the center states). Interestingly, the discrete energy levels are rather similar in both panels and depend only weakly on the Zeeman energy. However, the energy difference between the discrete levels increase slightly for larger Zeeman fields.

Additionally, there are some interesting features when regarding the energy difference between these discrete states within the surface gap. There is a relatively large discrete step $\tilde{\Omega}_{\mathrm{DS}}$ between the zero energy state and the first nonzero energy state. The energy differences between the other discrete states are significantly smaller and decrease when moving away from zero energy.

Analytical Results

In the following, analytical insights from Ref. [111] into the spectrum of the topological bound states are again presented in order to allow for a more detailed understanding of the numerical results obtained above. To this end, an effective surface Hamiltonian is derived. We assume the parameters to be deep inside the gapped phase with $\tilde{\delta} \gg \tilde{E}_Z$ and we consider the surface under investigation to have a large radius $\tilde{R} = \tilde{R}_{\gtrless} \gg 1$. Therefore, we only investigate the spectrum of the states at the outer radius, although the analysis remains valid for the inner radius if it is large as well. For a more detailed analytical analysis, the reader is again referred to Ref. [111].

Within these considerations, the Hamiltonian can be approximated by the leading order terms, which only act in the normal direction, orthogonal to the considered surface. This leads to the

effective Hamiltonian in the normal direction

$$\bar{H}_n/E_{\mathrm{so}} = \eta_x\, \bar{h}_n/E_{\mathrm{so}} \quad \text{with} \quad \bar{h}_n/E_{\mathrm{so}} = \left[(-\partial_{\tilde{r}}^2 - \tilde{\delta})\sigma_z + 2i\partial_{\tilde{r}}\sigma_y)\right] . \tag{7.39}$$

This Hamiltonian $\bar{h}_n/E_{\mathrm{so}}$ can be solved using plane waves, leading to zero energy states in the normal direction of

$$\bar{\psi}_n^{\gtrless}(\tilde{r},\sigma) \sim \begin{pmatrix} 1 \\ \pm 1 \end{pmatrix}_\sigma \left(e^{i\tilde{k}_1(\tilde{r}-\tilde{R})} - e^{i\tilde{k}_2(\tilde{r}-\tilde{R})}\right) \text{ with } \tilde{k}_{1,2} = \begin{cases} \pm\sqrt{\tilde{\delta}-1}+i & \text{for} \quad \tilde{\delta} > 1 \gg 1/\tilde{l}_B^2 \\ i(1 \pm \sqrt{1-\tilde{\delta}}) & \text{for} \quad 1/\tilde{l}_B^2 \ll \tilde{\delta} < 1 \end{cases} \tag{7.40}$$

with the spin index σ. Exploiting the fact that the surface gap is much smaller than the bulk gap in the regime $\tilde{\delta} \gg \tilde{E}_Z$, one can project the full Hamiltonian onto these solutions in order to arrive at a low-energy Hamiltonian

$$\pm\bar{H}_t^{\gtrless}/E_{\mathrm{so}} = \eta_x \frac{2}{\tilde{R}}(-i\partial_\varphi) + \eta_y \frac{1}{\tilde{l}_B^2}\, \sin\varphi \tag{7.41}$$

for the tangential part. In the following, we refer to this Hamiltonian as the effective surface Hamiltonian, which needs to be solved to obtain the missing tangential part of the solution.
This effective surface Hamiltonian is given by a Dirac model with a potential, that gaps out the *continuum* of edge states and acts as a mass term. Zero energy bound states occur when the mass term changes its sign [197], which happens for $\varphi = 0$ or $\varphi = \pi$.
We can easily extract the energies of possible bound states at this position from squaring the Hamiltonian

$$\tilde{H}_W \coloneqq (\bar{H}_t^{\gtrless}/E_{\mathrm{so}})^2 = -\frac{4}{\tilde{R}^2}\,\partial_\varphi^2 + \tilde{V}_W^{-\eta_z}(\varphi) \quad \text{with} \quad \tilde{V}_W^{\pm}(\varphi) = \frac{1}{\tilde{l}_B^4}\sin^2(\varphi) \mp \frac{2}{\tilde{R}\,\tilde{l}_B^2}\cos(\varphi)\,. \tag{7.42}$$

We now exemplarily consider the case $\eta_z = -1$ and $\varphi = 0$ since the other possibilities ($\eta_z = +1$ and/or $\varphi = \pi$) would not give rise to additional energy levels. Here, we can expand the potential to

$$\tilde{V}_W^{+}(\varphi) \approx \frac{\tilde{\Omega}_W^2}{4}\tilde{\varphi}^2 - \frac{\tilde{\Omega}_W^2}{2}\,, \tag{7.43}$$

with the dimensionless angle $\tilde{\varphi} = \varphi/\Delta\varphi$ and the dimensionless Witten frequency $\tilde{\Omega}_W = \Omega_W/E_{\mathrm{so}} = \frac{2}{\tilde{R}\Delta\varphi} = \frac{2}{\sqrt{\tilde{R}}\,\tilde{l}_B} = 2\sqrt{\frac{\tilde{E}_Z}{\tilde{R}}}$. $\Delta\varphi = \tilde{l}_B/\sqrt{\tilde{R}}$ denotes the spread of the bound corner states in the angular direction.
Defining the operators $a = \partial_{\tilde{\varphi}} + \tilde{\varphi}/2$ and $a^\dagger = -\partial_{\tilde{\varphi}} + \tilde{\varphi}/2$, the squared Hamiltonian can then be described by the harmonic oscillator $\tilde{H}_W^{+} = \tilde{\Omega}_W^2\, a^\dagger a$, which is known to have eigenenergies $\tilde{\Omega}_W^2 n$ with $n \in \mathbb{N}_0$. The energy of the topological bound states inside the surface gap are therefore given by their square root

$$|\tilde{\epsilon}_{n\sigma}^{\gtrless}| = \tilde{\Omega}_W\sqrt{n} = 2\sqrt{\frac{\tilde{E}_Z}{\tilde{R}}}\sqrt{n}\,. \tag{7.44}$$

We can immediately identify the Witten frequency $\tilde{\Omega}_W$ with the energy $\tilde{\Omega}_{\mathrm{DS}}$ of the first nonzero energy state. Since $\tilde{\Omega}_W$ scales with $\sqrt{\tilde{E}_Z}$, we further can understand why the energy of the first nonzero energy state increases with the Zeeman energy, but less significantly than the surface gap, which obeys a linear scaling. Additionally, the energies scale with the square root of their index n, which explains why the differences between energy levels are not equal but reduce for larger energies (larger concerning the absolute value $|\tilde{\epsilon}|$) as noted from the numerical results.

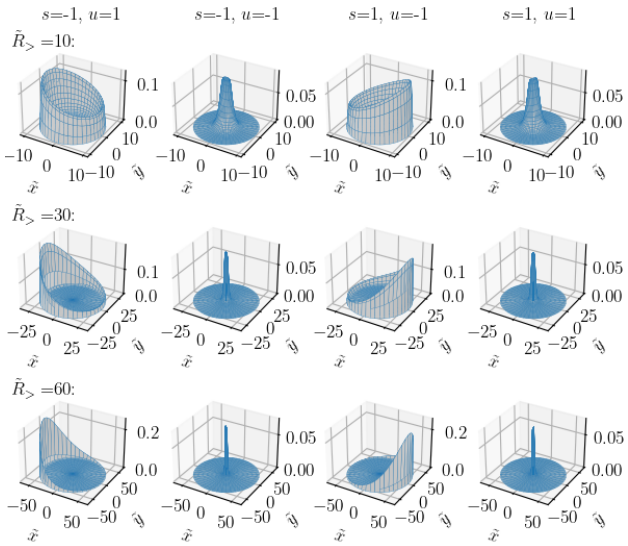

Figure 7.7: Numerical studies of the absolute value $\sum_{\eta,\sigma} |\bar{\psi}_{su}(\tilde{x}, \tilde{y}, \eta, \sigma)|^2$ of the zero energy states of a Corbino disk using a continuous model with an infinitesimal hole ($\tilde{R}_< = 0$) within the topological phase (at $\tilde{l}_B = 5$, $\tilde{\delta} = 1$) for different outer disk radii $\tilde{R}_>$. There are two states at the inner and two states at the outer boundary for all radii. It is visible that the angular localization of the outer boundary states gets increased for larger radii.

7.2.3 Zero Energy Bound States

After the intense investigation of the low energy spectrum using numerical as well as analytical methods, we now focus on the form of the zero energy bound states, which we investigate at the SUSY point $f = 0.5$. We refer to the states with an energy of nearly zero as zero energy states, although a small but finite splitting occurs for a finite Corbino disk. We already know from the investigation of the spectra, that there are no states at zero energy within the non-topological phase. Thus, only the topological and the Weyl phase are studied in the following.

Numerical Results

We extract the zero energy states from the continuum numerics on a disk with an infinite small hole by utilizing the four states with the energy being closest to zero. Due to the (quasi) degeneracy, it is numerically hard to separate the states since they can hybridize in an arbitrary way. In order to allow for comparison of states at different parameters as well as with analytical calculations, we extract the states as eigenstates of the chiral symmetry and the SUSY operator and we further name the states after their eigenvalues s and u concerning these symmetries. To this end, we diagonalize the operators S and U within the subspace of the zero energy states.

First, we analyze the states of the topological gapped phase, where we know from the analysis of the spectrum that four zero energy states are present at the SUSY point. In Fig. 7.7 the zero energy states are presented for different $\tilde{R}_>$ for an exemplary paramter point. Here, two of the zero energy states appear at the inner surface, while the other two are localized at the outer boundary for all radii.
We can further make some interesting observations about the localization of the states. We note that angular localization of the states at the outer boundary gets increased with increasing $\tilde{R}_>$. The $\tilde{R}_>$-dependence of the radial localization is difficult to extract due to the different scalings of the pictures in combination with the strong localization. Nonetheless, one can still observe that the radial localization length stays rather constant and no significant changes in the radial localization are visible.

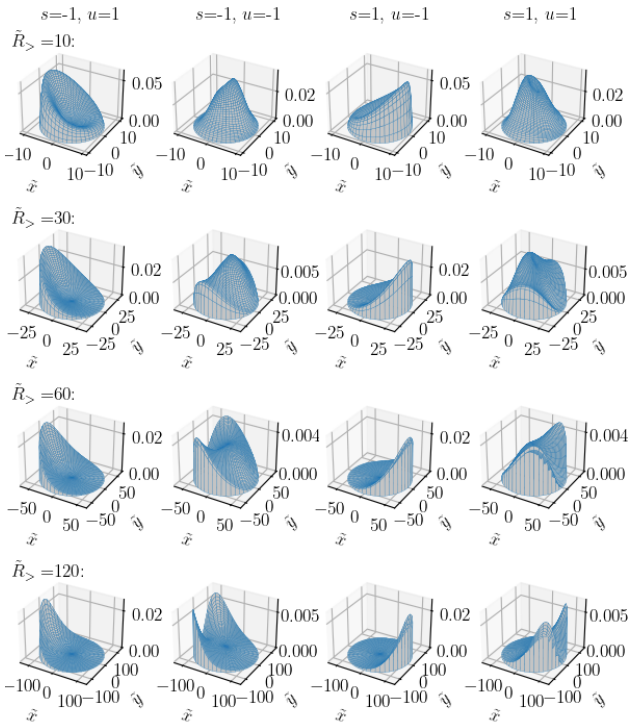

Figure 7.8: Numerical studies of the absolute value $\sum_{\eta,\sigma} |\bar{\psi}_{su}(\tilde{x}, \tilde{y}, \eta_z, \sigma_z)|^2$ of the zero energy states of a Corbino disk using the continuum model with an infinitesimal hole ($\tilde{R}_< = 0$) within the Weyl phase (at $\tilde{l}_B = 5$, $\tilde{\delta} = 0$) for different outer disk radii $\tilde{R}_>$. For small radii, the two states for $s = u$ seem to be located in the center of the disk. Only for sufficiently large radii, one can see that those states are localized at the outer boundary in the limit of an infinite disk surface with a minimum at $\varphi = 0, \pi$. Figure taken from Ref. [111].

Additionally, zero energy bound states can be extracted within the Weyl phase. At first sight, this is counter intuitive due to the gap closing within this phase. Nevertheless, all bulk states stay at an exponentially small, but finite energy for a finite system size. Therefore, we can extract the zero energy bound states, which have a finite but significantly smaller energy at the SUSY point (at least for a sufficiently large radius). Here, only a minuscule splitting can occur between the two pairs of zero energy states. Each of the pairs has to stay degenerate due to SUSY. In Fig. 7.8 the zero energy states are shown for an exemplary parameter set using different outer radii $\tilde{R}_>$.

First of all, we note that the form of the states drastically change with the radius, which was not found in the topological phase. For very small radius $\tilde{R}_> = 10$, the results seem to be rather similar to the ones of the topological phase, where two states were found at the inner and two at the outer boundary. Nevertheless, this is an artifact of the small radius and we note that the states, thought to be localized at the center of the disk, move to the outer surface when the outer radius is increased. At $\tilde{R}_> = 120$, all states are then clearly localized at the outer boundary, which is assumed to persist in the thermodynamic limit.

Interestingly, we now find two states ($u = -s$) localized at a single angle $\varphi = 0, \pi$, while there are two states ($u = s$) with two maxima and a minimum in between at the angle $\varphi = 0, \pi$. This is an indicator that the states with $u = -s$ are symmetric around $\varphi = 0, \pi$, while the states for $u = s$ are anti-symmetric around these angles. This conjecture is confirmed by analytical results below.

As already mentioned before, the states containing two peaks, significantly change their form when increasing $\tilde{R}_>$. Therefore, it is not possible to make any statements about their localization in dependence on the radius. In contrast to this, the states with a single maximum have a similar form for all radii. Here, we note a behavior analogous to the localization of the outer surface states within the gapped topological phase. The localization length of the angular direction decreases with an increasing outer radius $\tilde{R}$, while the radial localization seems to be rather unchanged.

Analytical Results

The positions of the zero energy bound states as well as their forms can also be calculated analytically [111], allowing for another crosscheck between methods and a deeper understanding of the behavior already found with numerical methods.
Although the form of the zero energy bound states in the topological phase could be directly constructed from the eigenstates of the Harmonic oscillator derived in the last subsection, we find these states in a different calculation allowing us to also consider the Weyl phase, as well as a strong Zeeman field. In the following, a large radius $\tilde{R} = \tilde{R}_>, \tilde{R}_<$ of the surface is considered. Although this assumption is not correct for the inner surface of our numerical results, we still include the states from the inner surface in the following as we will still be able to find agreeing properties between the analytical and numerical results. Again, the reader is referred to Ref. [111] for more details on the calculation.

We first rewrite the Hamiltonian as

$$\bar{H}_{1/2} = \begin{pmatrix} 0 & \bar{h} \\ \bar{h}^\dagger & 0 \end{pmatrix} \quad \text{with} \quad \bar{h}/E_{\text{so}} = (-\partial_{\tilde{r}}^2 - \tilde{\delta})\sigma_z + 2i\partial_{\tilde{r}}\sigma_y - \frac{2}{\tilde{r}} i\partial_\varphi \sigma_x - \frac{1}{\tilde{r}^2}\partial_\varphi^2 \sigma_z + \frac{1}{\tilde{r}^2} i\partial_\varphi - i\frac{1}{\tilde{l}_B^2}(\sigma_x \sin\varphi + \sigma_y \cos\varphi)\,. \tag{7.45}$$

and decompose the zero energy states $\bar{\psi}_{s,u}$ into

$$\bar{\psi}_{1,u}(\tilde{r},\varphi,\eta,\sigma) = \Phi^{(u)}(\tilde{r},\varphi,\sigma)\begin{pmatrix} 0 \\ 1 \end{pmatrix}_\eta,\ \bar{\psi}_{-1,u}(\tilde{r},\varphi,\eta,\sigma) = \Phi^{(-u)}(\tilde{r},\varphi+\pi,\sigma)\begin{pmatrix} 1 \\ 0 \end{pmatrix}_\eta$$
$$\text{with } \Phi^{(u)}(\tilde{r},\varphi,\sigma) = \frac{1}{\sqrt{2}}\left\{\chi_{-u}^{(u)}(\tilde{r},\varphi)\begin{pmatrix} 1 \\ 1 \end{pmatrix}_\sigma + \chi_u^{(u)}(\tilde{r},\varphi)\begin{pmatrix} 1 \\ -1 \end{pmatrix}_\sigma\right\}. \tag{7.46}$$

This leads to the coupled differential equations

$$\left(-\partial_{\tilde{r}}^2 - \tilde{\delta} \mp 2u\partial_{\tilde{r}} \pm \frac{u}{\tilde{l}_B^2}\cos\varphi - \frac{1}{\tilde{r}^2}\partial_\varphi^2\right)\chi_\pm^{(u)} - \left(\pm 2\frac{u}{\tilde{r}} i\partial_\varphi \pm i\frac{u}{\tilde{l}_B^2}\sin\varphi - \frac{1}{\tilde{r}^2} i\partial_\varphi\right)\chi_\mp^{(u)} = 0\,, \tag{7.47}$$

which need to be solved with the boundary condition that the state vanishes at the surface. In the case of large $\tilde{R}$, these equations can be expanded in linear order in $1/\sqrt{\tilde{R}}$, leading to

$$\left(-i\partial_{\tilde{r}} - \tilde{k}_1^{(u)}\right)\left(-i\partial_{\tilde{r}} - \tilde{k}_2^{(u)}\right)\hat{\chi}_\pm^{(\pm u)} = \pm\frac{2iu}{\tilde{R}}\partial_\varphi \hat{\chi}_\mp^{(\mp u)} \text{ with } \chi_\pm^{(u)}(\tilde{r},\varphi) = \frac{1}{\sqrt{N_t}} e^{\frac{1}{2\Delta\varphi^2}\cos\varphi}\hat{\chi}_\pm^{(u)}(\tilde{r},\varphi) \tag{7.48}$$

where we defined $\tilde{k}_{1/2}^{(u)} = iu \pm \sqrt{\tilde{\delta} - 1 - u/\tilde{l}_B^2}$ and allowed for a normalization factor N_t. Furthermore, the new functions can be separated into a radial and angular part, leading to

$$\hat{\chi}_+^{(u)}(\tilde{r},\varphi) = \hat{\chi}_{+,n}^{(u)}(\tilde{r}) \quad , \quad \hat{\chi}_-^{(u)}(\tilde{r},\varphi) = (\varphi/\Delta\varphi)\,\hat{\chi}_{-,n}^{(u)}(\tilde{r})\,. \tag{7.49}$$

There are now two possible solutions of the differential equation (7.48).
<u>First Solution:</u> The first solution can be found by using the ansatz $\hat{\chi}_{-,n}^{(u)}(\tilde{r}) = 0$. In combination with the form (7.49), this leads to only one differential equation

$$\left(-i\partial_{\tilde{r}} - \tilde{k}_1^{(u)}\right)\left(-i\partial_{\tilde{r}} - \tilde{k}_2^{(u)}\right)\hat{\chi}_+^{(u)} = 0. \tag{7.50}$$

This equation can be solved by

$$\hat{\chi}_{+,n}^{(u)}(\tilde{r}) = \frac{1}{\sqrt{a_{\text{so}} N^{(u)}}}\, e^{-u(\tilde{r}-\tilde{R})} \begin{cases} \sin\left[q^{(u)}\,(\tilde{r}-\tilde{R})\right] & \text{for } \tilde{\delta} > 1 + u/\tilde{l}_B^2 \\ \sinh\left[q^{(u)}\,(\tilde{r}-\tilde{R})\right] & \text{for } u/\tilde{l}_B^2 < \tilde{\delta} < 1 + u/\tilde{l}_B^2 \end{cases}, \tag{7.51}$$

where we defined $q^{(u)} = |\tilde{\delta} - 1 - u/\tilde{l}_B^2|^{1/2}$ and introduced another normalization factor $N^{(u)} = \frac{|\tilde{\delta}-1-u/\tilde{l}_B^2|}{4|\tilde{\delta}-u/\tilde{l}_B^2|}$. The total solution can then be written as

$$\bar{\psi}_{1,\pm1}(\tilde{r},\varphi,\eta,\sigma) = \frac{1}{\sqrt{2}} \begin{pmatrix} 0 \\ 1 \end{pmatrix}_\eta \begin{pmatrix} 1 \\ \mp 1 \end{pmatrix}_s \hat{\chi}_{+,n}^{(\pm1)}(\tilde{r}) \, \frac{1}{(2\pi)^{1/4}(\Delta\varphi_{\lessgtr})^{1/2}} \, e^{-\frac{1}{4}(\varphi/\Delta\varphi_{\lessgtr})^2} \tag{7.52}$$

with $\hat{\chi}_{+,n}^{(u)}(\tilde{r})$ according to Eq. (7.51) and $\Delta\varphi_{\lessgtr} = \tilde{l}_B/\sqrt{\tilde{R}_{\lessgtr}}$. Furthermore, we can find for the absolute value squared, which was shown for the numerical calculation,

$$\sum_{\eta,\sigma} |\bar{\psi}_{1,\pm1}(\tilde{r},\varphi,\eta,\sigma)|^2 = |\hat{\chi}_{+,n}^{(\pm1)}(\tilde{r})|^2 \, F_+^{\lessgtr}(\varphi) \text{ with } F_+^{\lessgtr}(\varphi) = \frac{e^{-\frac{1}{2}(\varphi/\Delta\varphi_{\lessgtr})^2}}{(2\pi)^{1/2}\Delta\varphi_{\lessgtr}} \, . \tag{7.53}$$

In order to investigate the existence of these states in the different phases, the normal localization lengths

$$\frac{1}{\tilde{\xi}_n^<} = \begin{cases} 1 & \text{for } \tilde{\delta} > 1 + \frac{1}{\tilde{l}_B^2} \\ 1 - \sqrt{1 + \frac{1}{\tilde{l}_B^2} - \tilde{\delta}} & \text{for } \frac{1}{\tilde{l}_B^2} < \tilde{\delta} < 1 + \frac{1}{\tilde{l}_B^2} \end{cases}, \quad \frac{1}{\tilde{\xi}_n^>} = \begin{cases} 1 & \text{for } \tilde{\delta} > 1 - \frac{1}{\tilde{l}_B^2} \\ 1 - \sqrt{1 - \frac{1}{\tilde{l}_B^2} - \tilde{\delta}} & \text{for } \frac{-1}{\tilde{l}_B^2} < \tilde{\delta} < 1 - \frac{1}{\tilde{l}_B^2} \end{cases} \tag{7.54}$$

at inner and outer surface, respectively, can be employed. The localization length at the inner surface diverges at the phase transition to the Weyl phase, showing that these states only exist in the topological phase. Contrary to this, the states at the outer surface remain present in the Weyl phase.

Second Solution: For the second solution, we assume a finite $\hat{\chi}_{+,n}^{(u)}(\tilde{r})$. Exploiting the separational ansatz (7.49) leads to the set of differential equations

$$\left(-i\partial_{\tilde{r}} - \tilde{k}_1^{(-u)}\right)\left(-i\partial_{\tilde{r}} - \tilde{k}_2^{(-u)}\right)\hat{\chi}_{-,n}^{(u)} = 0 \, , \quad \left(-i\partial_{\tilde{r}} - \tilde{k}_1^{(u)}\right)\left(-i\partial_{\tilde{r}} - \tilde{k}_2^{(u)}\right)\hat{\chi}_{+,n}^{(u)} = iu\frac{2}{\tilde{R}}\hat{\chi}_{-,n}^{(u)} \, . \tag{7.55}$$

The first equation can be solved according to Eq. (7.50). The solution of the second equation is more involved and it only exists in the Weyl phase. It turns out that $\hat{\chi}_{+,n}^{(u)}$ can be neglected in the end (see Ref. [111] for details) and can be set to zero. The solution of the first equation is then simply given by $\hat{\chi}_{-,n}^{(u)} = \hat{\chi}_{+,n}^{(u)}$ with $\hat{\chi}_{+,n}^{(u)}$ from Eq. (7.51) since the remaining differential equation from Eq. (7.55) agrees with Eq. (7.50). We then find the second solution

$$\bar{\psi}_{1,1}(\tilde{r},\varphi,\eta,\sigma) = \frac{1}{\sqrt{2}} \begin{pmatrix} 0 \\ 1 \end{pmatrix}_\eta \begin{pmatrix} 1 \\ 1 \end{pmatrix}_\sigma \hat{\chi}_{+,n}^{(-1)}(\tilde{r}) \, \frac{\varphi/\Delta\varphi_>}{(2\pi)^{1/4}(\Delta\varphi_>)^{1/2}} \, e^{-\frac{1}{4}(\varphi/\Delta\varphi_>)^2} \, . \tag{7.56}$$

Again, we can calculate the absolute value squared

$$\sum_{\eta,\sigma} |\bar{\psi}_{1,1}(\tilde{r},\varphi,\eta,\sigma)|^2 = |\hat{\chi}_{+,n}^{(-1)}(\tilde{r})|^2 \, F_-^>(\varphi) \text{ with } F_-^>(\varphi) = (\varphi/\Delta\varphi_>)^2 \, F_+^>(\varphi) \, . \tag{7.57}$$

The normal localization length of this additional anti-symmetric state is found to be given by

$$\frac{1}{\tilde{\xi}_n^{(\text{antisymm})}} = \begin{cases} 1 & \text{for } 1/\tilde{l}_B^2 > \tilde{\delta} > 1 - 1/\tilde{l}_B^2 \\ 1 - \sqrt{1 - 1/\tilde{l}_B^2 - \tilde{\delta}} & \text{for } -1/\tilde{l}_B^2 < \tilde{\delta} < 1 - 1/\tilde{l}_B^2 \end{cases} . \tag{7.58}$$

Comparison

Thanks to the analytical derivation, we can compare the results with our numerical calculations. In agreement with previously obtained results, we have found two states at the inner and two states at the outer surface in the topological phase, while all four zero energy bound states appear at the outer boundary in the Weyl phase. All states are localized either around $\varphi = 0$ or $\varphi = \pi$, which

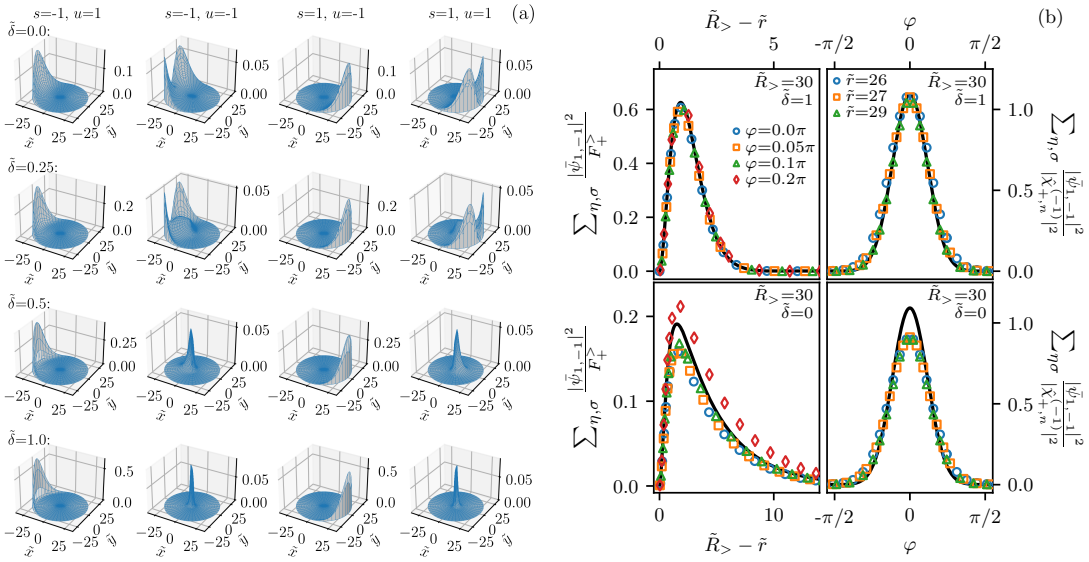

Figure 7.9: Numerical studies of the zero energy states of a Corbino disk using a continuous model with an infinitesimal hole ($\tilde{R}_< = 0$) at fixed $\tilde{l}_B = 2$. (a) Absolute value $\sum_{\eta,\sigma} |\bar{\psi}_{su}(\tilde{x}, \tilde{y}, \eta, \sigma)|^2$ as function of $\tilde{x} = x/a_{\mathrm{so}}$ and $\tilde{y} = y/a_{\mathrm{so}}$ of the zero energy states in dependence on the dimensionless coordinates $\tilde{x}$ and $\tilde{y}$ for an outer radius of $\tilde{R}_> = 30$. $\tilde{\delta}$ is varied from 0 (top row) to 1 (bottom row). For $\tilde{\delta} < 1/4$ all four states are present at the outer surface. For $\tilde{\delta} > 1/4$, there are two states at the inner and two at the outer boundary. At $\tilde{\delta} = 1/4$, the states switching between the surfaces at this point are present at both boundaries. (b) Comparison with the analytical results shown in black using $\tilde{R}_> = 30$ and $s = -u = 1$ for $\tilde{\delta} = 1$ (top) and $\tilde{\delta} = 0$ (bottom). Left: Comparison of the radial part by dividing by the polar component $F^{>}_{\pm}$. Right: Comparison of the polar part by dividing by the radial component $\tilde{\chi}^{(-1)}_{+,n}$. Analytical results are taken from Eqs. (7.51), (7.53) and (7.57). The color coding of the markers in the bottom panels is the same as in the top panels. Figure taken from Ref. [111] with small typos corrected, adaptations due to changes in the notation and lower two subpanels in (b) replaced.

perfectly agrees with the numerical findings. The zero energy state, which changes the position at the phase boundary, is an antisymmetric state in the Weyl phase, explaining while the probability at $\varphi = 0, \pi$ is minimal in Fig. 7.8. We can further compare the localization lengths at the outer surface with the impressions from Figs. 7.7 and 7.8. We note that the localization lengths in the normal direction, given by Eq. (7.54) and (7.58), indeed do not depend on the radius, as we have expected from the numerical results. Additionally, the angular spread $\Delta\varphi$ scales with $1/\sqrt{\tilde{R}}$, explaining the observation that the states get more localized in the angular direction when the radius of the disk is increased.

As just mentioned above, we have already observed in Figs. 7.7 and 7.8 that the positions of the topological zero energy states differ between the phases, which was also confirmed with analytical calculations. Here, it was additionally shown, that the localization length diverges when approaching the phase transition between the Weyl and the topological phase. The behavior of the states during the phase transition can be analyzed using the numerical methods as well. Therefore, we calculate the zero energy bound states for multiple values of $\tilde{\delta}$ within the different phases and on the phase transition point, which is presented in Fig. 7.9(a). We first analyze the states with $s = -u$, which remain at the outer boundary. These states show no significant changes as they are present in both phases without any changes at the phase transition point. Furthermore, the localization in the angular direction is not affected by the changes of $\tilde{\delta}$, which is expected from $\Delta\varphi = \tilde{l}_B/\sqrt{\tilde{R}}$. Nevertheless, the radial localization length decreases with increasing $\tilde{\delta}$, being consistent with Eq. (7.54). The states with $u = s$ show much more significant changes with $\tilde{\delta}$ since they change their position as already mentioned above. When coming from large $\tilde{\delta}$, we note that the radial localization length increases until it diverges at the phase transition at $\tilde{\delta} = 0.25$ (as pre-

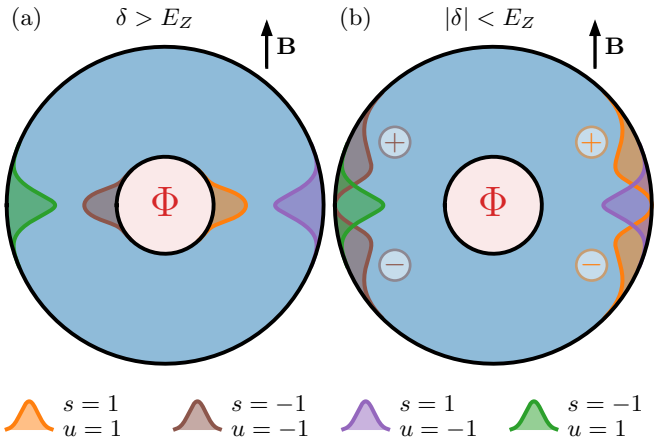

Figure 7.10: Positions of the topological zero energy states of a Corbino disk within (a) the topological phase and (b) the Weyl phase. The states are labelled with s and u corresponding to their eigenvalues under the chiral symmetry operator S and the SUSY operator $U_{1/2}$, respectively. (a) Two states in the center and two states at the outer surface of the Corbino disk. (b) All four states appear at the outer surface. The states that are center states in (a), are now at the outer boundary as well and anti-symmetric around $\phi = 0$ and $\phi = \pi$. Figure taken from Ref. [111].

dicted by Eq. (7.54)), where the state appears to be present at both boundaries. For even smaller $\tilde{\delta}$, the states then switch to the outer surface. Here, it is anti-symmetric, which was shown analytically and is confirmed due to the minimal probability at $\varphi = 0$ or π as already described above.

It was already concluded, that the numerical and analytical results agree qualitatively very well. Nevertheless, an additional comparison on a quantitative level is still missing. Therefore, we compare the absolute value squared with the analytical prediction for multiple fixed angles φ and radii $\tilde{r}$, which corresponds to various *cuts* through the system. We use the results from the continuum numerics shown in Fig. 7.9(a) for one of the symmetric states at the outer boundary. The radius-independent quantity $\sum_{\eta,\sigma} |\bar{\psi}_{1,-1}(\tilde{r},\varphi,\eta,\sigma)|^2/|\hat{\chi}^{(-1)}_{+,n}(\tilde{r})|^2 = F^{>}_{+}(\varphi)$ and the angle-independent quantity $\sum_{\eta,\sigma} |\bar{\psi}_{1,-1}(\tilde{r},\varphi,\eta,\sigma)|^2/F^{>}_{+}(\varphi) = |\hat{\chi}^{(-1)}_{+,n}(\tilde{r})|^2$ are computed numerically and the results are presented in Fig. 7.9(b). Additionally, the analytical prediction from Eqs. (7.51) and (7.53) are shown.
In the upper panels the results are shown for the topological phase at $\tilde{\delta} = 1$. Both, the radial (left panel) and angular (right panel) part show basically perfect agreement between the analytical (solid black line) and numerical results (colored markers). This agreement can be found for numerous angles and radii $\tilde{r}$. Nevertheless, we cannot go to too small $\tilde{r}$ and too large φ, since the absolute value of the states gets minuscule which can result in convergence problems of the numerical results obtained using continuum numerics.
In the lower two panels of Fig. 7.9(b), we set $\tilde{\delta} = 0$ and compare the same state within the Weyl phase. We still find good agreement with the theoretical results. However, some differences are visible. We note that the results are above the theoretical expectation for larger angles, while the opposite behavior occurs for small angles. Interestingly, we still find that the obtained results in the right subpanel (cuts at fixed $\tilde{r}$) are still basically independent of the radius although not perfectly following the black line expected from analytics. The small deviations to the theoretical description are assumed to arise due to the small chosen radius and they should disappear in the limit of an infinite radius. These differences are only visible at $\tilde{\delta} = 0$ (lower subpanels) and not at $\tilde{\delta} = 1$ (upper subpanels) since, in the first case, the state is less localized in the radial direction, making the choice of a larger radius necessary.

Finally, we summarize the positions of the topological zero energy states that we have found numerically, as well as analytically, in the Weyl and in the topological phase. In Fig. 7.10 the different states are sketched for the Corbino disk. In (a), for the topological phase with $\delta < E_Z$,

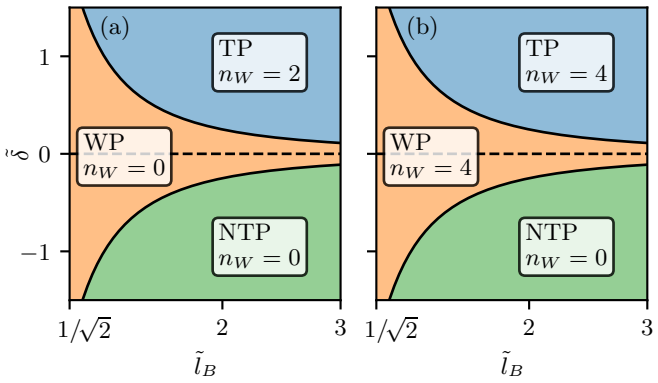

Figure 7.11: Topological phase diagrams with the corresponding Witten indices for (a) an infinite system with a single hole and (b) a Corbino disk. We note, that the Witten index changes for the topological and Weyl phase since there are states at the outer boundary of the Corbino disk which are not present in the single hole system. The Witten index agrees in both systems for the non-topological phase as no bound states are present in this phase leading to a Witten index of zero in both phases. Figure taken from Ref. [111].

there are two states at each boundary, which are localized around $\varphi = 0$ and $\varphi = \pi$. Those states can be labelled according to their eigenvalue u and s of the SUSY operator and of the chiral symmetry, respectively. The states at the inner surface have eigenvalues $u = s$, while we find $u = -s$ at the outer boundary. The angular position is determined by s, which is given by $s = 1$ for $\varphi = 0$ and $s = -1$ for $\varphi = \pi$.
In the Weyl phase (subpanel (b)) with $|\delta| < E_Z$, the states with $u = s$ occur at outer surface, but they are still localized around the same angle. Here, they turn out to be antisymmetric, meaning that the state vanishes at $\varphi = 0, \pi$.
In the non-topological phase with $\delta < -E_Z$, there are no zero energy states, since the system is gapped with no states inside the bulk gap.

7.3 Infinite System with a Hole

In the following, we discuss the case of a circular hole in an infinite system [111]. To this end, we can still consider the results from the Corbino disc and study the limit of an infinite outer radius. In this case, bound states are only present in the center of the system. Here, there are two center states in the topological phase at opposite sides of the hole with different chirality and different SUSY value.
Interestingly, due to the missing states of the outer surface, the states stay exactly at zero, regardless of the size of the circular hole. Due to the SUSY symmetry, the states cannot split and they cannot move away from zero due to the chiral symmetry of the system. This leads to the astonishing result of topological bound states at an energy of precisely zero regardless of the strong orbital overlap of the states.
In Fig. 7.11, we compare the phases of a single hole in an infinite system with the ones of the Corbino disk. Of course, the phase regions themselves do not differ since the gap closings are only defined by the bulk of the system. Nonetheless, the number of local zero energy bound states, which is denoted as Witten index n_W in the following, can differ as already mentioned. Due to the absence of the outer boundary, the Witten index changes within both, the Weyl and the topological phase. In the Weyl phase all states are present on the outer surface, leading to a Witten index of four in the Corbino disk and zero for the single hole system. In the topological phase, there are states on the outer and inner surface. Since the states always appear in pairs, the Witten index is given by four and two for a Corbino disk and a single hole system, respectively. Finally, since there exist no topological bound states on both surfaces in the non-topological phase, the Witten index is given by zero for both systems.

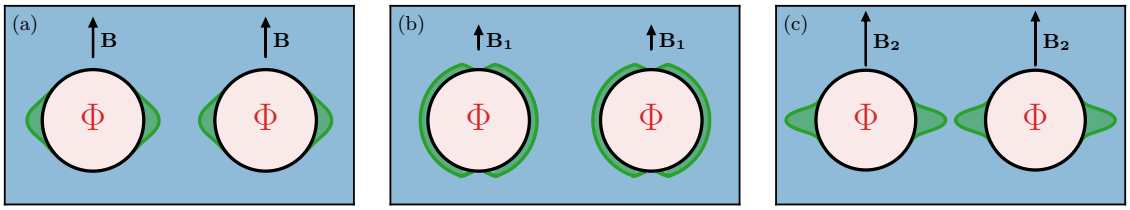

Figure 7.12: Sketch how to use a setup of two holes for topological engineering. The qualitative shape of the two center states is shown for (a) intermediate, (b) small, (c) large in-plane Zeeman fields. As discussed above, the radial (polar) localization increases (decreases), when the Zeeman field is enlarged. Therefore, an increased Zeeman field leads to a larger overlap of states from neighboring holes, allowing to actually tune the hybridisation of these states by adjusting the magnetic field. Figure taken from [111].

In this chapter, we solely focus on circular surfaces by studying a Corbino disk or a hole in an infinite system. Nonetheless, note that the analysis above can be generalized to arbitrary smooth surfaces as shown in Ref. [111].

7.4 Applications

Within this section, one of numerous possible applications of the mechanism leading to topological zero energy bound states protected by SUSY is introduced. Here, we focus on the possibility to employ the zero energy center states for topological engineering, discussed in Ref. [111]. The crucial ingredient is thereby, the potential of controlling the localization lengths of the states in the normal, as well as in the tangential direction by tuning the in-plane Zeeman field, which is responsible for the second order mechanism leading to these localized corner states. Since the localization lengths in the different directions react in an opposite way to an adaption of the Zeeman field, the shape of the hole states can be controlled.
Therefore, the orbital overlap between states from the same hole can be regulated and increases when decreasing the size of the Zeeman field. Although this does not lead to any hybridizing at the SUSY point, a slight detuning from half integer flux leads to a hybridization, and therefore a correlation that can be controlled by the in-plane magnetic field.
Furthermore, we can consider a setup of two holes as shown in Fig. 7.12 with different Zeeman field strengths. Here, we find the opposite behavior and the overlap of states from neighboring holes grows when the Zeeman field is increased as well. The hybridization then leads to an interaction, not only between states from the same hole, but even between the different holes in the system. The hybridization of states between neighboring holes even takes place at the SUSY point and no detuning from half integer flux is needed.
The shapes of the holes can be changed in numerous ways to more general surfaces, which still have topological zero energy states as noted above. This leads to an infinite number of possibilities of topological controlling of interactions (see Ref. [111]), which are beyond the scope of this thesis.

7.5 Conclusion & Outlook

In this chapter, a subclass of two-dimensionsal SOTIs was proven to have a supersymmetric spectrum if an Aharonov-Bohm flux of half a magnetic flux quantum is applied through its center. Interestingly, SUSY can protect topological zero energy bound states which uncovers a connection between high energy physics, where SUSY is regularly employed, and topological condensed matter physics.
Although the supersymmetric spectrum was found in a whole subgroup of 2D SOTIs, we focused on one element of this class, the BHZ model with an additional Zeeman field. The Zeeman term is responsible for the opening of the surface gap, which is in agreement with earlier research [50, 194–196]. The BHZ model was studied on a Corbino disk using numerical methods based on a

continuum and a tight binding approach. Furthermore, those results were compared to analytical insights from Ref. [111], showing a good agreement.
The spectrum was shown to be indeed supersymmetric in both, the absence and presence of a surface gap. Furthermore, the shape and appearing of topological zero energy bound states were investigated in the different phases of the model, which are given by a gapped topological, a gapped non-topological and a gapless Weyl phase. Interestingly, there are zero energy bound states in both the topological and the Weyl phase although they partly appear at different positions. This even leads to a switching of two states from the inner to the outer surface at the phase transition point. In the topological phase, two zero energy bound states occur at the inner surface and hence persist in the case of a single hole in an infinite system. Here, these hole states appear at exactly zero energy due to the combination of SUSY and chiral symmetry.
Moreover, we noted that the localization scales differently with the disk radius in the normal and tangential direction to the surface. From analytical insights from Ref. [111], one knows that the scaling with the Zeeman field is also different and even opposite in the two directions. This paves the way for possible control of the hybridization of states via a magnetic in-plane field.

The work from this chapter leads to numerous possible future research directions. Due to the great interest in this topic, some of these directions have already been investigated in the very recent past.
First of all, the proposed model can be studied and generalized to the three-dimensional case. This was recently done in Ref. [198], where the quantum Hall effect was studied on a torus using a three-dimensional version of the here investigated model.
Another research direction arising from this chapter is the question on how the results change for different shapes of the system. As already mentioned above, a generalization of arbitrary smooth surfaces was discussed in Ref. [111]. Nevertheless, this does not allow a treatment of sharp corners which were therefore studied in Ref. [199].
However, there are still numerous open questions. As already mentioned in the introduction, in addition to second-order topological insulators, second-order topological superconductors can exist as well (see e.g. Refs. [50, 52, 56]) and host Majorana zero energy bound states. Therefore, a similar study of supersymmetric spectra in second-order topological superconductors and a comparison with the results presented here, is another fascinating direction for the future.
Finally, the influence of additional terms is worth studying. Most importantly, the effect of interactions should be investigated in the future. Nevertheless, also other ingredients that do not break SUSY can be added and studied, such as additional longer ranged hoppings in the tight-binding version.
Finally, an experimental setup for the realization of a second order topological insulator or superconductor remains the most striking question for future research, which would allow to exploit the special properties of SUSY protected topological bound states at zero energy.

Chapter 8

Metastability of Subleading Superconducting Orders

This chapter is based on the following unpublished project:
[200] C. S. Weber, S. Gassner, D. M. Kennes, and M. Claassen, "Metastability of subleading instabilities in superconducting materials", (unpublished)
For this project, I carried out the numerical computations (time evolution based on Keldysh, phase diagrams, numerical stability criterion and free energy landscapes) and wrote the codes necessary for these calculations. Moreover, I did the analytical calculations (no-go theorem, stability criterion for the p_x-wave of square lattice model and non-existent coupling of one-band models). Furthermore, I am currently contributing to the writing of the manuscript.

In the last chapter, we analyzed an example of how a topological phase can arise for noninteracting Hamiltonians. However, topological phases can also occur in correlated systems. One example are topological superconductors that were briefly discussed in the introduction and which are of enormous interest since some of them can host Majorana zero modes [23, 25, 26, 32]. Since most materials do not obey topological (or other unconventional) superconducting phases in their ground state, a possible approach for their realization is the targeting of these exotic phases via a light pulse since metastable states with the corresponding order can exist at higher energy.

The realization of metastable states at higher energies using light pulses has been investigated in numerous subfields of condensed matter physics, including the induction of insulator-metal transitions via light [201–203], the induction of topological phases [204, 205], ultrafast switching to and between charge ordered phases [206–208], switching of the ferroelectic polatrization [209–211] and the manipulation of magnetic properties [212–214].
Concerning superconducting orders, the possibility of light-induced superconductivity has been experimentally observed in K_3C_{60} and other organic superconductors [215–219], as well as in cuprates [220, 221]. Here, a non-superconducting state gets driven into a possibly superconducting phase. Besides the experimental observation, numerous efforts for a theoretical explanation have been made [222–229].
Additionally, there have been multiple studies on possible driving between competing superconducting orders [144, 154]. In Ref. [154], even the possible driving to subleading superconducting instabilities, which we also want to discuss in this chapter, was investigated using models similar (and partially the same) to the ones employed in this chapter. However, Ref. [154] focused on the driving process between the different orders using a time-dependent Ginzburg Landau theory and quasi-particle dynamics in the absence of dissipation, while we focus on the question of stability in this chapter by employing the free energy landscape of the mean-field Hamiltonian, and quasi-particle dynamics from the Keldysh equations of motions allowing to consider a coupling to a fermionic bath.
The mentioned competing superconducting orders all belong to solutions of the gap equation (6.66) (or Eq. (6.28) for the general version including equal spin pairing and models where the spin sectors of the non-interacting Hamiltonian are coupled). Only the solution with the lowest free energy is

the ground state and will be occupied in equilibrium. There are other solutions with a higher free energy, corresponding to subleading instabilities. These subleading orders are still extremal points in the free energy landscape. Since they can be either minima, maxima or saddle points, it is not clear whether those instabilities are metastable or not. If the system is excited to a state close-by a subleading instability,it can only relax to the subleading order if this order forms a local minimum. If the instability belongs to a saddle point, the system relaxes back to the ground state as shown in Fig. 8.1(a).
In this chapter, we therefore analyze the (meta-)stability of subleading orders at higher energy on a mean-field level.

We first derive a no-go theorem for real valued pairing showing that two instabilities cannot be stable simultaneously by considering a rather general single-band model with time-reversal symmetry. This proves that metastable subleading order cannot exist in this case. Using a square lattice model with different pairing channels emerging due to effective attractions onsite and between nearest neighbors, we then confirm the results from the no-go theorem and find additionally that the result is also not changed when time-reversal symmetry is broken by a Zeeman term. Moreover, it is discovered that the phase difference between multiple order parameters is an essential key to understanding this phenomena. In the example shown in Fig. 8.1(b),(c), the subleading instability Δ_1 is stable when considering a real displacement in Δ_0 ($\Delta_{1,\mathbf{k}}+\alpha\Delta_{0,\mathbf{k}}$), while imaginary distortions ($\Delta_{1,\mathbf{k}}+i\alpha\Delta_{0,\mathbf{k}}$) are responsible for the subleading order to be unstable.
Strikingly, chiral topological superconductors have a complex valued pairing and the no-go theorem does not apply in this case. We prove that chiral topological superconducting phases can be subleading and metastable, meaning that topological superconducting phases are ideal targets for driving a conventional s-wave superconductor with light.
We then investigate whether states of different parity can be coupled in the assumed single-band models. Since such a coupling cannot occur, we additionally investigate the question of stability in multi-band models using the honeycomb lattice. Finally, models allowing for Cooper pairs consisting of particles with the same spin are considered.

In this chapter, the words stable and metastable are mostly used equivalently since we are only interested in stability on short time scales.

8.1 Real Value Pairing for General One-Band Models

As a starting point, we investigate the stability of multiple orders in rather general one-band models. Here, we assume that only electrons with opposite spin are paired and that the non-interacting Hamiltonian does not couple different spin sectors, so that the formalism and the equations described in Section 6.5 can be used.
In this section, we consider the case of real valued pairing, meaning that the form factors introduced in Section 6.5 are real (up to a possible constant phase, which can be gauged away). We consider the BdG-Hamiltonian (6.65) introduced in Section 6.5 and simplify it by defining

$$\epsilon_{\mathbf{k}} = \frac{\epsilon_{\mathbf{k},\uparrow} + \epsilon_{-\mathbf{k},\downarrow}}{2}\,, \quad \gamma_{\mathbf{k}} = \frac{\epsilon_{\mathbf{k},\uparrow} - \epsilon_{-\mathbf{k},\downarrow}}{2} \tag{8.1}$$

leading to

$$\mathcal{H}_{\mathrm{BdG}}(\mathbf{k}) = \begin{pmatrix} \epsilon_{\mathbf{k}} + \gamma_{\mathbf{k}} & \Delta_{\mathbf{k}} \\ \Delta_{\mathbf{k}}^{\dagger} & -\epsilon_{\mathbf{k}} + \gamma_{\mathbf{k}} \end{pmatrix}. \tag{8.2}$$

The free energy can be computed as explained in Section 6.5, which leads to

$$\bar{F} = \frac{F}{N} = \frac{E - TS}{N} \tag{8.3}$$

$$\bar{E} = \frac{E}{N} = \frac{1}{N}\sum_{\mathbf{k}} n_F(E_{\mathbf{k}} + \gamma_{\mathbf{k}})(E_{\mathbf{k}} + \gamma_{\mathbf{k}}) + n_F(-E_{\mathbf{k}} + \gamma_{\mathbf{k}})(-E_{\mathbf{k}} + \gamma_{\mathbf{k}}) - \sum_i \frac{|\Delta_i|^2}{v_i} \tag{8.4}$$

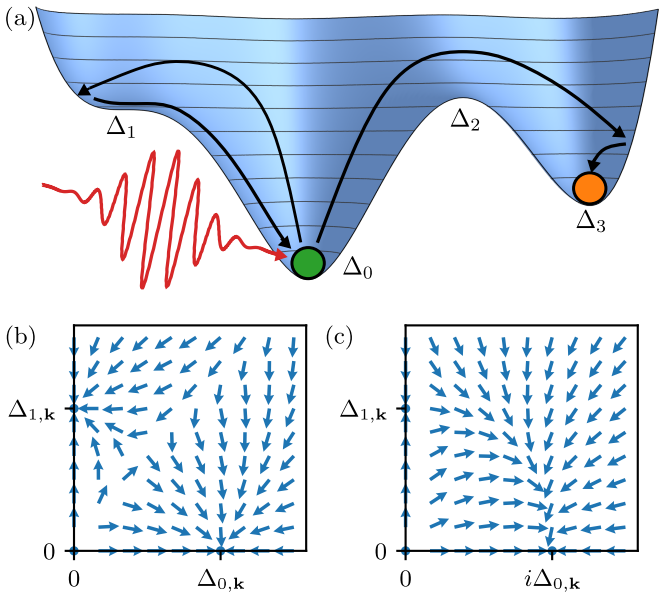

Figure 8.1: (a) Excitation of the superconducting ground state in a free energy landscape with multiple instabilities Δ_i using a light pulse. The relaxation process depends on the form of the free energy landscape. Only for a local minimum, the system relaxes to the nearby local extremum and does not relax back to the global minimum. Here, the local minimum belongs to a metastable subleading instability. In the case of a saddle point, the order is unstable and the system cannot get stuck at the higher energy state. (b),(c) Flow diagrams showing the important role of the phase difference between the different order parameters. In (b) no phase difference is assumed, which we call *real direction*; while in (c) a phase difference of $\pi/2$ is considered (*imaginary direction*). The phase difference between the order parameters is crucial since both instabilities are stable in the real direction, while the subleading instability Δ_1 is unstable in the imaginary direction. It thus belongs to a saddle point in the free energy landscape.

$$\bar{S} = \frac{S}{N} = \frac{1}{N}\sum_{\mathbf{k}}\Big[n_F(E_\mathbf{k}+\gamma_\mathbf{k})\log\left[n_F(E_\mathbf{k}+\gamma_\mathbf{k})\right] + \left[1-n_F(E_\mathbf{k}+\gamma_\mathbf{k})\right]\log[1-n_F(E_\mathbf{k}+\gamma_\mathbf{k})]$$
$$+ n_F(-E_\mathbf{k}+\gamma_\mathbf{k})\log[n_F(-E_\mathbf{k}+\gamma_\mathbf{k})] + \left[1-n_F(-E_\mathbf{k}+\gamma_\mathbf{k})\right]\log[1-n_F(-E_\mathbf{k}+\gamma_\mathbf{k})]\Big] \tag{8.5}$$

with $E_\mathbf{k} = \sqrt{\epsilon_\mathbf{k}^2 + |\Delta_\mathbf{k}|^2}$ and the Fermi function $n_F(E)$.
For the following analysis, it is sufficient to calculate the curvature of the free energy density $\bar{F}$ at the points corresponding to the different orders in the imaginary direction ($\Delta_\mathbf{k} = \Delta_i \not{f}_{i,\mathbf{k}} + i\Delta_j \not{f}_{j,\mathbf{k}}$ with $\not{f}_{i,\mathbf{k}}, \not{f}_{j,\mathbf{k}}$ being the form factors as introduced in Section 6.5), meaning that there is a phase difference of $\pi/2$ between the different orders. We prove below that considering only this direction is sufficient to show that two instabilities cannot be stable at the same time making the consideration of other phase differences redundant. In the case of the imaginary direction, there is a connection between the curvature and the first derivative with respect to Δ_j^2, which is given by

$$\left.\frac{d^2\bar{F}}{d\Delta_j^2}\right|_{\Delta_j=0} = \left[\frac{d}{d\Delta_j}\frac{d\bar{F}}{d\Delta_j}\right]_{\Delta_j=0} = \left[\frac{d}{d\Delta_j}\left(\frac{d\bar{F}}{d(\Delta_j^2)}2\Delta_j\right)\right]_{\Delta_j=0} = 2\left.\frac{d\bar{F}}{d(\Delta_j^2)}\right|_{\Delta_j=0}, \tag{8.6}$$

where we exploited that the free energy only depends on Δ_j^2. Therefore, we only need to derive the derivative with respect to Δ_j^2. We obtain

$$\frac{d\bar{E}}{d(\Delta_j^2)} = \frac{1}{N}\sum_k \not{f}_{j,\mathbf{k}}^2 \left\{\frac{1}{2E_\mathbf{k}}\left[n_F(E_\mathbf{k}+\gamma_\mathbf{k}) - n_F(-E_\mathbf{k}+\gamma_\mathbf{k})\right]\right.$$

$$+\frac{1}{2E_{\mathbf{k}}}(E_{\mathbf{k}}+\gamma_{\mathbf{k}})\frac{-\beta e^{\beta(E_{\mathbf{k}}+\gamma_{\mathbf{k}})}}{[e^{\beta(E_{\mathbf{k}}+\gamma_{\mathbf{k}})}+1]^2}+\frac{1}{-2E_{\mathbf{k}}}(-E_{\mathbf{k}}+\gamma_{\mathbf{k}})\frac{-\beta e^{\beta(-E_{\mathbf{k}}+\gamma_{\mathbf{k}})}}{[e^{\beta(-E_{\mathbf{k}}+\gamma_{\mathbf{k}})}+1]^2}\Bigg\}-\frac{1}{v_j} \quad (8.7)$$

and

$$\begin{aligned}
-\frac{d\bar{S}}{d(\Delta_j^2)} =&\frac{1}{N}\sum_k \not{f}_{j,\mathbf{k}}^2\Bigg\{[\log n_F(E_{\mathbf{k}}+\gamma_{\mathbf{k}})-\log(1-n_F(E_{\mathbf{k}}+\gamma_{\mathbf{k}}))]\,\frac{1}{2E_{\mathbf{k}}}\frac{-\beta e^{\beta(E_{\mathbf{k}}+\gamma_{\mathbf{k}})}}{(e^{\beta(E_{\mathbf{k}}+\gamma_{\mathbf{k}})}+1)^2}\\
&+[\log n_F(-E_{\mathbf{k}}+\gamma_{\mathbf{k}})-\log(1-n_F(-E_{\mathbf{k}}+\gamma_{\mathbf{k}}))]\,\frac{1}{-2E_{\mathbf{k}}}\frac{-\beta e^{\beta(-E_{\mathbf{k}}+\gamma_{\mathbf{k}})}}{(e^{\beta(-E_{\mathbf{k}}+\gamma_{\mathbf{k}})}+1)^2}\Bigg\}\\
=&\frac{1}{N}\sum_k \not{f}_{j,\mathbf{k}}^2\Bigg\{\log\left(\frac{1}{n_F(E_{\mathbf{k}}+\gamma_{\mathbf{k}})}-1\right)\frac{1}{2E_{\mathbf{k}}}\frac{\beta e^{\beta(E_{\mathbf{k}}+\gamma_{\mathbf{k}})}}{(e^{\beta(E_{\mathbf{k}}+\gamma_{\mathbf{k}})}+1)^2}\\
&-\log\left(\frac{1}{n_F(-E_{\mathbf{k}}+\gamma_{\mathbf{k}})}-1\right)\frac{1}{2E_{\mathbf{k}}}\frac{\beta e^{\beta(-E_{\mathbf{k}}+\gamma_{\mathbf{k}})}}{(e^{\beta(-E_{\mathbf{k}}+\gamma_{\mathbf{k}})}+1)^2}\Bigg\}\\
=&\frac{1}{N}\frac{\beta}{2E_{\mathbf{k}}}\sum_k f_2(k)^2\Bigg\{(E_{\mathbf{k}}+\gamma_{\mathbf{k}})\frac{\beta e^{\beta(E_{\mathbf{k}}+\gamma_{\mathbf{k}})}}{(e^{\beta(E_{\mathbf{k}}+\gamma_{\mathbf{k}})}+1)^2}-(-E_{\mathbf{k}}+\gamma_{\mathbf{k}})\frac{\beta e^{\beta(-E_{\mathbf{k}}+\gamma_{\mathbf{k}})}}{(e^{\beta(-E_{\mathbf{k}}+\gamma_{\mathbf{k}})}+1)^2}\Bigg\}\,,
\end{aligned} \quad (8.8)$$

where we used that $n_F(E)=1/[\exp(\beta E)+1]$. Combining these results yields

$$\frac{d\bar{F}}{d(\Delta_j^2)}=\frac{d\bar{E}}{d(\Delta_j^2)}-T\frac{d\bar{S}}{d(\Delta_j^2)}=\frac{1}{N}\sum_k \not{f}_{j,\mathbf{k}}^2\frac{1}{2E_{\mathbf{k}}}\left[n_F(E_{\mathbf{k}}+\gamma_{\mathbf{k}})-n_F(-E_{\mathbf{k}}+\gamma_{\mathbf{k}})\right]-\frac{1}{v_j}\,. \quad (8.9)$$

The curvature at a specific instability Δ_i is therefore given by

$$\left.\frac{d^2\bar{F}}{d\Delta_j^2}\right|_{\Delta_i}=\frac{1}{N}\sum_k \not{f}_{j,\mathbf{k}}^2\frac{1}{E_{\mathbf{k}}(\Delta_i)}\left[n_F(E_{\mathbf{k}}(\Delta_i)+\gamma_{\mathbf{k}})-n_F(-E_{\mathbf{k}}(\Delta_i)+\gamma_{\mathbf{k}})\right]-\frac{2}{v_j}\,. \quad (8.10)$$

where we defined $E_{\mathbf{k}}(\Delta_i)=\sqrt{\epsilon_{\mathbf{k}}+\Delta_i^2\not{f}_{i,\mathbf{k}}^2}$. Furthermore, the gap equation is valid at the equilibrium point of the second instability Δ_j, where it is given by

$$\Delta_j=v_j\frac{1}{N}\sum_{\mathbf{k}}\not{f}_{j,\mathbf{k}}\left\langle c_{-\mathbf{k},\downarrow}c_{\mathbf{k},\uparrow}\right\rangle\Big|_{\Delta_j}=v_j\frac{1}{N}\sum_{\mathbf{k}}\not{f}_{j,\mathbf{k}}\frac{\Delta_j\not{f}_{j,\mathbf{k}}}{2E_{\mathbf{k}}(\Delta_j)}\left[n_F(E_{\mathbf{k}}(\Delta_j)+\gamma_{\mathbf{k}})-n_F(-E_{\mathbf{k}}(\Delta_j)+\gamma_{\mathbf{k}})\right]. \quad (8.11)$$

Based on this result, we replace v_j to obtain the final result for the curvature

$$\left.\frac{d^2\bar{F}}{d\Delta_j^2}\right|_{\Delta_i}=\frac{1}{N}\sum_{\mathbf{k}}\not{f}_{j,\mathbf{k}}^2\left[\chi(\Delta_i)-\chi(\Delta_j)\right] \quad (8.12)$$

with

$$\chi(\Delta_j)=\frac{n_F(E_{\mathbf{k}}(\Delta_j)+\gamma_{\mathbf{k}})-n_F(-E_{\mathbf{k}}(\Delta_j)+\gamma_{\mathbf{k}})}{E_{\mathbf{k}}(\Delta_j)}\,. \quad (8.13)$$

We now consider two arbitrary real instabilities with order parameters $\Delta_1\not{f}_1(\mathbf{k})$ and $\Delta_2\not{f}_2(\mathbf{k})$. In case of a subleading metastable instability, both curvatures would need to be positive at the same time. Therefore, the artificial function

$$g(x,y)=x\cdot\left.\frac{d^2\bar{F}}{d\Delta_2^2}\right|_{\Delta_1}+y\cdot\left.\frac{d^2\bar{F}}{d\Delta_1^2}\right|_{\Delta_2}=\frac{1}{N}\sum_{\mathbf{k}}(x\not{f}_{2,\mathbf{k}}^2-y\not{f}_{1,\mathbf{k}}^2)\left[\chi(\Delta_1)-\chi(\Delta_2)\right] \quad (8.14)$$

containing both curvatures and with x, y being arbitrary real numbers has to remain positive for all $x,y>0$ in that case.

Time Reversal Symmetric Case

In the following, we investigate the simplified case of a model with a time-reversal symmetric non-interacting part of the Hamiltonian, meaning that they fulfill $h_{\mathbf{k},\uparrow} = h_{-\mathbf{k},\downarrow}$. In this thesis, we simply refer to these as time-reversal symmetric models disregarding the form of the interaction and the order parameter. For the chosen one-band modes, time-reversal symmetry thus corresponds to $\gamma_{\mathbf{k}} = 0$, leading to the simplification

$$\chi(\Delta_j) = \frac{n_F(E_{\mathbf{k}}(\Delta_j)) - n_F(-E_{\mathbf{k}}(\Delta_j))}{E_{\mathbf{k}}(\Delta_j)} = -\frac{\tanh\frac{\beta E_{\mathbf{k}}(\Delta_j)}{2}}{E_{\mathbf{k}}(\Delta_j)} \tag{8.15}$$

Moreover, we employ specific values for x and y and consider

$$g(|\Delta_2|^2,|\Delta_1|^2) = \frac{1}{N}\sum_{\mathbf{k}} \left(|\Delta_2|^2 \measuredangle_2(\mathbf{k})^2 - |\Delta_1|^2 \measuredangle_1(\mathbf{k})^2\right) [\chi(\Delta_1) - \chi(\Delta_2)] \,. \tag{8.16}$$

Importantly, the inequality

$$\chi(\Delta_1)) \lesseqgtr \chi(\Delta_2) \quad \text{for} \quad |\Delta_1|^2 \measuredangle_1(\mathbf{k})^2 \gtreqless |\Delta_2|^2 \measuredangle_2(\mathbf{k})^2 \tag{8.17}$$

holds. Therefore, all terms in the sum are negative, meaning that the whole expression

$$g(|\Delta_2|^2, |\Delta_1|^2) < 0 \,. \tag{8.18}$$

This proves that it is impossible for both instabilities to be stable at the same time.

General Case $\gamma_{\mathbf{k}} \neq 0$

We now briefly study the more general case with a finite $\gamma_{\mathbf{k}} \neq 0$. Here, the proof from above is not valid since the generalization of Eq. (8.17) does not hold for all $E_{\mathbf{k}}$ and $\gamma_{\mathbf{k}}$.
Nevertheless, it is expected that terms breaking time reversal symmetry do not change the no-go theorem proved above. If these terms are small compared to the other energy scales, the changes to $g(|\Delta_2|^2, |\Delta_1|^2)$ are tiny. Even if some terms of $g(|\Delta_2|^2, |\Delta_1|^2)$ are positive in that case, the total sum over the momenta of the Brioullin zone is presumed to stay negative. Furthermore, for too large time reversal symmetry breaking terms $\gamma_{\mathbf{k}}$ (for all $\mathbf{k}$), there is no superconductivity in the system for a model with the considered BdG Hamiltonian (8.2). Thus, there is still no possibility of a subleading metastable instability. This conjecture is supported by numerical evidence below and the obstacle of finding a rigorous proof is left for future research.

8.2 Square Lattice Model

We verify the results found above by investigating a single-band model on a square lattice. Here, a nearest-neighbor hopping term and a Zeeman field are considered leading to

$$h_{\mathbf{k},\sigma} = -2t_{\mathrm{h}} \left[\cos(k_x) + \cos(k_y)\right] + \sigma E_z - \mu \tag{8.19}$$

with the spin $\sigma \in \{\uparrow,\downarrow\} = \{1,-1\}$, the hopping amplitude t_{h}, the Zeeman energy E_z and the chemical potential μ. In this chapter, we denote the hopping amplitude with t_{h} to distuingish it from the time t. Furthermore, we do all calculations in units of t_{h} and set $t_{\mathrm{h}} = 1$ in the remainder of this chapter. Additionally, we already included the chemical potential into the Hamiltonian for convenience (as already done in Chapters 5 and 6) which technically yields the grand canonical potential. We consider form factors representing a standard s-wave arising due to a local interaction U, as well as p-wave channels emerging from a nearest-neighbor coupling U' with form factors

$$\begin{aligned} \measuredangle_{s,\mathbf{k}} &= 1\,, & v_s &= U\,, \\ \measuredangle_{p_i,\mathbf{k}} &= \sqrt{2}\sin(k_i)\,, & v_{p_i} &= U' \quad \text{for } i = x, y. \end{aligned} \tag{8.20}$$

Due to the origin of the different form factors, the model is thus closely connected to the attractive extended Hubbard model. However, additional pairing channels that can occur for systems with

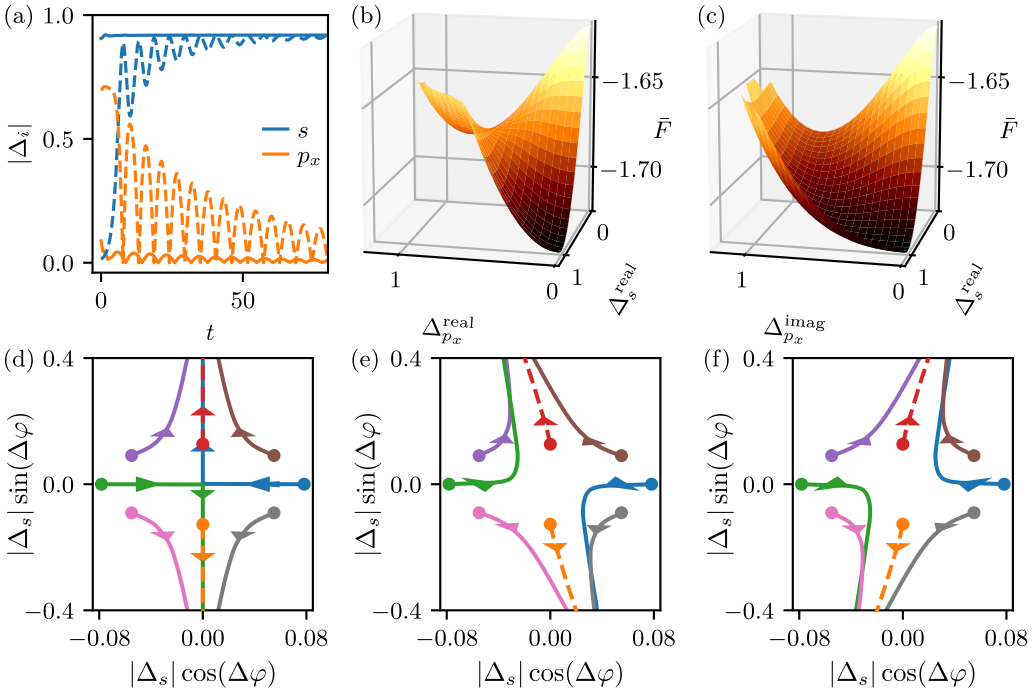

Figure 8.2: Unstable p_x-wave ordering in the square lattice model for $U = -3.3$, $V = -3$, $T = 0.05$, $\Gamma = 0.1$, $N = 20 \times 20$, $E_z = 0$ and (a)-(d) $\mu = 0$. (a) Time evolutions starting in the vicinity of the leading s-wave order (solid) or the subleading p_x-wave (dashed). In both cases, the system relaxes into the state corresponding to the leading instability. (b), (c) Free energy landscapes (Γ neglected) with a phase difference of (b) $\Delta\varphi = 0$ and (c) $\Delta\varphi = \pi/2$ revealing that p_x corresponds to a local minimum for $\Delta\varphi = 0$ but to a saddle point for $\Delta\varphi = \pi/2$. (d)-(e) Float diagram in dependence on the chemical potential with (d) $\mu = 0$, (e) $\mu = -0.1$ and (f) $\mu = 0.1$. The diagrams show the value for Δ_s with the absolute value being the radius and the phase difference denoted by the angle (real direction on x-axis and imaginary direction on y-axis). Different colors denote time evolutions for different initial displacements. While the flow occurs in the imaginary direction at half filling, the results are tilted for $\mu \neq 0$ in opposite directions for different signs of μ.

nearest-neighbor interactions are not included here. Note that in the following, we mostly use the time evolution procedure introduced in Sections 6.4 or 6.5.3, where an additional coupling Γ to an external bath is included. This bath coupling is necessary to introduce dissipation allowing for the relaxation of the system to a local or global minimum. We thus assume a finite Γ in the following. Only if free energy landscapes are shown, the bath coupling is neglected.

8.2.1 Real Order Parameters

In order to investigate the stability of real valued pairing, we simplify the model even further and neglect one of the p-waves instabilities. This leads to a model with only two competing orders. Here, we choose s and p_x-wave but the results would not change if p_y order was chosen instead. Furthermore, the parameters are tuned in a way that s-wave order is leading and present in the ground state, while the p_x-wave is subleading.
In a first step, arbitrary but small modifications to the order parameters representing one of the competing instabilities are assumed. We then check whether the system relaxes back to the close-by order or to the ground state phase. To this end, the time evolution procedure from Chapter 6 is used. Furthermore, it is assumed that the system was held in the same state (constant $\Delta_{\mathbf{k}}$) before the relaxation process which allows to calculate the collision integral needed. The results are shown in Fig. 8.2(a), where we note that the system relaxes back to the ground state in both cases. This indicated that p_x is indeed an unstable subleading order in that case.

We can confirm this behavior by investigating the free energy landscape. To this end, we again need to neglect the bath coupling Γ by setting $\Gamma = 0$ since this cannot be included in the free energy landscape as mentioned before. The free energy landscape can be computed in a four-dimensional space spanned by the real and imaginary parts of the order parameters belonging to the competing pairing channels. Since the global phase of the gap does not have a physical meaning, one of the dimensions can be eliminated. In Fig. 8.2(b),(c), there are thus two distinct two-dimensional free energy landscapes with different phase differences of (a) $\varphi = 0$ and (b) $\varphi = \pi/2$ between the orderings, leading to a total superconducting gap of (a) $\Delta_{\mathbf{k}} = \Delta_s^{\text{real}} \not{f}_{\mathbf{k},s} + \Delta_p^{\text{real}} \not{f}_{\mathbf{k},p}$ and (b) $\Delta_{\mathbf{k}} = \Delta_s^{\text{real}} \not{f}_{\mathbf{k},s} + i\Delta_p^{\text{imag}} \not{f}_{\mathbf{k},p}$. Here, we only show one of the quadrants, since the other ones are equivalent. We note that the free energy landscape strongly depends on the phase difference between the parameters. For a phase difference of 0, which is called *real* direction as mentioned above, the p_x-wave instability corresponds to a local minimum in the free energy landscape. In contrast to this, we find an unstable saddle point for a phase difference of $\pi/2$, also called *imaginary* direction, showing that the relative phase has a crucial influence on the question of stability.
Moreover, we can compute a float diagram to investigate how the unstable p_x-wave order is left. Using the same parameter set, the results are shown in Fig. 8.2(d), where distortions of the real and imaginary s-wave directions are shown on the x- and y-axis, respectively. Starting from different points in the vicinity of p_x, we note that the p_x-wave order is always left in the imaginary direction, which is in agreement with the shown free energy landscapes. Interestingly, the unstable direction gets slightly tilted in when moving away from half filling. In these cases, the float diagram is slightly rotated clockwise for $\mu > 0$ and anti-clockwise for $\mu < 0$ as shown in Figs. 8.2(e),(f).
Since it is unclear whether the same unstable behavior is found for arbitrary parameters, a more detailed analysis is taken out in the following, allowing for the determination of stability for the p_x-wave in the whole phase diagram. Here, we concentrate on the half-filled case and exploit that the most unstable direction appears to be the imaginary one.

8.2.2 Stability Criterion

In the following, an analytical stability criterion is derived in order to have more direct insights into the question of whether a subleading instability is stable or not. At the beginning, the derivation is kept general but we focus on the p_x-wave instability of the square lattice model in the end. We consider an instability with an order parameter $\Delta_{\mathbf{k}}^0$ and assume to add a small perturbation $\delta_{\mathbf{k}}$ leading to a total gap function of

$$\Delta_{\mathbf{k}} = \Delta_{\mathbf{k}}^0 + \delta_{\mathbf{k}}\,. \tag{8.21}$$

Derivative of Order Parameter

We want to compute the time derivative of the order parameter to check whether the system relaxes back to the $\Delta_{\mathbf{k}}$. In the following, we consider systems that are described by a BdG-Hamiltonian of form (6.65), which means that they only support Cooper pairs consisting of electrons with opposite spins and that they have a non-interacting part, which does not couple different spin sectors. We remind ourselves about the set of differential equations (6.82)-(6.88) including

$$\begin{aligned} i\partial_t f_{\mathbf{k}}(t) =& h_{\mathbf{k},\uparrow}(t) f_{\mathbf{k}}(t) + f_{\mathbf{k}}(t) h^{\star}_{-\mathbf{k},\downarrow}(t) - \Delta_k(t)\left(n^{\star}_{-\mathbf{k},\downarrow}(t) - 1\right) - n_{\mathbf{k},\uparrow}(t)\Delta_k^{\alpha\beta}(t) \\ & - i\Gamma\left(2f_{\mathbf{k}}(t) - I_{\mathbf{k}}^D(t)\right) \end{aligned} \tag{8.22}$$

$$\Delta_{\mathbf{k}}^{\alpha\beta}(t) = \frac{1}{N}\sum_{\mathbf{k}',\alpha',\beta'} V_{\mathbf{k},\mathbf{k}'}^{\alpha\beta,\alpha'\beta'} f_{\mathbf{k}'}^{\alpha'\beta'}(t)\,. \tag{8.23}$$

We can combine these equations to end up with the derivative of the order parameter

$$\begin{aligned} i\partial_t \Delta_{\mathbf{k}}^{\alpha\beta}(t) =& \frac{1}{N}\sum_{\mathbf{k}',\alpha',\beta'} V_{\mathbf{k},\mathbf{k}'}^{\alpha\beta,\alpha'\beta'} i\partial_t f_{\mathbf{k}'}^{\alpha'\beta'}(t) \\ =& \frac{1}{N}\sum_{\mathbf{k}',\alpha',\beta'} V_{\mathbf{k},\mathbf{k}'}^{\alpha\beta,\alpha'\beta'} \left[h_{\mathbf{k}',\uparrow}(t) f_{\mathbf{k}'}(t) + f_{\mathbf{k}'}(t) h^{\star}_{-\mathbf{k}',\downarrow}(t) - \Delta_{\mathbf{k}'}(t)\left(n^{\star}_{-\mathbf{k}',\downarrow}(t) - 1\right)\right. \end{aligned}$$

$$-n_{\mathbf{k}',\uparrow}(t)\Delta_{\mathbf{k}'}(t) - i\Gamma\left(2f_{\mathbf{k}'}(t) - I^D_{\mathbf{k}'}(t)\right)\big]_{\alpha',\beta'} \,. \tag{8.24}$$

We insert Eq. (8.21) and exploit that $\Delta^0_{\mathbf{k}}$ is a stationary solution, meaning that $\partial_t \Delta^0_{\mathbf{k}} = 0$, which leads to

$$\begin{aligned} i\partial_t \delta\Delta^{\alpha\beta}_{\mathbf{k}}(t) = \frac{1}{N}\sum_{\mathbf{k}',\alpha',\beta'} V^{\alpha\beta,\alpha'\beta'}_{\mathbf{k},\mathbf{k}'} \big[& h_{\mathbf{k}',\uparrow}(t)\delta f_{\mathbf{k}'}(t) + \delta f_{\mathbf{k}'}(t) h^\star_{-\mathbf{k}',\downarrow}(t) - \Delta^0_{\mathbf{k}'}\delta n^\star_{-\mathbf{k}',\downarrow}(t) \\ & -\delta\Delta_{\mathbf{k}'}(t)\left(n^\star_{-\mathbf{k}',\downarrow}(t) - 1\right) - n_{\mathbf{k}',\uparrow}(t)\delta\Delta_{\mathbf{k}'}(t) - \delta n_{\mathbf{k}',\uparrow}(t)\Delta^0_{\mathbf{k}'} - i\Gamma\left(2\delta f_{\mathbf{k}'}(t) - \delta I^D_{\mathbf{k}'}(t)\right)\big]_{\alpha',\beta'} \,. \end{aligned} \tag{8.25}$$

in leading order, where

$$\begin{aligned} &\delta n_{\mathbf{k}} = n_{\mathbf{k}} - n^0_{\mathbf{k}}\,, \quad \delta f_{\mathbf{k}} = f_{\mathbf{k}} - f^0_{\mathbf{k}}\,, \quad \delta\Delta_{\mathbf{k}} = \frac{1}{N}\sum_{\mathbf{k}'} V_{\mathbf{k},\mathbf{k}'} f_{\mathbf{k}'} - \Delta^0_{\mathbf{k}} = \frac{1}{N}\sum_{\mathbf{k}'} V_{\mathbf{k},\mathbf{k}'}\delta f_{\mathbf{k}'}\,, \\ &\delta I^D_{\mathbf{k}} = I^D_{\mathbf{k}}\Big|_{\Delta^0_{\mathbf{k}}+\delta\Delta_{\mathbf{k}}} - I^D_{\mathbf{k}}\Big|_{\Delta^0_{\mathbf{k}}}\,. \end{aligned} \tag{8.26}$$

Here, we find $\delta\Delta_{\mathbf{k}} \neq \delta_{\mathbf{k}}$ since we are not at equilibrium solution at this point and therefore, the gap equation is not fulfilled. Furthermore, we assume that the system was held in the same state (constant $\Delta_{\mathbf{k}}$) since $t = -\infty$ for the calculation of the collision integral.
We note that this expression is the general form of the derivative of $\Delta_{\mathbf{k}}$ for systems described by a BdG-Hamiltonian of form (6.65). For a further analysis we need expressions for $n_{\mathbf{k},\sigma}$, $f_{\mathbf{k}}$, $\delta n_{\mathbf{k},\sigma}$, $\delta f_{\mathbf{k}}$, $\delta I^D_{\mathbf{k}}$ in linear order in $\delta_{\mathbf{k}}$.

Analytical Expressions in Diagonal Basis

In order to find analytical expressions for $n_{\mathbf{k}}$, $f_{\mathbf{k}}$ and $I^D_{\mathbf{k}}$, we first calculate expressions for the diagonal versions for the matrices $N_{\mathbf{k}}$ and $I_{\mathbf{k}} \coloneqq I^K_{\mathbf{k}}$, defined via Eqs. (6.79) and (6.80), respectively. We thus calculate the matrix elements $N(E)$ and $I(E)$ of the diagonal matrices for eigenvalues E of the BdG Hamiltonian.
For $N(E)$, this venture is straightforward, since we have already identified the analytical expression (6.39) for $G^<(E, \Delta t = 0)$ in Subsection 6.3.3. Inserting this result leads to

$$\begin{aligned} N(E) =& \frac{1}{i}G^<(E,\Delta t=0) \\ =& \frac{1}{2} - \frac{1}{2}\Bigg\{ \tanh\left(\frac{\beta}{2}(E+i\Gamma)\right) + \frac{2}{\beta}\frac{2i\Gamma}{\left(i\frac{\pi}{\beta} - E\right)^2 + \Gamma^2} \\ & + \frac{1}{i\pi}\left[\Psi\left(1 + \frac{1}{2} + \Gamma\frac{\beta}{2\pi} + iE\frac{\beta}{2\pi}\right) - \Psi\left(1 + \frac{1}{2} - \Gamma\frac{\beta}{2\pi} + iE\frac{\beta}{2\pi}\right)\right]\Bigg\}\,. \end{aligned} \tag{8.27}$$

We now focus on the analytic expression of the integral $I(E)$. Here, we find

$$\begin{aligned} I(E) &= \frac{1}{2\Gamma}\int_0^\infty d\tau \left[G^R(E,\Delta t=\tau) + G^R(E,\Delta t=\tau)^\dagger\right]\Sigma^K(\tau) \\ &= \int_0^\infty d\tau(-i)\left(e^{(-iE-\Gamma)\tau} + e^{(+iE-\Gamma)\tau}\right)\left[\beta\sinh\left(\frac{\pi\tau}{\beta}\right)\right]^{-1} \\ &= -\frac{i}{\pi}\int_0^\infty dx\left(e^{(-iE-\Gamma)\frac{\beta}{\pi}x} + e^{(+iE-\Gamma)\frac{\beta}{\pi}x}\right)[\sinh(x)]^{-1} \\ &= -\frac{i}{\pi}\int_0^\infty dx\, 2\,\mathrm{Re}\left[\left(e^{-(iE+\Gamma)\frac{\beta}{\pi}x}\right)[\sinh(x)]^{-1}\right] \\ &= 2\lim_{t\to 0}\mathrm{Re}\left[-\frac{i}{\pi}\int_t^\infty dx\left(e^{-(iE+\Gamma)\frac{\beta}{\pi}x}\right)[\sinh(x)]^{-1}\right] \end{aligned}$$

$$= 2 \lim_{t\to 0} \mathrm{Re}\left[-\frac{i}{\pi} \frac{-2e^{t-(\Gamma+iE)t}\, {}_2F_1\left(1, \frac{1}{2} - \frac{(\Gamma+iE)}{2}, \frac{3}{2} - \frac{(\Gamma+iE)}{2}, e^{2t}\right)}{-1+(\Gamma+iE)} + i^{1+(\Gamma+iE)} \frac{\pi}{\cos\left(\frac{(\Gamma+iE)\pi}{2}\right)} \right]. \tag{8.28}$$

Basis Transformation to Original Basis

As mentioned above, the calculation has so far been quite general. In order to further evolve an analytical expression, we exploit that we want to analyze real valued pairing for the square lattice model with real valued pairing orders. In the following, we thus consider

- only one-band models, simplifying $h_{\mathbf{k},\sigma}$, $\Delta^0_{\mathbf{k}}$, $n_{\mathbf{k},\sigma}$, $\delta\Delta_{\mathbf{k}}$, $\delta n_{\mathbf{k},\sigma}$, $\delta f_{\mathbf{k}}$, $\delta I^D_{\mathbf{k}}$ to scalars,
- instabilities that are both "real", meaning that $\not{f}_{i,\mathbf{k}}$ can be chosen to be real for all $\mathbf{k}$.

Moreover, we can fix $\Delta^0_{\mathbf{k}}$ to be real for all $\mathbf{k}$ which corresponds to setting the unimportant global phase to a fixed value. In order to arrive at the most general form possible, we assume the form of arbitrary one-band model from Eq. (8.2)

$$\mathcal{H}_{\mathrm{BdG}}(\mathbf{k}) = \begin{pmatrix} \epsilon_{\mathbf{k}} + \gamma_{\mathbf{k}} & \Delta_{\mathbf{k}} \\ \Delta^\dagger_{\mathbf{k}} & -\epsilon_{\mathbf{k}} + \gamma_{\mathbf{k}} \end{pmatrix}, \tag{8.29}$$

allowing us to replace

$$h_{\mathbf{k},\uparrow} = \epsilon_{\mathbf{k}} + \gamma_{\mathbf{k}}\,, \quad h_{-\mathbf{k},\downarrow} = \epsilon_{\mathbf{k}} - \gamma_{\mathbf{k}} \tag{8.30}$$

for the non-interacting part of the Hamiltonian.
For this BdG Hamiltonian, the eigenvalues and eigenvectors can be explicitly computed and we obtain

$$E_{\mathbf{k},1} = \gamma_{\mathbf{k}} + \sqrt{\epsilon^2_{\mathbf{k}} + \Delta^2_{\mathbf{k}}}\,, \quad E_{\mathbf{k},2} = \gamma_{\mathbf{k}} - \sqrt{\epsilon^2_{\mathbf{k}} + \Delta^2_{\mathbf{k}}} \tag{8.31}$$

for the eigenvalues as well as

$$\mathbf{v}_{\mathbf{k},1} = \begin{bmatrix} -\frac{\Delta_{\mathbf{k}}}{\sqrt{2(\Delta^2_{\mathbf{k}}+\epsilon^2_{\mathbf{k}}) - 2\epsilon_{\mathbf{k}}\sqrt{\Delta^2_{\mathbf{k}}+\epsilon^2_{\mathbf{k}}}}} \\ \frac{\epsilon_{\mathbf{k}} - \sqrt{\Delta^2_{\mathbf{k}}+\epsilon^2_{\mathbf{k}}}}{\sqrt{2(\Delta^2_{\mathbf{k}}+\epsilon^2_{\mathbf{k}}) - 2\epsilon_{\mathbf{k}}\sqrt{\Delta^2_{\mathbf{k}}+\epsilon^2_{\mathbf{k}}}}} \end{bmatrix}, \quad \mathbf{v}_{\mathbf{k},1} = \begin{bmatrix} -\frac{\Delta_{\mathbf{k}}}{\sqrt{2(\Delta^2_{\mathbf{k}}+\epsilon^2_{\mathbf{k}}) + 2\epsilon_{\mathbf{k}}\sqrt{\Delta^2_{\mathbf{k}}+\epsilon^2_{\mathbf{k}}}}} \\ \frac{\epsilon_{\mathbf{k}} + \sqrt{\Delta^2_{\mathbf{k}}+\epsilon^2_{\mathbf{k}}}}{\sqrt{2(\Delta^2_{\mathbf{k}}+\epsilon^2_{\mathbf{k}}) + 2\epsilon_{\mathbf{k}}\sqrt{\Delta^2_{\mathbf{k}}+\epsilon^2_{\mathbf{k}}}}} \end{bmatrix}. \tag{8.32}$$

Furthermore, we define the matrix

$$V_{\mathbf{k}} = \begin{bmatrix} \mathbf{v}_{\mathbf{k},1} & \mathbf{v}_{\mathbf{k},2} \end{bmatrix} \tag{8.33}$$

to allow for transformations between the original and the diagonal basis of the BdG Hamiltonian.

Results for $\delta n_{\mathbf{k}}$ and $\delta f_{\mathbf{k}}$

Using the eigenvalues and eigenvectors, we can write the change of the matrix $N_{\mathbf{k}}$ compared to the equilibrium position in first order in $\delta_{\mathbf{k}}$ as

$$\delta N_{\mathbf{k}} = V^0_{\mathbf{k}} \cdot \bar{N}^0_{\mathbf{k}} \cdot \delta V^\dagger_{\mathbf{k}} + V^0_{\mathbf{k}} \cdot \delta\bar{N}_{\mathbf{k}} \cdot \left(V^0_{\mathbf{k}}\right)^\dagger + \delta V_{\mathbf{k}} \cdot \bar{N}^0_{\mathbf{k}} \cdot \left(V^0_{\mathbf{k}}\right)^\dagger \tag{8.34}$$

with $\bar{N}_{\mathbf{k}}$ denoting the diagonal matrix of $N_{\mathbf{k}}$. $V^0_{\mathbf{k}}$, $\bar{N}^0_{\mathbf{k}}$ denote the matrices at the equilibrium position; and $\delta\bar{N}_{\mathbf{k}}$ and $\delta V_{\mathbf{k}}$ are the linear order contribution in $\delta_{\mathbf{k}}$ of $\bar{N}_{\mathbf{k}}$ and $V_{\mathbf{k}}$, respectively. These can be obtained by expanding the matrices $V_{\mathbf{k}}$ and $\bar{N}_{\mathbf{k}}$ in $\delta_{\mathbf{k}}$, which yields $V_{\mathbf{k}} = V^0_{\mathbf{k}} + \delta V_{\mathbf{k}} + \mathcal{O}(\delta^2_{\mathbf{k}})$ and $\bar{N}_{\mathbf{k}} = \bar{N}^0_{\mathbf{k}} + \delta\bar{N}_{\mathbf{k}} + \mathcal{O}(\delta^2_{\mathbf{k}})$ with

$$V^0_{\mathbf{k}} = \begin{bmatrix} -\frac{\Delta^0_{\mathbf{k}}}{\sqrt{2\left[(\Delta^0_{\mathbf{k}})^2+\epsilon^2_{\mathbf{k}}\right] - 2\epsilon_{\mathbf{k}}\sqrt{(\Delta^0_{\mathbf{k}})^2+\epsilon^2_{\mathbf{k}}}}} & -\frac{\Delta^0_{\mathbf{k}}}{\sqrt{2\left[(\Delta^0_{\mathbf{k}})^2+\epsilon^2_{\mathbf{k}}\right] + 2\epsilon_{\mathbf{k}}\sqrt{(\Delta^0_{\mathbf{k}})^2+\epsilon^2_{\mathbf{k}}}}} \\ \frac{\epsilon_{\mathbf{k}} - \sqrt{(\Delta^0_{\mathbf{k}})^2+\epsilon^2_{\mathbf{k}}}}{\sqrt{2\left[(\Delta^0_{\mathbf{k}})^2+\epsilon^2_{\mathbf{k}}\right] - 2\epsilon_{\mathbf{k}}\sqrt{(\Delta^0_{\mathbf{k}})^2+\epsilon^2_{\mathbf{k}}}}} & -\frac{\epsilon_{\mathbf{k}} + \sqrt{(\Delta^0_{\mathbf{k}})^2+\epsilon^2_{\mathbf{k}}}}{\sqrt{2\left[(\Delta^0_{\mathbf{k}})^2+\epsilon^2_{\mathbf{k}}\right] + 2\epsilon_{\mathbf{k}}\sqrt{(\Delta^0_{\mathbf{k}})^2+\epsilon^2_{\mathbf{k}}}}} \end{bmatrix}, \tag{8.35}$$

$$\delta V_{\mathbf{k}} = i\,\mathrm{Im}(\delta_{\mathbf{k}}) \begin{bmatrix} \frac{-1}{\sqrt{2\left[(\Delta^0_{\mathbf{k}})^2+\epsilon^2_{\mathbf{k}}\right]-2\epsilon_{\mathbf{k}}\sqrt{(\Delta^0_{\mathbf{k}})^2+\epsilon^2_{\mathbf{k}}}}} & \frac{-1}{\sqrt{2\left[(\Delta^0_{\mathbf{k}})^2+\epsilon^2_{\mathbf{k}}\right]+2\epsilon_{\mathbf{k}}\sqrt{(\Delta^0_{\mathbf{k}})^2+\epsilon^2_{\mathbf{k}}}}} \\ 0 & 0 \end{bmatrix}$$
$$+\mathrm{Re}(\delta_{\mathbf{k}}) \begin{bmatrix} \frac{\epsilon_{\mathbf{k}}((\Delta^0_{\mathbf{k}})^2+2\epsilon^2_{\mathbf{k}}-2\epsilon_{\mathbf{k}}\sqrt{(\Delta^0_{\mathbf{k}})^2+\epsilon^2_{\mathbf{k}}})}{\sqrt{(\Delta^0_{\mathbf{k}})^2+\epsilon^2_{\mathbf{k}}}(2\left[(\Delta^0_{\mathbf{k}})^2+\epsilon^2_{\mathbf{k}}\right]-2\epsilon_{\mathbf{k}}\sqrt{(\Delta^0_{\mathbf{k}})^2+\epsilon^2_{\mathbf{k}}})^{3/2}} & \frac{-\epsilon_{\mathbf{k}}((\Delta^0_{\mathbf{k}})^2+2\epsilon^2_{\mathbf{k}}+2\epsilon_{\mathbf{k}}\sqrt{(\Delta^0_{\mathbf{k}})^2+\epsilon^2_{\mathbf{k}}})}{\sqrt{(\Delta^0_{\mathbf{k}})^2+\epsilon^2_{\mathbf{k}}}(2\left[(\Delta^0_{\mathbf{k}})^2+\epsilon^2_{\mathbf{k}}\right]+2\epsilon_{\mathbf{k}}\sqrt{(\Delta^0_{\mathbf{k}})^2+\epsilon^2_{\mathbf{k}}})^{3/2}} \\ \frac{\epsilon_{\mathbf{k}}\Delta(\epsilon^2_{\mathbf{k}}-\epsilon_{\mathbf{k}}\sqrt{(\Delta^0_{\mathbf{k}})^2+\epsilon^2_{\mathbf{k}}})}{\sqrt{(\Delta^0_{\mathbf{k}})^2+\epsilon^2_{\mathbf{k}}}(2\left[(\Delta^0_{\mathbf{k}})^2+\epsilon^2_{\mathbf{k}}\right]-2\epsilon_{\mathbf{k}}\sqrt{(\Delta^0_{\mathbf{k}})^2+\epsilon^2_{\mathbf{k}}})^{3/2}} & \frac{-\epsilon_{\mathbf{k}}\Delta(\epsilon^2_{\mathbf{k}}+\epsilon_{\mathbf{k}}\sqrt{(\Delta^0_{\mathbf{k}})^2+\epsilon^2_{\mathbf{k}}})}{\sqrt{(\Delta^0_{\mathbf{k}})^2+\epsilon^2_{\mathbf{k}}}(2\left[(\Delta^0_{\mathbf{k}})^2+\epsilon^2_{\mathbf{k}}\right]+2\epsilon_{\mathbf{k}}\sqrt{(\Delta^0_{\mathbf{k}})^2+\epsilon^2_{\mathbf{k}}})^{3/2}} \end{bmatrix}, \tag{8.36}$$

$$\bar{N}^0 = \begin{bmatrix} N(E^0_{\mathbf{k},1}) & 0 \\ 0 & N(E^0_{\mathbf{k},2}) \end{bmatrix}, \tag{8.37}$$

$$\delta\bar{N} = \mathrm{Re}(\delta_{\mathbf{k}}) \begin{bmatrix} \partial_E N(E^0_{\mathbf{k},1}) \frac{\Delta^0_{\mathbf{k}}}{\sqrt{(\Delta^0_{\mathbf{k}})^2+\epsilon^2_{\mathbf{k}}}} & 0 \\ 0 & -\partial_E N(E^0_{\mathbf{k},2}) \frac{\Delta^0_{\mathbf{k}}}{\sqrt{(\Delta^0_{\mathbf{k}})^2+\epsilon^2_{\mathbf{k}}}} \end{bmatrix}. \tag{8.38}$$

Here, $E^0_{\mathbf{k},i}$ denote the eigenvalues of the BdG Hamiltonian at the equilibrium position.
Additionally, the zeroth order contribution of $N_{\mathbf{k}}$ can be obtained via $N^0_{\mathbf{k}} = V^0_{\mathbf{k}}\bar{N}_{\mathbf{k}}(V^0_{\mathbf{k}})^\dagger$ leading to

$$\left[N^0_{\mathbf{k}}\right]_{0,0} = \frac{N(E^0_{\mathbf{k},1})\left[(\Delta^0_{\mathbf{k}})^2+\epsilon^2_{\mathbf{k}}+\epsilon_{\mathbf{k}}\sqrt{(\Delta^0_{\mathbf{k}})^2+\epsilon^2_{\mathbf{k}}}\right] + N(E^0_{\mathbf{k},2})\left[(\Delta^0_{\mathbf{k}})^2+\epsilon^2_{\mathbf{k}}-\epsilon_{\mathbf{k}}\sqrt{(\Delta^0_{\mathbf{k}})^2+\epsilon^2_{\mathbf{k}}}\right]}{2\left[(\Delta^0_{\mathbf{k}})^2+\epsilon^2_{\mathbf{k}}\right]}, \tag{8.39}$$

$$\left[N^0_{\mathbf{k}}\right]_{0,1} = \left[N^0_{\mathbf{k}}\right]_{1,0} = \frac{\left[N(E^0_{\mathbf{k},1}) - N(E^0_{\mathbf{k},2})\right]\Delta_{\mathbf{k}}}{2\sqrt{(\Delta^0_{\mathbf{k}})^2+\epsilon^2_{\mathbf{k}}}}, \tag{8.40}$$

$$\left[N^0_{\mathbf{k}}\right]_{1,1} = \frac{N(E^0_{\mathbf{k},1})\left[(\Delta^0_{\mathbf{k}})^2+\epsilon^2_{\mathbf{k}}-\epsilon_{\mathbf{k}}\sqrt{(\Delta^0_{\mathbf{k}})^2+\epsilon^2_{\mathbf{k}}}\right] + N(E^0_{\mathbf{k},2})\left[(\Delta^0_{\mathbf{k}})^2+\epsilon^2_{\mathbf{k}}+\epsilon_{\mathbf{k}}\sqrt{(\Delta^0_{\mathbf{k}})^2+\epsilon^2_{\mathbf{k}}}\right]}{2\left[(\Delta^0_{\mathbf{k}})^2+\epsilon^2_{\mathbf{k}}\right]}. \tag{8.41}$$

We now exploit the knowledge from our empirical study of the p_x-wave order in the chosen square lattice model. Here, we noted in the float diagram shown in Fig. 8.2(d), that the most unstable direction is on the imaginary axis for the half-filled case. In the following we therefore consider an imaginary $\delta_{\mathbf{k}}$.
This assumption dramatically simplifies the calculation, since $\delta\bar{N} = 0$ and

$$\delta V = \begin{bmatrix} \frac{-\delta_{\mathbf{k}}}{\sqrt{2\left[(\Delta^0_{\mathbf{k}})^2+\epsilon^2_{\mathbf{k}}\right]-2\epsilon_{\mathbf{k}}\sqrt{(\Delta^0_{\mathbf{k}})^2+\epsilon^2_{\mathbf{k}}}}} & \frac{-\delta_{\mathbf{k}}}{\sqrt{2\left[(\Delta^0_{\mathbf{k}})^2+\epsilon^2_{\mathbf{k}}\right]+2\epsilon_{\mathbf{k}}\sqrt{(\Delta^0_{\mathbf{k}})^2+\epsilon^2_{\mathbf{k}}}}} \\ 0 & 0 \end{bmatrix}. \tag{8.42}$$

We thus obtain the first order contribution

$$\delta N_{\mathbf{k}} = V_{\mathbf{k}}\bar{N}_{\mathbf{k}}\delta V^\dagger_{\mathbf{k}} + \delta V_{\mathbf{k}}\bar{N}_{\mathbf{k}}V^\dagger_{\mathbf{k}} = \delta_{\mathbf{k}} \begin{bmatrix} 0 & \frac{N(E^0_{\mathbf{k},1})-N(E^0_{\mathbf{k},2})}{2\sqrt{(\Delta^0_{\mathbf{k}})^2+\epsilon^2_{\mathbf{k}}}} \\ -\frac{N(E^0_{\mathbf{k},1})-N(E^0_{\mathbf{k},2})}{2\sqrt{(\Delta^0_{\mathbf{k}})^2+\epsilon^2_{\mathbf{k}}}} & 0 \end{bmatrix}, \tag{8.43}$$

which, in combination with Eqs. (8.39)-(8.41), leads to

$$\delta n_{\mathbf{k},\sigma} = 0, \tag{8.44}$$

$$\delta f_{\mathbf{k}} = \delta_{\mathbf{k}} \frac{N(E^0_{\mathbf{k},1}) - N(E^0_{\mathbf{k},2})}{2\sqrt{(\Delta^0_{\mathbf{k}})^2+\epsilon^2_{\mathbf{k}}}}, \tag{8.45}$$

$$\delta\Delta_{\mathbf{k}} = \frac{1}{N}\sum_{\mathbf{k}'} V_{\mathbf{k},\mathbf{k}'}\delta f_{\mathbf{k}'} = \frac{1}{N}\sum_{\mathbf{k}'} V_{\mathbf{k},\mathbf{k}'}\delta_{\mathbf{k}'} \frac{N(E^0_{\mathbf{k}',1}) - N(E^0_{\mathbf{k}',2})}{2\sqrt{\Delta^2_{\mathbf{k}'}+\epsilon^2_{\mathbf{k}'}}}, \tag{8.46}$$

$$n_{\mathbf{k},\uparrow} = \frac{N(E^0_{\mathbf{k},1})\left[(\Delta^0_{\mathbf{k}})^2+\epsilon^2_{\mathbf{k}}+\epsilon_{\mathbf{k}}\sqrt{(\Delta^0_{\mathbf{k}})^2+\epsilon^2_{\mathbf{k}}}\right] + N(E_{\mathbf{k},2})\left[(\Delta^0_{\mathbf{k}})^2+\epsilon^2_{\mathbf{k}}-\epsilon_{\mathbf{k}}\sqrt{(\Delta^0_{\mathbf{k}})^2+\epsilon^2_{\mathbf{k}}}\right]}{2\left[(\Delta^0_{\mathbf{k}})^2+\epsilon^2_{\mathbf{k}}\right]}, \tag{8.47}$$

$$1-n^*_{-\mathbf{k},\downarrow}=\frac{N(E^0_{\mathbf{k},1})\left[(\Delta^0_{\mathbf{k}})^2+\epsilon^2_{\mathbf{k}}-\epsilon_{\mathbf{k}}\sqrt{(\Delta^0_{\mathbf{k}})^2+\epsilon^2_{\mathbf{k}}}\right]+N(E^0_{\mathbf{k},2})\left[(\Delta^0_{\mathbf{k}})^2+\epsilon^2_{\mathbf{k}}+\epsilon_{\mathbf{k}}\sqrt{(\Delta^0_{\mathbf{k}})^2+\epsilon^2_{\mathbf{k}}}\right]}{2\left[(\Delta^0_{\mathbf{k}})^2+\epsilon^2_{\mathbf{k}}\right]} \tag{8.48}$$

in first and zeroth order in $\delta_{\mathbf{k}}$.

Results for $I^D_{\mathbf{k}}$

The result for $\delta I^D_{\mathbf{k}}$ can be obtained in a similar way. We note due to Eq. (8.26) that the change of the integral arises from $\delta\Delta_{\mathbf{k}}$. We thus replace $\delta_{\mathbf{k}}$ with $\delta\Delta_{\mathbf{k}}$ in Eq. (8.36) and denote the result with $\delta V'_{\mathbf{k}}$. Importantly, the result is still linear in $\delta_{\mathbf{k}}$, since we consider only its first order contribution to $\delta\Delta_{\mathbf{k}}$, defined via Eq. (8.46).
In the following, the results are again obtained for an imaginary $\delta_{\mathbf{k}}$ (directly yielding an imaginary $\delta\Delta_{\mathbf{k}}$ in first order), which leads to $\delta\bar{I}=0$ and

$$\delta V'=\begin{bmatrix} \frac{-\delta\Delta_{\mathbf{k}}}{\sqrt{2\left[(\Delta^0_{\mathbf{k}})^2+\epsilon^2_{\mathbf{k}}\right]-2\epsilon_{\mathbf{k}}\sqrt{(\Delta^0_{\mathbf{k}})^2+\epsilon^2_{\mathbf{k}}}}} & \frac{-\delta\Delta_{\mathbf{k}}}{\sqrt{2\left[(\Delta^0_{\mathbf{k}})^2+\epsilon^2_{\mathbf{k}}\right]+2\epsilon_{\mathbf{k}}\sqrt{(\Delta^0_{\mathbf{k}})^2+\epsilon^2_{\mathbf{k}}}}} \\ 0 & 0 \end{bmatrix}. \tag{8.49}$$

The change of the whole integral matrix I can then be calculated using

$$\delta I_{\mathbf{k}}=V^0_{\mathbf{k}}\bar{I}^0_{\mathbf{k}}\delta V'^{\dagger}_{\mathbf{k}}+\delta V'_{\mathbf{k}}\bar{I}^0_{\mathbf{k}}\left(V^0_{\mathbf{k}}\right)^{\dagger}=\delta\Delta_{\mathbf{k}}\begin{bmatrix} 0 & \frac{I(E^0_{\mathbf{k},1})-I(E^0_{\mathbf{k},2})}{2\sqrt{(\Delta^0_{\mathbf{k}})^2+\epsilon^2_{\mathbf{k}}}} \\ -\frac{I(E^0_{\mathbf{k},1})-I(E^0_{\mathbf{k},2})}{2\sqrt{(\Delta^0_{\mathbf{k}})^2+\epsilon^2_{\mathbf{k}}}} & 0 \end{bmatrix} \tag{8.50}$$

leading to

$$\delta I^D_{\mathbf{k}}=\delta\Delta_{\mathbf{k}}\frac{I(E^0_{\mathbf{k},1})-I(E^0_{\mathbf{k},2})}{2\sqrt{(\Delta^0_{\mathbf{k}})^2+\epsilon^2_{\mathbf{k}}}}\,. \tag{8.51}$$

Final Results

We insert our results into the derivative (8.25) (details can be found in Appendix B) to obtain

$$\begin{aligned} i\partial_t\delta\Delta_{\mathbf{k}}=&\frac{1}{N}\sum_{\mathbf{k}'}V_{\mathbf{k},\mathbf{k}'}\epsilon_{\mathbf{k}'}\frac{N(E^0_{\mathbf{k}',1})-N(E^0_{\mathbf{k}',2})}{\sqrt{(\Delta^0_{\mathbf{k}'})^2+\epsilon^2_{\mathbf{k}'}}}\left(\delta_{\mathbf{k}'}-\delta\Delta_{\mathbf{k}'}\right)\\ &-2i\Gamma\left(1-\frac{1}{2N}\sum_{\mathbf{k}'}V_{\mathbf{k},\mathbf{k}'}\frac{I(E^0_{\mathbf{k}',1})-I(E^0_{\mathbf{k}',2})}{2\sqrt{(\Delta^0_{\mathbf{k}'})^2+\epsilon^2_{\mathbf{k}'}}}\right)\delta\Delta_{\mathbf{k}'}\,. \end{aligned} \tag{8.52}$$

as the final result.
We can simplify this expression even further for the square lattice model under consideration. Here, we want to investigate the stability of the p_x-wave order in direction of the s-wave. Therefore, we only consider a distortion in the s-wave component of the gap and replace $\delta_{\mathbf{k}}=\delta$ and $\delta\Delta_{\mathbf{k}}=\delta\Delta$.[1] This leads to

$$i\partial_t\delta\Delta=\frac{U}{N}\sum_{\mathbf{k}'}\epsilon_{\mathbf{k}'}\frac{N(E^0_{\mathbf{k}',1})-N(E^0_{\mathbf{k}',2})}{\sqrt{(\Delta^0_{\mathbf{k}'})^2+\epsilon^2_{\mathbf{k}'}}}\left(\delta-\delta\Delta\right)-2i\Gamma\left(1-\frac{U}{2N}\sum_{\mathbf{k}'}\frac{I(E^0_{\mathbf{k}',1})-I(E^0_{\mathbf{k}',2})}{2\sqrt{(\Delta^0_{\mathbf{k}'})^2+\epsilon^2_{\mathbf{k}'}}}\right)\delta\Delta\,. \tag{8.53}$$

We note that the first part vanishes at half filling, while it remains finite for finite μ, which is in agreement with the float diagrams found in Fig. 8.2(d)-(e).
For the half-filled case, we can thus write

$$\partial_t\delta\Delta=-2\Gamma\left(1-\frac{U}{4N}\sum_{\mathbf{k}'}\frac{I(E^0_{\mathbf{k}',1})-I(E^0_{\mathbf{k}',2})}{\sqrt{(\Delta^0_{\mathbf{k}'})^2+\epsilon^2_{\mathbf{k}'}}}\right)\delta\Delta\,. \tag{8.54}$$

[1] We note that $\delta\Delta_{\mathbf{k}}$ is only non-zero in the s-wave component up to linear order, if $\delta_{\mathbf{k}}$ is of s-wave character.

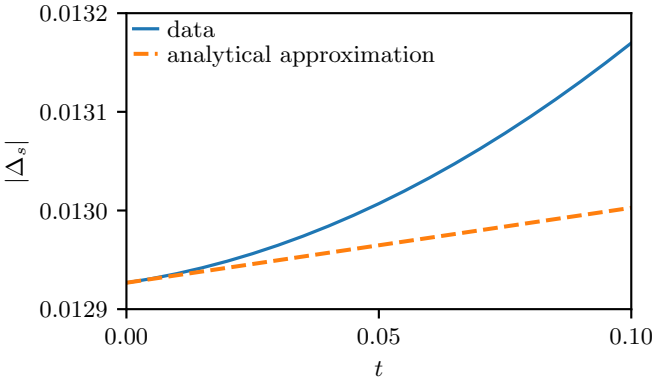

Figure 8.3: Comparison of the analytical approximation with the actual data. The approximation perfectly matches the initial slope, indicating that the initial derivative is correctly described by Eq. (8.54). The parameters are $U = -3.3$, $U' = -3$, $N = 21 \times 21$, $T = 0.05$, $\Gamma = 0.1$.

We can check this result by comparing it with numerical data. To this end, results starting from the vicinity of the p_x-wave with a small imaginary s-wave distortion are shown in Fig. 8.3. We additionally add a line showing the exponential function that the approximation (8.54) yields. We note that the approximation indeed perfectly fits the slope at the beginning and it therefore provides the correct result for the initial derivative. After this, there are deviations that arise due to higher order contributions and due to the fact that the approximation does not use the correct collision integral anymore as we assumed that the system was held in the same state (constant $\Delta_{\mathbf{k}}$) since $t = -\infty$ for its calculation.
From Eq. (8.54), one obtains that the subleading p_x-wave instability is only stable if

$$\alpha = -2\Gamma \left(1 - \frac{U}{4N} \sum_{\mathbf{k}'} \frac{I(E^0_{\mathbf{k}',1}) - I(E^0_{\mathbf{k}',2})}{\sqrt{(\Delta^0_{\mathbf{k}'})^2 + \epsilon^2_{\mathbf{k}'}}} \right) < 0 \,. \tag{8.55}$$

and we define the critical value for the local interaction as

$$U_c = \frac{1}{\frac{1}{4N} \sum_{\mathbf{k}'} \frac{I(E^0_{\mathbf{k}',1}) - I(E^0_{\mathbf{k}',2})}{\sqrt{(\Delta^0_{\mathbf{k}'})^2 + \epsilon^2_{\mathbf{k}'}}}} \,. \tag{8.56}$$

Phase Diagrams

By employing this result, we obtain the regions of stability for p_x and show them in Fig. 8.4. Here, an odd system size was used in both dimensions to ensure $(\Delta^0_{\mathbf{k}'})^2 + \epsilon^2_{\mathbf{k}'} \neq 0$. The different lines denote U_c for different temperatures and p_x is stable only in the region to the right of these stability lines. Moreover, we obtained the leading instability by comparing the critical temperatures. This assumes that there is no second transition temperature where a transition between the different superconducting orders occurs. Importantly, small changes to the phase boundary at lower temperatures due to additional transition temperatures are insignificant for the results shown below since the stability directly at the phase boundary is only discussed at the critical temperature. In this case, the critical temperature is the correct criterion. Therefore, we can employ the critical temperature as the criterion for the leading instability in the remainder of this chapter. Based on this criterion, we find regions with leading s-wave (red) or leading p-wave (dark blue) and a phase boundary (grey), where the critical temperatures agree within the chosen revolution.
In Fig. 8.4(a) the phase diagram is shown in the case of $E_z = 0$. We note that there is no overlap between the stable region and the regime, where p_x is subleading. In the limit of $\Gamma \to 0$, this is in perfect agreement with the no-go theorem derived above in Section 8.1. However, the case of finite Γ was in principle not included in the no-go theorem since the derivation was performed using the free energy of a system without dissipation. In the present example, we note that the inclusion of a finite coupling to an external bath does not yield a subleading metastable instability either. Interestingly, there are regions, where p_x appears to be leading and unstable. Here, there

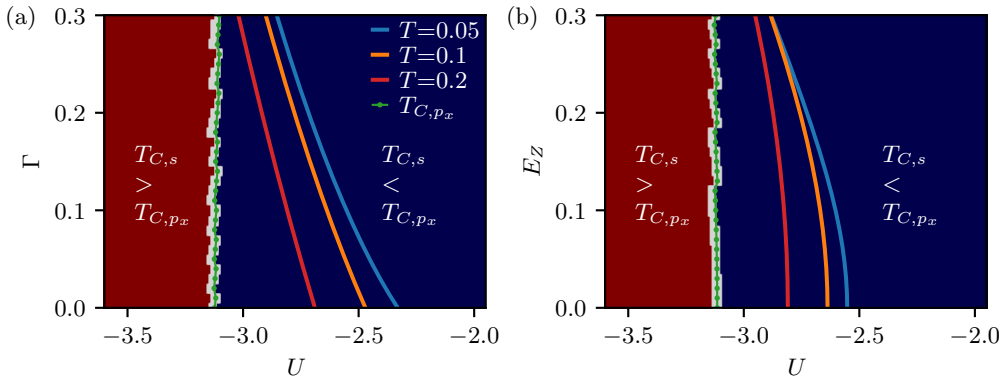

Figure 8.4: Phase diagrams for the half filled square lattice model in the presence of s- and p_x-wave instabilities as a function of the local interaction U and (a) the bath coupling Γ or (b) the Zeeman energy E_z. The leading order is determined via the critical temperature. The other parameters are given by $U' = -3$, $\mu = 0$, $N = 21 \times 21$ and (a) $E_z = 0$ or (b) $\Gamma = 0$. The lines indicate the critical U_c from Eq. (8.56), above which p_x is stable. For T_{C,p_x} the largest temperature yielding a p_x-wave order solution of the gap equation, within the resolution of $\Delta T = 0.01$, is used and, in this case, U_c was only calculated at discrete points, where the critical temperature T_{C,p_x} is known. p_x-wave order appears to never be subleading and (meta-)stable at the same time.

is a global minimum formed by a mixed state of s and p_x with an even lower energy in which the system relaxes. The region of stability gets enhanced, when the temperature gets increased. At the critical temperature of p_x, which is here defined as the largest temperature solving the gap equation within the chosen resolution of $\Delta T = 0.01$, the stability line appears on the phase transition line within the chosen resolutions. This means, that in this case, the region where p_x is stable perfectly aligns with the region, where p_x is the leading instability.
In Fig. 8.4(b) the same results are obtained in dependence on the Zeeman energy. In this case, the no-go theorem is also not applicable since the time reversal symmetry of the non-interacting part of the Hamiltonian is broken. Remarkably, we find comparable results in the presence of a finite Zeeman term. Once again, it is not possible to find a stable but subleading p_x-wave order. Additionally, the phase transition line agrees with U_c within the chosen resolution when the temperature is set to the value of the critical temperature of p_x.

8.2.3 Numerical Determination of Stability

In the section above, we obtained an analytical stability criterion for the p_x-wave of the square lattice model from Eqs. (8.19) and (8.20). Nevertheless, this criterion is not applicable to arbitrary instabilities, such as the complex valued pairing orders that are studied below. Here, it is still possible to investigate the stability by evaluating the corresponding derivatives numerically. In the following, we derive an approach that can be employed for general models and pairing channels (including models with various bands and same spin pairing).

To this end, we need to calculate the matrix A from the relation

$$\partial_t \boldsymbol{\delta\Delta} = A \cdot \boldsymbol{\delta\Delta}\,, \tag{8.57}$$

where $\boldsymbol{\delta\Delta}$ is a vector containing all possible *directions* of displacement (real and imaginary components of all pairing channels corresponding to the different form factors). It is given by

$$\boldsymbol{\delta\Delta} = \left[\ \mathrm{Re}\left(\delta\Delta_1\right),\ \ \mathrm{Im}\left(\delta\Delta_1\right),\ \ \mathrm{Re}\left(\delta\Delta_2\right),\ \ \mathrm{Im}\left(\delta\Delta_2\right),\ \ \cdots,\ \ \mathrm{Re}\left(\delta\Delta_{n/2}\right),\ \ \mathrm{Im}\left(\delta\Delta_{n/2}\right)\ \right]^T \tag{8.58}$$

with Δ_i being the gap concerning a specific form factor and n being the size of the array.

For a unique definition of A, n pairs of $\boldsymbol{\delta\Delta}$ and their derivatives $\partial_t\boldsymbol{\delta\Delta}$ are needed. Therefore, we apply distortions in all possible directions

$$\boldsymbol{\Delta}^{(i)} = d\,\mathbf{e}_i\,, \quad \boldsymbol{\delta\Delta}^{(i)} = \sum_j \mathbf{e}_j \left[\frac{1}{N} \sum_{\mathbf{k}'\alpha'\beta'} v_i \left(f^{\alpha\beta}_{i,\mathbf{k}'} \right)^* \langle \hat{c}_{-\mathbf{k}'\beta'\downarrow} \hat{c}_{\mathbf{k}'\alpha'\uparrow} \rangle \Big|_{\boldsymbol{\Delta}=\boldsymbol{\Delta}^0+\boldsymbol{\Delta}^{(i)}} \right] - \boldsymbol{\Delta}^0 \tag{8.59}$$

for $i = 1, \ldots, n$, where $\boldsymbol{\Delta}^0$ describes the gap of the investigated instability in the same basis. The corresponding derivatives can be calculated using either the combinations of Eqs. (6.84) and (6.85) (no same spin pairing or coupling of different spin sectors in the non-interacting part) or Eqs. (6.54) and (6.55) (general version), where we again assume that the system was held in the same state (constant $\Delta_{\mathbf{k}}$) before the relaxation. Since we can use the analytical expression (8.28) with a basis transformation for the collision integral, this approach is in principle exact as long as a small enough displacement d is applied and the threshold used for solving the gap equation (see Subsection 6.3.3) is chosen small enough.
For convenience, we sort the results into matrices

$$X = \left[\; \boldsymbol{\delta\Delta}^{(1)}, \quad \boldsymbol{\delta\Delta}^{(2)}, \quad \cdots, \quad \boldsymbol{\delta\Delta}^{(n)} \;\right], \quad Y = \left[\; \partial_t\boldsymbol{\delta\Delta}^{(1)}, \quad \partial_t\boldsymbol{\delta\Delta}^{(2)}, \quad \cdots, \quad \partial_t\boldsymbol{\delta\Delta}^{(n)} \;\right], \tag{8.60}$$

allowing to write the problem to be solved as the matrix multiplication

$$Y = A \cdot X\,. \tag{8.61}$$

or equivalently $Y^T = X^T A^T$. The matrix A can then be calculated from X and Y using the least squares estimator from multiple linear regression (see e.g. Ref. [230]). This estimator minimizes the least square function [230], which is in the present case given by the matrix norm $\left\| Y^T - X^T \cdot A^T \right\|$. The final formula is given by

$$A = Y \cdot X^T \cdot \left(X^T \cdot X \right)^{-1}\,. \tag{8.62}$$

Finally, the eigenvalues of A are calculated and only if all of them are negative, the instability is stable for the chosen parameters.
Importantly, if the instability under investigation (e.g. p_x in the scenario above) shall be included into the vectors of displacement, this can only be done for the real direction of this order (meaning that there is no phase difference between the equilibrium gap and the distortion). This is the case since the derivative in the imaginary direction only belongs to a change of the global phase of the order parameter which should therefore just lead to a derivative of zero. If the form factor of the instability under investigation is included in the vector from Eq. (8.58), this leads thus to an odd size n of the vector and one imaginary part needs to be removed in comparison to the form shown in Eq. (8.58).
Nevertheless, the real direction of this order can also be ignored as it is shown numerically below. This can be justified since it is known that the order parameter is stable regarding these changes and because the portion of $\boldsymbol{\delta\Delta}^{(i)}$ in the p_x directions is small if $\boldsymbol{\Delta}^{(i)}$ has no weight here (leading basically to a decoupling from the other directions).

In Fig. 8.5, results from this numerical approach are compared to the ones from the analytical analysis above. Here, half filling is considered, where both results should be identical. We apply the introduced criterion in two different ways. In the first case, all three possible directions (real and imaginary direction of s- and real direction of p_x-wave) are included. In the second case, we neglect the form factor from the investigated p_x-wave and end up with a 2×2 matrix.
We note that both lines agree with each other and with the analytical results within the resolution used for numerical results. This numerical resolution is chosen to be $\Delta U = 0.01$ for the remainder of this chapter. The numerical criterion can thus be trusted and we can neglect the directions from the form factor belonging to the instability under investigation without hesitation. The introduced method is employed in the rest of this chapter for the verification of stability for various systems and instabilities.

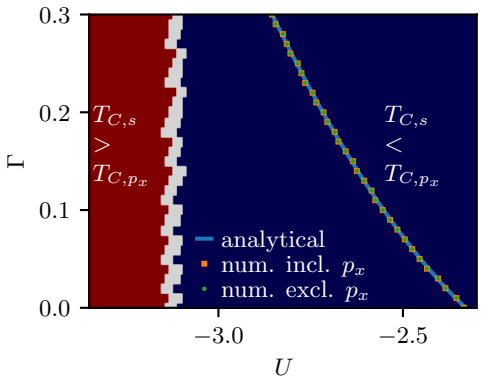

Figure 8.5: Comparison of the numerical stability criterion with the analytical approach used before for the square lattice model at half filling. The stability of the p_x order is characterized for $N = 21 \times 21$, $U' = -3$, $E_z = 0$, $\Gamma = 0.1$ and $T = 0.05$ and we thus use the same phase diagram as in Fig. 8.4(a). The numerical line is calculated once including the p_x-wave itself and once without the p_x-wave. Both numerical lines perfectly agree, showing that the instability under investigation can be left out. Additionally, the numerical results are in agreement with the analytical result within the chosen resolution of $\Delta U = 0.01$. Error bars are not included here since they are too small.

8.2.4 Chiral Order Parameters

In the previous parts of the chapter, we saw that real order parameters cannot correspond to metastable subleading instabilities in one-band models, which we extensively studied at the example of a model on the square lattice in the presence of an s-wave and a p_x-wave instability. In the following, we investigate the case of chiral order parameters using the same model as before.
To this end, we consider the presence of both p-waves with form factors defined in Eq. (8.20). In this situation, the chiral topological combinations $p_x \pm ip_y$, which we call $p \pm ip$ in the following, are energetically favoured over $p_{x/y}$ waves that were studied before. The form factors of the chiral orders are given by

$$\not{f}_{p\pm ip} = \frac{1}{\sqrt{2}} \left(\not{f}_{p_x} \pm i \not{f}_{p_y} \right) . \tag{8.63}$$

Moreover, both chiral p-waves are degenerate. In the following, we thus focus on $p+ip$, although the investigation of $p-ip$ would lead to the same results. Importantly, the no-go theorem from above does not apply to the topological chiral orders since these are complex valued pairing orders. We repeat the analysis from above and show the results in Fig. 8.6.
In (a) and (b), minor changes to the order parameters corresponding to one of the instabilities are again considered. In both cases (starting close to s or $p+ip$), the system relaxes to the closer order indicating that both order parameters correspond to stable minima in the free energy landscape. We can confirm the stability of $p+ip$ by investigating the flow diagram, which is shown in Fig. 8.6(c). Here, the system flows back to the $p+ip$ order from all possible directions. Imaginary displacements in $p-ip$ are not shown and the results are therefore projected onto the three-dimensional displayed subspace. However, it is confirmed that $p+ip$ is also stable in the imaginary $p-ip$ direction.
Furthermore, free energy landscapes are presented in Fig. 8.6(d) and (e). In (d) the results are shown in dependence on Δ_s and Δ_{p+ip} with a relative phase of either 0 or $\pi/2$. These are equivalent since they are connected by rotational symmetry. We note that we indeed find a subtle local minimum for the chiral p-wave confirming that $p+ip$ is stable in the imaginary and real s-wave direction as already extracted from the float diagram. In Fig. 8.6(e) the free energy landscape is shown for $p+ip$ and $p-ip$ with a phase difference of zero. We note that degenerate minima occur at $p \pm ip$, showing that the chiral orders are indeed preferred over real valued $p_{x/y}$ orders. This confirms that $p+ip$ is also stable in the real $p-ip$ direction as it was found in the float diagram as well.

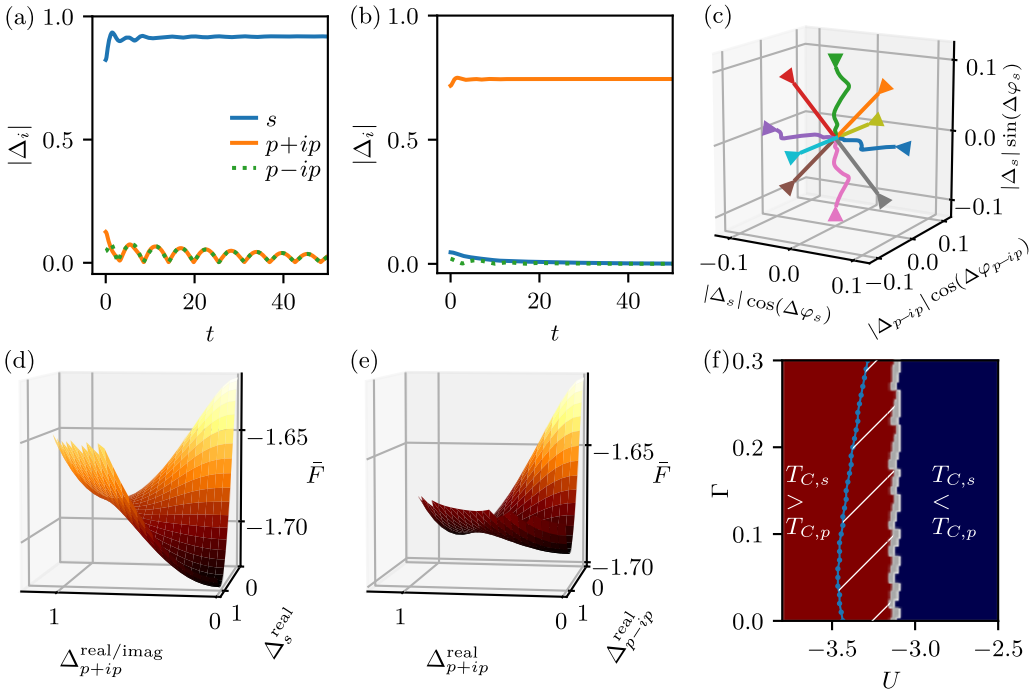

Figure 8.6: Metastable chiral orders for $U' = -3$, $N = 20 \times 20$, $E_z = 0$, $T = 0.05$, $U = -3.3$ for (a)-(e) and $\Gamma = 0.1$ for (a)-(c). (a),(b) Time evolution starting from a random state in the vicinity of (a) the leading s-wave and (b) the subleading $p+ip$-wave. The order parameter relaxes back to the gap function corresponding to the close-by order in both cases. (c) Float diagram starting from different directions in the vicinity of the $p+ip$-wave order showing that the system floats to the subleading order from all shown directions. (d) Free energy landscape (by setting $\Gamma = 0$) in dependence on Δ_{p+ip} and Δ_s with a phase difference of either 0 or $\pi/2$. The s-wave order belongs to the global minimum, while the chiral p-wave forms a subtle local minimum. (e) Free energy landscape in dependence on both chiral p-waves with a phase dependence of $\Delta\varphi = 0$. The minima occur for the chiral waves, which have a smaller energy than the real pairing orders p_x and p_y. (f) Phase diagram as a function of the local interaction U and the bath coupling Γ ($U' = -3$, $N = 20 \times 20$ as before) indicating the stability line for the chiral $p+ip$-wave at $T = 0.05$. In the hatched region, we find a stable but subleading $p+ip$-wave. The critical temperature was determined using a resolution of $\Delta T = 0.01$.

Finally, the phase diagram for the square lattice model is presented (see Fig 8.6(f)). Here, a blue line is drawn indicating the critical interaction U_c (for a fixed temperature) above which $p+ip$ is stable. This line was obtained with the algorithm that was explained in Subsection 8.2.3. We note that there is indeed a region where $p+ip$ is stable although being a subleading instability (hatched regime).

8.2.5 Doping away from Half-Filling

For the square lattice model, the question of stability has so far only been answered at half-filling. Therefore, we consider finite doping in the following. In Figure 8.2(e),(f) float diagrams for the p_x-wave were already shown at finite chemical potential, where we noticed that p_x is not left in the imaginary direction. Therefore, the analytical stability criterion from Eq. (8.56) cannot be applied. Instead, we use the numerical criterion from Subsection 8.2.3, which leads to the phase diagram shown in Fig. 8.7(a). Once again, the lines indicate the minimal U_c for which p_x is stable. Remarkably, the results are extremely similar to the ones obtained at half filling and we find again that p_x cannot be stable and subleading at the same time. Additionally, the stability line at the critical temperature agrees with the phase boundary within the resolutions that were chosen for the local interaction U and the temperature T.

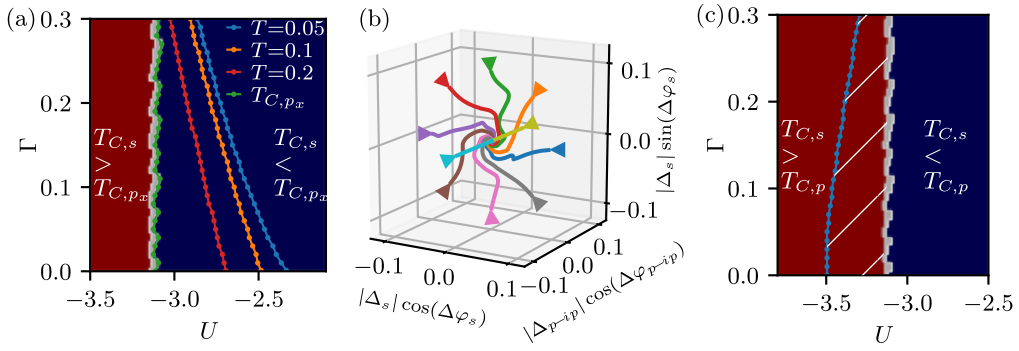

Figure 8.7: Result at a finite chemical potential of $\mu = -0.1$ for the square lattice model. (a) Phase diagram as a function of U and Γ based on critical temperatures including stability lines for the p_x-wave, which can never be stable and subleading at the same time. For the critical temperature the highest temperature solving the gap equation within the resolution of $\Delta T = 0.01$ was used. The other parameters are $U' = -3$, $N = 20 \times 20$ and $E_z = 0$. (b) Float diagram to the chiral $p+ip$-wave using real and imaginary s-wave distortions and real $p-ip$-wave distortions. The parameters are the same as in (a) with fixed $U = -3.3$ and $\Gamma = 0.1$. The state floats to the $p+ip$ order from all directions, but distortions in the s-wave directions show a spiral in the relaxation process. (c) Phase diagram for the chiral p-waves using the same parameters as in (a) with a stability line for $T = 0.05$ showing that $p+ip$ is metastable and subleading in the hatched region.

Furthermore, we can investigate a possible metastable subleading chiral p-wave. To this end, the float diagram of $p+ip$ is shown in Fig. 8.7(b), which is again projected onto a three-dimensional subspace by neglecting the imaginary $p-ip$ direction. Indeed, we find a flow towards the origin, which represents the state with the subleading $p+ip$ order. We can therefore conclude that a subleading metastable chiral p-wave can also exist beyond the half-filled case.

Nevertheless, we note in the flow diagram that some curves show a spiral during the relaxation process. Interestingly, this is not an artifact of large displacements and is also found for infinitesimal distortions. Furthermore, the direction of the spiral is reversed when changing the sign of the chemical potential. It is unclear, how exactly a finite chemical potential induces the spiral behavior. Within this thesis, we concentrate on the question of metastability and leave this question to future research.
In the following, we again want to find a stability criterion, allowing us to draw a phase diagram including stability lines for the chiral p-waves. However, at first sight, it is unclear if the numerical stability criterion from Subsection 8.2.3 is still applicable since we assumed that eigenvectors with real eigenvalues exist for Eq. (8.57). Nevertheless, we can trace back the rotated case shown here to the unrotated one (where no spiral appears) and argue that our approach remains valid. To this end, we decompose the derivatives into the present rotation and the derotated derivatives. This leads to

$$Y = R \cdot \tilde{Y}\,, \tag{8.64}$$

where R denotes the rotation matrix and $\tilde{Y}$ is the matrix containing the derotated derivatives. We thus find for the stability matrix

$$A = R \cdot \tilde{A}\,, \tag{8.65}$$

where $\tilde{A}$ contains the needed real eigenvalues, which describe whether the spiral turns inwards or outwards. However, the rotation matrix R should not change the sign of the real part of the eigenvalues. This can be seen by applying the most simple case, where all of eigenvalues of $\tilde{A}$ are equal and given by $\tilde{a}$. The eigenvalues of A are then given by

$$a = e^{i\theta}\,\tilde{a} \text{ with } |\theta| < \frac{\pi}{2} \tag{8.66}$$

which leads to the result that

$$\mathrm{Sgn}[\mathrm{Re(a)}] = \mathrm{Sgn}[\tilde{\mathrm{a}}]\,. \tag{8.67}$$

Therefore, we can read off the stability by studying the sign of the real part of the eigenvalues. In Appendix D it is shown that the signs are also not changed for a 2×2-matrix with different eigenvalues.

The phase diagram is presented in Fig. 8.7(c) including the resulting stability line for a temperature of $T = 0.05$. The results again resemble the ones that we obtained at half filling. We do find a region, where $p+ip$ is subleading and metastable (hatched part).

8.3 Driving of One-Band Models

In the previous part of this chapter, we have considered one-band models, which allowed for an analytical treatment in addition to our numerical results. This leads to the conclusion that chiral orders can be metastable subleading instabilities, which was shown using a standard s-wave and a chiral p-wave. These two specific instabilities correspond to superconducting states with different parities, which is of special importance since inversion symmetry suppresses the relaxation process to the global minimum in that case [154]. Therefore, we now investigate the process of driving the system between states with superconducting order from different inversion symmetry sectors and examine whether they can be coupled in the case of a general one-band model, which can be described by the simplified BdG-Hamiltonian (6.65). For this analysis, we again neglect the coupling to the bath and only treat the case $\Gamma = 0$ for convenience, but a finite bath coupling is not expected to change our results.

We employ the full time evolution as derived in Subsection 6.5.3 with the final result shown in Eqs. (6.82)-(6.88). Inserting $\Gamma = 0$ and exploiting that the objects in Eqs. (6.82)-(6.88) are scalars in the case of one-band models simplifies these equations to

$$i\partial_t n_{\mathbf{k},\uparrow} = \Delta_{\mathbf{k}} f^*_{\mathbf{k}} - \Delta^*_{\mathbf{k}} f_{\mathbf{k}}\,, \tag{8.68}$$
$$i\partial_t n_{\mathbf{k},\downarrow} = \Delta_{-\mathbf{k}} f^*_{-\mathbf{k}} - \Delta^*_{-\mathbf{k}} f_{-\mathbf{k}}\,, \tag{8.69}$$
$$i\partial_t f_{\mathbf{k}} = f_{\mathbf{k}}(h_{\mathbf{k},\uparrow} + h_{-\mathbf{k},\downarrow}) + \Delta_{\mathbf{k}}(1 - n_{\mathbf{k},\uparrow} - n_{-\mathbf{k},\downarrow})\,. \tag{8.70}$$

We now change the basis to

$$\begin{aligned} \bar{n}_{\mathbf{k},\sigma} &= n_{\mathbf{k},\sigma} + n_{-\mathbf{k},\sigma}\,, & t_{\mathbf{k}} &= f_{\mathbf{k},1} + f_{\mathbf{k},2} = f_{\mathbf{k}} - f_{-\mathbf{k}}\,, \\ m_{\mathbf{k},\sigma} &= n_{\mathbf{k},\sigma} - n_{-\mathbf{k},\sigma}\,, & s_{\mathbf{k}} &= f_{\mathbf{k},1} - f_{\mathbf{k},2} = f_{\mathbf{k}} + f_{-\mathbf{k}}\,, \end{aligned} \tag{8.71}$$

leading to the gaps

$$\begin{aligned} \Delta^t_{\mathbf{k}} &= \Delta_{\mathbf{k}} - \Delta_{-\mathbf{k}} = \frac{1}{N}\sum_{\mathbf{k}'} V_{\mathbf{k},\mathbf{k}'} t_{\mathbf{k}'}\,, \\ \Delta^s_{\mathbf{k}} &= \Delta_{\mathbf{k}} + \Delta_{-\mathbf{k}} = \frac{1}{N}\sum_{\mathbf{k}'} V_{\mathbf{k},\mathbf{k}'} s_{\mathbf{k}'}\,. \end{aligned} \tag{8.72}$$

We can calculate the time derivatives within this basis and obtain

$$\begin{aligned} i\partial_t t_{\mathbf{k}} =& i\partial_t\,(f_{\mathbf{k}} - f_{-\mathbf{k}}) \\ =& f_{\mathbf{k}}(h_{\mathbf{k},\uparrow} + h_{-\mathbf{k},\downarrow}) - f_{-\mathbf{k}}(h_{\mathbf{k},\downarrow} + h_{-\mathbf{k},\uparrow}) - \Delta_{\mathbf{k}}(n_{-\mathbf{k},\downarrow} + n_{\mathbf{k},\uparrow}) + \Delta_{-\mathbf{k}}(n_{-\mathbf{k},\uparrow} + n_{\mathbf{k},\downarrow}) \\ &+ (\Delta_{\mathbf{k}} - \Delta_{-\mathbf{k}}) \\ =& \left[\frac{1}{2}(h_{\mathbf{k},\uparrow} + h_{-\mathbf{k},\uparrow}) + \frac{1}{2}(h_{\mathbf{k},\downarrow} + h_{-\mathbf{k},\downarrow})\right] t_{\mathbf{k}} + \left[\frac{1}{2}(h_{\mathbf{k},\uparrow} - h_{-\mathbf{k},\uparrow}) - \frac{1}{2}(h_{\mathbf{k},\downarrow} - h_{-\mathbf{k},\downarrow})\right] s_{\mathbf{k}} \\ &- \left[\frac{1}{2}(n_{-\mathbf{k},\downarrow} + n_{\mathbf{k},\downarrow}) + \frac{1}{2}(n_{-\mathbf{k},\uparrow} + n_{\mathbf{k},\uparrow})\right] \Delta^t_{\mathbf{k}} - \left[\frac{1}{2}(n_{-\mathbf{k},\downarrow} - n_{\mathbf{k},\downarrow}) - \frac{1}{2}(n_{-\mathbf{k},\uparrow} - n_{\mathbf{k},\uparrow})\right] \Delta^s_{\mathbf{k}} \end{aligned}$$

$$
\begin{aligned}
&+\Delta^t_{\mathbf{k}} \\
=&\frac{\bar{h}_{\mathbf{k},\downarrow}+\bar{h}_{\mathbf{k},\uparrow}}{2}t_{\mathbf{k}}+\frac{\Delta h_{\mathbf{k},\uparrow}-\Delta h_{\mathbf{k},\downarrow}}{2}s_{\mathbf{k}}-\frac{\bar{n}_{\mathbf{k},\downarrow}+\bar{n}_{\mathbf{k},\uparrow}-2}{2}\Delta^t_{\mathbf{k}}+\frac{m_{\mathbf{k},\uparrow}+m_{\mathbf{k},\downarrow}}{2}\Delta^s_{\mathbf{k}}\,,
\end{aligned}
\tag{8.73}
$$

with $\bar{h}_{\mathbf{k},\sigma}=h_{\mathbf{k},\sigma}+h_{-\mathbf{k},\sigma}$ and $\Delta h_{\mathbf{k},\sigma}=h_{\mathbf{k},\sigma}-h_{-\mathbf{k},\sigma}$. Equally, we compute

$$
i\partial_t s_{\mathbf{k}}=\frac{\bar{h}_{\mathbf{k},\downarrow}+\bar{h}_{\mathbf{k},\uparrow}}{2}s_{\mathbf{k}}+\frac{\Delta h_{\mathbf{k},\uparrow}-\Delta h_{\mathbf{k},\downarrow}}{2}t_{\mathbf{k}}-\frac{\bar{n}_{\mathbf{k},\downarrow}+\bar{n}_{\mathbf{k},\uparrow}-2}{2}\Delta^s_{\mathbf{k}}+\frac{m_{\mathbf{k},\uparrow}+m_{\mathbf{k},\downarrow}}{2}\Delta^t_{\mathbf{k}}\,. \tag{8.74}
$$

Furthermore, we find

$$
i\partial m_{\mathbf{k},\uparrow}=i\partial(n_{\mathbf{k},\uparrow}-n_{-\mathbf{k},\uparrow})=\Delta_{\mathbf{k}}f^*_{\mathbf{k}}-\Delta^*_{\mathbf{k}}f_{\mathbf{k}}-\Delta_{-\mathbf{k}}f^*_{-\mathbf{k}}+\Delta^*_{-\mathbf{k}}f_{-\mathbf{k}} \tag{8.75}
$$

$$
i\partial m_{\mathbf{k},\downarrow}=i\partial(n_{\mathbf{k},\downarrow}-n_{-\mathbf{k},\downarrow})=\Delta_{-\mathbf{k}}f^*_{-\mathbf{k}}-\Delta^*_{-\mathbf{k}}f_{-\mathbf{k}}-\Delta_{\mathbf{k}}f^*_{\mathbf{k}}+\Delta^*_{\mathbf{k}}f_{\mathbf{k}} \tag{8.76}
$$

leading to

$$
i\partial_t(m_{\mathbf{k},\uparrow}+m_{\mathbf{k},\downarrow})=0\,. \tag{8.77}
$$

At $t=-\infty$ we have $m_{\mathbf{k},\uparrow}=m_{\mathbf{k},\downarrow}=0$ due to inversion symmetry and therefore, we can set $m_{\mathbf{k},\uparrow}+m_{\mathbf{k},\downarrow}=0$ at all times. Additionally, we utilize

$$
\Delta h_{\mathbf{k},\uparrow}-\Delta h_{\mathbf{k},\downarrow}=0\,, \tag{8.78}
$$

which applies for realistic physical models that we investigate in this chapter. A finite $\Delta h_{\mathbf{k},\uparrow}-\Delta h_{\mathbf{k},\downarrow}$ could for example be realized by employing an unphysical spin-dependent hopping but a standard Zeeman field would still yield $\Delta h_{\mathbf{k},\uparrow}-\Delta h_{\mathbf{k},\downarrow}=0$ although it breaks the spin flip symmetry of the model.
Thus, we arrive at the final result of separated differential equations

$$
i\partial_t t_{\mathbf{k}}=\frac{\bar{h}_{\mathbf{k},\downarrow}+\bar{h}_{\mathbf{k},\uparrow}}{2}t_{\mathbf{k}}-\frac{\bar{n}_{\mathbf{k},\downarrow}+\bar{n}_{\mathbf{k},\uparrow}-2}{2}\Delta^t_{\mathbf{k}}\,,\quad i\partial_t s_{\mathbf{k}}=\frac{\bar{h}_{\mathbf{k},\downarrow}+\bar{h}_{\mathbf{k},\uparrow}}{2}s_{\mathbf{k}}-\frac{\bar{n}_{\mathbf{k},\downarrow}+\bar{n}_{\mathbf{k},\uparrow}-2}{2}\Delta^s_{\mathbf{k}}\,, \tag{8.79}
$$

showing that the even and odd combinations cannot be coupled and that photo-induced switching between them is unfeasible in realistic single-band models with a BdG Hamiltonian of form (6.65).

8.4 Multi-Band Models

As we have just derived, light-induced switching between superconducting states of different parity is unfeasible for realistic single-band models that we have studied so far. At the same time, such a coupling is of significant interest due to the long lifetime of the metastable state as mentioned above. Therefore, we now investigate a prototypical multi-band model on a honeycomb lattice and verify whether the properties found above also apply for multi-band models.

8.4.1 Stability Analysis

For the honeycomb lattice model, nearest-neighbor hopping and a Kane-Mele spin orbit coupling [231, 232] is considered, with a non-interacting Hamiltonian of

$$
h^\sigma_{\mathbf{k}}=\begin{pmatrix} \sigma\lambda a_{\mathbf{k}}-\mu & -t_{\mathrm{h}}b_{\mathbf{k}} \\ -t_{\mathrm{h}}b^\dagger_{\mathbf{k}} & -\sigma\lambda a_{\mathbf{k}}-\mu \end{pmatrix} \tag{8.80}
$$

with

$$
a_{\mathbf{k}}=\sin\left(\frac{k_x}{2}\right)\left(\cos\left(\frac{k_x}{2}\right)-\cos\left(\frac{\sqrt{3}k_y}{2}\right)\right)\,,\quad b_{\mathbf{k}}=-1-2e^{\frac{1}{2}i\sqrt{3}k_y}\cos\left(\frac{k_x}{2}\right)\,, \tag{8.81}
$$

the spin $\sigma \in \{\uparrow,\downarrow\} = \{1,-1\}$, the hopping amplitude $t_\mathrm{h} = 1$, the spin-orbit coupling strength λ and the chemical potential μ. The s- and p-wave instabilities of this model obey form factors (and prefactors) of [233]

$$\begin{aligned} \measuredangle^{\alpha\beta}_{s,\mathbf{k}} &= \delta_{\alpha\beta}/\sqrt{2}\,, & v_s &= U\,, \\ \measuredangle^{\alpha\beta}_{p_1,\mathbf{k}} &= \delta_{\alpha\bar{\beta}}\left[\measuredangle_{p_1}(k_x,k_y)\,\delta_{\alpha A} + \measuredangle_{p_1}(k_x,-k_y)\,\delta_{\alpha B}\right]\,, & v_{p_x} &= U'\,, \\ \measuredangle^{\alpha\beta}_{p_2,\mathbf{k}} &= \delta_{\alpha\bar{\beta}}\left[\measuredangle_{p_2}(k_x,k_y)\,\delta_{\alpha A} - \measuredangle_{p_2}(k_x,-k_y)\,\delta_{\alpha B}\right]\,, & v_{p_y} &= U'\,, \end{aligned} \tag{8.82}$$

with

$$\measuredangle_{p_1} = i\,e^{-i\sqrt{3}k_y/2}\sin(k_x/2)\,, \quad \measuredangle_{p_2} = \left[-1 + e^{-i\sqrt{3}k_y/2}\cos(k_x/2)\right]/\sqrt{3}\,. \tag{8.83}$$

We identify the pairing orders $p_x \coloneqq p_1$ and $p_y \coloneqq p_2$ due to the behavior of their form factors around $\mathbf{k} = 0$, where we find $\measuredangle_{p_1} \propto k_x$ and $\measuredangle_{p_2} \propto k_y$. Due to the additional orbital index of the form factors, these do not have to be real valued for p_x and p_y-wave instabilities. We still refer to them as real valued pairing orders to distinguish them from the complex chiral combinations $p\pm ip$. In order to connect the model to the results that we have found for the single-band models before, we employ the spin orbit strength to obtain a large gap (we set $\lambda = 0.5$) and tune the chemical potential into the center of the lower band ($\mu = -2.0$). We then repeat the analysis from before by calculating the phase diagrams over the comparison of critical temperatures and by finding stability lines numerically as explained in Subsection 8.2.3. The results are presented in Fig. 8.8(a),(b), where we note substantial similarities with the phase diagrams from the square lattice model presented above. In (a) only the p_x-wave is included, while both p_x- and p_y-waves are included in (b) leading to the formation of chiral orders $p\pm ip$. The stability boundaries for (a) p_x and (b) $p\pm ip$ (where they change from unstable to stable) are drawn as solid lines. As in the previous cases, the considered p-wave order is (meta-)stable if the local interaction U is larger than the critical value indicated by the corresponding line. In (a), we note that this can only occur in the region, where p_x is already the leading instability independent of the chosen temperature. The region of stability can be enlarged by increasing the temperature but only to the point where the phase boundary perfectly agrees with the critical U as we have already noticed for the square lattice model. Additionally, there are again regions where p_x is not stable but leading due to a ground state consisting of a combination of both orders.
Remarkably, in the same manner as in the case of the one-band model, chiral combinations can form metastable instabilites in the regime where the s-wave is the leading order. For a temperature of $T = 0.05$, the stability line is marked in Fig. 8.8(b) leading to metastable and subleading chiral p-wave order in the hatched region.
This indicates that the results obtained above are valid beyond the case of a single-band model, where analytical calculations were possible. Once again, we find that real valued ordering cannot be simultaneously stable and subleading, as well as the potential of subleading metastable chiral waves.

8.4.2 Coupling of Different Parities

Since one of the reason for investigating multi-band models was the possibility of coupling states with different parity, we briefly verify that the multi-band model under investigation can indeed couple even and odd states making a driving between them feasible. To this end, the effect of a prototypical driving protocol is studied, using a circular polarized Gaussian light pulse

$$\frac{e}{c}\mathbf{A}(t) = M\,e^{-\left(\frac{t-t_\mathrm{mean}}{t_\sigma}\right)^2} \quad \left[\ \cos(\omega t)\,, \quad \pm\sin(\omega t)\ \right]^T \tag{8.84}$$

with +1 (-1) for right (left) polarized light. Here, the handedness of the light pulse influences which chiral order gets more enhanced due to the light pulse. In Fig. 8.8(c), the results for a left handed light pulse are shown, where $p+ip$ gets more enhanced. We note that states being even and odd under inversion can indeed be coupled for multi-band models. This allows to drive an s-wave into a metastable chiral p-wave order, although the state relaxes to the leading s-wave in the present example. As mentioned above, the metastable state is, in this case, rather long lived

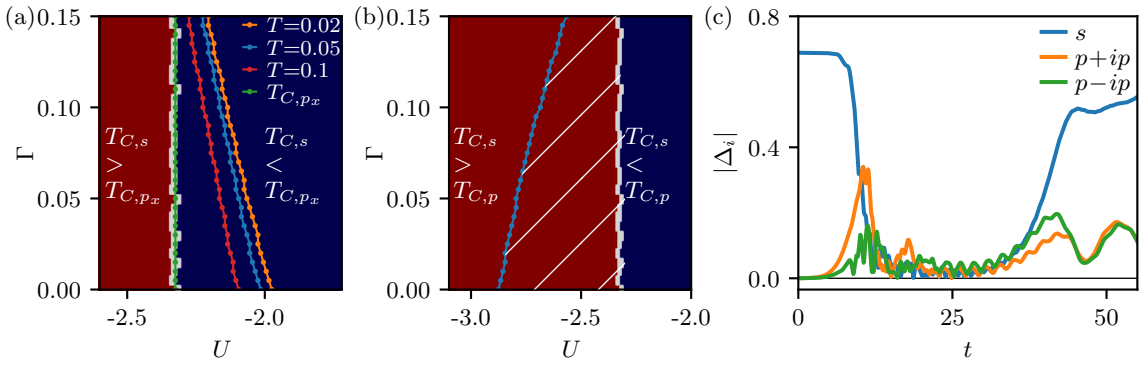

Figure 8.8: (a),(b) Phase diagrams of the honeycomb lattice based on critical temperatures (using a resolution of $\Delta T = 0.05$) and boundaries for the stability of the corresponding p-wave orders with similar results as for the single-band model with $U' = 3$, $\lambda = 0.5$ and $N = 20 \times 20$. (a) Only the p_x-wave is considered. The solid lines indicate the stability criterion and show above which U p_x-wave ordering is (meta-) stable. Since these lines never appear for smaller U than the phase transition, p_x order cannot be stable if it is not the leading order parameter. (b) Both p-waves are included forming chiral combinations $p\pm ip$. Here, the stability line for $T = 0.05$ appears for lower U than the phase transition and the hatched region refers to the region where the chiral p-waves are metastable but subleading. (c) Driving with a Gaussian left-circular polarized light pulse given by Eq. (8.84) with $M = t_\sigma = t_{\text{mean}}/3 = 5$ and $\omega = \pi/2$. The chiral p-waves (parity odd) can be enhanced starting from the s-wave state (parity even). The magnitude of the $p+ip$ clearly exceeds the one of s temporarily. Nevertheless, the system relaxes back to the ground state for this specific light pulse. Parameters as in (a),(b) with additional fixed $U = -2.5$, $\Gamma = 0.05$ and $T = 0.05$.

since the back relaxation process is restrained due to inversion symmetry present in the absence of a light pulse.
The uncovering of a driving protocol where the state actually relaxes to p-wave order, leading to switching to the metastable subleading state, is left for future research.

8.5 Same Spin Pairing

Finally, we briefly study the case where same spin pairing is included as well, which leads to additional pairing channels. In this case, the more general version of the BdG Hamiltonian and time evolution is needed as it was introduced in Sections 6.3 and 6.4. In the following, the form factors thus have an additional dimension in comparison to the ones from Eq. (8.20).
We investigate the aforementioned square lattice model and again consider only two instabilities for simplification: the standard singlet s-wave, which was already included in the stability analysis in Section 8.2, and a p_x-wave pairing only spin down particles. We choose the spin down version since it is preferred for finite Zeeman fields with $E_z > 0$. For the spin dependent version of the BdG Hamiltonian (6.30), the non-interacting part of the Hamiltonian has to be rewritten including a spin index, leading to

$$h_{\mathbf{k}}^{\sigma\sigma'} = 2\left[\cos(k_x) + \cos(k_y)\right]\delta_{\sigma\sigma'} - \mu\delta_{\sigma\sigma'}\,. \tag{8.85}$$

We additionally have spin dependent form factors

$$\begin{aligned} f_s^{\sigma\sigma'} &= \delta_{\sigma,\sigma'}\left(\delta_{\sigma,\uparrow} - \delta_{\sigma,\downarrow}\right)\,, & v_s &= U\,, \\ f_{p_{x,\downarrow}}^{\sigma\sigma'} &= \sqrt{2}\delta_{\sigma,\sigma'}\delta_{\sigma,\downarrow}\,, & v_{p_{x,\downarrow}} &= U'\,. \end{aligned} \tag{8.86}$$

The analysis from before gets repeated for these form factors and a phase diagram is found based on critical temperatures as shown in Fig. 8.9. Additionally, stability lines are included from the $p_{x,\downarrow}$ order indicating the smallest U, where this order is stable. The results shown in Fig. 8.9 are

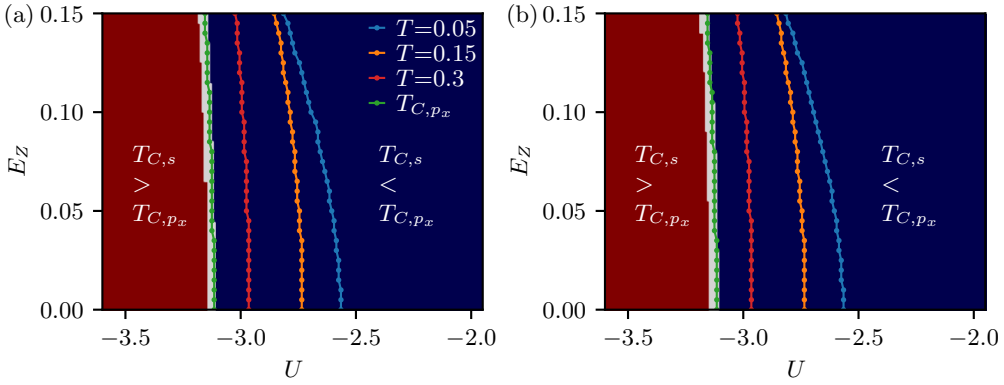

Figure 8.9: Phase diagrams for the square lattice model including the same spin p_x ordering for spin $\downarrow$ electrons and the standard s-wave based on critical temperatures as a function of the local interaction U and the Zeeman energy E_z. In the grey regions, the critical temperatures agree within the chosen resolution of $\Delta T = 0.01$. The additional parameters are given by $U' = 3$, $\Gamma = 0.1$, $N = 20 \times 20$ and (a) $\mu = 0.0$, (b) $\mu = -0.1$. The solid lines indicate the critical U, below which the $p_{x,\downarrow}$ order is unstable. For all temperatures, the critical U is larger than or equal to the one of the phase transition. For the critical temperature, which is here defined as the highest possible temperature still solving the gap equation using the mentioned temperature resolution, the stability line is exactly on top of the phase transition. Therefore, there is no overlap between the regions, where $p_{x,\downarrow}$ is subleading (red region) and where it is stable (to the right of solid lines). Therefore, $p_{x,\downarrow}$ cannot be a metastable subleading instabilty.

extremely similar to the results obtained before for other real valued pairing orders. Once again, we note that for all possible temperatures (all temperatures with $T \leq T_{C,p_x}$), a subleading p_x-instability cannot be metastable since the stability boundary appears for larger U than the phase transition. We can increase the temperature in order to increase the region of stability but only find the critical U to coincide with the phase transition in case of the highest possible temperature, the critical temperature of $p_{x,\downarrow}$. This indicates that the no-go theorem does also apply for models with same spin pairing although this was not proven analytically. The realization of metastable subleading chiral instabilities in models with same spin pairing seems to be more involved and is therefore left for future research.

8.6 Conclusion & Outlook

In this chapter, we have investigated a possibility to realize unconventional superconductivity by driving a conventional superconductor with light. We focused on the question of stability of subleading orders and found that topological chiral orders are extremely suitable to be targeted with a light pulse.

The reason for this is a no-go theorem for real valued pairing orders. This no-go theorem was found in the case of a time-reversal symmetric one-band model with a BdG Hamiltonian of form (6.65).

We investigated this behavior further by considering a model with s- and p-wave instabilities on the square lattice. Here, an analytical stability criterion for the p_x-wave was found at half filling. This was used to confirm the no-go theorem and to show that a finite coupling to an external bath, which was strictly speaking not included in the no-go theorem, does not change the result in the investigated example. Moreover, we found that breaking the time reversal symmetry with a Zeeman field does not yield a metastable subleading p_x-wave instability either. Using numerical techniques, we were able to prove that topological chiral orders, for which the no-go theorem does not apply, can be metastable and subleading. This result as well as the nonexistence of a stable and subleading p_x-wave in the square lattice model was also confirmed for the case of a system which is tuned away from half filling.

Since it was proven that even and odd pairing orders cannot be coupled in realistic one band models

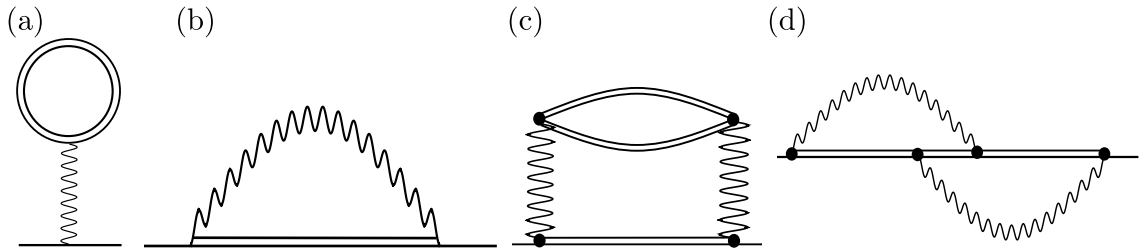

Figure 8.10: (a),(b) Feynman diagrams included in the generalized BCS theory. (c),(d) Next order Feynman diagrams that can be employed to include additional correlation effects into the self-energy.

(with a BdG Hamiltonian of form (6.65)), we also investigated the case of multi-band models at the example of a model on the honeycomb lattice, where we again only included the presence of s- and p-wave order. The results were similar to the ones of the square lattice model and we found that subleading real pairing orders cannot be metastable while chiral orders can.
Finally, we briefly discussed the opportunity of same spin pairing for the square lattice model, where the employed real valued pairing order was again observed to never be subleading and metastable.

There are various ways to continue this project in the future. Most importantly, the open ends, that were already discussed, should be addressed. These include a rigorous proof showing that the no-go theorem is still valid for models with time-reversal symmetry breaking. Moreover, it would be interesting to understand the origin of the spiral appearing in the relaxation process when a finite chemical potential is chosen (see Fig. 8.7(b)). Furthermore, the development of a driving protocol leading to a switching between leading and subleading orders is of further interest, as well as finding a subleading metastable order relying on same spin pairing.
In general, a more detailed investigation of multi-band models and systems with same spin pairing would be interesting to study. Additionally, the inclusion of more form factors leading to more complicated models should be investigated. Most importantly, this includes the study of realistic tight-binding models, as for example in the case of monolayer tungsten ditelluride as already mentioned in Ref. [154]. For this compound, a tight-binding model based on Ref. [60] is already implemented containing 68 form factors. A future goal is to first simplify the model before examining the free energy landscape for metastable chiral orders.
Once similar results have been obtained for a realistic tight-binding model representing a material, the experimental realization of a light induced unconventional pairing order is the ultimate goal of future research on the proposed mechanism.
Another possible path to pursue is the inclusion of correlations beyond mean-field into the results shown above. It is unclear whether additional correlations can actually stabilize real valued pairing orders. To this end, additional diagrams need to be included in the self-energy, which appears in the Green's functions. While in our mean-field approach, only diagrams from Fig. 8.10(a),(b) are employed, the next order diagrams from Fig. 8.10(c),(d) could be included as well. Since Feynman diagrams were not introduced in this thesis, the reader is referred to textbooks such as Ref. [132] for a detailed introduction and to Ref. [138] for a detailed explanation on the evaluation of different diagram techniques within the Keldysh formalism.

Chapter 9

Unconventional Superconductivity in Bilayer Heterostructures

This chapter is based on the following publications, where the results were already published (except for the added Fig. 9.6):
[125] C. S. Weber, D. Kiese, D. M. Kennes, and M. Claassen, "Intertwined superconductivity and magnetism from repulsive interactions in kondo bilayers", (2024), arXiv:2408.02847 [cond-mat.str-el]
For this project, I performed the DMRG and ED simulations. For the DMRG simulations I wrote a code based on the TeNPy library [120]. For simulations with ED, I reused a code written by Prof. Martin Claassen and made some adaptions. Furthermore, I contributed to the creation of the manuscript.
Note that the analysis of the single rung included in Section 9.2 was originally performed by Prof. Martin Claassen.

In the last chapter, we introduced a possible way to realize unconventional superconductivity by driving a conventional superconductor with light. Nevertheless, there are also systems showing unconventional superconductivity in their ground state. In this chapter, we concentrate on unconventional superconductivity from purely repulsive electronic interactions due to an emerging effective attractive coupling in the system.
Several efforts regarding mechanisms leading to superconductivity from repulsive electronic interactions have already been made for both systems with weak and strong couplings with respect to the band width. In the case of weak coupling, there are multiple mechanisms that have been analyzed using approaches relying on small interactions, such as methods relying on perturbation theory or renormalization group. Here, one possible example is Hund's pairing, where the effect from the repulsive density-density exchange gets surpassed by the Hund's coupling yielding an effective attractive interaction term in the Hubbard-Kanomori form of the interaction [234, 235]. Additionally, approaches based on spin fluctuations have been discussed [236–239]. Here, the system is in the vicinity of a spin-density wave phase and short-ranged spin fluctuations lead to an effective attraction. Moreover, there is the Kohn-Luttinger mechanism, which was established in Ref. [240] and since then it has been employed for a vast number of different models [241–245]. In this mechanism, weak repulsive interactions get renormalized by screening effects, leading to an effective attractive interaction. Strong coupling mechanisms have been investigated more recently and were mainly studied using numerical techniques, such as DMRG [246–250] or dynamical mean-field theory [251–254]. In this limit, only few theories have been developed to explain underlying mechanisms, e.g. in the case of spinless fermionic models [255] or inhomegenous Hubbard models [256]. Lately, a new mechanism based on an effective staggered potential and virtual excitations processes involving three electrons has been in the focus of the condensed matter community [257–260].

In this chapter, a new strong-coupling mechanism is established, found in a Kondo bilayer system which is composed of a strongly-correlated Mott insulator and a second nearly metallic layer. Here,

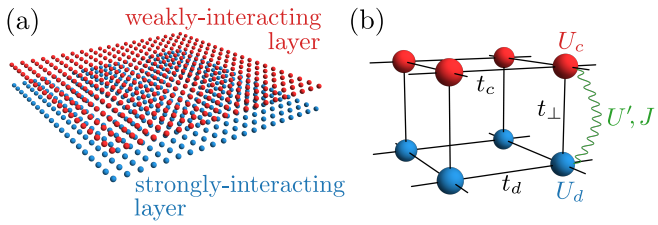

Figure 9.1: Bilayer system under consideration. (a) Illustration of the heterostructure beeing composed of a weakly-interacting and a strongly-interacting layer on a square lattice, which are coupled to each other. (b) Graphical representation of the Hamiltonian including local Hubbard repulsions U_c, U_d, an interlayer density repulsion U', a Hund's exchange J, intra-layer hoppings t_c, t_d and an interlayer hopping $t_\perp$. Figure taken from Ref. [125].

the leading order of the Kondo exchange is repulsive, while higher order terms have an attractive character. The mechanism explained here relies on the fact that the higher order terms can be enhanced due to additional interlayer interactions resulting in a net attraction between electrons. In contrast to other strong coupling theories mentioned above, superconductivity can be intertwined with magnetic ordering in the approach proposed in this chapter. This is of specific interest in multiple superconductors that have recently drawn a lot of attention, such as superconductors on Kondo lattices including Heavy fermion systems [261, 262], where magnetic moments are present, and infinite layer nickelates, where short-range magnetic correlations exist in addition to the superconducting Cooper pairs [263–268].

After a detailed introduction of the considered model, the mechanism proposed in this chapter is explained in the strong-coupling regime by the investigation of a single rung of the bilayer heterostructure. Using a one-dimensional variant of our model, we further investigate the model numerically, using DMRG and ED. First, we study the magnetic phase diagram, which includes 2-rung antiferromagnetic (AFM) and 4-rung AFM order, as well as a phase separation regime where multiple phases are degenerate. For the superconducting phase diagram, we find that superconductivity persists well beyond the strong coupling regime.
Interestingly, for a remarkable region of parameters, the superconducting order parameter varies in real space corresponding to Cooper pairs with finite momenta, which have been neglected in previous parts of this thesis. Those states have first been investigated in the presence of strong magnetic fields breaking time reversal symmetry in Refs. [269, 270] and are called Fulde–Ferrell–Larkin–Ovchinnikov (FFLO) states in this context [271–273]. Nevertheless, spatially modulated order parameters can also arise without explicit time reversal symmetry breaking. In this case they are referred to as pair density waves (PDWs) [272, 274].
The pair density waves found in this chapter obey an order parameter in the form of a Fulde-Ferrel (FF) or Larkin-Ovchinikov (LO) order parameter (see below, compare e.g. to Ref. [275]). Therefore, both terms are used equivalently in this thesis as it has also been implemented in other works (see e.g. Ref. [276]).

9.1 Model

We investigate a Kondo bilayer consisting of a weakly-interacting layer, behaving nearly metalically, and strongly-interacting layer, which is in a Mott-insulating state, as depicted in Fig. 9.1(a). The Hamiltonian of this model is given by

$$H = -\sum_{\langle ij\rangle\sigma}\left(t_d d^\dagger_{i\sigma} d_{j\sigma} + t_c c^\dagger_{i\sigma} c_{i\sigma}\right) + H_{\text{rung}} \tag{9.1}$$

where t_d and t_c denote the intra-layer hoppings withing both layers, and $c^{(\dagger)}_{i\sigma}$ and $d^{(\dagger)}_{i\sigma}$ annihilate (create) an electron with spin σ on site i within the weakly- and strongly-interacting layer, respectively. There are additional terms, which are only local on the different rungs that the

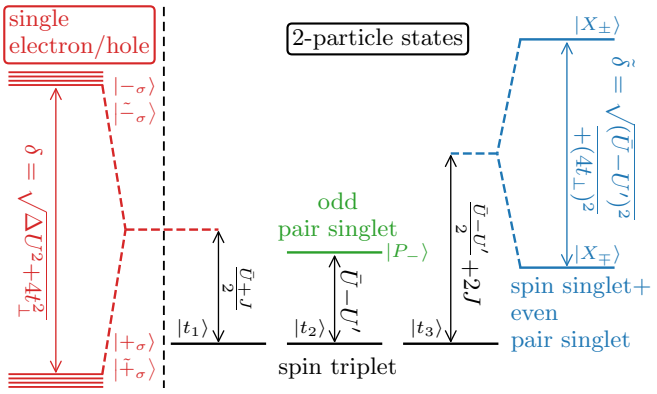

Figure 9.2: Eigenenergies and states of a single rung in dependence on the intra-layer hopping $t_\perp$, the interlayer density repulsion U', the Hund's exchange J, the average Hubbard repulsion $\bar{U} = (U_c + U_d)/2$, and the local interaction difference $\Delta U = (U_d - U_c)/2$ with U_d and U_c being the local Hubbard repulsions within the layers. The states can be separated into half filled states with 2 particles (left) and states containing either one or three electrons (right). Furthermore, there are states that are fully occupied or empty. Those states are not shown in this figure since they are at high energies due to the strong local Hubbard repulsion U_d of the Mott insulating layer, making them negligible. The single particle states $|+_\sigma\rangle, |-_\sigma\rangle$ / single hole states $\left|\tilde{+}_\sigma\right\rangle, \left|\tilde{-}_\sigma\right\rangle$ split up into two groups, which are both four-times degenerate (red). The states containing two electrons decompose into spin triplet $|t_1\rangle, |t_2\rangle, |t_3\rangle$ (shown in black), an odd pair singlet $|P_-\rangle$ (shown in green) and two states being a combination of spin singlet and even pair singlet $|X_+\rangle, |X_-\rangle$ (shown in blue, energetic ordering depends on $\bar{U} \gtrless U'$). If the single electron/hole states are genetically preferred, the ground state of a system containing multiple coupled rungs is expected to be superconducting due to the arising bosonic charge 2e particles. Figure taken from Ref. [125].

heterostructure consists of. Those are given by

$$H_{\text{rung}} = -t_\perp \sum_{i\sigma} \left(c^\dagger_{i\sigma} d_{i\sigma} + \text{ h.c. } \right) + H_{\text{int}} \tag{9.2}$$

including an inter-layer hopping $t_\perp$, as well as multiple interaction terms that can be brought into the Hubbard-Kanamori form

$$\begin{aligned} H_{\text{int}} = &\sum_{i,\alpha} U_\alpha \left(n^\alpha_{i\uparrow} - \frac{1}{2} \right) \left(n^\alpha_{i\downarrow} - \frac{1}{2} \right) + U' \sum_i \left(n^c_{i\uparrow} n^d_{i\downarrow} + n^c_{i\downarrow} n^d_{i\uparrow} \right) + (U' - J) \sum_i \left(n^c_{i\uparrow} n^d_{i\uparrow} + n^c_{i\downarrow} n^d_{i\downarrow} \right) \\ &+ J \sum_i \left(-d^\dagger_{i\uparrow} d_{i\downarrow} c^\dagger_{i\downarrow} c_{i\uparrow} + d^\dagger_{i\uparrow} d^\dagger_{i\downarrow} c_{i\downarrow} c_{i\uparrow} + \text{h.c.} \right) - \left(U' - \tfrac{J}{2} \right) \sum_{i\alpha\sigma} n^\alpha_{i\sigma} \,. \end{aligned} \tag{9.3}$$

Here, U_α describes the local Hubbard repulsion in the layer $\alpha \in \{c, d\}$ with $U_d \gg U_c$, U' is the density repulsion between the layers and J denotes the Hund's coupling. We note that the bilayer is in a particle-hole symmetric form. All terms are additionally visualized in Fig. 9.1(b). If the grand-canonical ensemble is applied, the additional term $-\mu \sum_{i\alpha\sigma} n^\alpha_{i\sigma}$ is directly added to the Hamiltonian as it was already done in some of the previous chapters, leading then to a half-filled system at $\mu = 0$.

9.2 Strong Coupling Regime: Investigation of a Single Rung

In order to understand the mechanism in more detail, we start from the strong coupling regime with small interlayer interactions $t_c, t_d \ll U', t_\perp, J < U_d$ and assume the second local interaction U_c to be small as well ($U_c \ll U_d$) as already mentioned above. In this regime, the intra-layer hoppings can be neglected and individual rungs are nearly decoupled, allowing to understand the mechanism by investigating the spectrum of a single rung. Here, all possible eigenstates and eigenvalues can be computed analytically [125]. For this calculation, we first consider the single rung as a closed

system (disregarding the chemical potential) and discuss the meaning of the chemical potential in the end. The results are shown in Fig. 9.2 except for the fully occupied and empty states, which are negligible due to their higher energy as a consequence of the strong Hubbard repulsion U_d on the Mott insulating layer. There are states containing two particles (right side) and states with one or three particle (single particle/single hole; left side).
The two-particle states can be decomposed even further. There are spin triplet states $|t_1\rangle = |\uparrow_d,\uparrow_d\rangle$, $|t_2\rangle = |\downarrow_d,\downarrow_d\rangle$ and $|t_3\rangle = (|\uparrow_d,\downarrow_c\rangle + |\downarrow_d,\uparrow_c\rangle)/\sqrt{2}$, which are shown in black, and an odd pair singlet $|P_-\rangle = (|\uparrow\downarrow_d,0_c\rangle - |0_d,\uparrow\downarrow_c\rangle)/\sqrt{2}$, which is marked in green. The additional blue states $|\chi_+\rangle, |\chi\rangle$ are a superposition of spin singlet $|s\rangle = (|\uparrow_d,\downarrow_c\rangle - |\downarrow_d,\uparrow_c\rangle)/\sqrt{2}$ and even pair singlet $|P_+\rangle = (|\uparrow\downarrow_d,0_c\rangle - |0_d,\uparrow\downarrow_c\rangle)/\sqrt{2}$ and are given by $|X_+\rangle = \cos(\phi/2)\,|s\rangle + \sin(\phi/2)\,|P_+\rangle$ and $|X_-\rangle = \sin(\phi/2)\,|s\rangle - \cos(\phi/2)\,|P_+\rangle$. Here, the mixing angle ϕ is defined over $\tan(\phi) = 4t_\perp/(\bar{U}-U')$ with $\phi \in [-\pi/2,\pi/2]$, $\bar{U} = (U_d+U_c)/2$. Which of these states is at lower energy, depends on the sign of $\bar{U}-U'$.
Finally, there are states containing a single electron or hole (three electrons). Those states are degenerate at $\mu = 0$ due to particle-hole symmetry and they split up in two groups. At lower energy, there are the bonding states $|+_\sigma\rangle = \cos(\theta/2)\,|\sigma_d,0_c\rangle + \sin(\theta/2)\,|0_d,\sigma_c\rangle$ and $\left|\tilde{+}_\sigma\right\rangle = \cos(\theta/2)\,|\sigma_d,\uparrow\downarrow_c\rangle - \sin(\theta/2)\,|\uparrow\downarrow_d,\sigma_c\rangle$, while the anti-bonding states $|-_\sigma\rangle = \sin(\theta/2)\,|\sigma_d,0_c\rangle - \cos(\theta/2)\,|0_d,\sigma_c\rangle$, $\left|\tilde{-}_\sigma\right\rangle = \sin(\theta/2)\,|\sigma_d,\uparrow\downarrow_c\rangle + \cos(\theta/2)\,|\uparrow\downarrow_d,\sigma_c\rangle$ appear at higher energy. Here, the mixing angle is given by $\tan\theta = 2t_\perp/\Delta U$ with $\theta \in [0,\pi/2]$ and $\Delta U = (U_d-U_c)/2$.
If the bonding single particle/hole states have the lowest energy, the ground states contain a single electron on one layer and a possible Cooper pair on the other layer. Here, the single electron leads to an effective local $S = 1/2$-spin. For a system containing multiple rungs at finite intra-layer hoppings one would further expect those spins to interact, which would result in a magnetic ordering in addition to a superconducting behavior based on the existence of Cooper pairs. In such a system, the chemical potential is then responsible for adjusting the number of Cooper pairs in the system, while the magnetic moment remains present as long as the filling is between one quarter and three quarters.

In the following, we identify the regime, where the single particle/hole states are energetically favored. From Fig. 9.2, we can read that the single particle/hole states have the lowest energy if

$$\frac{\delta}{2} > \frac{\bar{U}+J}{2}\,, \tag{9.4}$$

$$\frac{\bar{U}+J}{2} - \frac{\delta}{2} < \bar{U}-U'\,, \tag{9.5}$$

$$\frac{\bar{U}+J}{2} - \frac{\delta}{2} < \frac{\bar{U}-U'}{2} + 2J - \frac{\tilde{\delta}}{2} \tag{9.6}$$

are fulfilled. We can summarize these conditions to the overall result, that the single electron and hole states are preferred if

$$\delta > \max\left\{\bar{U}+J, 2U'-\bar{U}+J, U'-3J+\tilde{\delta}\right\}\,. \tag{9.7}$$

An intertwined superconducting and magnetic behavior is then expected for small but finite intra-layer hoppings t_c, t_d as mentioned above.
From the eigenenergies in Fig. 9.2, we can also extract the local energy gain of the rung due to charge disportion. This expresses the energy that the rung gained by occupying it with one or three particles instead of two and is given by

$$\Delta E_{\text{local}} = \min E(2 \text{ particles}) - \min E(1 \text{ or } 3 \text{ particles}) \tag{9.8}$$

$$= \min\left[\frac{\delta}{2} - \frac{\bar{U}+J}{2}\,,\quad -U' + \frac{\bar{U}-J}{2} + \frac{\delta}{2}\,,\quad \frac{-U'-\tilde{\delta}+3J+\delta}{2}\right]\,. \tag{9.9}$$

In the following, we always fix one of the parameters to maximize the local energy gain for the other chosen parameters. We choose the inter-layer hopping $t_\perp$, which needs to be fixed to

$$t_\perp = t_\perp^{\max} = \frac{1}{2}\sqrt{J}\cdot\sqrt{4J+2|\bar{U}-U'|}\,. \tag{9.10}$$

Finally, we can briefly investigate how spins and Cooper pairs are split up between both layers. In the strong coupling limit, the local interaction difference $\Delta U = (U_d - U_c)/2$ is rather large leading to a small mixing angle θ. Therefore, the Cooper pairs are mainly present in the proximal metallic layer, while the single electrons being responsible for the local spin are mainly localized in Mott insulating layer. Nevertheless, we note that Eq. (9.7) shows that the mixing angle θ cannot be too small since Eq. (9.7) cannot be fulfilled for a too small inter-layer hopping $t_\perp$. Therefore, superconductivity and magnetic ordering are expected to be present on both layers and thus, to be intertwined.

9.3 Parent State: Magnetic Ordering

In the following, the bilayer model (9.3) is studied numerically using DMRG calculations at fixed filling in finite, as well as infinite systems. A one-dimensional two-leg ladder variant of the model is employed due to the problems of tensor networks in higher dimensions as discussed in Chapter 4. The application of exact numerical methods allows to explore the proposed mechanism well beyond the strong coupling regime where the analysis of a single rung is not sufficient anymore. Unfortunately, the employment of a one-dimensional system has the drawback that correlation functions are not long ranged but can only show a critical quasi long-ranged decay, meaning that they follow a power-law. For our numerical studies, we set $U_d = 1$ and $U_c = 0$ for convenience in addition to fixing $t_\perp$ corresponding to Eq. (9.10) as already mentioned above.

We start this investigation by considering the parent state at quarter filling, where every rung is occupied with one electron. Here, no Cooper pairs are expected in the system based on the strong coupling analysis. Only at larger fillings one-electron and one-hole states mix if Eq. (9.7) is fulfilled, which leads to the occurrence of bound electron pairs. Although no superconductivity is expected at quarter filling, we can still find magnetic ordering due to the local spin of the single-electron states.
The spin of the rung can be connected to electronic annihilation and creation operators via

$$\mathbf{S}_i = \frac{1}{2} \sum_{\alpha=x,y,z} \sum_{b=c,d} \left[\begin{pmatrix} b_{i\uparrow}^\dagger & b_{i\downarrow}^\dagger \end{pmatrix} \sigma^\alpha \begin{pmatrix} b_{i\uparrow} \\ b_{i\downarrow} \end{pmatrix} \right] \boldsymbol{e}_\alpha \tag{9.11}$$

with σ^α being the corresponding Pauli matrix. For the characterization of the magnetic ordering, the spin-spin correlation function

$$C_{i,j}^{\text{spin}} = \langle \mathbf{S}_i \cdot \mathbf{S}_j \rangle = C^{\text{spin}}(R = j - i) \tag{9.12}$$

needs to be analyzed, which only depends on the distance due to translational invariance. Most importantly, we are interested in the Fourier transform

$$S(k) = \frac{1}{L} \sum_{i,j} e^{-ik(i-j)} C_{i,j}^{\text{spin}} = \sum_R e^{ikR} C^{\text{spin}}(R)\,, \tag{9.13}$$

which is also known as the structure factor and which allows for a detailed analysis of the periodicity of the spin-spin correlation.

Numerically, the structure factor is computed in the following way: We use the results from iDMRG calcuations and apply a Gaussian window $g(R) = \exp(-R^2/\sigma^2)$ around $R = 0$ using $\sigma = 100$. Before performing the Fourier transform, we add additional zeros at large distances. Due to the window function, the results are almost zero in this region allowing us to safely assume that zeros were measured here. This leads to a further smoothening of the Fourier transform and a more precise determination of the peak.
For some exemplary values, the magnetic structure factor is shown in Fig. 9.3. From these results, we read off the phases by investigating the main peak. For a maximum at $k = \pi$, the parameter set

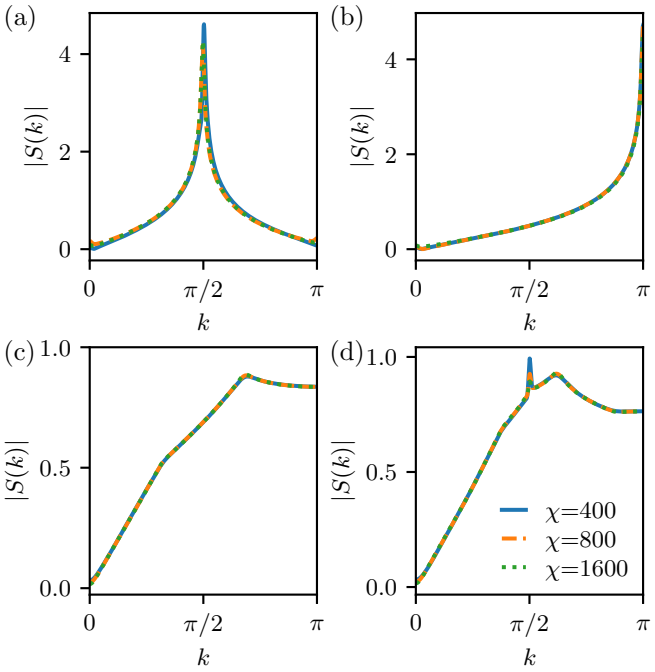

Figure 9.3: Magnetic structure factor for parameters from different phases at quarter filling using multiple bond dimensions. The evaluation of the shape and the peaks of these results, as described in the text, assigns a 4-rung AFM phase to (a), a 2-rung AFM phase to (b) and a disordered phase to (c). For the results of (d), no phase can uniquely be identified. The parameters are given by $U' = 0.4$ and $J, t_c, t_d =$ (a) $1.5, 0.25, -0.25$, (b) $1.5, 0.25, 0.25$, (c) $0.1, 0.5, 0.5$; and (d) $0.3, 0.5, -0.5$. Figure taken from Ref. [125].

is classified into the 2-rung AFM phase as in the case of Fig. 9.3(a), while a maximum at $k = \pi/2$ is identified as 4-rung AFM ordering as e.g. in Fig. 9.3(b). Furthermore, there are parameters where the structure shows no clear visible peak as shown in Fig. 9.3(c). In this case, the system is disordered since no magnetic ordering can be assigned. To find a proper definition of the disordered regime, we compare the maximal height of the peak with the value found at $k = \pi$ for the same parameters. If the peak is less than 1.5 times the value at $k = \pi$, the magnetic phase is denoted to be disorderd. We note that small variations of the treshold do not lead to noteworthy changes of the phase diagram. For some parameters, we are not able to uniquely define the phase as in the example of Fig. 9.3(d). The main shape of the structure factor seems to belong to the disordered regime. Nevertheless, there is a peak at $k = \pi/2$ decaying with the bond dimension and it is unknown whether this peak prevails for infinite bond dimension. Therefore, we disregard parameter sets showing such a behavior and grey them out when showing phase diagrams below. Additionally, correlation functions showing an incommensurable peak are disregarded as well.

Importantly, in order to call a phase magnetically ordered, correlations have to be long ranged or in one dimension quasi long ranged meaning that they have to decay with a power-law. To verify this, the absolute value of the spacial correlation function is extrapolated to infinite bond dimension using the method described in Section 4.6 using bond dimensions of $\chi = 200, 800, 400$. This procedure is only done for even R to get rid of a 2-rung periodicity of the absolute value (coming from a 4-rung periodic correlation function) as we are only interested in the decay of the envelope function. Then, the results at infinite bond dimension are used and an exponential decaying as well as power-law decaying function are fitted to the data. To this end, the fit is performed using a linear function on a logarithmic or double logarithmic scale. The range which is employed for the fitting procedure is found by comparing the results obtained with the smallest and the largest bond dimension used for the extrapolation. Using a logarithm with base 10, the range is cut when the difference exceeds the value 2 ($\log_{10} |y(D_{\max}) - y(D_{\min})| > 2$). In order to

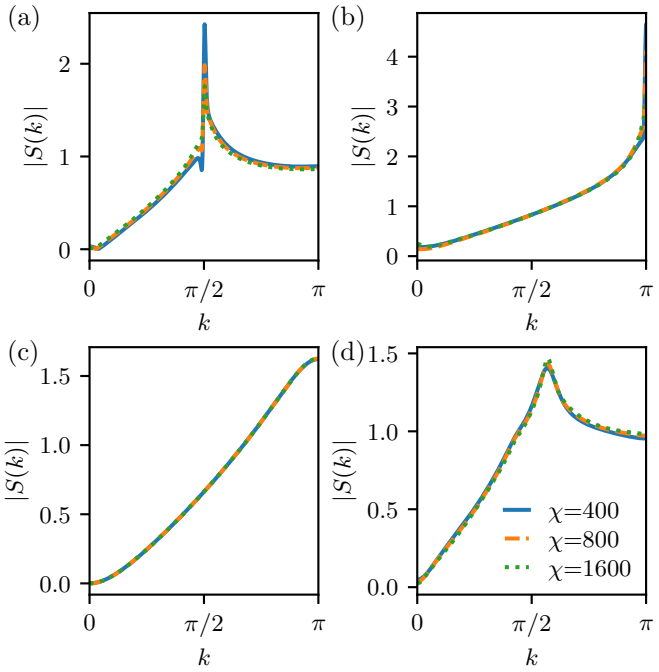

Figure 9.4: Magnetic structure factor for parameters sets from different phases at half filling using multiple bond dimensions. Based on these results, the sets are classified into the (a) 4-rung AFM , (b) 2-rung AFM and (c),(d) disordered phase. The parameter sets are $t_d, t_c, J =$ (a) $2.0, 0.25, 0.25$, (b) $0.0, 0.25, -0.5$, (c) $1.5, 0.25, -0.25$ and (d) $1.0, 0.25, 0.25$ and $U' = 0.4$ for all subpanels. Figure taken from Ref. [125].

define whether the correlations are long ranged, we compare the sum of the squared deviations

$$\sum_{R\,\text{even}} \left[\log(y_R) - f(R)\right]^2 , \tag{9.14}$$

which were minimized during the fit. If the exponential fit corresponds to the smaller sum, the system is denoted as disordered as well. For the magnetic ordering at quarter filling, this mostly appears at the phase boundaries, which we grey out below when drawing the final phase diagram.

Besides from being interested in the magnetic ordering of the parent state at quarter filling, the interplay between the spin-1/2 magnetic moments and the Cooper pairs in the system is investigated as well. Thus, we also analyze the magnetic phases being present at half filling in the same manner as before. In contrast to quarter filling the evaluation of the decay is done using two sets of bond dimensions $\chi = 200, 400, 800$ and $\chi = 400, 800, 1600$, as well as two possible ranges defined by allowing a difference of 1 and 2 between the logarithms with base 10. This is important since a large disordered phase with short-range correlations can be found at half filling making a more careful analysis of the decay essential. If the results do not agree for the different values, the correlation cannot be assigned to a clear phase, usually occurring at the phase transition points. Some exemplary results for the structure factor are shown in Fig. 9.4. Here, (a) and (b) show clear peaks at (a) $k = \pi/2$ and (b) $k = \pi$, which are therefore assigned with the 4-rung AFM and 2-rung AFM phases. In (c) and (d) no such sharp maximum is visible. While (d) is already classified as disordered from the shape of the magnetic structure factor as explained above, (c) still shows a shallow maximum $k = \pi$. Nevertheless, both correlations follow short-ranged exponential decays in real space, identifying both as disordered.

9.3.1 Phase Separation Regime

For certain parameters at quarter filling, the magnetic ordering cannot be analyzed in the way described above, since DMRG calculations lead to unconverged behavior and are incapable of find-

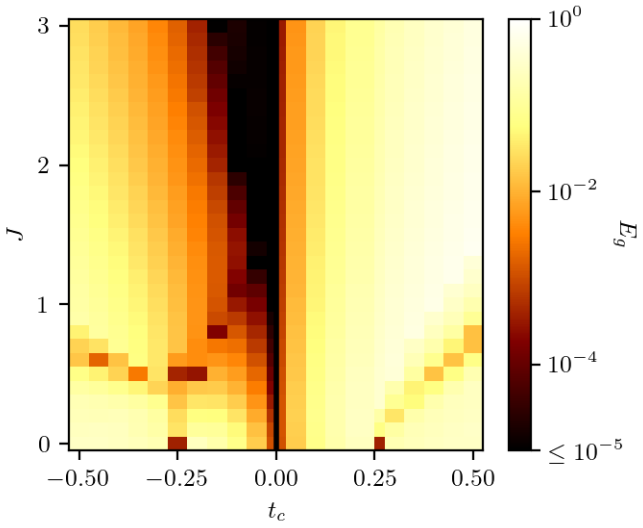

Figure 9.5: Energy difference E_g between the ground state and the lowest excited state with a different magnetic ordering in dependence on the intra-layer hopping t_c of the metallic layer and the Hund's exchange J for $\rho = 1/4$, $t_d = |t_c|$, $J = 3.0$ and $U' = 0.4$m computed with a system size of $L = 8$. There is a part with drastically smaller E_g which we identify as a phase separation regime. On the line $t_c = t_d = 0$, the gap vanishes. Here, the rungs are not coupled leading to no magnetic ordering. The additional minimal lines of the gap are expected to belong to phase boundaries. Figure taken from Ref. [125].

ing the true ground state. In these cases, even the periodicity of the magnetic correlations, used for the classification of different magnetic phases, dramatically change when the start state, the system size or the bond dimension is differed. We find this convergence issue in DMRG calculation for both infinite and finite systems. This fundamental failure of DMRG already indicates that different states assigned to multiple magnetic phases are degenerate. This means that no unique ground state can be identified leading to a phase separation, where multiple phases coexist in large systems. Here, DMRG chooses one of the various degenerate (or nearly degenerate for a finite system size) ground states assigned to one of the multiple possible phases by accident.

To allow for a deeper understanding of this behavior, we aim for comparing energies in order to prove that there are indeed multiple degenerate phases present in this regime. To this end, the whole spectrum of a small and periodic system is calculated using ED. For the classification of all states into magnetic phases, the structure factor (here, no windowing is needed) is calculated for $k = 0, \pi/2$ and π. The momentum corresponding to the largest magnitude is then utilized to identify the magnetic phase (FM for $k = 0$, 2-rung AFM for $k = \pi$ and 4-rung AFM for $k = \pi/2$). We define the energy gap E_g over the difference between the ground state energy and the energy of the first excited state assigned to a different magnetic phase than the ground state. In Fig. 9.5 the results are shown for for a wide range of parameters including a region (large Hund's coupling and small negative intra-layer hopping t_c), where DMRG calculations failed as described above. In the same region, the energy gap is significantly smaller than in the rest of the phase diagram. Both of these observations together are strong evidences for the existence of phase separation in this part of the phase diagram. Furthermore, we find $E_g = 0$ for $t_c = t_d = 0$. Here, there is no coupling between the rungs, leading to no magnetic ordering in the system. All possible orders are therefore degenerate in that case. Finally, we note that there are several supplemental lines where the energy gap is significantly decreased. Those lines are expected to belong to phase boundaries, which is verified below, as the gap closes whenever the phase of the ground state changes.

Additionally, it is possible to investigate the behavior of E_g with the system size. In a phase separation regime, we expect an exact degeneracy in the thermodynamic limit, meaning that the gap should decrease with the system size L. For large system sizes this scaling is expected to scale

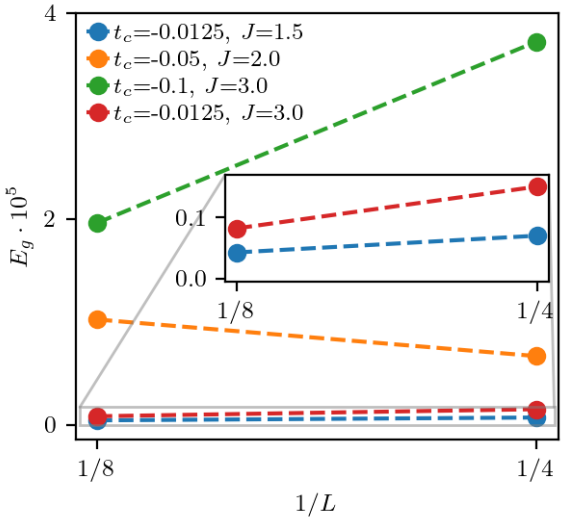

Figure 9.6: Energy difference E_g between the ground state and the lowest excited state with a different magnetic ordering as a function of the system size L for various parameter sets in the phase separation regime identified based on Fig. 9.5. Due to the limitations of ED, only $L = 4$ and $L = 8$ are feasible system sizes respecting the expected periodicties. In the majority of cases, the gap decreases with an increasing system size. The scaling seems to be already nearly proportional to $1/L$. Only for one parameter set, the energy difference slightly increases for a larger system size, which is expected to be due to the small system sizes used for this analysis.

with $1/L$. As already mentioned in Chapter 3, ED is, for an interacting system, limited to a few sites. We can therefore only compare small system sizes and study $L = 4$ and $L = 8$ since both of these sizes are compatible with the magnetic orderings that we have found. In Fig. 9.6, we plot E_g for both system sizes at multiple parameter sets laying within the regime that we identified to host a phase separation. We note that the gap indeed increases with the system size for most parameter sets. Remarkably, the scaling is close to a $1/L$ scaling even for these miniture system sizes. Only for one parameter set, the gap increases when the system size is enlarged, which is presumably an artifact due to the limited number of rungs. We still expect the gap to decrease if system size is further increased.
Due to the results found in this chapter, the phase separation regime is defined using the size of the gap E_g at a system size of $L = 8$. For $E_g < 10^{-4.5}$, the corresponding parameter set is assigned to the phase separation regime.

9.3.2 Magnetic Phase Diagrams

Finally, we summarize the obtained results in phase diagrams, which are shown in Fig. 9.7(a)-(c). At individual points, convergence issues can occur. In these cases, the phase is extrapolated from the surrounding points. For panels (a) and (b), a system at quarter filling in the absence of any Cooper pairs is considered. The difference between both diagrams is that the intra-layer hopping of the Mott-insulating layer is fixed to $t_d = 0.25$ in (a), while both intra-layer hoppings have the same magnitude in (b) due to $t_d = |t_c|$. Both cases have significant similarities. The main part of the phase diagram obeys 2-rung AFM order. Furthermore, there are disordered phases for a small Hund's exchange and large intra-layer hoppings. In this regime, intra-layer hoppings are not negligible and the strong coupling analysis above is not valid anymore leading to the possibility of a disordered magnetic phase. Moreover, 4-rung AFM magnetic behavior is visible in both cases for some regimes with $t_c/t_d < 0$ (in (a) even $t_c \leq -0.25$). Nevertheless, differences between both diagrams are visible as well. For the case with a fixed hopping t_d, shown in (a), an additional regime with a 2-rung AFM ordering is present for large negative t_c and large Hund's exchange. Additionally, the fact that both intra-layer hoppings can get small at the same time in (b) leads to the emergence of the phase separation regime (PS) that was discussed above. We also note that

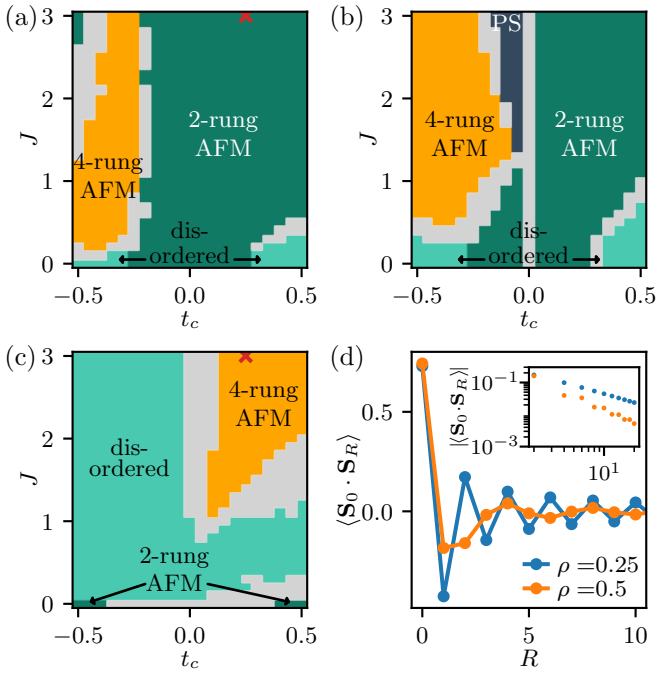

Figure 9.7: Magnetic phases at quarter and half filling. (a), (b) Magnetic phase diagram at quarter filling for fixed $U' = 0.4$ and (a) $t_d = 0.25$, (b) $t_d = |t_c|$ in dependence on the second intra-layer hopping t_c and the Hund's interaction J. In (a) the majority of the phase diagram is classified as a 2-rung AFM phase. Nevertheless, there are also regions with 4-rung AFM ordering and disordered phases. In (b) similar results are found but with a supplemental phase separation regime (PS) appearing at large Hund's exchange and small $t_c < 0$. (c) Phases for half filling utilizing the same parameters as in (a) with a major part being disordered. For large Hund's couplings J and $t_c > 0$ a 4-rung AFM regime arises, while 2-rung AFM prevails for large $|t_c|$ and small J. (d) Spatial spin-spin correlation function for quarter and half filling at the point $t_c = t_d = 0.25$, $J = 3$, $U' = 0.4$, where the red cross is drawn in (c). The ordering changes from 2-rung AFM at quarter filling to 4-rung AFM at half filling. In the inset the absolute value is shown on a log-log scale for every second rung (due to the 4-rung periodicity at half filling), indicating that the magnetic correlations follow a quasi-long-range power-law in both cases. Figure taken from Ref. [125].

there is no magnetic ordering at $t_c = t_d = 0$ since the rungs are decoupled in that case.
The investigation of magnetic order at half filling shows that additional particles and therefore the possible emergence of Cooper pairs can influence the magneric ordering. In Fig. 9.7(c) the phase diagram for a half filled system using the same parameters as in (a) is shown and a significant change compared to the results at quarter filling is visible. Here, the majority of the phase diagram is disordered showing no quasi-long-ranged magnetic ordering. Interestingly, there are still some regimes where 2-rung, as well as 4-rung AFM order can prevail. 2-rung AFM order only exists for extremely small Hund's interactions and intra-layer hoppings with a large absolute value $|t_c|$. The region with 4-rung AFM order is significantly larger appearing for a large Hund's exchange and (significantly large) $t_c > 0$. For an exemplary parameter set of this regime (marked by the red cross), we compare the spatial correlation functions for quarter and half filling as shown in Fig. 9.7(d). We see how the periodicity of the correlation function is indeed different although the amplitude follows a power-law in both cases, suggesting that different quasi long-range order can occur for different fillings.

9.4 Evidences for Superconductivity

After the investigation of the magnetic ordering of the system, especially of the parent state at quarter filling, but also with additional particles in the system, we concentrate on the supercon-

ducting properties in this section. We use multiple indicators for superconductivity which all providecompatible results. This suggests that there is indeed a superconducting regime present in the proposed system. Using these numerical methods, we find that the superconductivity also persists beyond the regime where the strong-coupling analysis of the single rung from above is valid.

9.4.1 Pair Binding Energy

As a first metric for superconductivity, we introduce the pair binding energy

$$E_{\mathrm{B}} = 2E_{N_\uparrow-1,N_\downarrow} - E_{N_\uparrow-1,N_\downarrow-1} - E_{N_\uparrow,N_\downarrow}\,, \tag{9.15}$$

where $E_{N_\uparrow,N_\downarrow}$ is the energy for the system including N_σ electrons with spin σ. Here, it is crucial to converge the results with system size as the pair binding energy is only well defined in the thermodynamic limit [277]. Although a positive pair binding energy $E_{\mathrm{B}} > 0$ is only a necessary but not sufficient indication for superconductivity, it is commonly used to indicate that a system is superconducting in the present form [246, 277–279] or in a slightly adapted version [280, 281]. We can gather a deeper understanding of the pair binding energy by rewriting it as

$$E_{\mathrm{B}} = \underbrace{\left[-\left(E_{N_\uparrow,N_\downarrow} - E_{N_\uparrow-1,N_\downarrow-1}\right)\right]}_{\text{energy gain of a Cooper pair}} - \underbrace{2\cdot\left[-\left(E_{N_\uparrow,N_\downarrow-1} - E_{N_\uparrow-1,N_\downarrow-1}\right)\right]}_{\text{energy gain of 2 single particles}}, \tag{9.16}$$

where we see that the pair binding energy describes the difference of the energy gain (or the negative energy cost) of a Cooper pair and two unbound particles, which is sometimes also used as direct definition of the binding energy (see e.g. Ref. [281] for the case of skyrmions). If the pair binding energy is positive, this shows that adding a pair of two particles is energetically favorable over putting two individual particles. Therefore, it is likely that the two electrons form a bound state (a Cooper pair) and the system is superconducting.
Interestingly, between 1/4 and 3/4 filling, when the strongly-correlated layer is half filled and the weakly-interacting layer is partially filled, the pair binding energy agrees with twice the local energy gain if the intra-layer hoppings are zero, which can be seen from

$$E_{\mathrm{B}} = \underbrace{E_{N_\uparrow-1,N_\downarrow} - E_{N_\uparrow,N_\downarrow}}_{\substack{\text{gain due to adding a}\\ \text{third particle to a rung with two particles}}} + \underbrace{E_{N_\uparrow-1,N_\downarrow} - E_{N_\uparrow-1,N_\downarrow-1}}_{\substack{\text{gain due to removing the}\\ \text{second particle of a rung with two particles}}} \overset{t_c=t_d=0}{=} 2\,\Delta E_{\mathrm{local}}\,. \tag{9.17}$$

Therefore, the pair binding energy has to approach $2\,\Delta E_{\mathrm{local}}$ in the limit $t_c, t_d \to 0$. In Fig. 9.8 the results from the pair binding energy are shown in dependence on the filling and the intra-layer hoppings which are set to be equal. Here, there is a regime with a positive pair binding energy above quarter filling. At quarter filling, it was already expected from the analysis of the single rung that no superconducting phase occurs since no bound electron pairs are present and every rung contains only one electron. Additionally, the pair binding energy indeed approaches twice the local energy gain in the limit of vanishing intra-layer hoppings. Nevertheless, no superconductivity can occur at $t_c = t_d = 0$ since the rungs are uncorrelated. Furthermore, the pair binding energy decreases with larger intra-layer hoppings.

9.4.2 Pair Correlation Function

As mentioned above, the pair binding energy can only be used as a necessary, but not sufficient criterion for superconductivity. Therefore, we employ additional metrics to confirm the existence of superconductivity in our model. One accurate possibility is the evaluation of the singlet pair correlation function

$$C_{i,j}^{\mathrm{pair}} = \frac{1}{4}\left\langle (d_{i,\uparrow}^\dagger d_{i,\downarrow}^\dagger + d_{i,\downarrow}d_{i,\uparrow} - c_{i,\uparrow}^\dagger c_{i,\downarrow}^\dagger - c_{i,\downarrow}c_{i,\uparrow})\cdot(d_{j,\uparrow}^\dagger d_{j,\downarrow}^\dagger + d_{j,\downarrow}d_{j,\uparrow} - c_{j,\uparrow}^\dagger c_{j,\downarrow}^\dagger - c_{j,\downarrow}c_{j,\uparrow})\right\rangle\,. \tag{9.18}$$

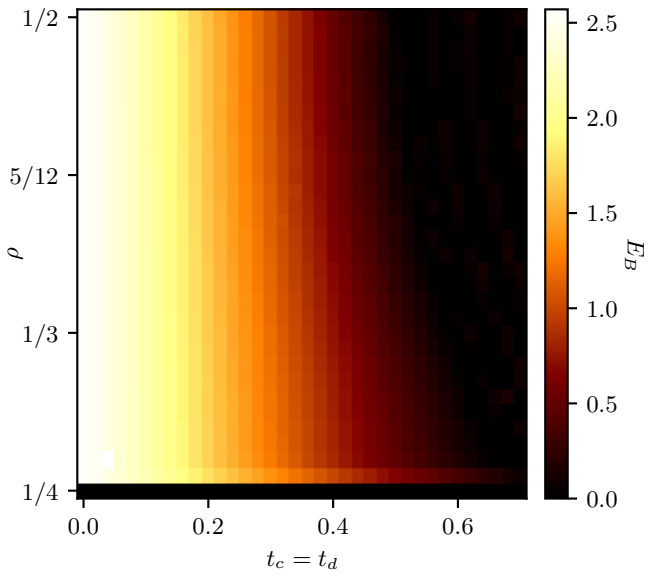

Figure 9.8: Superconducting phase characterized by the pair binding energy in dependence on the intra-layer hoppings $t_c = t_d$ and the filling ρ with $U' = 0.4$ and $J = 3$. Only above quarter filling, a finite pair binding energy can arise. For $t_c = t_d = 0$ the pair binding energy is given by twice the local energy gain (but no superconductivity exists since the rungs are not coupled) and it decreases when the intra-layer hoppings are increased until it reaches zero and there is no superconducting behavior in the system. Additionally, at larger intra-layer hoppings, there is a slight decrease, when the filling approaches 1/2. Figure taken from Ref. [125].

We consider the singlet correlator since this choice should be favoured based on the single rung ground states $|\tilde{+}_\sigma\rangle$ and $|+_\sigma\rangle$. However, a sign change is not expected to lead to significantly different results since the Cooper pairs are expected to be mainly present in the weakly-coupled layer as mentioned before.

Criterion to Find Superconducting Phases

The pair correlation has a long-ranged character if the system is superconducting. Since we analyze a one-dimensional variant of our model, correlation functions can never be truly long-ranged but only critical as already mentioned before. Therefore, even in the superconducting phase, the pair correlation function will decay, but this decay will be algebraic and not exponential. In one-dimensional systems, the pair correlation function can still be quasi long ranged in the non-superconducting regime since several correlation functions can simultaneously be algebraic [282]. Nevertheless, we still expect the pair correlation function to decay faster outside the superconducting regime. Therefore, it is helpful to characterize the speed of the decay via the pairing strength [283, 284]

$$D = \sum_{R=R_1}^{R_2} |C^{\text{pair}}(R)| \tag{9.19}$$

with chosen distances R_1 and R_2. Importantly, R_1 and R_2 needs to be varied to verify the qualitative result (regime of superconductivity) to be independent of the exact values of $R_{1/2}$. Results from the pairing strength are postponed to Subsection 9.4.4, where we compare the pairing strength with the pair binding energy and other traces of superconductivity.

Periodicity and Pair Density Waves

The pair correlation function cannot only be employed to determine the regime of superconductivity but also for the identification of the superconducting phase. To this end, the periodicity of the

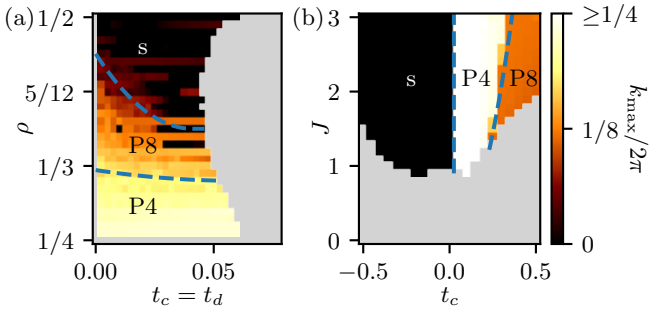

Figure 9.9: Periodicity of the pair correlation function in the superconducting phases based on the maximum of the Fourier transform of the pair correlation function. Here, the Fourier transform was performed with a window function centered around $R = 0$ and bond dimensions between 400 and 3200. (a) The results are shown in dependence on intra-layer hoppings $t_c = t_d$ and filling ρ with $J = 0.45$ and $U' = 0.5$. There are phases with different periodicity: 0-rung (denoted as s), 4-rung (P4) and 8-rung (P8), with the latter ones being pair density waves. Interestingly, the transitions between those phases are found to smooth and only approximate phase transition lines can be drawn. (b) The results are shown in dependence on t_c and the Hund's exchange J with $t_d = 0.25$, $U' = 0.4$ and $\rho = 3/8$. We find a standard s-wave behavior for $t_c \leq 0$ and different FFLO phases with a periodicity of 4 or 8 rungs for $t_c > 0$. In contrast to (a), discrete phases without smooth transitions form. Figure taken from Ref. [125].

correlations are investigated. We differentiate between a monotonic decay, which is denoted with s-wave within this chapter (as an s-wave is expected in this case due to the rung-local effective attraction) and a pair density wave (PDW) or Fulde–Ferrell–Larkin–Ovchinnikov (FFLO) phase when the decay overlaps with a periodic function.

To identify the periodicity, we perform a Fourier transform in the same way as already done to obtain the magnetic structure factor, where we applied a Gaussian window around $R = 0$ before applying the Fourier transform and where we append additional zeros at the ends of the measured correlations. In contrast to the analysis of the magnetic structure factor, we employ results obtained with a finite size DMRG for $L = 60$ within this subsection, unless it is noted otherwise. This has the advantage that various different fixed fillings can be treated which are beyond the reach of iDMRG since huge unit cells would be needed. Additionally, a thinner window function with $\sigma = 20$ is employed. To determine the phase, the maximal value with momentum $k_{\max}$ is used. In Fig. 9.9 these momenta are depicted in the superconducting regime leading to multiple phases. Here, the superconducting regime is identified using the pair binding energy in the case of finite intra-layer hoppings. To circumvent the small fluctuations of the pair binding energy in the non-superconducting regime (due to finite size effects, numerical errors or finite bond dimension), a threshold above zero was employed ((a)$E_B > 0.003$, (b)$E_B > 0.05$).
In the phase diagrams, there are phases with a monotonic decay of the correlation function ($k_{\max} = 0$), while others have an overlapping decay with a periodic function ($k_{\max} \neq 0$). The phases with a uniform decaying correlation function is denoted with s, since an s-wave is expected as explained above. Correlation functions where the decay overlaps a periodic function are associated with PDW or FFLO states (denoted with P4 or P8 associated with the periodicity). Interestingly, the phases can change either continuously as in Fig. 9.9(a), where the filling is varied, or abruptly as e.g. in the phase diagram shown in Fig. 9.9(b) with constant doping. In (a) it is therefore only possible to indicate vague phase transition lines for the dicrete phases of uniform superconductivity, 4-rung and 8-rung periodic FFLO orders. In between these orders, incommensurable FFLO states are likely to appear leading to the observed continuous changes of $k_{\max}$. In both cases, the presented results are only converged on a qualitative level with the bond dimensions. The exact values could slightly change and single points at the boundary could switch phases for significantly larger bond dimensions. Nevertheless, those adjustments are negligible for the presented investigation.
So far, only the maximal value of the momentum dependent pair correlation function has been investigated. In the following, we therefore take a look at the shape to study the pair correlations in

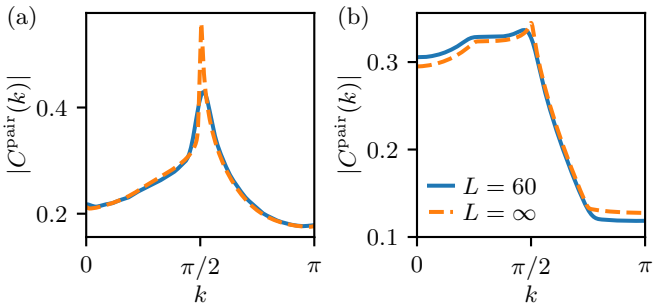

Figure 9.10: Pair correlation function in momentum space obtained by performing a Fourier transform centered around $R = 0$. In both cases, the maximum appears at $\pi/2$ leading to a 4-rung periodic PDW. Nevertheless, the shapes of the peaks are clearly distinguishable with a strong peak in (a) and only a shallow maximum in (b). This result is obtained for both a finite system size with $L = 60$ and an infinite system. Parameters are given by $\rho = 3/8$, $t_d = 0.25$, $J = 3$, $U' = 0.4$ and (a) $t_c = 0.05$, (b) $t_c = 0.25$. Figure taken from Ref. [125].

more detail. Results for two representative parameter sets are depicted in Fig. 9.10. Both parameters are taken from the 4-rung periodic FFLO phase. Nevertheless, only in (a) a well-pronounced peak is visible at $k_{\max} = \pi/2$; in (b) there is a plateau in the regime $0 \leq k_{\max} \leq \pi/2$. In this case, 4-rung and 8-rung periodicity have a very similar weight although the actual maximum is found at $k_{\max} = \pi/2$. To ensure that this broadening is no consequence of finite system sizes, iDMRG simulations are additionally performed for these parameter sets (here, $\sigma = 100$ is applied), leading to the same features. Thus, the absence of a clear peak cannot been traced back to finite size effects. Additionally, at some parameters, it is observed that the found phase does not agree with the real space behavior at large distances. Thus, the analysis is redone in a slightly different way, allowing to avoid the influence of any short ranged behavior.

For the second method, we first divide the correlation by its power-law decay which is obtained by performing a corresponding fit in the system's bulk. This has the big advantage that the decay of the correlation function does not influence the results of the analysis. Moreover, it is crucial to extrapolate the periodicity from the long-range behavior of the correlation function since we aim for avoiding unintended effects coming from short distances. Therefore, the window function is not applied around $R = 0$ but is instead centered within the tail of the correlation function. The correlator $C^{\text{pair}}_{15,x}$ is employed and the window is again centered at $x = 30$ belonging to the bulk of the system. Here, a Gaussian window with $\sigma = 10$ is utilized. Although, the introduced approach for the calculation of the momentum dependent correlations has several advantages, it is still accompanied with a major drawback. Due to the small magnitude of the results in the tail, the correlation function is exceedingly hard to converge here, leading to significant convergence issues for the Fourier transformed pair correlations.
The superconducting phase diagrams in Fig. 9.9 are recalculated with the second method and the results are presented in Fig. 9.11. In contrast to Fig. 9.9, there are three subpanels since the results of (a) exceed the used colorbar. Therefore, the results from (a) are shown again in (c) using a different color-scheme. The shown phase diagrams are converged on a qualitative level, meaning that only insignificant changes to the obtained phases are expected at higher bond dimensions. Nevertheless, due to the poor convergence of the results in tail, noticeable changes to the obtained phase diagram cannot be ruled out completely. Additionally, note that only a very thin window function was used to avoid any influence of the system's boundary.
In panels (a) and (c), a continuously changing $k_{\max}$ is found starting from $k_{\max} = \pi/2$ and decreasing with larger filling factors. This is in agreement with the results obtained before in Fig. 9.9, where a similar behavior was found. Interestingly, at half filling there is a sudden change in $k_{\max}$ suggesting a transition back to a 4-rung periodic phase that was not obtained in Fig. 9.9(a). Additionally, a 2-rung periodic phase seems form at larger intra-layer hoppings, which was also not present before (with the first method). Due to the complicated phase diagram we refrain from indicating any phase boundaries here.

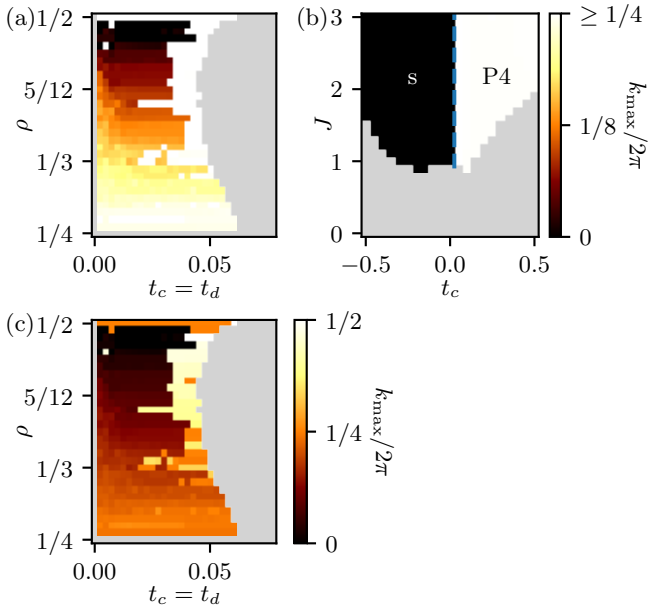

Figure 9.11: Periodicity of the pair correlation function in the superconducting phases. In contrast to Fig. 9.9, the window function is employed in the tail after dividing the correlation function by the corresponding power-law. The parameters are chosen in agreement with Fig. 9.9 and the same bond dimension were used. (a) and (b) are also shown using the same colorbar, while (c) shows the same results as (a) on a different color scheme. (a), (c) For small intra-layer couplings, we find smoothly changing phases with $0 \leq k_{\max} \lesssim \pi/2$ in agreement with Fig. 9.11(a). Only at half filling the system change suddenly back to a 4-rung periodicity, which has not been observed in Fig. 9.11(a). For larger intra-layer hoppings, an additional 2-rung periodic FFLO seems to arise. (b) In agreement with Fig. 9.9, there are discrete phases with a uniform phase for $t_c \leq 0$ and a PDW for $t_c > 0$. Nevertheless, no PDW with a periodicity of 8-rungs is found, but instead the complete PDW phase is suggested to show a 4 rung periodicity. Figure taken from Ref. [125].

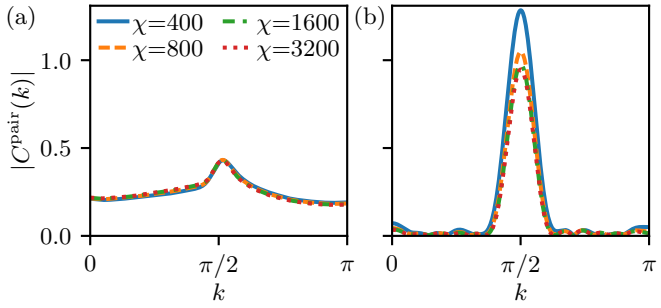

Figure 9.12: Pair correlation function in momentum space comparing the two introduced methods. (a) The window function is applied around the center $R = 0$ before the Fourier transform. (b) The window function is applied to the tail of the correlation after a correction by the corresponding power-law. For this specific parameter sets, both results are converged with the bond dimension χ and have their maximum at the same momentum value. Parameters are given by $\rho = 3/8$, $t_c = 0.05$, $t_d = 0.25$, $U' = 0.4$ and $J = 3$. Figure taken from Ref. [125].

In panel (b), a uniform phase is found for $t_c \leq 0$, while the presence of a 4-rung periodic PDW is suggested for $t_c > 0$. When comparing these results with the one obtained from applying a Fourier transform around $R = 0$ in Fig. 9.9, many similarities are found. Only the previously found 8-rung periodic FFLO phase disappeared and is replaced by an enlarged 4-rung periodic FFLO regime. In both panels we thus note regimes where both aforementioned approaches agree, as well as regions where they lead to different results making no clear decision on the exact phase possible.

Importantly, for (b) both methods agree on the question where a uniform superconducting state is formed and where a PDW occurs.
In addition to comparing the resulting phase diagrams, we are also interested in understanding the different shapes of the complementary approaches. In Fig. 9.12, both methods are compared for a parameter set, where their results agree and where both are well converged. Interestingly, the momentum dependent correlations show a much larger background than the results obtained by centering the window in the tail.
As already mentioned above, there are still many parameters for which the results in the tail are not converged. Some of these are shown in Appendix E.

The presented analysis, where the Fourier transform is found based on the periodicity of the tail has also been performed to obtain the magnetic structure factor. Since there are no significant changes in the magnetic phase diagram, the corresponding inquiry does not lead to any new insights and is therefore not shown.

9.4.3 Computation of an Order Parameter

As we have seen in Chapter 6, where the generalized BCS theory was introduced, as well as in the last chapter, superconducting systems can usually be characterized with an order parameter defined by the expectation value of two annihilation operators. We are currently studying a model which is conserving the total number of particles meaning that any expectation values containing not an equal number of creation and annihilation operator have to be zero. Therefore, the calculation of such an order parameter cannot lead to a finite value. However, one can include a small symmetry breaking term, called pairing field [285], that is not conserving the number of electrons and therefore allows for finite expectation values of two annihilation operators and thus a finite order parameter. The pairing due to the proposed mechanism appears locally on the rungs as we noted in the strong coupling analysis above. Therefore, the pairing field should reflect this behavior and we add rung-local terms

$$H_{\text{pairing}} = h \sum_j \frac{\Delta_j + (\Delta_j)^\dagger}{2} \tag{9.20}$$

to the original Hamiltonian with a small and adjustable pairing field strength h, leading to a local order parameter given by the expectation value $|\langle \Delta_j \rangle|$.
We employ a singlet pairing field with $\Delta_j \propto (d_{j,\downarrow} d_{j,\uparrow} - c_{j,\downarrow} c_{j,\uparrow})$ in accordance with the chosen correlation function from above. The most simple case would be a constant $\Delta_j = (d_{j,\downarrow} d_{j,\uparrow} - c_{j,\downarrow} c_{j,\uparrow})$ belonging to a standard s-wave. However, we have observed that, for some parameters, the correlation functions did not show a monotonic power-law decay but instead display an additional oscillation with a certain periodicity, possibly belonging to an FFLO state. It is necessary that the corresponding pairing field captures this behavior too. Therefore, it is natural to use either an order parameter of $\Delta_j^{\text{FF}} = \exp(j \cdot k)(d_{j,\downarrow} d_{j,\uparrow} - c_{j,\downarrow} c_{j,\uparrow})$ belonging to a Fulde-Ferrel (FF) state or alternatively $\Delta_j^{\text{LO}} = \cos(j \cdot k)(d_{j,\downarrow} d_{j,\uparrow} - c_{j,\downarrow} c_{j,\uparrow})$ which represents a Larkin-Ovchinikov (LO) state. Here, k reflects the periodicity of the pair correlation function.
In numerous systems, both pairing fields give compatible results on the regime where an FFLO phase is present [271]. Nevertheless, in systems without spin-orbit coupling, it is known that the LO state is typically energetically more favourable that the FF state [271, 286–289]. Therefore, we apply an LO state pairing field in the following. The local order parameter is then not uniform on all sites and we define the global order parameter as its maximum

$$\Delta = |\langle \Delta_j \rangle| \quad \text{for} \quad \cos(j \cdot k) = 1\,. \tag{9.21}$$

We study this order parameter around a region where the pair binding energy suggests a superconducting phase transition. We additionally include various pairing field strengths h into the analysis. Since it is natural that the response to the pairing field increases for larger h, we normalize the order parameter by h. The results can be found in Fig. 9.13, where the response to the artificial

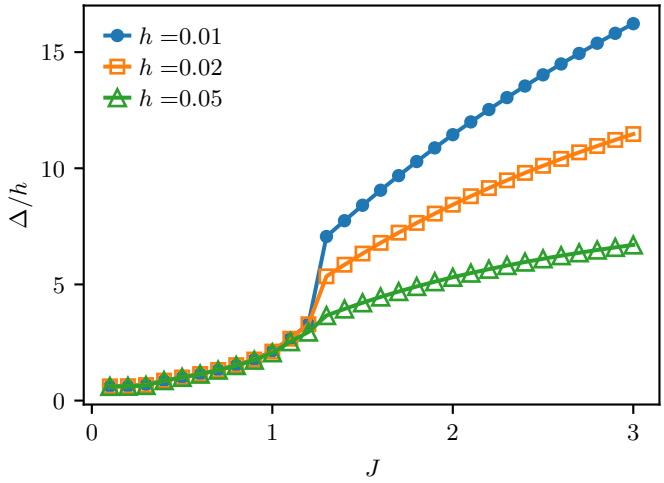

Figure 9.13: Normalized order parameter Δ/h in dependence on the Hund's coupling J with $t_c = t_d = 0.25$ and multiple pairing field strengths h. We note a jump for $1.2 < J < 1.3$ which gets enlarged with decreasing h, being an evidence for a phase transition point. In the non-superconducting phase $J \leq 1.2$ the results are nearly independent of h, while there is a strong dependence in the superconducting phase $J \geq 1.3$. Figure taken from Ref. [125].

pairing field is shown as a function of the Hund's exchange J. For the definition of the periodicity of the pairing field, $k = \pi/2$ is chosen based on the results found in the analysis of the correlation function. For small pairing field strengths, the order parameter shows a jump at $1.2 < J < 1.3$, which is already significant evidence for a phase transition, leading to a classification of superconducting regime for $J \gtrsim 1.3$. Furthermore, this discontinuity gets enlarged when the strength of the pairing fields is decreased. This leads to an infinite jump in the limit $h \to 0$, underlining the conjecture, that a superconducting phase transition exists, even further. Notably, the jump occurs as a consequence of the different h-dependence in the two phases. While the normalized order parameter is nearly independent of the pairing field strength in the non-superconducting phase, a clear dependence is visible in the supposedly superconducting phase. Here, it increases when the pairing field strength is decreased.

This analysis can also been done using the aforementioned FF state instead, leading to an increasing jump at the same position and therefore to the same phase transition point.

Due to the significant difference of the dependence on the pairing field strength, the scaling with this quantity is investigated in the following. Therefore, the order parameter for two exemplary values of J are shown in Fig. 9.14 in dependence of the strength of the artificial pairing field. Here, the results for $J = 0.5$ and $J = 3.0$ are shown since they are located deep inside the identified non-superconducting and superconducting regime, respectively. We find a significantly different behavior in the two phases. The most obvious observation is the fact, that the response is substantially larger in the superconducting regime, explaining the jump that we found for the order parameter when entering this phase. Nevertheless, we note that the order parameter vanishes for $h \to 0$ in both cases, which can be used as an argument for the absence of superconductivity in higher dimensions [285]. However, this argument is not valid in one dimension due to the Mermin-Wagner theorem [290], which states that the continuous $U(1)$ symmetry of the order parameter cannot be broken spontaneously. This immediately leads to the fact that the order parameter has to vanish at $h \to 0$.

Therefore, the predominant observation is the actual scaling of the response. We note that there is a linear dependence on the pairing field strength for the non-superconducting phase, while the curve from the superconducting regime gets steeper for smaller pairing field strengths. In the regime of small pairing fields, the data then follows a powerlaw with an exponent smaller then one.

In the inset of the same plot, the results of the order parameter normalized by the pairing field strength are shown in analogy to the data of Fig. 9.13. Here, we can also read off, how the pairing

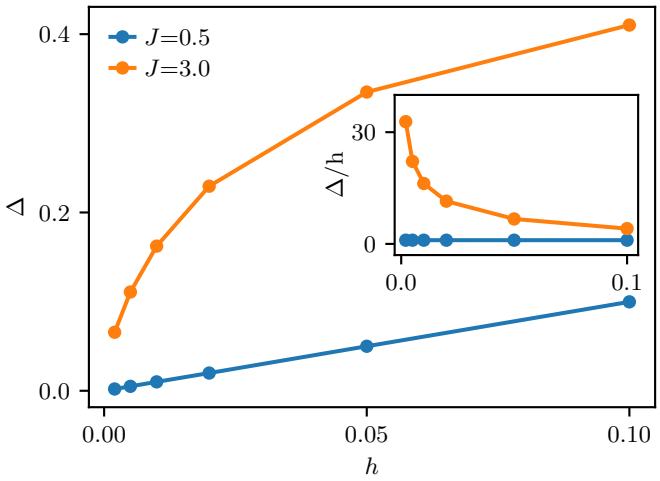

Figure 9.14: Order parameter Δ in dependence on the strength of the artificial pairing field. Exemplary values from the superconducting ($J = 3.0$) and non-superconducting regime ($J = 0.5$) were chosen with $U' = 0.4$ and $t_c = t_d = 0.25$. The response in the superconducting regime is much stronger and shows a distinctive scaling behavior. While the response in the non-superconducting phase scales nearly linear with the pairing field strength, the results concerning the superconducting parameter set show a power-law where the exponent is below one. Inset: Normalized order parameter Δ/h with a diverging behavior for $J = 3.0$ at $h = 0$ while the results for $J = 0.5$ approach a finite value. Figure taken from Ref. [125].

susceptibility

$$\chi_{\text{pair}} = \lim_{h \to 0} \frac{\Delta}{h} \tag{9.22}$$

behaves for the different cases. Due to the linear scaling of the order parameter in the non-superconducting phase, we see an approximately constant value $\Delta/h \approx 1$ leading to the same value for the susceptibility. In stark contrast to this, the data taken from the superconducting phase rapidly increases when the pairing field strength gets reduced and diverges when approaching zero, leading to an infinite pairing susceptibility. This means that an infinitely small pairing field already triggers a finite response of the order parameter.

9.4.4 Combining Various Evidences

In the following, all introduced evidences for superconductivity are compared and fused to gain understanding of the superconducting phases. To this end, results using these different approaches are shown in Fig. 9.15. In (a) the pair binding energy is again depicted in dependence on intra-layer hoppings t_c, t_d and the filling ρ. In contrast to Fig. 9.8, different parameters are used. Most importantly, these parameters fulfill $U' - J > 0$ showing that the proposed mechanism can lead to a superconducting behavior outside the Hund's regime, where $U' - J < 0$ leads to a negative interaction in the Hamiltonian (9.3). Nevertheless, a similar behavior as in Fig. 9.8 is visible, with a finite pair binding energy only above quarter filling, which reduces for larger intra-layer hoppings. Additionally, the pair binding energy is presented at a fixed filling in dependence on the intra-layer hopping t_c and the Hund's exchange J (see Fig. 9.15(b)). Here, we note that a positive pair binding energy does not occur for too small Hund's J, which gets stricter for increasing intra-layer hoppings. Nevertheless, a positive pair binding energy, and therefore a superconducting phase, can be present beyond the strong coupling regime that was studied above. Furthermore, based on the periodicity of the pair correlation function a PDW was identified for $t_c > 0$, while the regime $t_c \leq 0$ appears to belong to a uniform s-wave superconducting phase.
For the parameters employed for this phase diagram, we additionally validate the existence of superconductivity by applying the other methods introduced in this chapter. We first verify that the pair correlation function is quasi long ranged and decays with a power-law. Using an exemplary

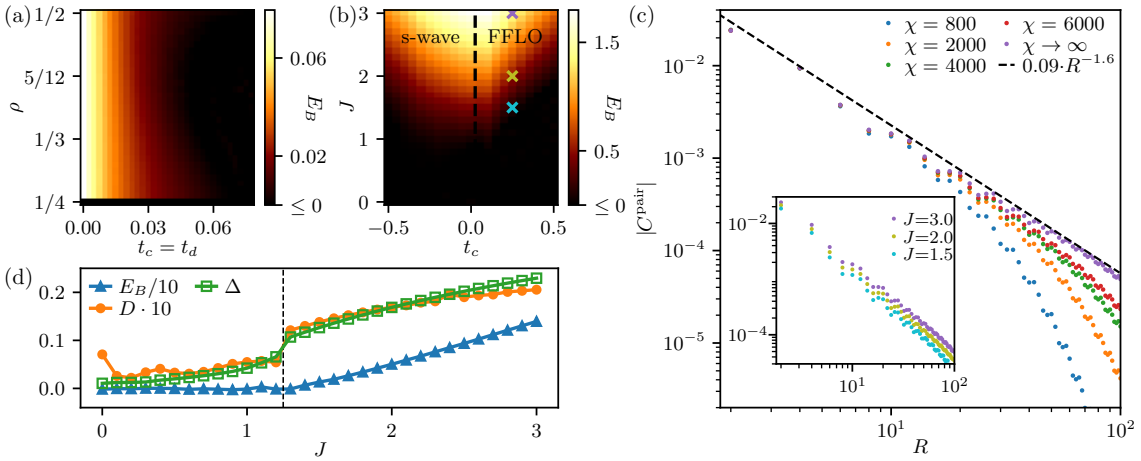

Figure 9.15: Summary of evidences for superconductivity in the proposed bilayer heterostructure. (a), (b) Pair binding energy defining the phase diagrams (a) in dependence on the intra-layer hoppings $t_c = t_d$ and the filling ρ for $J = 0.45$, $U' = 0.5$ and (b) in dependence on t_c (with $t_d = 0.25$) and the Hund's exchange J with $U' = 0.4$. In (a), we note that the pair binding energy is only finite above quarter filling and decreases for larger intra-layer hoppings. Importantly, the parameters are chosen outside the Hund's regime. In (b) finite pair binding energies occur for larger and intermediate Hund's interactions. Numerical results of the pair correlation function suggest a phase transition between a standard s-wave and a PDW phase. (c) Quasi long ranged character of the pair correlation function for the parameters marked by a purple cross in (b) ($t_c = 0.25$, $J = 3$) using even R. The results for different bond dimensions (including the extrapolation to infinite bond dimension) are presented and approach a power-law shown as a dashed line. Inset: Results at infinite bond dimension for different parameters within the superconducting regime, marked by crosses in the corresponding colors in (b) ($t_c = 0.25$, varying J), all showing power-law decays. (d) Comparison of the used superconducting evidences along the line $t_c = 0.25$ in (b) including the pair binding energy, the order parameter computed using an artificial pairing field with strength $h = 0.02$ and the pairing strength D using $R_1 = 5$, $R_2 = 44$ calculated from the pair correlation function. Figure taken from Ref. [125].

parameter set from the superconducting phase, the absolute value of the correlation function is shown in Fig. 9.15(c) for different bond dimensions, where we note that the correlation approaches a power-law behavior for increasing bond dimensions. Using the extrapolation method explained in Section 4.6, we further determine results in the limit of infinite bond dimension which then follow a power-law. For this analysis only results at even R were employed avoiding falsified results from the 4-rung periodicity, leading to a 2-rung periodicity of the absolute value. In the inset, we further notice, that the correlations retain a power-law scaling for other parameters within the superconducting phase, even close to the superconducting phase transition.

Based on the correlation functions, the aforementioned pairing strength is computed and compared to the pair binding energy along a line from phase diagram in (b). Furthermore, we compute the response to a pairing field for the same line with a pairing field strength of $h = 0.02$. Interestingly, the order parameter and the pairing strength have a discontinuity at the same point, agreeing with the phase boundary observed from demanding a positive pair binding energy. Therefore, we can conclude that all three suggested observables provide coinciding results and suggest a superconducting phase transition at approximately the same value for J.

Let us briefly summarize what we have observed in this section. The one-dimensional ladder variant of our model shows certain regimes with a positive pair binding energy, being a necessary but not sufficient criterion for the formation of Cooper pairs. Furthermore, we have studied one of these regimes in more detail and found a power-law decaying pair correlation function. The phase transition can be characterized in multiple ways. We have seen that the pairing strength and the order parameters both show a jump when the pair binding energy gets finite. Furthermore, the

order parameter shows a qualitatively distinguishable scaling in the different presumed phases, leading to an infinite susceptibility in the superconducting regime. For all these reasons, it is likely that our model does indeed show certain regimes with superconductivity.

9.5 Conclusion & Outlook

In this chapter, a new mechanism for the realization of unconventional superconductivity from purely repulsive electronic interactions was introduced and investigated. Based on a heterostructure consisting of a strongly-interacting Mott insulator and a proximal metallic layer, intertwined magnetic ordering and superconducting behavior was found. After the investigation of the strong coupling limit based on the analysis of a single rung, the approach was studied numerically, which suggested that it can lead to superconductivity beyond the regime where this analysis is valid. Tensor network methods and ED were employed to investigate the magnetic and superconducting phase diagrams based on a one-dimensional variant of the model. For the parent state at quarter filling, mainly antiferromagnetic behavior with a periodicity of 2- and 4-rungs was found, although the results also indicated a disordered regime and a region where a phase separation occurs. Notably, doping can change the magnetic phase diagram since the magnetic moments and the possible appearance of Cooper pairs are not independent. Superconductivity, indicated by multiple metrics, was observed in a wide range beyond the strong coupling regime. Here, both uniform superconducting pairing as well as pair density waves with an alternating order parameter in real space were found.

There is still a variety of open questions that should be targeted in the future, with the most pressing one being finding experimental evidence for the proposed mechanism. Multiple material candidates were already mentioned at the beginning of this chapter.
One specific example is twisted trilayer graphene. Here, the coexistence and interaction of dispersive Dirac cones and flat bands have been reported and studied using theoretical and experimental methods [291–300]. These dirac cones and the nearly flat band can play the role of the introduced weakly- and strongly-interacting layer, respectively.
A second candidate is given by infinite-layer nickelates, where a strong Coulomb repulsion has been found in Nickel $3d$ orbitals, which can therefore operate as the Mott insulating constituent. As already mentioned above, it is also known that infinite-layer nickelate superconductors displays short-ranged magnetic correlations. [263–268].

Additionally, a further theoretical investigation is worthwhile, allowing for an even deeper understanding of the mechanism.
Within this chapter, only a one-dimensional variant has been treated numerically. Although a two-dimensional effective low-energy Hamiltonian has been investigated using semiclassical Monte Carlo simulations in Ref. [125], the analysis of the full model in two dimensions is a fascinating route for future research. Although this is expected to be numerically challenging, one could try investigating the model on a small cylinder using DMRG. Apart from a more precise analysis of the two-dimensional case, this would allow to study and compare results on different lattices, e.g. using the triangular or Honeycomb lattice. Although the investigation of the strong coupling regime based on a single rung is not affected by the lattice, the results beyond the validity regime of this analysis may differ.
Furthermore, the influence of supplementary terms added to the Hamiltonian can be studied. Examples are spin-orbit coupling terms, inter-rung interactions or an external magnetic field coupled to the spins of the local rungs. Interestingly, the inclusion of additional effects can lead to the appearance of another competing effective attraction leading to a second pairing channel. This would allow to realize the situation of a metastable subleading superconducting instability, which was analyzed in the last chapter.

Chapter 10

RKKY Interaction for Flat-Band Systems in One Dimension

This chapter is based on the following publication, where the results except for the ones of the spin polarization were already published:
[301] K. Laubscher, C. S. Weber, M. Hünenberger, H. Schoeller, D. M. Kennes, D. Loss, and J. Klinovaja, "Rkky interaction in one-dimensional flat-band lattices", Phys. Rev. B **108**, 155429 (2023)
For this project, I implemented a code to calculate the RKKY interaction based on the algorithm for Green's function in Section 5.4, optimized the code as explained in Chapter 10 and did calculations for the exact RKKY interaction with this code. Partly, I also did the calculations for the exact RKKY coupling with ED and the calculations using the perturbative standard approach (including the necessary implementations). Nevertheless, the data from these two methods shown in the publication were computed by Dr. Katharina Laubscher. Moreover, I contributed to the calculations of the Matsubara Green's functions in real and momentum space. Furthermore, I contributed to the writing of the manuscript.
Note that Dr. Katharina Laubscher and I both calculated the Matsubara Green's functions analytically, but the real space versions were brought into the compact forms (10.19) *and* (10.25) *by Dr. Katharina Laubscher. Furthermore, Figs. 10.1, 10.2, 10.4, 10.5, 10.6, 10.8, containing only my data, are based on similar figures from Dr. Katharina Laubscher, where she used mostly her and partially my data, shown in Ref. [301].*

After the investigation of superconductivity from strong interactions, we now want to investigate the properties of systems, where such strong correlations can be present. One example that we are considering in this chapter are flat-band systems, which have been in the focus of condensed matter research in past years [302–310]. Here, correlation effects are usually dominant due to the vanishing kinetic energy. However, only non-interacting flat band systems are considered in this thesis and the inclusion of correlations is left for the future as it is pointed out at the end of this chapter.
Flat-band systems have been found to be able to host unconventional superconductivity [311–316] and exotic magnetic behavior [317–320], which were the emergent phenomena realized in the last chapter. Moreover, these systems have also been shown to be able to tip the superconducting state towards FFLO phases due to the fact that the momentum of particles on a flat band can be changed without influencing the kinetic energy [321–323].
Flat-band systems have mostly been realized in Moiré materials. These can, for example, be formed by multiple layers with a small twist angle, which introduces a so-called Moiré pattern with a larger unit cell than the original one. The most famous example of a flat-band Moiré material is magic-angle twisted bilayer graphene, which has extensively been studied experimentally and theoretically [324–330]. Another Moiré material with a nearly flat band is twisted trilayer graphene [291–300], which was even mentioned in the last chapter as a possible material, where the explained mechanism can be found.
For all these reasons, flat-band systems are a promising candidate for the realization of the mech-

anism proposed in the last chapter, where strong correlations lead to intertwined magnetism and superconductivity, with an FFLO ground state for a significant part of the superconducting regime. Therefore, these systems are investigated in the following.

When treating quantum systems, we usually investigate them theoretically by studying a clean system. Nevertheless, quantum systems in reality will never be perfectly clean and will always contain impurities. In the following, we therefore study the effect of magnetic impurities. Those can interact with the electrons on the lattice which carry a spin. In particular, we focus on the Ruderman-Kittel-Kasuya-Yosida (RKKY) interaction, which describes the effective indirect interaction of two impurity spins due to their coupling to itinerant electrons of the system [331–333]. The RKKY coupling is of special interest since it has been investigated in a wide range of different fields [334–338], including various unconventional superconductors [338–340]. Interestingly, the RKKY coupling can even be employed for the realization of (unconventional) topological superconductivity (see e.g. Refs. [341–344]), which, however, is beyond the scope of this thesis. Nevertheless, only few efforts have been made to understand the RKKY interaction in flat-band systems, mostly by treating the coupling between the magnetic impurities and the itinerant electrons in second-order perturbation theory, which is the standard approach for the calculation of the RKKY interaction [345–347]. Nevertheless, it was also noted that this approach is not sufficient to cover the full influence of the flat band using the Lieb lattice [348]. Therefore, indirect exchange couplings of impurity spins in the case of flat-band systems are studied carefully and exactly in this chapter using zero temperature and a chemical potential of $\mu = 0$ leading to a partially filled flat band.

In the remainder of this chapter, the RKKY interaction of magnetic impurities is introduced first and the standard perturbative approach for the calculation is discussed. We argue that this formula is not necessarily valid in a flat-band system and a more exact formula is presented. After this, the flat-band models that we investigate are introduced and the qualitative difference between them is explained. We then quickly discuss how the coupling constant between the impurity spins can be calculated numerically in a very efficient way. Afterwards, the RKKY interaction of the models under investigation is presented in dependence on the inter-impurity distance and the local exchange coupling strength, where we note that the results cannot be covered by the standard expression for the RKKY coupling. Interestingly, the results crucially depend on the fact whether the flat band is isolated by a band gap. Finally, we end with an analysis of the RKKY coupling for the transition between the two different models that we use within this chapter.

10.1 RKKY Interaction

The RKKY interaction was first introduced in the 1950s by Rudermann, Kittel, Kasuya and Yosida [331–333], after whom this famous coupling is named. As already briefly mentioned above, the RKKY interaction is an indirect coupling between magnetic impurities (or in general localized magnetic moments), which is mediated by the itinerant electrons in the system. The main idea is that both impurities interact with the spinful fermions of the lattice, and therefore, these fermions are responsible for an effective coupling between the impurities.
RKKY interactions typically occur in metals and they were originally investigated in the electron gas. In the three-dimensional case, they are described by the well known formula (see e.g. [349–351])

$$J_{\mathrm{RKKY}} \propto \frac{x\cos x - \sin x}{x^4} \text{ with } x = 2k_F R, \tag{10.1}$$

where R denotes the distance between the localized spins and k_F is the Fermi momentum. This shows that in this case the standard RKKY interaction has two interesting features: Firstly, it is quasi long ranged and decays with a power-law and secondly, it shows oscillations [351]. Due to these oscillations, the appearance of different signs for the RKKY interaction in the same system is not surprising. Importantly, both of these properties were later confirmed for an electron gas for arbitrary dimension $d \geq 1$ and it was shown that the RKKY interaction decays with R^{-d} at large distances in this case [349].

In gapped system, the indirect exchange coupling of magnetic impurities is exponentially suppressed. In this case, no inherent itinerant electrons are present, but excited electrons still lead to an exponentially decaying indirect exchange coupling, known as the Bloembergen-Rowland interaction [352].
Detailed introductions to the RKKY interaction can, for example, be found in Refs. [335, 351].
Interestingly, the RKKY interaction is usually the most important coupling term between the magnetic impurities and overpowers the direct exchange coupling of the magnetic moments, as well as the magnetic dipole-dipole interaction [253]. Therefore, we only consider the indirect RKKY contributions in the following and neglect the other coupling terms between the impurities. Additionally, the underlying system is presumed to be a lattice model and the RKKY interaction is introduced and defined for this specific case below.

We assume that the system under investigation can be described by H_0 in its non-perturbed form. The magnetic impurities affect the system via a local coupling to the spin of the electrons

$$H_{\text{imp}}^{(i)} = \frac{\tilde{J}_i}{2} \sum_{\sigma,\sigma'} c_{n_i,l_i,\sigma}^{\dagger} \left[\mathbf{S}_i \cdot \boldsymbol{\sigma}\right]^{\sigma\sigma'} c_{n_i,l_i,\sigma'} \,, \tag{10.2}$$

where $c_{n_i,l_i,\sigma}^{(\dagger)}$ denotes the annihilation (creation) operator of a spin-σ electron in the n_i-th unit cell on sublattice l_i. Additionally, we have introduced the classical impurity spin $\mathbf{S}_i$ with $S_i = |\mathbf{S}_i| \gg 1$, as well as the pauli matrix vector $\boldsymbol{\sigma} = (\sigma_x, \sigma_y, \sigma_z)^T$. Since it will turn out to be more useful to shift the factor S_i into the prefactor, we rewrite

$$H_{\text{imp}}^{(i)} = \frac{J_i}{2} \sum_{\sigma,\sigma'} c_{n_i,l_i,\sigma}^{\dagger} \left[\mathbf{s}_i \cdot \boldsymbol{\sigma}\right]^{\sigma\sigma'} c_{n_i,l_i,\sigma'} \tag{10.3}$$

with the local exchange coupling constant $J_i = \tilde{J}_i S_i$ and the normalized vector $\mathbf{s}_i = \mathbf{S}_i / S_i$.

In the following, we consider two impurities in a one-dimensional system, which are placed on sublattices $l_1 = \alpha$ and $l_2 = \beta$, as well as in an inter-impurity distance of $R = (n_2 - n_1)a$. Here, the RKKY interaction only depends on R and not on n_1, n_2 due to the translational invariance of the system. Furthermore, the inter-impurity distance is defined as the distance of the unit cells since the exact distance could be changed by a slight distortion of the individual unit cells, which would not change the considered model.
The full Hamiltonian can be described as

$$H = H_0 + H_{\text{imp}}^{(1)} + H_{\text{imp}}^{(2)} \,. \tag{10.4}$$

In this thesis, we only investigate systems that do not exhibit any spin-orbit coupling. Therefore, the RKKY coupling induced by the itinerant electrons has to be isotropic. We therefore find

$$H_{\text{RKKY}} = J_{\text{RKKY}}^{\alpha\beta}(R)\ \mathbf{s}_1 \cdot \mathbf{s}_2 \tag{10.5}$$

in leading order. In the following, possibilities for determining the RKKY exchange coupling constant $J_{\text{RKKY}}^{\alpha\beta}(R)$ are introduced.

10.1.1 Standard RKKY Expression

The conventional method to calculate the prefactor of the indirect exchange interaction between the two spin impurities is to use a second order perturbation theory. The main idea is to consider the influence of the first impurity on the electrons at the position of the second impurity in first order. We can write [353]

$$H_{\text{RKKY}} = -\frac{J}{2} \sum_{i=1,2} \mathbf{S}_i \cdot \Delta\boldsymbol{\rho}_{(1.\text{order})}\left(n_i, l_i\right) \,. \tag{10.6}$$

Here, $\Delta\boldsymbol{\rho}_{(1.\text{order})}(n_i, l_i)$ is the change of the spin density (in first order in the impurity coupling constant) at the position (n_i, l_i) of one impurity due to the influence of the other magnetic impurity. It is given by

$$\Delta\boldsymbol{\rho}_{(1.\text{order})}(n_i, l_i) = \sum_{\alpha,\beta} \boldsymbol{\sigma}_{\sigma\sigma'} \left\langle n_{\sigma\sigma'}(n_i, l_i) \right\rangle_{(1.\text{order})} \tag{10.7}$$

with $n_{\sigma,\sigma'}(n_i, l_i) = c^\dagger_{n_i,l_i,\sigma} c_{n_i,l_i,\sigma'}$. This leads to the second order contribution in the local exchange coupling strength, which is the leading order of the RKKY interaction. We refrain from discussing the detailed derivation here and the reader is referred to [353] for the full calculation.
After expressing the second order contribution with Green's functions, one arrives at an interaction of the form (10.5) with [347, 353–356]

$$J^{\alpha\beta}_{\text{RKKY}}(R) = -\frac{J_1 J_2}{2\pi} \int_{-\infty}^{0} d\omega \, \text{Im}[G^{R,(0)}_{\alpha\beta}(R,\omega) G^{R,(0)}_{\beta\alpha}(-R,\omega)] \tag{10.8}$$

for zero temperature and a chemical potential of $\mu = 0$, which is assumed for the entire chapter. Here, $G^{R,(0)}_{\alpha\beta}(r,\omega)$ denotes the retarded Green's function of the unperturbed system for a single spin sector, where we assume $H^{(0)}_\uparrow = H^{(0)}_\downarrow = H^{(0)}$. For the numerical evaluation of this expression, we aim for avoiding an integration path close to the poles on the real axis. To archive this, the integral can be transferred to the Matsubara space, which leads (at zero temperature) to

$$J^{\alpha\beta}_{\text{RKKY}}(R) = -\frac{J_1 J_2}{\pi} \int_{-\infty}^{\infty} d\omega \, \text{Im}\left[G^{R,(0)}_{\alpha\beta}(R,\omega) G^{R,(0)}_{\beta\alpha}(-R,\omega)\right] n_\text{F}(\omega) \tag{10.9}$$

$$= -\frac{J_1 J_2}{\pi} \int_{0}^{\infty} d\omega \, G^{(0)}_{\alpha\beta}(R, i\omega) \left[G^{(0)}_{\alpha\beta}(R, -i\omega)\right]^\star , \tag{10.10}$$

which is used for all numerical calculations within this chapter.

10.1.2 RKKY Interaction in Flat Bands

As already mentioned above, the standard expression for the RKKY interaction relies on perturbation theory and is therefore only valid if the local coupling constants are small compared to the other energy scales, such as the bandwidth. For a vanishing bandwidth, it is thus unclear whether the standard approach is applicable for the calculation of the RKKY coupling. In this case, it is still possible to investigate the RKKY interaction which can be calculated via the energy difference between an aligned (ferromagnetic, FM) and anti-aligned (antiferromagnetic, AFM) configuration of the two impurities [334, 357]

$$J^{\alpha\beta}_{\text{RKKY}}(R) = \frac{E^{\alpha\beta}_{\text{FM}}(R) - E^{\alpha\beta}_{\text{AFM}}(R)}{2} . \tag{10.11}$$

We can confirm this by an explicit calculation of the energy difference for the effective leading order Hamiltonian $H_0 + J^{\alpha\beta}_{\text{RKKY}}(R)\ \mathbf{s}_1 \cdot \mathbf{s}_2$. We find

$$E^{\alpha\beta}_{\text{FM}}(R) = \left\langle H^{\text{FM}} \right\rangle = E_0 + J^{\alpha\beta}_{\text{RKKY}}(R) , \quad E^{\alpha\beta}_{\text{AFM}} = \left\langle H^{\text{AFM}} \right\rangle = E_0 - J^{\alpha\beta}_{\text{RKKY}}(R) \tag{10.12}$$

where E_0 denotes the ground state energy of the impurity free model. Here, we dropped that the Hamiltonians depend on α, β and R for convenience. From Eqs. (10.12) one can then immediately derive Eq. (10.11). This expression of the RKKY interaction is evidently not restricted to flat-band systems but can be used for systems with purely dispersive bands as well. In this case, the exact formula (10.11) leads to the same result as the perturbative alternative (10.8).

10.2 Flat-Band Models

Flat-band systems have been realized on a variety of different lattices. Examples are the Lieb (first introduced in Ref. [358]), dice (first introduced in Ref. [359]) and Kagome lattices in the

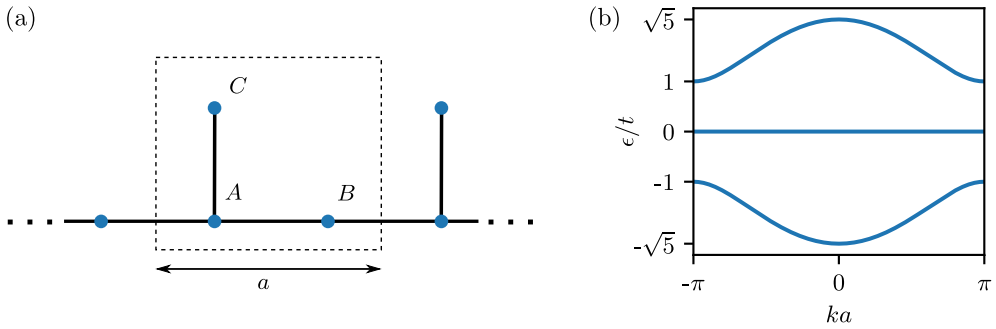

Figure 10.1: Introduction of the stub lattice. (a) Schematic representation of the stub lattice, where connected sites are coupled with a hopping t. The unit cell with size a is denoted with the dashed lines. The sublattices are named A, B and C. (b) Band structure showing that the flat band is isolated from the dispersive bands by a gap of size $|t|$. Figure based on a part of a similar figure in Ref. [301].

case of two-dimensional systems. Nevertheless, flat-band lattices can also be constructed in one-dimensional systems, including the cross lattice or the sawtooth chain. The reader is referred to Refs. [307, 360–362] for more detailed studies on numerous flat-band lattices including descriptions of the lattices mentioned above.
In this chapter, in order to investigate the effect of magnetic impurities in systems with flat bands, two one-dimensional systems, the stub and the diamond lattice, are studied. Those two models are especially suitable since they represent two qualitatively distinguishable cases. One of them has an isolated flat band, while the flat band of the other one crosses two dispersive bands.

10.2.1 Stub Lattice

The first model that is introduced in the following is the stub lattice. This lattice consists of unit cells with three sites that we label with A, B, and C. The structure of the model is shown in Fig. 10.1(a), where we see that neighboring A and B sites, as well as A and C sites within the same unit cell, are coupled with the hopping parameter t. In this chapter, the hopping parameter is chosen to be t in contrast to previous chapters, but note that the additional sign can be gauged away for the models used in the following. The Hamiltonian of the stub lattice is given by

$$H_{\text{stub}} = t \sum_n \left(c^\dagger_{n,A} c_{n,B} + c^\dagger_{n,C} c_{n,A} + c^\dagger_{n+1,B} c_{n,A} \right) + \text{h.c.} \tag{10.13}$$

with $c^{(\dagger)}_{n,X}$ being the annihilation (creation) operator of a spinless fermion on site X in the n-th unit cell. Performing a Fourier transform, one can translate the model to momentum space which leads to

$$H = \sum_k \psi^\dagger_k \mathcal{H}(k) \psi_k \text{ with } \psi_k = (c_{k,A}, c_{k,B}, c_{k,C})^T \,. \tag{10.14}$$

Here, $c_{k,X} = \sum_{n,X} e^{-ikn} c_{n,X}$ and $c^\dagger_{k,X} = \sum_{n,X} e^{ikn} c^\dagger_{n,X}$ are the annihilation and creation operator in momentum space and the matrix $\mathcal{H}(k)$ is given by

$$\mathcal{H}_{\text{stub}}(k) = t \begin{pmatrix} 0 & 1+e^{ika} & 1 \\ 1+e^{-ika} & 0 & 0 \\ 1 & 0 & 0 \end{pmatrix}, \tag{10.15}$$

for the stub lattice.
We diagonalize this matrix and find a band structure of

$$\epsilon_1(k) = 0 \quad \epsilon_2(k) = -\sqrt{3+2\cos(ka)}\, t \quad \epsilon_3(k) = \sqrt{3+2\cos(ka)}\, t \tag{10.16}$$

with one flat and two dispersive bands. The band structure is shown in Fig. 10.1(b). We see that the flat band lies in the center of the gap between the two dispersive bands and is separated from both of them by a gap of size $|t|$. The eigenvectors are given by

$$\mathbf{v}_1(k) = \sqrt{\frac{2+2\cos(ka)}{3+2\cos(ka)}} \begin{pmatrix} 0 \\ -\frac{1}{e^{ika}+1} \\ 1 \end{pmatrix}, \qquad \mathbf{v}_2(k) = \frac{1}{\sqrt{6+4\cos(ka)}} \begin{pmatrix} -\sqrt{3+2\cos(ka)} \\ 1+e^{-ika} \\ 1 \end{pmatrix},$$
$$\mathbf{v}_3(k) = \frac{1}{\sqrt{6+4\cos(ka)}} \begin{pmatrix} \sqrt{3+2\cos(ka)} \\ 1+e^{-ika} \\ 1 \end{pmatrix}. \tag{10.17}$$

Interestingly, the eigenstates of the flat band vanish on sublattice A and thus they are only present on sublattices B and C.

We now calculate the Matsubara Green's functions of an infinite system analytically. This allows to calculate the perturbative expression (10.8) by exploiting its form (10.10) without any finite size effects. For convenience, we compute the Matsubara Green's functions with $a = t = 1$. The general results could be obtained by replacing $G^{(0)}(k, i\omega) \to G^{(0)}(ka, i\omega/t)/t$ and $G^{(0)}(r, i\omega) \to G^{(0)}(r/a, i\omega/t)/t$. In momentum space we find according to $G^{(0)}(k, i\omega) = [i\omega - \mathcal{H}(k)]^{-1}$ (see Appendix F for details)

$$G^{(0)}(k,i\omega) = \frac{1}{6+4\cos(k)} \cdot$$
$$\begin{pmatrix} -\frac{2i\omega[3+2\cos(k)]}{\omega^2+3+2\cos(k)} & -\frac{2(1+e^{ik})[3+2\cos(k)]}{\omega^2+3+2\cos(k)} & -\frac{2[3+2\cos(k)]}{\omega^2+3+2\cos(k)} \\ -\frac{2[3+2\cos(k)](1+e^{-ik})}{\omega^2+3+2\cos(k)} & -\frac{2i\omega[2+2\cos(k)]}{\omega^2+3+2\cos(k)} + \frac{2}{i\omega} & -\frac{2i\omega(1+e^{-ik})}{\omega^2+3+2\cos(k)} - \frac{2[2+2\cos(k)]}{i\omega(e^{ik}+1)} \\ -\frac{2[3+2\cos(k)]}{\omega^2+3+2\cos(k)} & -\frac{2i\omega(1+e^{ik})}{\omega^2+3+2\cos(k)} - \frac{2(2+2\cos(k))}{i\omega(1+e^{-ik})} & \frac{-2i\omega}{\omega^2+3+2\cos(k)} + \frac{2[2+2\cos(k)]}{i\omega} \end{pmatrix}. \tag{10.18}$$

The real space Matsubara Green's function is then given by the Fourier transform $G^{(0)}_{\alpha\beta}(r, i\omega) = \int_{-\pi}^{\pi} \frac{dk}{2\pi} G^{(0)}_{\alpha\beta}(k, i\omega)\, e^{ikr}$ with $G^{(0)}_{\alpha\beta}(r, i\omega) = [G^{(0)}(r, i\omega)]_{\alpha\beta}$ and $G^{(0)}_{\alpha\beta}(k, i\omega) = [G^{(0)}(k, i\omega)]_{\alpha\beta}$. These integrals can be solved rather easily by replacing $z = e^{ikr}$ and applying the residue theorem (see Appendix F for details). The real space Matsubara Green's function is then given

$$G^{(0)}(r, i\omega) =$$
$$\begin{pmatrix} -\frac{i\,2^{-r}\omega(-\omega^2-3+\eta)^r}{\eta} & \frac{2^{-r-1}\left(-\omega^2-5+\eta\right)\left(-\omega^2-3+\eta\right)^r}{\omega^2+5} & -\frac{2^{-r}(-\omega^2-3+\eta)^r}{\eta} \\ \frac{2^{-r-1}\left(\omega^2+5+\eta\right)\left(-\omega^2-3+\eta\right)^r}{\omega^2+5} - \delta_{r,0} & -\left(1+\frac{1}{\omega^2}\right)\frac{i\,2^{-r}\omega(-\omega^2-3+\eta)^r}{\eta} & \frac{2^{-r-1}\left(\omega^2+5+\eta\right)\left(-\omega^2-3+\eta\right)^r}{i\omega(\omega^2+5)} - \frac{\delta_{r,0}}{i\omega} \\ -\frac{2^{-r}(-\omega^2-3+\eta)^r}{\eta} & \frac{2^{-r-1}\left(-\omega^2-5+\eta\right)\left(-\omega^2-3+\eta\right)^r}{i\omega(\omega^2+5)} & \frac{i\,2^{-r}(-\omega^2-3+\eta)^r}{\omega\eta} + \frac{\delta_{r,0}}{i\omega} \end{pmatrix} \tag{10.19}$$

with $r \geq 0$, $\omega \neq 0$ and $\eta = \sqrt{(\omega^2+1)\,(\omega^2+5)}$.

10.2.2 Diamond Lattice

The second model under investigation is the diamond lattice, which has a flat band that is not seperated by a gap in contrast to the stub lattice. The structure of the diamond and the stub lattice is very similar, but there is an additional hopping between the C and the A site of the neighboring unit cells leading to an equivalence of the B and C sites. The model structure is shown in Fig. 10.2, which leads to a Hamiltonian of

$$H_{\text{dia}} = t \sum_n \left(c^\dagger_{n,A} c_{n,B} + c^\dagger_{n,A} c_{n,C} + c^\dagger_{n+1,A} c_{n,B} + c^\dagger_{n+1,A} c_{n,C} \right) + \text{h.c.} \tag{10.20}$$

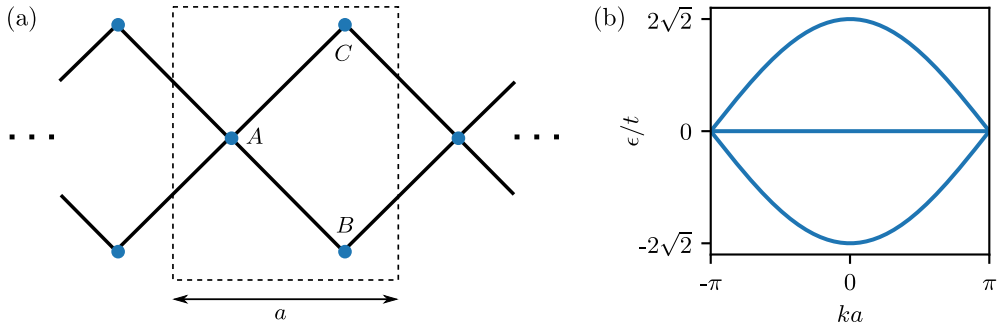

Figure 10.2: Introduction of the diamond lattice. (a) Representation of the diamond lattice similar to the one of the stub lattice in Fig 10.1(a). There is an additional hopping between A and C sites of neighboring unit cells in comparison to the stub lattice. (b) Band structure of the diamond lattice. Here, there is no energy gap separating the flat band, which qualitatively distinguishes this model from the stub lattice. Figure based on a part of a similar figure in Ref. [301].

We can rewrite the Hamiltonian in momentum space according to Eq. (10.14), which leads to

$$\mathcal{H}_{\text{dia}}(k) = t \begin{pmatrix} 0 & 1+e^{ika} & 1+e^{ika} \\ 1+e^{-ika} & 0 & 0 \\ 1+e^{-ika} & 0 & 0 \end{pmatrix} . \tag{10.21}$$

Diagonalizing the matrix leads to energy bands of

$$\epsilon_1(k) = 0\,, \quad \epsilon_2(k) = -2\sqrt{2}\cos(ka/2)t, \quad \epsilon_3(k) = 2\sqrt{2}\cos(ka/2)t\,, \tag{10.22}$$

which are shown in Fig. 10.2(b). As already mentioned above, the dispersive bands cross the flat band so that it is not isolated for this model. The corresponding eigenvectors are

$$\mathbf{v}_1(k) = \frac{1}{\sqrt{2}} \begin{pmatrix} 0 \\ -1 \\ 1 \end{pmatrix}, \qquad \mathbf{v}_2(k) = \frac{1}{2} \begin{pmatrix} -\sqrt{2}e^{ika/2} \\ 1 \\ 1 \end{pmatrix}, \qquad \mathbf{v}_3(k) = \frac{1}{2} \begin{pmatrix} \sqrt{2}e^{ika/2} \\ 1 \\ 1 \end{pmatrix}, \tag{10.23}$$

indicating that the flat band is again only present on sublattices B and C.
We can calculate the Matsubara Green's function in the same way as for the stub lattice for $a = t = 1$ and find

$$G^{(0)}(k, i\omega) = \frac{1}{4} \begin{pmatrix} \frac{-4i\omega}{\omega^2+8\cos^2(k/2)} & \frac{-8\cos(k/2)e^{ik/2}}{\omega^2+8\cos^2(k/2)} & \frac{-8\cos(k/2)e^{ik/2}}{\omega^2+8\cos^2(k/2)} \\ \frac{-8\cos(k/2)e^{-ik/2}}{\omega^2+8\cos^2(k/2)} & \frac{2}{i\omega} - \frac{2i\omega}{\omega^2+8\cos^2(k/2)} & -\frac{2}{i\omega} - \frac{2i\omega}{\omega^2+8\cos^2(k/2)} \\ \frac{-8\cos(k/2)e^{-ik/2}}{\omega^2+8\cos^2(k/2)} & -\frac{2}{i\omega} - \frac{2i\omega}{\omega^2+8\cos^2(k/2)} & \frac{2}{i\omega} - \frac{2i\omega}{\omega^2+8\cos^2(k/2)} \end{pmatrix} \tag{10.24}$$

in momentum space (see Appendix F for details), while the real space version is given by

$$G^{(0)}(r, i\omega) = \begin{pmatrix} \frac{-i\left[-1+\frac{\omega}{4}(-\omega+\gamma)\right]^r}{\gamma} & \frac{4^{-1-r}(\omega-\gamma)[-4+\omega(-\omega+\gamma)]^r}{\gamma} & \frac{4^{-1-r}(\omega-\gamma)[-4+\omega(-\omega+\gamma)]^r}{\gamma} \\ \frac{4^{-1-r}(\omega+\gamma)[-4+\omega(-\omega+\gamma)]^r}{\gamma} - \frac{\delta_{r,0}}{2} & \frac{1}{2}\left(\frac{-i\left[-1+\frac{\omega}{4}(-\omega+\gamma)\right]^r}{\gamma} + \frac{\delta_{r,0}}{i\omega}\right) & \frac{1}{2}\left(\frac{-i\left[-1+\frac{\omega}{4}(-\omega+\gamma)\right]^r}{\gamma} - \frac{\delta_{r,0}}{i\omega}\right) \\ \frac{4^{-1-r}(\omega+\gamma)[-4+\omega(-\omega+\gamma)]^r}{\gamma} - \frac{\delta_{r,0}}{2} & \frac{1}{2}\left(\frac{-i\left[-1+\frac{\omega}{4}(-\omega+\gamma)\right]^r}{\gamma} - \frac{\delta_{r,0}}{i\omega}\right) & \frac{1}{2}\left(\frac{-i\left[-1+\frac{\omega}{4}(-\omega+\gamma)\right]^r}{\gamma} + \frac{\delta_{r,0}}{i\omega}\right) \end{pmatrix} \tag{10.25}$$

with $r \geq 0$, $\omega \neq 0$ and $\gamma = \text{sgn}(\omega)\sqrt{8+\omega^2}$ (see Appendix F for details).

10.3 Effective Calculation of the RKKY coupling

The RKKY interaction can be calculated exactly using Eq. (10.11) as already mentioned above. Here, it is straightforward to calculate the energy difference using exact diagonalization with the full Hamiltonian that can be represented by a $6N \times 6N$ matrix for a system with N unit cells. Each matrix dimension is given by *sites per unit cell* $\times$ *spin degrees of freedom* $\times$ *number of unit cells*$= 6N$. Nevertheless, there are multiple ways to reduce the numerical effort, so that computation time is saved and the maximal simulatable system size gets increased.
Below, we observe that the different spin sectors can be decoupled and connected, so that the matrix dimensions can be reduced by a factor of 2. Additionally, we discuss how the RKKY interaction (10.11) can be calculated via Green's functions and how this can be done in an efficient way using the algorithm that was presented in Section 5.4.

10.3.1 Decoupling of Spin Sectors

We first note, that the different spin sectors of the Hamiltonian do not couple even in the presence of magnetic impurities. We can therefore write

$$\mathcal{H} = \begin{pmatrix} \mathcal{H}_\uparrow & 0 \\ 0 & \mathcal{H}_\downarrow \end{pmatrix} \tag{10.26}$$

and diagonalize $\mathcal{H}_\uparrow$ and $\mathcal{H}_\downarrow$ separately. This reduces the numerical cost already significantly since ED typically scales with D^3 with D denoting the matrix dimension. Nevertheless, the numerical effort of ED can be diminished even further by connecting $\mathcal{H}_\uparrow$ with $\mathcal{H}_\downarrow$. In this case, only the diagonalization of one of the spin sectors is necessary and we gain another factor of two.
To this end, we exploit that the Hamiltonians of spin-up and spin-down in the presence of the impurities are given by

$$H_\uparrow = H^{(0)} + H_{\text{imp}}\,, \quad H_\downarrow = H^{(0)} - H_{\text{imp}}\,, \tag{10.27}$$

respectively. As the sign of the hopping can be changed via gauge transformations (equivalent to the case of a chain shown in Ref. [363]), we find the connection

$$H_\uparrow = -H_\downarrow \tag{10.28}$$

between the two uncoupled spin parts of the Hamiltonian. In the exact diagonalization approach it is therefore sufficient to diagonalize only one of the two matrices in order to get the full single particle spectrum for both spins. The spectrum of the other spin sector can be simply obtained via $\epsilon_{i,\uparrow} = -\epsilon_{i,\downarrow}$. Additionally, the eigenstates of both sectors coincide in the new gauge and they could be back-transformed to achieve the eigenstates in the original gauge.

10.3.2 Calculation using Green's Functions

It is also possible to calculate the energy of the ground state by using Green's functions. We can use this approach to calculate the energy difference between the ferromagnetic and the antiferromagnetic configuration, and therefore the RKKY interaction. Since the different spin sectors decouple according to Eq. (10.26), we can calculate the energy difference for both sectors separately. In the end, we will see that the energy differences of spin up and spin down are connected so that it is again sufficient to calculate only one of them. In the following, only one spin sector is considered and the spin index is dropped for convenience. We can then write the energy difference as

$$\begin{aligned}
\Delta E =\ & E_{FM} - E_{AFM} = \left\langle H^{\text{FM}} \right\rangle - \left\langle H^{\text{AFM}} \right\rangle \\
&= \sum_{n\nu,m\lambda} \mathcal{H}^{\text{FM}}_{n\nu,m\lambda} \left\langle c^\dagger_{n,\nu} c_{m,\lambda} \right\rangle_{\text{FM}} - \sum_{n\nu,m\lambda} \mathcal{H}^{\text{AFM}}_{n\nu,m\lambda} \left\langle c^\dagger_{n,\nu} c_{m,\lambda} \right\rangle_{\text{AFM}} \\
= &\left(\sum_{n\nu,m\lambda} \mathcal{H}^{\text{FM}}_{n\nu,m\lambda} \frac{1}{2\pi} \int_{-\infty}^{\infty} d\omega\, e^{i\omega 0^+} G^{\text{FM}}_{m\lambda,n\nu}(i\omega) \right) - \left(\sum_{n\nu,m\lambda} \mathcal{H}^{\text{AFM}}_{n\nu,m\lambda} \frac{1}{2\pi} \int_{-\infty}^{\infty} d\omega\, e^{i\omega 0^+} G^{\text{AFM}}_{m\lambda,n\nu}(i\omega) \right).
\end{aligned} \tag{10.29}$$

Here, we used that the needed expectation values are given by

$$\begin{aligned}\left\langle c^\dagger_{n,\nu} c_{m,\lambda}\right\rangle &= \frac{1}{i} G^<_{m\lambda,n\nu}(0,0) = \frac{1}{2\pi}\int d\omega\, G^<_{m\lambda,n\nu}(\omega) \qquad (10.30)\\ &= -\int d\omega\, n_{\mathrm{F}}(\omega)\left[\frac{1}{\omega-\mathcal{H}+i0^+} - \frac{1}{\omega-\mathcal{H}-i0^+}\right]_{m\lambda,n\nu}\\ &= \lim_{T\to 0}\frac{1}{\beta}\sum_{i\omega_n} G_{m\lambda,n\nu}(i\omega_n) e^{i\omega_n 0^+}\\ &= \frac{1}{2\pi}\int_{-\infty}^{\infty} d\omega\, G_{m\lambda,n\nu}(i\omega) e^{i\omega_n 0^+} \qquad (10.31)\end{aligned}$$

at zero temperature with $n_{\mathrm{F}}(\omega)$ being the Fermi-Dirac distribution. We refrain from using the integral along the real axis in form (10.30) and use the Matsubara integral instead since this turns out to be computationally more efficient due to the numerous divergences close to the real frequency space.
As the Hamiltonian is block-tridiagonal and we only need the diagonal and the first next-diagonal blocks of the Green's functions, we can use the inversion algorithm introduced in Section 5.4. This leads to an immense advantage in numerics since the algorithm scales only linearly with the system size as already explained in Section 5.4.

Solving the Matsubara Integral

In order to solve the Matsubara integral numerically, only finite integral limits can be chosen and the remaining parts need to be calculated analytically. To this end, we consider the matrix $\rho(\mathcal{H})$, which consists of matrix elements $\rho_{m\lambda,n\nu} = \left\langle c^\dagger_{n,\nu} c_{m,\lambda}\right\rangle$ and which therefore depends on the present Hamiltonian $H = \sum_{n\nu,m\lambda} \mathcal{H}_{(n\nu),(m\lambda)} c^\dagger_{n,\nu} c_{m,\lambda}$. We separate the integral into different parts, which leads to

$$\begin{aligned}\rho(\mathcal{H}) &= \frac{1}{2\pi}\int_{-\infty}^{\infty} d\omega \frac{1}{i\omega-\mathcal{H}} e^{i\omega 0^+} \qquad (10.32)\\ &= \frac{1}{2\pi}\left[\int_{-\omega_0}^{\omega_0} d\omega \frac{1}{i\omega-\mathcal{H}} e^{i\omega 0^+} + \int_{-\infty}^{-\omega_0} d\omega \frac{1}{i\omega-\mathcal{H}} e^{i\omega 0^+} + \int_{\omega_0}^{\infty} d\omega \frac{1}{i\omega-\mathcal{H}} e^{i\omega 0^+}\right] \qquad (10.33)\\ &= \frac{1}{2\pi}\left[\int_{-\omega_0}^{\omega_0} d\omega \frac{1}{i\omega-\mathcal{H}} + \int_{-\infty}^{-\omega_0} d\omega \frac{1}{i\omega} e^{i\omega 0^+} + \int_{\omega_0}^{\infty} d\omega \frac{1}{i\omega} e^{i\omega 0^+}\right]. \qquad (10.34)\end{aligned}$$

Here, we assumed that ω_0 is sufficiently large, so that $\frac{1}{i\omega-\mathcal{H}}$ can be replaced by $\frac{1}{i\omega}$ for $\omega > \omega_0$ and we exploited that we can set $0^+ = 0$ in the finite integral. We now replace $\mathcal{H} \to -\mathcal{H}$ and find

$$\begin{aligned}\rho(-\mathcal{H}) &= \frac{1}{2\pi}\left[\int_{-\omega_0}^{\omega_0} d\omega \frac{1}{i\omega+\mathcal{H}} + \int_{-\infty}^{-\omega_0} d\omega \frac{1}{i\omega} e^{i\omega 0^+} + \int_{\omega_0}^{\infty} d\omega \frac{1}{i\omega} e^{i\omega 0^+}\right]\\ &= \frac{1}{2\pi}\left[\int_{-\omega_0}^{\omega_0} d\omega \frac{-1}{-i\omega-\mathcal{H}} + \int_{-\infty}^{-\omega_0} d\omega \frac{1}{i\omega} e^{i\omega 0^+} + \int_{\omega_0}^{\infty} d\omega \frac{1}{i\omega} e^{i\omega 0^+}\right]\\ &= \frac{1}{2\pi}\left[-\int_{-\omega_0}^{\omega_0} d\omega \frac{1}{i\omega-\mathcal{H}} + \int_{-\infty}^{-\omega_0} d\omega \frac{1}{i\omega} e^{i\omega 0^+} + \int_{\omega_0}^{\infty} d\omega \frac{1}{i\omega} e^{i\omega 0^+}\right]. \qquad (10.35)\end{aligned}$$

By adding up $\rho(\mathcal{H})$ and $\rho(-\mathcal{H})$ we find

$$1 = \rho(\mathcal{H}) + \rho(-\mathcal{H}) = \frac{2}{2\pi}\left[\int_{-\infty}^{-\omega_0} d\omega \frac{1}{i\omega} e^{i\omega 0^+} + \int_{\omega_0}^{\infty} d\omega \frac{1}{i\omega} e^{i\omega 0^+}\right], \qquad (10.36)$$

where we exploit the fact that the sum of both densities has to be the identity. Note that the same result can also be found by solving the integral directly [118, 364]. This leads to the final result

$$\rho(\mathcal{H}) = \frac{1}{2\pi}\int_{-\infty}^{\infty} d\omega \frac{1}{i\omega-\mathcal{H}} = \frac{1}{2\pi}\int_{-\omega_0}^{\omega_0} d\omega \frac{1}{i\omega-\mathcal{H}} + \frac{1}{2}. \qquad (10.37)$$

Thus, the density is calculated by integrating the Matsubara Green's function from $-\omega_0$ to ω_0 and adding 1/2. Of course, it is necessary to check that ω_0 was chosen large enough so that the result is converged with ω_0.
Inserting these results into Eq. (10.29) leads to the final result of

$$\begin{aligned}\Delta E =& \frac{1}{2\pi}\int_{-\omega_0}^{\omega_0} d\omega \left(\sum_{n\nu,m\lambda} \mathcal{H}^{\mathrm{FM}}_{n\nu,m\lambda} G^{\mathrm{FM}}_{m\lambda,n\nu}(i\omega) - \sum_{n\nu,m\lambda} \mathcal{H}^{\mathrm{AFM}}_{n\nu,m\lambda} G^{\mathrm{AFM}}_{m\lambda,n\nu}(i\omega) \right) \\ &+ \frac{1}{2}\sum_{n\nu} \left(\mathcal{H}^{\mathrm{FM}}_{n\nu,n\nu} - \mathcal{H}^{\mathrm{AFM}}_{n\nu,n\nu} \right) \qquad (10.38) \\ =& \frac{1}{\pi}\int_{0}^{\omega_0} d\omega \,\mathrm{Re}\left[\left(\sum_{n\nu,m\lambda} \mathcal{H}^{\mathrm{FM}}_{n\nu,m\lambda} G^{\mathrm{FM}}_{m\lambda,n\nu}(i\omega) - \sum_{n\nu,m\lambda} \mathcal{H}^{\mathrm{AFM}}_{n\nu,m\lambda} G^{\mathrm{AFM}}_{m\lambda,n\nu}(i\omega) \right) \right] \\ &+ \frac{1}{2}\sum_{n\nu} \left(\mathcal{H}^{\mathrm{FM}}_{n\nu,n\nu} - \mathcal{H}^{\mathrm{AFM}}_{n\nu,n\nu} \right) , \qquad (10.39)\end{aligned}$$

where we have also exploited that it is numerically more efficient to rewrite ΔE into a single integral.

Connection of Spin Sectors

Using the Green's function approach, it is also possible to exploit the connection (10.28) to further reduce the computation time by a factor two. Therefore, we first investigate the relation of the equal time lesser Green's function using the new gauge $\mathcal{H} = \mathcal{H}_\uparrow = -\mathcal{H}_\downarrow$. We find

$$\begin{aligned} G^{<,\uparrow}_{m\lambda,n\nu}(0,0) &= i\,\langle c^\dagger_{n,\nu,\uparrow} c_{m,\lambda,\uparrow}\rangle \\ &= \frac{1}{2\pi}\int_{-\infty}^{\infty} d\omega\, G^{<,\uparrow}_{m\lambda,n\nu}(\omega) \\ &= -\frac{2\pi i}{2\pi}\int_{-\infty}^{\infty} d\omega\, n_F(\omega) \left[\frac{1}{\omega - \mathcal{H} + i0^+} - \frac{1}{\omega - \mathcal{H} - i0^+} \right]_{m\lambda,n\nu} \\ &= -i\int_{-\infty}^{0} d\omega \left[\frac{1}{\omega - \mathcal{H} + i0^+} - \frac{1}{\omega - \mathcal{H} - i0^+} \right]_{m\lambda,n\nu} , \qquad (10.40) \\ G^{<,\downarrow}_{m\lambda,n\nu}(0,0) &= i\,\langle c^\dagger_{n,\nu,\downarrow} c_{m,\lambda,\downarrow}\rangle \\ &= \frac{1}{2\pi}\int_{-\infty}^{\infty} d\omega\, G^{<,\downarrow}_{m\lambda,n\nu}(\omega) \\ &= -\frac{2\pi i}{2\pi}\int_{-\infty}^{\infty} d\omega\, n_F(\omega) \left[\frac{1}{\omega + \mathcal{H} + i0^+} - \frac{1}{\omega + \mathcal{H} - i0^+} \right]_{m\lambda,n\nu} \\ &= -i\int_{-\infty}^{\infty} d\omega\, n_F(-\omega) \left[\frac{-1}{\omega - \mathcal{H} - i0^+} - \frac{-1}{\omega - \mathcal{H} + i0^+} \right]_{m\lambda,n\nu} \\ &= -i\int_{0}^{\infty} d\omega \left[\frac{1}{\omega - \mathcal{H} + i0^+} - \frac{1}{\omega - \mathcal{H} - i0^+} \right]_{m\lambda,n\nu} , \qquad (10.41)\end{aligned}$$

where we used that the calculations are done at zero temperature and with the chemical potential $\mu = 0$. This leads to

$$\begin{aligned}\langle c^\dagger_{n,\nu,\uparrow} c_{m,\lambda,\uparrow}\rangle + \langle c^\dagger_{n,\nu,\downarrow} c_{m,\lambda,\downarrow}\rangle &= \frac{-i}{i}\int_{-\infty}^{\infty} d\omega \left[\frac{1}{\omega - \mathcal{H} + i0^+} - \frac{1}{\omega - \mathcal{H} - i0^+} \right]_{m\lambda,n\nu} \\ &= \delta_{m,n}\delta_{\lambda,\nu} . \qquad (10.42)\end{aligned}$$

Here, we exploited that the integral belongs to the expectation value $\langle c^\dagger_{n,\nu} c_{m,\lambda}\rangle$ of a fully occupied system of spinless fermions. It is therefore possible to calculate the expectation values for spin down with the results of the spin up sector via

$$\langle c^\dagger_{n,\nu,\downarrow} c_{m,\lambda,\downarrow}\rangle = \delta_{m,n}\delta_{\lambda,\nu} - \langle c^\dagger_{n,\nu,\uparrow} c_{m,\lambda,\uparrow}\rangle . \qquad (10.43)$$

We recall that the Hamiltonians of the spin up and down sector, after applying the gauge transformation to $H_\downarrow$, are given by

$$H_\uparrow = -t \sum_{\langle m\lambda, n\nu\rangle} (c^\dagger_{n,\nu,\uparrow} c_{m,\lambda,\uparrow} + c^\dagger_{m,\lambda,\uparrow} c_{n,\nu,\uparrow}) + \frac{J_1\sigma_1}{2} c^\dagger_{i,\alpha,\uparrow} c_{i,\alpha,\uparrow} + \frac{J_2\sigma_2}{2} c^\dagger_{j,\beta,\uparrow} c_{j,\beta,\uparrow}\,, \tag{10.44}$$

$$H_\downarrow = +t \sum_{\langle m\lambda, n\nu\rangle} (c^\dagger_{n,\nu,\downarrow} c_{m,\lambda,\downarrow} + c^\dagger_{m,\lambda,\downarrow} c_{n,\nu,\downarrow}) - \frac{J_1\sigma_1}{2} c^\dagger_{i,\alpha,\downarrow} c_{i,\alpha,\downarrow} - \frac{J_2\sigma_2}{2} c^\dagger_{j,\beta,\downarrow} c_{j,\beta,\downarrow}\,, \tag{10.45}$$

respectively, with $\sigma_1, \sigma_2 = \pm 1$. The expectation values of the energy can therefore be written as

$$E_\uparrow = -t \sum_{\langle m\lambda, n\nu\rangle} \left(\left\langle c^\dagger_{n,\nu,\uparrow} c_{m,\lambda,\uparrow} \right\rangle + \left\langle c^\dagger_{m,\lambda,\uparrow} c_{n,\nu,\uparrow} \right\rangle \right) + \frac{J_1\sigma_1}{2} \left\langle c^\dagger_{i,\alpha,\uparrow} c_{i,\alpha,\uparrow} \right\rangle + \frac{J_2\sigma_2}{2} \left\langle c^\dagger_{j,\beta,\uparrow} c_{j,\beta,\uparrow} \right\rangle \tag{10.46}$$

$$E_\downarrow = +t \sum_{\langle m\lambda, n\nu\rangle} \left(\left\langle c^\dagger_{n,\nu,\downarrow} c_{m,\lambda,\downarrow} \right\rangle + \left\langle c^\dagger_{m,\lambda,\downarrow} c_{n,\nu,\downarrow} \right\rangle \right) - \frac{J_1\sigma_1}{2} \left\langle c^\dagger_{i,\alpha,\downarrow} c_{i,\alpha,\downarrow} \right\rangle - \frac{J_2\sigma_2}{2} \left\langle c^\dagger_{j,\beta,\downarrow} c_{j,\beta,\downarrow} \right\rangle . \tag{10.47}$$

Using Eq. (10.43), the different terms of the energy can be connected via

$$+t \left\langle c^\dagger_{n,\nu,\downarrow} c_{m,\lambda,\downarrow} \right\rangle = -t \left\langle c^\dagger_{n,\nu,\uparrow} c_{m,\lambda,\uparrow} \right\rangle \text{ for } (m,\lambda) \neq (n,\nu), \tag{10.48}$$

$$-\frac{J_\ell\sigma_\ell}{2} \left\langle c^\dagger_{n,\nu,\downarrow} c_{n,\nu,\downarrow} \right\rangle = -\frac{J_\ell\sigma_\ell}{2} + \frac{J_\ell\sigma_\ell}{2} \left\langle c^\dagger_{n,\nu,\uparrow} c_{n,\nu,\uparrow} \right\rangle . \tag{10.49}$$

We need to consider $\sigma_1 = \sigma_2$ for the FM and $\sigma_1 = -\sigma_2$ for the AFM configuration. Here, we can choose $\sigma_1 = \sigma_2 = 1$ for the FM and $\sigma_1 = -\sigma_2 = 1$ for the AFM case, leading to

$$E^{\mathrm{FM}}_\downarrow = E^{\mathrm{FM}}_\uparrow - \frac{J_1 + J_2}{2}\,, \quad E^{\mathrm{AFM}}_\downarrow = E^{\mathrm{AFM}}_\uparrow - \frac{J_1 - J_2}{2}\,. \tag{10.50}$$

The total energy difference is then given by

$$\Delta E_{\mathrm{tot}} = E^{\mathrm{FM}} - E^{\mathrm{AFM}} = \Delta E_\uparrow + \Delta E_\downarrow = 2\,\Delta E_\uparrow - J_2\,. \tag{10.51}$$

Using this connection, again we only need to do the calculation for one spin sector, e.g. spin up, and we can reduce the numerical effort in the same way as for ED. We note, that this connection does change when the choice of σ_1 and σ_2 is changed but the final RKKY interaction is invariant. Interestingly, the additional term explicitly cancels the term from the infinite integral in Eq. (10.39), leading to the final results of

$$\Delta E_{\mathrm{tot}} = 2\frac{1}{\pi} \int_0^{\omega_0} d\omega\, \mathrm{Re} \left[\left(\sum_{n\nu,m\lambda} \mathcal{H}^{\mathrm{FM},\uparrow}_{n\nu,m\lambda} G^{\mathrm{FM},\uparrow}_{m\lambda,n\nu}(i\omega) - \sum_{n\nu,m\lambda} \mathcal{H}^{\mathrm{AFM},\uparrow}_{n\nu,m\lambda} G^{\mathrm{AFM},\uparrow}_{m\lambda,n\nu}(i\omega) \right) \right] \tag{10.52}$$

for sufficiently large ω_0. This formula is used for the simulations of the exact RKKY interaction within the remainder of this chapter unless noted otherwise.

Comparison of ED and Green's Function Approach

In the previous part of this section, possibilities to optimize the calculation of the exact RKKY interaction (10.11) were discussed. Most importantly, this led to the Green's function approach, which is based on Eq. (10.52) and the inversion algorithm of Section 5.4. The results calculated with this approach can now be compared to the results that are obtained by using simple exact diagonalization (where we still exploit the decoupling of the spin sectors). In Fig. 10.3 the results for the absolute value of the RKKY interaction are shown as a function of the inter-impurity distance R for the sublattice configuration BB of the diamond lattice. We note that the approaches agree with each other as expected since both of them are in theory exact. Nevertheless, there are small differences visible at large distances R. Here, the values are so small that numerical uncertainties

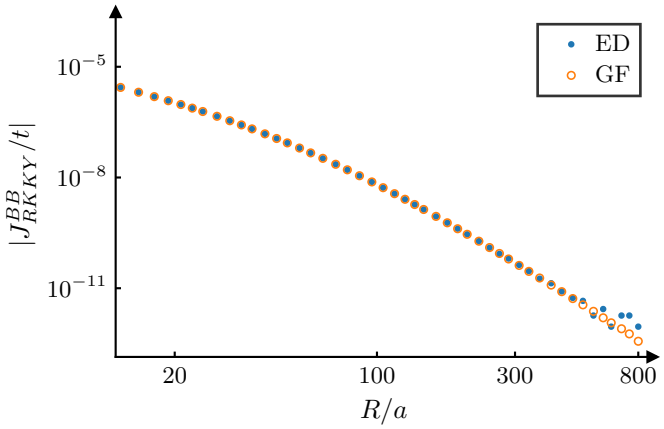

Figure 10.3: Absolute value of the RKKY interaction calculated with ED and the Green's function approach introduced in this section. Here, $|J^{BB}_{\mathrm{RKKY}}/t|$ for the diamond lattice is shown as a function of the inter-impurity distance R. The local coupling constants are set to $J_1 = J_2 = 0.2t$ and 4000 unit cells are used in both cases to compare numerical uncertainties as well. The results with both methods agree for small and intermediate R since both of them are in theory exact (up to numerical errors). Differences at larger R appear due to numerical uncertainties showing that ED runs into the numerical limits before the Green's function method. Figure taken from Ref. [301].

are visible in the ED results. The data obtained with the Green's function method are still exact, showing that smaller values for the RKKY coupling and therefore results at larger inter-impurity distances R can be computed with the introduced Green's functions approach. This indicates another advantage of the Green's function method in addition to efficiency due to the linear scaling with the system size.

10.4 Results

In the following, the RKKY interaction of the two introduced flat-band models is investigated. Therefore, we use the non-perturbative expression (10.11) and evaluate it effectively as described above. Additionally, results are calculated using the standard approach (10.8), which allows for a comparison between both approaches and the possibility to understand which part of the indirect coupling are covered with this perturbative method. We start with the stub lattice which is a prototypical model with an isolated flat band as mentioned above. After this, we investigate the diamond lattice and note the qualitative difference of the RKKY interaction due to the absence of a gap. Finally, we study how the form of the RKKY interaction changes smoothly when transitioning from the stub to the diamond lattice.

10.4.1 Stub Lattice

We start with the investigation of the RKKY interaction in dependence on the inter-impurity distance R. We consider different sublattice configurations $\alpha\beta$, where α (β) denotes the sublattice position of the first (second) impurity. In Fig. 10.4, the results are shown, where we refrain from showing the configurations BA, CA and CB since they can be connected to AB, AC and BC, respectively, using

$$J^{AB}_{\mathrm{RKKY}}(R) = J^{BA}_{\mathrm{RKKY}}(R+1)\,, \quad J^{AC}_{\mathrm{RKKY}}(R) = J^{CA}_{\mathrm{RKKY}}(R)\,, \quad J^{BC}_{\mathrm{RKKY}}(R) = J^{CB}_{\mathrm{RKKY}}(R-1)\,. \tag{10.53}$$

We find that the decay is exponential for all sublattice configurations. Interestingly, the RKKY interaction is enhanced when at least one of the impurities is placed on the B or C sublattice, where the eigenstates of the flat band are present. This enhancement is even stronger if both impurities are located on sublattices B and C.

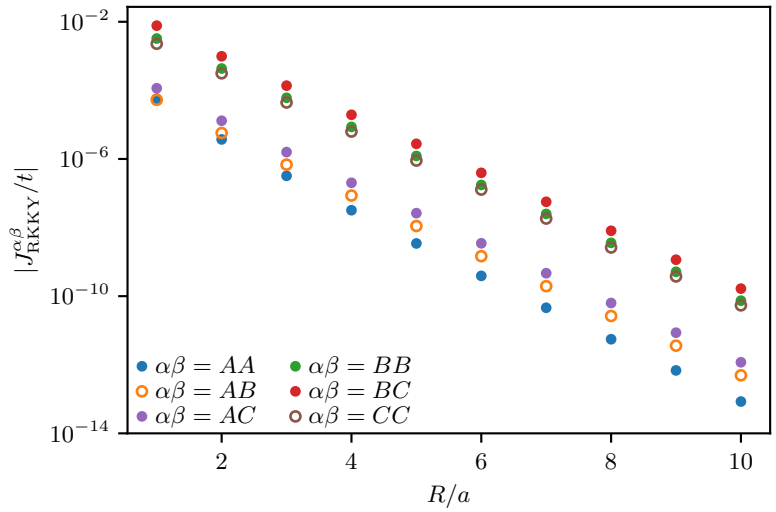

Figure 10.4: Dependence of the RKKY coupling on the distance R between the impurities in the stub lattice for the sublattice configurations AA, AB, AC, BB, BC, CC. The local impurity couplings are chosen to be $J_1 = J_2 = 0.2t$. Independent of the sublattices where the impurities are placed, the absolute value $|J^{\alpha\beta}_{\mathrm{RKKY}}/t|$ shows an exponential decay with the inter-impurity distance R. Figure based on a similar figure in Ref. [301].

In the following, we investigate how the RKKY interaction depends on the local exchange couplings J_i. To this end, we fix one coupling and explore the results as a function of the other local coupling constant. Importantly, both local coupling constants should be small enough, fulfilling $|J_i/t| \ll 1$, so that they are small compared to the bandwidths of the dispersive bands. The results are shown in Fig. 10.5 for all possible sublattice configurations. First of all, we note that the sign of the RKKY interaction depends on the sublattices where the impurities are placed. Here, a positive sign, and therefore an antiferromagnetic coupling is found if one impurity spin is located on sublattice A, while the other one is on B or C. In all other cases, the coupling is negative, leading to a ferromagnetic order. Interestingly, this can be understood by the observation that the stub lattice is a bipartite lattice, since it can be decomposed into sublattice A and the union of the B and C sublattices with hoppings only between the different parts of the bipartition. For bipartite lattices, it was shown in Ref. [365] that the RKKY interaction in a bipartite lattice at half filling is antiferromagnetic if both impurity spins are placed on different subparts of the bipartition and ferromagnetic otherwise.

Additionally, the results show a linear dependence of J^{AA}_{RKKY} on the local coupling constant J_1. This is in perfect agreement with the results from the standard RKKY expression (10.8) shown as a red dashed line. Here, the flat bands do not have a notable influence on the RKKY interaction since the impurities are placed on sites where no eigenstates of the flat band are present and therefore, no direct coupling to the flat band occurs. Therefore, the exponential decay of the indirect interaction is expected for the AA sublattice configuration based on the standard result for gapped systems yielding the Bloembergen-Rowland interaction described above.

Furthermore, we see that the RKKY coupling is almost linear in J_1 if one of the impurities are located on sublattice A as visible in Fig. 10.5. Here, only one of the impurities is directly coupled to the flat band. The results are approximately described by the perturbative RKKY expression although small deviations occur at larger J_1. Therefore, we note that the flat band leads to contributions beyond the reach of the standard approach. These deviations are more visible if the first impurity is placed on B or C (where the eigenstates of the flat band are located), since the influence of the flat band is more severe for large J_1 in this case.

Finally, we investigate the case with both impurities placed on sublattices B or C. In these cases, both impurities can directly couple to the flat band and the RKKY coupling does not show a linear dependence for the chosen cutout, even not approximately. Additionally, the results cannot be compared to the standard perturbative RKKY expression (10.8) since this expression diverges.

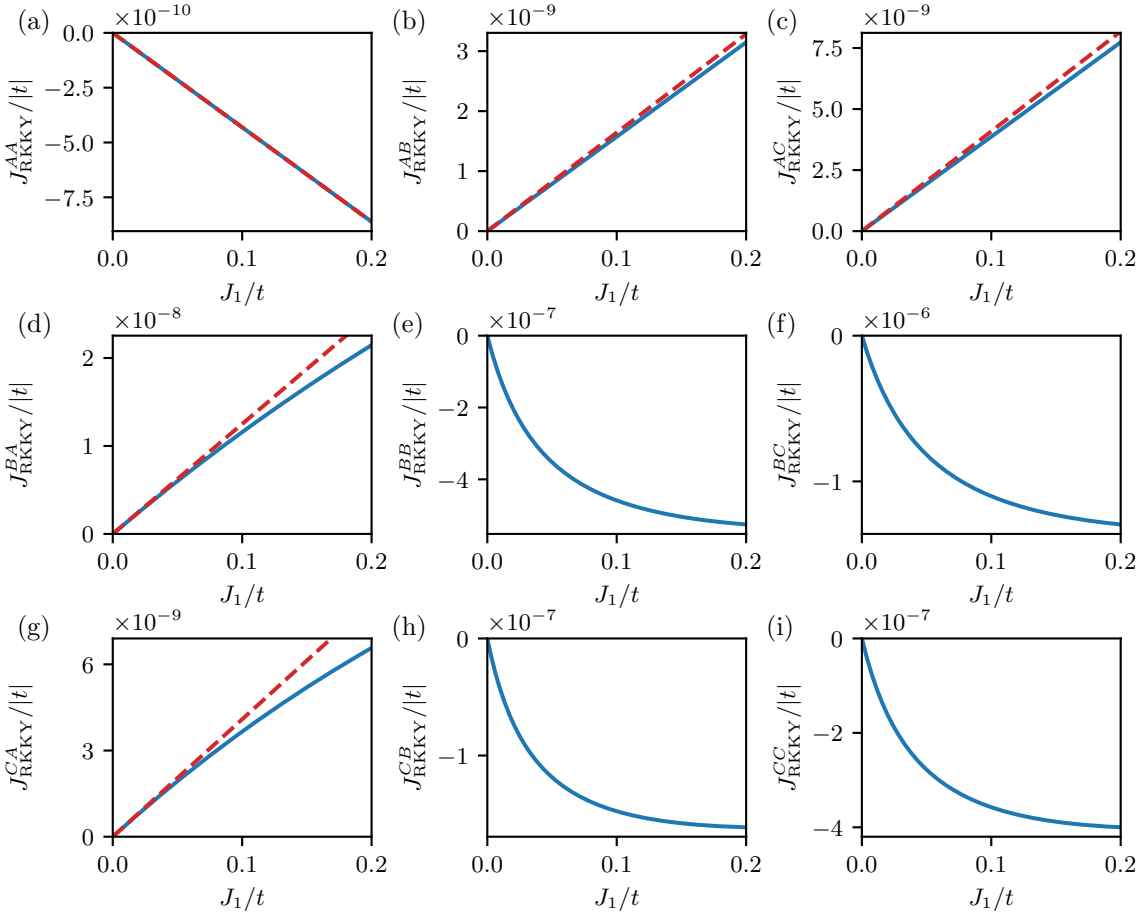

Figure 10.5: RKKY interaction $J^{\alpha\beta}_{\mathrm{RKKY}}$ for all possible $\alpha\beta$ as a function of the local impurity coupling strength J_1 in the stub lattice at an inter-impurity distance of $R = 5a$. The other impurity coupling strength is fixed to $J_2 = 0.05t$. We compare the exact numerical data calculated using Eq. (10.11) (blue lines) with the results from the standard approach (10.8) (red dashed lines). For the AA results, perfect agreement between both approaches is found. In the case where only one of the impurities is on the A sublattice, the results still coincide for small J_1, but deviations are found for larger J_1. Interestingly, these deviations are stronger if the second impurity is placed on A ($\beta = A$). If both impurities are placed on the B or C sublattices, no results from the standard approach are shown since they do not converge. Figure based on a similar figure in Ref. [301].

Therefore, there is no red line present in the corresponding subpanels of Fig. 10.5. The RKKY coupling is in this case not covered by the perturbative standard approach due to presence of the flat band.

10.4.2 Diamond Lattice

We now investigate the diamond lattice and compare the results with the ones found for the stub lattice. Again, we start by investigating the RKKY coupling as a function of the inter-impurity distance. The corresponding results are shown in Fig. 10.6. Here, only the sublattice configurations AA, AB and BB are presented since the sublattices B and C are equivalent and AB can be connected to BA in the same way as for the stub lattice. We note that the behavior of the RKKY interaction is qualitatively different since we find a decay approaching a power-law in the limit of $R \to \infty$ instead of the exponential decay of the stub lattice. The exponent of the decay is crucially dependent on the exact sublattice configuration. Here, we have to separate different cases depending on whether the impurity spins are located on A (the sublattice, where the eigenstates of the flat band are not present) or on B and C. If both impurities are placed on A, they cannot

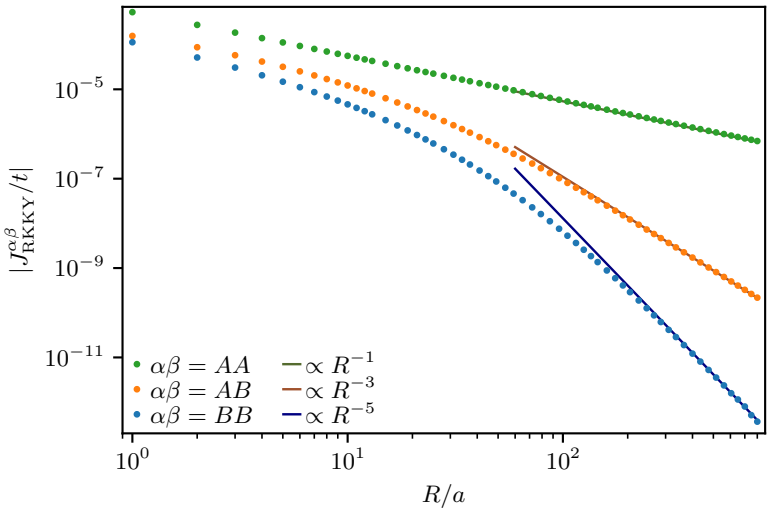

Figure 10.6: RKKY interaction as a function of the distance R between the impurities for the diamond lattice. Here, the absolute value $|J^{\alpha\beta}_{\mathrm{RKKY}}|$ is shown for $\alpha\beta = AA, AB, BB$. The other combinations are equivalent due to the interchangeability of sublattices B and C or can be obtained by shifting the inter-impurity distance R by one. The dots represent exact numerical data approaching power-law decays at large inter-impurity distances R which are drawn as slightly darker lines. The exponent depends on the sublattice configuration. We find $|J^{\alpha\beta}_{\mathrm{RKKY}}| \propto R^{-1}$ for AA, $\propto R^{-3}$ for AB and $\propto R^{-5}$ for the BB configuration at large inter-impurity distances. Figure based on a similar Figure in Ref. [301].

couple to the flat band directly and the power-law is proportional to R^{-1}. In the other cases, at least one of the impurities couples directly to the flat band and the RKKY coupling decays more rapidly. If both impurity spins are placed on B or C, the decay scales with R^{-5} at large distances. If one impurity is located on B or C, while the other one is present on A, an intermediate result is found with an RKKY interaction approaching a R^{-3} decay.
Interestingly, the different decaying behavior from the various sublattice configurations is connected to the decay of the spin polarizations occuring due to the individual spin impurities. The spin polarization $n_\uparrow - n_\downarrow$ is investigated by placing only a single impurity in the system. For this evaluation, we exploit Eqs. (10.31) and (10.43), which allow us to use the efficient algorithm from Section 5.4 again. In Fig. 10.7 the absolute value of the results are shown for different sublattice positions of the impurity spin. Once again, the results approach a power-law for large distances r from the impurity. The polarization decays with r^{-1} for a spin on the A sublattice and with r^{-3} in the other cases. Interestingly, the exponent does not depend on the sublattice where the spin polarization was measured. Nevertheless, the sign of the spin polarization differs for measurements on different sublattices. If the impurity is located on the A sublattice, we find a negative spin polarization for the measurement on A, and a positive spin polarization on B or C. Contrarily, if the impurity spin is placed on B or C, the opposite behavior is found.
Moreover, the exponent b of the RKKY interaction can be linked to the exponents $c(\alpha)$ and $c(\beta)$ of the individual spin polarization functions via the simple expression

$$b = c(\alpha) + c(\beta) + 1 \tag{10.54}$$

with $c(A) = -1$ and $c(B) = c(C) = -3$. A detailed understanding of this connection is left for future research.

We continue by studying the RKKY interaction in dependence on one of the local coupling constants J_i, which is presented in Fig. 10.8. Once again, only the results comprising sublattices A and B are shown due to the equivalence of B and C. First of all, we note that the signs of the RKKY expressions coincide with the ones found for the stub lattice. We find a negative AFM coupling if both spins are located on the same sublattice, meaning that both are either on A or on

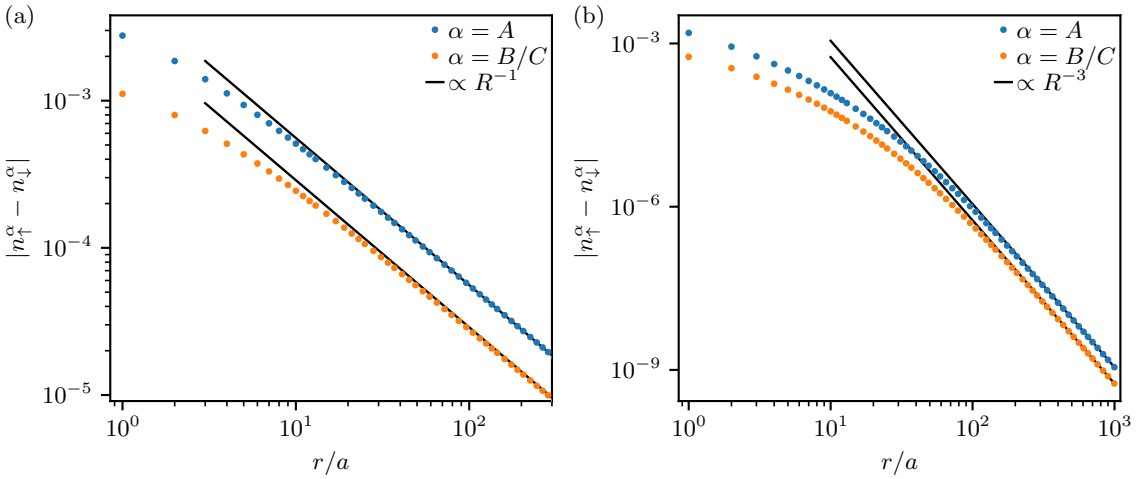

Figure 10.7: Spin polarization in dependence on the distance r from the impurity for an impurity placed on site (a) A and (b) B/C with $J = 0.2t$. The different colors denote the measurement on different sublattices. In both cases, the spin polarization approaches a power-law, which is proportional to (a) r^{-1} and (b) r^{-3} (shown as black lines). The exponent of the power-law is independent of the sublattice where the spin polarization was measured.

B/C. In the other cases, the RKKY coupling favors a FM ordering of the impurity spins, which is again expected due to the results for general bipartite lattices in Ref. [365]. Notably, this is also in perfect agreement with the results obtained from the spin polarization above, where we found a negative spin polarization on the sublattices belonging to the same part of the bipartition as the sublattice with the impurity, and a positive spin polarization on the other sublattices.
Interestingly, the results in Fig. 10.8 show a linear scaling with J_1 if the first impurity is placed on the A sublattice. In the case of J^{AA}_{RKKY}, the results perfectly agree the with the prediction of the standard expression (10.8). Here, both impurity spins are placed on sublattice A, where the eigenstates of the flat band are not present, and the flat band does not significantly influence the RKKY coupling. Therefore, it is not surprising that a R^{-1} decay was found above. This agrees with the standard result for the RKKY interaction in metals, where a decay of R^{-d} with dimension d is present at large distances [349] as mentioned above. Nevertheless, J^{AB}_{RKKY} is not covered by the standard expression. Here, only the linear scaling with J_1 is predicted correctly but the slope is not described by the perturbative result since the second impurity is placed on sublattice B (or C) leading to an impact of the flat band.
For the configurations, where the first impurity is placed on B (or C) the behavior is qualitatively different. We find that the RKKY interaction increases only for very small J_1 and is then followed by a decline. Nevertheless, we note that the slope for $J_1 \to 0$ is correctly predicted by the perturbative expression (10.8) for J^{BA}_{RKKY}. In this limit, the local exchange coupling of the impurity placed on sublattice B or C (with the presence of flat band eigenstates) vanishes. Therefore, the direct coupling of the impurities with the flat band vanishes as well and the influence of the flat band is negligible. This reasoning does not hold for the BB configuration and therefore, the slope is not covered by the standard RKKY expression in this case.

10.4.3 Transition from Stub to Diamond Lattice

So far, we have studied the RKKY interaction of two fundamentally different models: The stub lattice with an isolated flat band, and the diamond lattice with two dispersive bands crossing the flat band. When looking at the Hamiltonians (10.13) and (10.20), one notices that these Hamiltonians can easily be connected since the diamond lattice only includes an additional hopping. We therefore define

$$H_{\mathrm{trans}} = \sum_n \left(t\, c^\dagger_{n,A} c_{n,B} + t\, c^\dagger_{n,A} c_{n,C} + t\, c^\dagger_{n+1,A} c_{n,B} + t'\, c^\dagger_{n+1,A} c_{n,C} \right) + \mathrm{H.c.} \tag{10.55}$$

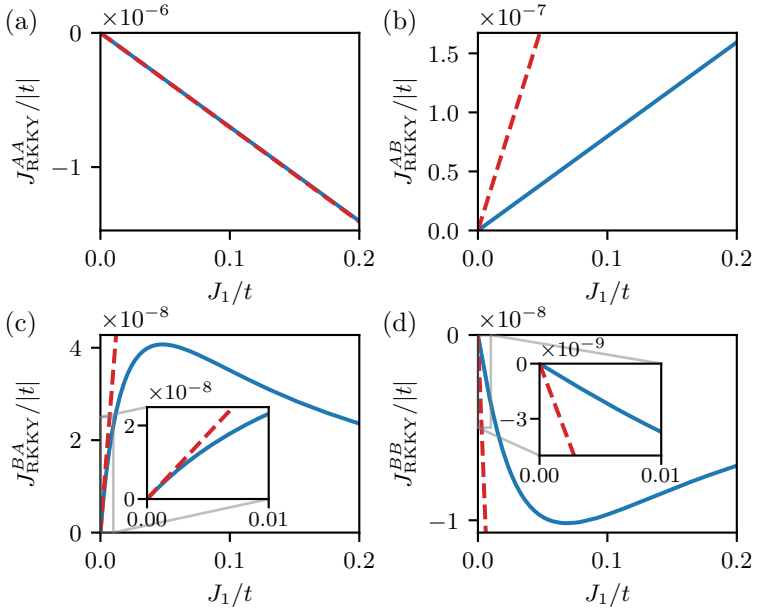

Figure 10.8: RKKY interaction in the diamond lattice as a function of one of the local exchange coupling constant J_1 with the other coupling constant being fixed at $J_2 = 0.05t$ for different sublattice configurations. The inter-impurity distance is $R = 100a$. The blue lines denote the exact numerical results calculated from Eq. (10.11). The red dashed lines indicate the results from the standard approach (10.8). The RKKY coupling is negative for the AA and BB configurations, while it is positive for the AB and BA configurations. Only in the AA configuration, where the impurities do not couple to the flat band directly, the results can be accurately described by the perturbative expression. Nevertheless, the slope of the RKKY interaction can still be described accurately in the limit of $J_1 \to 0$ for the BA sublattice configuration. Figure based on a similar figure in Ref. [301].

with $t'/t \in [0, 1]$. For $t' = 0$ the Hamiltonian represents the stub lattice. When increasing t', the gap between the flat and the dispersive bands decreases until it closes at $t'/t = 1$, where the Hamiltonian of the diamond lattice is recovered.

Using a Fourier transform this Hamiltonian is transferred to its momentum space expression $H_{\mathrm{trans}} = \sum_k \psi_k^\dagger \mathcal{H}_{\mathrm{trans}}(k)\psi_k$ with

$$\mathcal{H}_{\mathrm{trans}}(k) = t \begin{pmatrix} 0 & 1 + e^{ika} & 1 + \frac{t'}{t} e^{ika} \\ 1 + e^{-ika} & 0 & 0 \\ 1 + \frac{t'}{t} e^{-ika} & 0 & 0 \end{pmatrix} . \tag{10.56}$$

Diagonalizing this matrix leads to a flat band at $\epsilon_1(k) = 0$, as well as two dispersive bands at $\epsilon_2(k) = -\sqrt{(t')^2 + 3t^2 + 2t(t' + t)\cos(ka)}$, $\epsilon_3(k) = \sqrt{(t')^2 + 3t^2 + 2t(t' + t)\cos(ka)}$. In Fig. 10.9 the band structure is plotted for different t'. We can indeed observe how the band structure transforms from the one of the stub lattice to the one of the diamond lattice and how the gap closes monotonically.

The results for the RKKY coupling in dependence of the inter-impurity distance are presented for different sublattice combinations and different t' in Fig. 10.10. Here, the size of the local coupling constant is fixed allowing to observe the crossover from a gap which is significantly larger than the coupling constant to a vanishing gap with intermediate situations where both are of similar size.

We note that the form of the RKKY interaction changes from an exponential form for $t' = 0$ to a power-law form for $t' = t$ as one would expect from the previous result for the stub and the diamond lattice. When t' is increased, which causes a reduction of the gap, the decay gets slower until it approaches a power-law at large inter-impurity distances for $t = t'$.

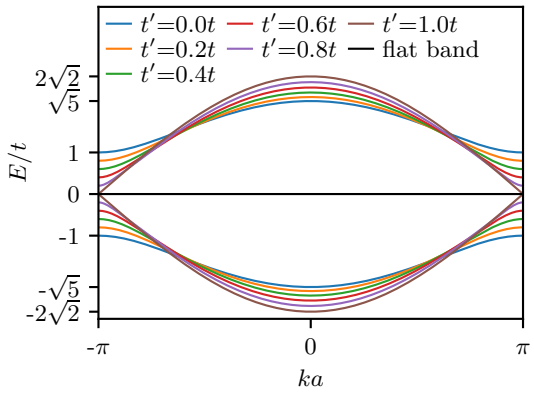

Figure 10.9: Spectrum of the transition Hamiltonian (10.55) for different values of t'. We recover the stub lattice for $t' = 0$ and the diamond lattice for $t' = t$. In between these values, there is a transition between the spectra and the gap closes. The flat band remains untouched and is independent of t'.

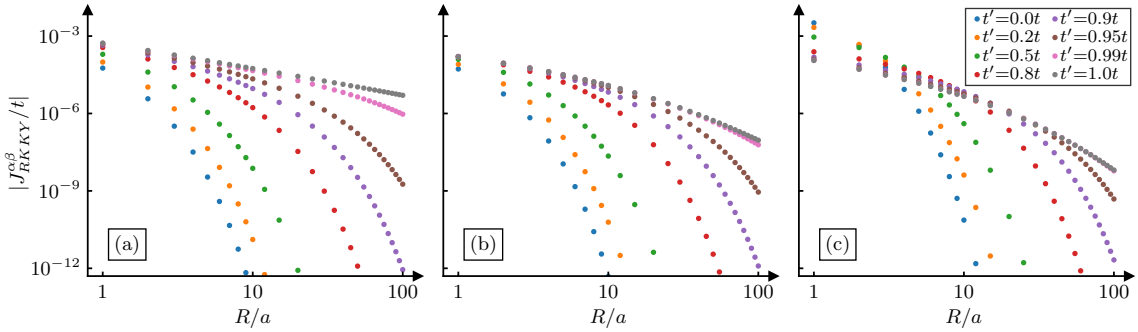

Figure 10.10: RKKY interaction for different t' in the Hamiltonian (10.55) in dependence on the distance R between the impurities. $|J^{\alpha\beta}_{\mathrm{RKKY}}/t|$ is shown for the sublattice configurations $\alpha\beta$ being (a) AA, (b) AB and (c) BB, meaning that either none, one or both impurities are set onto sites where the flat band eigenstates are present. The local exchange coupling constants are set to $J_1 = J_2 = 0.2t$. In agreement with the previous analysis, we find an exponential decay for $t' = 0$, where the stub lattice is recovered and decay approaching a power-law for $t' = t$, where the obtained lattice is the diamond lattice. For $0 < t' < t$ a crossover between those cases is visible and the decay gets slower for larger t'. Figure taken from Ref. [301].

10.5 Conclusion & Outlook

In this chapter we have investigated the RKKY interaction of two classical impurity spins in one-dimensional flat-band lattices. We focused on the stub lattice with an isolated flat band, and the diamond lattice with a flat band crossing other dispersive bands, which we both studied at a chemical potential of $\mu = 0$, leading to a partially filled flat band.

Before analyzing the results, we discussed how the exact expression for the indirect coupling of two classical magnetic impurities can be calculated efficiently by using Green's functions and by exploiting the connection of the different spin sectors, which allowed for a significant speed-up and the use of larger system sizes.

The results that we found crucially depend on whether the flat band is isolated by a gap. For the stub lattice with the isolated flat band, the RKKY interaction decays exponentially for all sublattice configurations. In contrast to this, a power-law decay was found in the limit of large inter-impurity distances in case of the diamond lattice. Here, the results approach a decay of R^{-1} if no impurity is placed on the sublattices where the eigenstates of the flat bands are located. In the other cases, the decay is faster and is for large inter-impurity distances described by R^{-3} or R^{-5} for one or both impurities located on the sublattices with the flat band, respectively. Interestingly,

these exponents can be connected to the decay of the spin polarizations from a single impurity.
In both cases, the results of the AA sublattice configuration (no impurity on the sublattices with the flat band) are perfectly described by the standard approach (10.8), which is based on perturbation theory. In the other cases, the results were not accurately reproduced by the perturbative standard approach due to the vanishing band width of the flat band.
Moreover, the failure of the standard approach is stronger if both impurities are placed on the sublattices, where the eigenstates of the flat band occur. For the stub lattice, the standard expression even diverges in that case. If one of the impurities is placed on the sublattice, where the flat band eigenstates are not present, the results in dependence on one of the coupling constants (J_1) are at least partially covered. For the stub lattice, the results approximately follow the perturbative expression and deviations only arise for large J_1. For the diamond lattice, either the linear scaling or the slope in the limit of vanishing J_1 is correctly predicted.
Finally, we studied the crossover between the stub and the diamond lattice by gradually increasing the additional hopping that is only present in the diamond lattice. Here, a transition from exponential to power-law decay takes place.

There are several directions that would be very interesting to pursue in the future. First, one should try to extend the present analysis to higher dimensional, especially two-dimensional, lattices. This would be of particular interest since most flat-band systems in the focus of attention, such as magic-angle twisted bilayer and trilayer graphene, are (quasi) two-dimensional. Therefore, such an extension could be applied to experiments.
Interestingly, flat bands in two dimensions can also carry a nonzero Chern number and obey a topological character [366], since a Chern number is one example of a topological invariant introduced in the introduction [15]. This leads to a Wannier obstruction which means that the band cannot be constructed from exponentially localized Wannier functions. Nevertheless, the exponential decay of the RKKY interaction in the stub lattice, presented in Fig. 10.4, was shown in Ref. [301] to appear as a results of exponentially localized Wannier functions. This argument is not valid in case of a topological flat band. It would be very interesting to compare the RKKY interactions of topological and trivial two-dimensional flat bands and to analyze whether the decay of the RKKY interaction depends on the flat band's Chern number.
Here, a further future path would be to study a (nearly) flat band with fragile topology, which for example occurs in magic-angle twisted bilayer graphene [367, 368], but was also found in single-layer graphene using an additional periodic potential [369]. Fragile topological bands were introduced in Ref. [370] and have a Chern number of zero but can still not be represented using exponentially localized Wannier states. In contrast to a band with conventional symmetry-protected topology, the Wannier obstruction of a band with fragile topology can be removed by adding trivial bands. Therefore, conventional and fragile topology are qualitatively different and it is unclear whether the RKKY interaction distinguishes these different classifications of topology.
Furthermore, we have only studied non-interacting lattices and it is a priori not clear if and how interactions might influence our results. Therefore, a study of an interacting lattice model would also be of considerable interest. Here, the one-dimensional lattices introduced at the beginning of this chapter can for example be studied using DMRG in the presence of interactions.
Finally, the RKKY interaction in nearly-flat bands should be investigated since all bands in real materials will never be perfectly flat. Here, we expect our results to hold for small but finite bandwidths as well, as long as the local exchange couplings are still not small compared to the bandwidth. Nevertheless, the study of the crossover between flat and dispersive bands is worth investigating.

Part IV

Conclusion & Outlook

Chapter 11

Conclusion

In this thesis, various ways to realize of emergent phenomena have been investigated. We focused on topology and unconventional superconductivity, but we also found magnetic ordering which was intertwined with superconductivity in a bilayer system. Multiple, static as well as dynamical, mechanisms were found to lead to several emergent collective phases in both, non-interacting and interacting models. These models were studied in one and two dimensions by employing a variety of methods for continuous and discrete lattice systems. These include ED, DMRG, generalized BCS theory and a Green's function approach for block-tridiagonal Hamiltonians. Furthermore, beyond simply applying numerical techniques, efficient ways for the calculation of the needed observables were discussed. Remarkably, this thesis includes both, numerical as well as analytical studies. These different approaches lead to concurring and at the same time complementary results, which allowed for a deep and detailed understanding of the investigated phenomena.

After the introduction of the different methods applied in this thesis, we first considered topological properties and started with the case of non-interacting models. Here, a specific subgroup of two-dimensional second order topological insulators, including the well known BHZ-model, were investigated. These topological insulators show a supersymmetric spectrum if a half integer Aharanov Bohm flux is applied through the system's center. Remarkably, the topological zero-energy bound states are protected by a combination of chiral symmetry and the mentioned supersymmetry. The phase diagram with a topological phase, non-topological phase and Weyl phase was discussed by studying the spectrum and the form of bound states on a Corbino disk, where topological states were shown to exist on the inner and outer surface, depending on the phase.

Nevertheless, topological properties do not only exist in non-interacting systems but can also arise due to interactions. In this thesis, subleading superconducting instabilities were analyzed on mean-field level with the focus on topological chiral superconducting orders. In contrast to real valued pairing orders (such as $p_{x,y}$), subleading chiral instabilites can be metastable. Here, a no-go theorem for real valued pairing was provided based on time-reversal one-band models with total $S_z = 0$-pairing. By employing numerical methods it was shown that chiral orders can be metastable subleading instabilities and that the established outcome persists in the case of more general models. This analysis leads to the natural proposal of establishing unconventional chiral superconducters by manipulating conventional superconductors with light.

Furthermore, another possibility for the realization of unconventional superconductivity was proposed in this thesis. In contrast to the first mechanism, this approach leads to unconventional superconducting behavior in equilibrium and no light pulse is required. Here, we investigated a bilayer heterostructure, which comprises two layers, one weakly- and one strongly-correlated layer. With purely repulsive interactions, we found superconductivity with Cooper pairs mainly localized in the weakly-interacting layer interweaved with magnetic correlations. Although the main mechanism can be understood by investigating the strong Coupling regime, where the analysis of a single rung is sufficient, detailed numerical simulations were performed. Based on a one-dimensional version of the proposed model, this yields a deeper understanding of the phase diagram even outside the strong Coupling regime. Interestingly, the numerical results suggest that, in some regions of the phase diagram, the proposed mechanism leads to exotic pair density wave pairing instead of

uniform superconductivity.
Finally, systems were considered that are likely to provide the strong correlations required for this mechanism. Here, we focused on flat-band systems (which were however studied in the absence of electronic interactions) and RKKY interactions between classical impurity spins were investigated. The analysis was restricted to one-dimensional lattices with a partially-filled flat band. First, before concentrating on the results, an effective way to compute the exact RKKY interaction was introduced. After this, it was shown that the spatial decay of this indirect exchange coupling depends on the characteristics of the flat band. A quasi long-ranged character (approaching power-laws with different exponents) was found if the flat band crosses additional dispersive bands while an exponential short-ranged decay is present in the case of an isolated flat band. Notably, the results are not covered by the standard expression of RKKY if at least one of the impurities is placed on a sublattice, where eigenstates of the flat band are present. This relies on the fact that the size of the impurity coupling needs to be small compared to other energy scales, such as the band width, since the standard expression originates from perturbation theory.

Chapter 12

Outlook

In the individual chapters of this thesis, possible future paths were already discussed. In the following, only a general overview of interesting directions, which can be pursued, is thus presented.

Most importantly, adding electronic interactions to the non-interacting models from Chapters 7 and 10 is an open subject that should be addressed in the future. Here, it is unclear if and how the results are changed by these additional interactions. As already discussed in Chapter 10, the application of DMRG to the one-dimensional flat-band models would allow to include interactions and thus to understand if and how RKKY interactions in flat-band systems are affected by correlations. Moreover, it would be interesting to investigate the subleading instabilities studied in Chapter 8 beyond mean-field level by including correlations resulting from higher order diagrams.

Furthermore, only one-dimensional models have been investigated in Chapters 9 and 10. Here, the exact treatment of the two-dimensional case is left for future research.
In the non-interacting case, the RKKY couplings can again be computed by exploiting the efficient Green's functions algorithm from Section 5.4. The interacting case is more involved. Here, methods capable of including interactions for large scale calculations on a perturbative level, such as functional renormalization group [371–375], could be used. Since this technique can be applied to two-dimensional lattices without translational symmetry using real space [376], it can be employed for the study of RKKY interactions in flat-band systems in the case of two-dimensional lattices with moderate interactions.
For the exact two-dimensional study of the superconducting mechanism from strong correlations, introduced in Chapter 9, one could try to apply DMRG on a small cylinder although it is unclear whether large enough system sizes can be treated due to the entanglement growth.

In general, the investigation of the shown physical behavior in more complicated systems is of future interest. Apart from the aforementioned generalization to higher dimensions and the addition of interactions, this includes the study of the superconductivity mechanism from Chapter 9 in models with even more layers and additional terms as well as a more detailed investigation of subleading instabilities discussed in Chapter 8 in multi-band models and systems that include same spin pairing. Additionally, further studies of disorder effects are left for the future. Although Chapter 10 deals with magnetic impurities in flat-band systems, a detailed study of disorder effects for the superconductivity mechanism presented in Chapter 9 would be very interesting. Furthermore, investigating the robustness of the topological properties of the second-order topological insulators from Chapter 7 against disorder is an open path that should be followed. While a short and qualitative study is already included in Ref. [111], a more detailed and quantitative study should be carried out in future research. Additionally, one could also add disordered hoppings or onsite potentials to the models discussed in Chapter 10 and investigate how this influences the obtained RKKY interaction.

Another future direction is the application of other methods to the research problems considered in this thesis with some examples already presented above.
Additionally, since machine learning methods have recently been used extensively for condensed

matter research [377–383], it is natural to investigate how machine learning methods can be employed for the topics presented in this thesis. One example is a detailed study of the stability of subleading superconducting instabilities using machine learning methods [384]. This could gain numerous insights and lead to a deeper understanding of the properties the instability needs to provide to be metastable. Furthermore, more complex systems with numerous instabilities could be studied. To this end, one could, for example, use reinforcement learning approaches for neural networks in order to find stable subleading superconducting instabilities. Here, it could be exploited that two instabilities with a positive curvature in the free energy landscape are needed. Therefore, the main idea would be to reward the network when the curvature of the subleading instability gets increased, while the curvature of the leading instability remains above a fixed treshold.
Moreover, machine learning methods could also be used for finding driving protocols that lead to a switching between the competing orders. Here, the network could be reinforced, whenever a change of parameters leads to a slower relaxation to the global minimum.

Furthermore, it would be fascinating to study whether the properties investigated in this thesis can also be found for other emergent phases. Here, one could, for example, explore subleading instabilities of other orderings, such as magnetic or charge order. It is unclear whether the development of metastable instabilities at higher energy is as challenging as for superconductors or whether these instabilities are in general metastable.

Finally, the experimental investigation of the presented behavior is of enormous interest for condensed matter research. In some chapters, possible realizations were already discussed.

Part V

Appendices

Appendix A

Analytical Expression for the Optimization of Solving the Gap Equation

In order to optimize solving the gap equation (6.33), we aim for the analytical solution of the integral (6.38). Therefore, we fist decompose this integral into two parts:

$$\begin{aligned} G^{<}(E)(\Delta t = 0) &= \frac{-1}{2\pi} \int d\omega \left(\frac{1}{2} - \frac{1}{2} \tanh\left(\frac{\beta\omega}{2} \right) \right) \frac{-2i\Gamma}{(\omega - E)^2 + \Gamma^2} \\ &= \frac{-1}{2\pi} \int d\omega \frac{-i\Gamma}{(\omega - E)^2 + \Gamma^2} + \frac{-1}{2\pi} \int d\omega \tanh\left(\frac{\beta\omega}{2} \right) \frac{-i\Gamma}{(\omega - E)^2 + \Gamma^2} \\ &= A_1 + A_2 \end{aligned} \tag{A.1}$$

We solve the parts separately by transforming them into Matsubara space. For the first integral, we find

$$\begin{aligned} A_1 &= -\frac{1}{2\pi} \int d\omega \frac{1}{2} \frac{-2i\Gamma}{(\omega - E)^2 + \Gamma^2} \\ &= \frac{1}{4\pi} \int d\omega \frac{2i\Gamma}{[(\omega - E) - i\Gamma][(\omega - E) + i\Gamma]} \\ &= \frac{1}{4\pi} 2\Gamma i \frac{2\pi i}{2i\Gamma} \\ &= \frac{1}{2} i \,. \end{aligned} \tag{A.2}$$

For the second integral, the result is given by

$$\begin{aligned} A_2 &= \frac{1}{2\pi} \int d\omega \frac{1}{2} \tanh\left(\frac{\beta\omega}{2} \right) \frac{-2i\Gamma}{(\omega - E)^2 + \Gamma^2} \\ &= \frac{-1}{2} \frac{2i\Gamma}{2\pi} 2\pi i \left[\tanh\left(\frac{\beta}{2}(E + i\Gamma) \right) \frac{1}{2i\Gamma} + \frac{2}{\beta} \sum_{n=0}^{\infty} \frac{1}{\left(i(2n+1)\frac{\pi}{\beta} - E \right)^2 + \Gamma^2} \right] \\ &= -\frac{1}{2} i \left[\tanh\left(\frac{\beta}{2}(E + i\Gamma) \right) + \frac{2}{\beta} \sum_{n=0}^{\infty} \frac{2i\Gamma}{\left(i(2n+1)\frac{\pi}{\beta} - E \right)^2 + \Gamma^2} \right] \\ &= -\frac{1}{2} i \left[\tanh\left(\frac{\beta}{2}(E + i\Gamma) \right) + \frac{2}{\beta} \frac{2i\Gamma}{\left(i\frac{\pi}{\beta} - E \right)^2 + \Gamma^2} + B \right] \end{aligned} \tag{A.3}$$

with

$$
\begin{aligned}
B &= \frac{2}{\beta}\sum_{n=1}^{\infty}\frac{2i\Gamma}{\left(i(2n+1)\frac{\pi}{\beta}-E\right)^2+\Gamma^2} \\
&= \frac{2}{\beta}\sum_{n=1}^{\infty}\left[\frac{1}{\left(i(2n+1)\frac{\pi}{\beta}-E\right)-i\Gamma}-\frac{1}{\left(i(2n+1)\frac{\pi}{\beta}-E\right)+i\Gamma}\right] \\
&= \frac{2}{\beta}\frac{\beta}{2\pi i}\sum_{n=1}^{\infty}\left[\frac{1}{n+\frac{1}{2}-\Gamma\frac{\beta}{2\pi}+iE\frac{\beta}{2\pi}}-\frac{1}{n+\frac{1}{2}+\Gamma\frac{\beta}{2\pi}+iE\frac{\beta}{2\pi}}\right]. \qquad \text{(A.4)}
\end{aligned}
$$

We can now exploit that the digamma function is given by

$$
\Psi(1+z) = -\gamma + \sum_{k=1}^{\infty}\left(\frac{1}{k}-\frac{1}{z+k}\right) \quad \text{for } z \neq -1,-2,-3,\ldots . \qquad \text{(A.5)}
$$

This leads to

$$
\begin{aligned}
B &= \frac{1}{i\pi}\sum_{n=1}^{\infty}\left[\frac{1}{n+\left(\frac{1}{2}-\Gamma\frac{\beta}{2\pi}+iE\frac{\beta}{2\pi}\right)}-\frac{1}{n+\left(\frac{1}{2}+\Gamma\frac{\beta}{2\pi}+iE\frac{\beta}{2\pi}\right)}\right] \qquad \text{(A.6)} \\
&= \frac{1}{i\pi}\left[\Psi\left(1+\frac{1}{2}+\Gamma\frac{\beta}{2\pi}+iE\frac{\beta}{2\pi}\right)-\Psi\left(1+\frac{1}{2}-\Gamma\frac{\beta}{2\pi}+iE\frac{\beta}{2\pi}\right)\right] \qquad \text{(A.7)}
\end{aligned}
$$

and the final expression

$$
\begin{aligned}
G^{<}(E)(\Delta t=0) =& \frac{i}{2}-\frac{i}{2}\left\{\tanh\left(\frac{\beta}{2}(E+i\Gamma)\right)+\frac{2}{\beta}\frac{2i\Gamma}{\left(i\frac{\pi}{\beta}-E\right)^2+\Gamma^2}\right. \\
&\left.+\frac{1}{i\pi}\left[\Psi\left(1+\frac{1}{2}+\Gamma\frac{\beta}{2\pi}+iE\frac{\beta}{2\pi}\right)-\Psi\left(1+\frac{1}{2}-\Gamma\frac{\beta}{2\pi}+iE\frac{\beta}{2\pi}\right)\right]\right\} \qquad \text{(A.8)}
\end{aligned}
$$

for $\frac{1}{2}-\frac{\Gamma\beta}{2\pi}+i\frac{E\beta}{2\pi} \neq -1,-2,-3,\ldots$.

Appendix B

Perturbative Result for the Derivative of Gap Function

To arrive at the formula (8.53) for the derivative of the gap function, we use Eq. (8.25) and insert the results (8.44)-(8.48) and (8.51) that were derived in Section 8.2.2. We find

$$
\begin{aligned}
i\partial_t \delta\Delta_k = & \frac{1}{N}\sum_{\mathbf{k}'} V_{\mathbf{k},\mathbf{k}'} \left[2\epsilon_{\mathbf{k}'}\delta_{\mathbf{k}'} \frac{N(E^0_{\mathbf{k},1}) - N(E^0_{\mathbf{k},2})}{2\sqrt{(\Delta^0_{\mathbf{k}'})^2+\epsilon^2_{\mathbf{k}'}}} \right. \\
& -\delta\Delta_{\mathbf{k}'} \left(-\frac{N(E^0_{\mathbf{k},1}) \left[(\Delta^0_{\mathbf{k}'})^2 + \epsilon^2_{\mathbf{k}'} - \epsilon_{\mathbf{k}'}\sqrt{(\Delta^0_{\mathbf{k}'})^2+\epsilon^2_{\mathbf{k}'}} \right] + N(E^0_{\mathbf{k},2}) \left[(\Delta^0_{\mathbf{k}'})^2 + \epsilon^2_{\mathbf{k}'} + \epsilon_{\mathbf{k}'}\sqrt{(\Delta^0_{\mathbf{k}'})^2+\epsilon^2_{\mathbf{k}'}} \right]}{2\left[(\Delta^0_{\mathbf{k}'})^2+\epsilon^2_{\mathbf{k}'}\right]} \right. \\
& \left. \left. + \frac{N(E^0_{\mathbf{k},1}) \left[(\Delta^0_{\mathbf{k}'})^2 + \epsilon^2_{\mathbf{k}'} + \epsilon_{\mathbf{k}'}\sqrt{(\Delta^0_{\mathbf{k}'})^2+\epsilon^2_{\mathbf{k}'}} \right] + N(E^0_{\mathbf{k},2}) \left[(\Delta^0_{\mathbf{k}'})^2 + \epsilon^2_{\mathbf{k}'} - \epsilon_{\mathbf{k}'}\sqrt{(\Delta^0_{\mathbf{k}'})^2+\epsilon^2_{\mathbf{k}'}} \right]}{2\left[(\Delta^0_{\mathbf{k}'})^2+\epsilon^2_{\mathbf{k}'}\right]} \right) \right. \\
& \left. -i\Gamma \left(2\delta_{\mathbf{k}'} \frac{N(E^0_{\mathbf{k},1}) - N(E^0_{\mathbf{k},2})}{2\sqrt{(\Delta^0_{\mathbf{k}'})^2+\epsilon^2_{\mathbf{k}'}}} - \delta I^D_{\mathbf{k}'} \right) \right] \\
= & \frac{1}{N}\sum_{\mathbf{k}'} V_{\mathbf{k},\mathbf{k}'} \left[2\epsilon_{\mathbf{k}'}\delta_{\mathbf{k}'} \frac{N(E^0_{\mathbf{k},1}) - N(E^0_{\mathbf{k},2})}{2\sqrt{(\Delta^0_{\mathbf{k}'})^2+\epsilon^2_{\mathbf{k}'}}} - \delta\Delta_{\mathbf{k}'} \left(\frac{(N(E^0_{\mathbf{k},1}) - N(E^0_{\mathbf{k},2}))2(\epsilon_{\mathbf{k}'}\sqrt{(\Delta^0_{\mathbf{k}'})^2+\epsilon^2_{\mathbf{k}'}})}{2((\Delta^0_{\mathbf{k}'})^2+\epsilon^2_{\mathbf{k}'})} \right) \right. \\
& \left. -i\Gamma \left(2\delta_{\mathbf{k}'} \frac{N(E^0_{\mathbf{k},1}) - N(E^0_{\mathbf{k},2})}{2\sqrt{(\Delta^0_{\mathbf{k}'})^2+\epsilon^2_{\mathbf{k}'}}} - \delta I^D_{\mathbf{k}'} \right) \right] \\
= & \frac{1}{N}\sum_{\mathbf{k}'} V_{\mathbf{k},\mathbf{k}'}\epsilon_{\mathbf{k}'} \frac{N(E^0_{\mathbf{k},1}) - N(E^0_{\mathbf{k},2})}{\sqrt{(\Delta^0_{\mathbf{k}'})^2+\epsilon^2_{\mathbf{k}'}}} (\delta_{\mathbf{k}'} - \delta\Delta_{\mathbf{k}'}) - \frac{i\Gamma}{N}\sum_{\mathbf{k}'} V_{\mathbf{k},\mathbf{k}'} \left(\delta_{\mathbf{k}'} \frac{N(E^0_{\mathbf{k},1}) - N(E^0_{\mathbf{k},2})}{\sqrt{(\Delta^0_{\mathbf{k}'})^2+\epsilon^2_{\mathbf{k}'}}} - \delta I^D_{\mathbf{k}'} \right) \\
= & \frac{1}{N}\sum_{\mathbf{k}'} V_{\mathbf{k},\mathbf{k}'}\epsilon_{\mathbf{k}'} \frac{N(E^0_{\mathbf{k},1}) - N(E^0_{\mathbf{k},2})}{\sqrt{(\Delta^0_{\mathbf{k}'})^2+\epsilon^2_{\mathbf{k}'}}} (\delta_{\mathbf{k}'} - \delta\Delta_{\mathbf{k}'}) - 2i\Gamma \left(1 - \frac{1}{2N}\sum_{\mathbf{k}'} V_{\mathbf{k},\mathbf{k}'} \frac{I_1 - I_2}{2\sqrt{(\Delta^0_{\mathbf{k}'})^2+\epsilon^2_{\mathbf{k}'}}} \right) \delta\Delta_{\mathbf{k}'} \,,
\end{aligned}
\tag{B.1}
$$

where we used in the last step that

$$
\delta\Delta_{\mathbf{k}} = \frac{1}{N}\sum_{\mathbf{k}'} V_{\mathbf{k},\mathbf{k}'}\delta f_{\mathbf{k}'} = \frac{1}{N}\sum_{\mathbf{k}'} V_{\mathbf{k},\mathbf{k}'}\delta_{\mathbf{k}'} \frac{N(E^0_{\mathbf{k}',1}) - N(E^0_{\mathbf{k}',2})}{2\sqrt{(\Delta^0_{\mathbf{k}'})^2+\epsilon^2_{\mathbf{k}'}}} \tag{B.2}
$$

in first order in $\delta_{\mathbf{k}}$.

Appendix C

Matrix Products for Derivations of Eqs. (6.82)-(6.88)

$$
\begin{aligned}
[h_{\mathbf{k}}, n_{\mathbf{k}}] &= \begin{pmatrix} h_{\mathbf{k},\uparrow} n_{\mathbf{k},\uparrow} & 0 \\ 0 & h_{\mathbf{k},\downarrow} n_{\mathbf{k},\downarrow} \end{pmatrix} - \begin{pmatrix} n_{\mathbf{k},\uparrow} h_{\mathbf{k},\uparrow} & 0 \\ 0 & n_{\mathbf{k},\downarrow} h_{\mathbf{k},\downarrow} \end{pmatrix} \\
&= \begin{pmatrix} [h_{\mathbf{k},\uparrow}, n_{\mathbf{k},\uparrow}] & 0 \\ 0 & [h_{\mathbf{k},\downarrow}, n_{\mathbf{k},\downarrow}] \end{pmatrix} \qquad \text{(C.1)} \\
\Delta_{\mathbf{k}} f_{\mathbf{k}}^{\dagger} - f_{\mathbf{k}} \Delta_{\mathbf{k}}^{\dagger} &= \begin{pmatrix} \Delta_{\mathbf{k},1} f_{\mathbf{k},1}^{\dagger} & 0 \\ 0 & \Delta_{\mathbf{k},2} f_{\mathbf{k},2}^{\dagger} \end{pmatrix} - \begin{pmatrix} f_{\mathbf{k},1} \Delta_{\mathbf{k},1}^{\dagger} & 0 \\ 0 & f_{\mathbf{k},2} \Delta_{\mathbf{k},2}^{\dagger} \end{pmatrix} \\
&= \begin{pmatrix} \tilde{\Delta}_{\mathbf{k}} \tilde{f}_{\mathbf{k}}^{\dagger} - \tilde{f}_{\mathbf{k}} \tilde{\Delta}_{\mathbf{k}}^{\dagger} & 0 \\ 0 & \tilde{\Delta}_{-\mathbf{k}}^{T} \tilde{f}_{-\mathbf{k}}^{*} - \tilde{f}_{-\mathbf{k}}^{T} \tilde{\Delta}_{-\mathbf{k}}^{*} \end{pmatrix} \qquad \text{(C.2)} \\
h_{\mathbf{k}} f_{\mathbf{k}} + f_{\mathbf{k}} h_{-\mathbf{k}}^{*} &= \begin{pmatrix} 0 & h_{\mathbf{k},\uparrow} f_{\mathbf{k},1} \\ h_{\mathbf{k},\downarrow} f_{\mathbf{k},2} & 0 \end{pmatrix} + \begin{pmatrix} 0 & f_{\mathbf{k},1} h_{-\mathbf{k},\downarrow}^{*} \\ f_{\mathbf{k},2} h_{-\mathbf{k},\uparrow}^{*} & 0 \end{pmatrix} \\
&= \begin{pmatrix} 0 & h_{\mathbf{k},\uparrow} \tilde{f}_{\mathbf{k}} + \tilde{f}_{\mathbf{k}} h_{-\mathbf{k},\downarrow}^{*} \\ -h_{\mathbf{k},\downarrow} \tilde{f}_{-\mathbf{k}}^{T} - \tilde{f}_{-\mathbf{k}}^{T} h_{-\mathbf{k},\uparrow}^{*} & 0 \end{pmatrix} \qquad \text{(C.3)} \\
\Delta_{\mathbf{k}} n_{-\mathbf{k}}^{*} + n_{\mathbf{k}} \Delta_{\mathbf{k}} &= \begin{pmatrix} 0 & \Delta_{\mathbf{k},1} n_{-\mathbf{k},\downarrow}^{*} \\ \Delta_{\mathbf{k},2} n_{-\mathbf{k},\uparrow}^{*} & 0 \end{pmatrix} + \begin{pmatrix} 0 & n_{\mathbf{k},\uparrow} \Delta_{\mathbf{k},1} \\ n_{\mathbf{k},\downarrow} \Delta_{\mathbf{k},2} & 0 \end{pmatrix} \\
&= \begin{pmatrix} 0 & \tilde{\Delta}_{\mathbf{k}} n_{-\mathbf{k},\downarrow}^{*} + n_{\mathbf{k},\uparrow} \tilde{\Delta}_{\mathbf{k}} \\ -\tilde{\Delta}_{-\mathbf{k}}^{T} n_{-\mathbf{k},\uparrow}^{*} - n_{\mathbf{k},\downarrow} \tilde{\Delta}_{-\mathbf{k}}^{T} & 0 \end{pmatrix} \qquad \text{(C.4)}
\end{aligned}
$$

Appendix D

Rotation of Matrix with Different Eigenvalues

In Subsection 8.2.5 it was shown that the rotation of the stability matrix does not change the sign of the real part of the eigenvalues for a matrix, where all eigenvalues agree. In the following a 2×2 matrix with different eigenvalues a and b is considered. In this case, the matrix $\tilde{A}$ can be written as

$$\tilde{A} = \tilde{R} \cdot \begin{pmatrix} a & 0 \\ 0 & b \end{pmatrix} \cdot \tilde{R}^{-1} \,. \tag{D.1}$$

Since different rotations commute, we find

$$A = \tilde{R} \cdot R \cdot \begin{pmatrix} a & 0 \\ 0 & b \end{pmatrix} \cdot \tilde{R}^{-1} \,. \tag{D.2}$$

Thus, it is sufficient to consider the eigenvalues of $R \cdot \begin{pmatrix} a & 0 \\ 0 & b \end{pmatrix}$ with $R = \begin{pmatrix} \cos\theta & \sin\theta \\ -\sin\theta & \cos\theta \end{pmatrix}$ and $|\theta| < \pi/2$. These eigenvalues are given by

$$\lambda_{1/2} = \frac{a+b}{2} \cos\theta \pm \sqrt{\left(\frac{a+b}{2} \cos\theta\right)^2 - ab} = x \pm y \,. \tag{D.3}$$

If a and b have the same sign, we find $\mathrm{Re}(y) < |x|$. Thus, λ_1 and λ_2 have the same sign as a and b. If a and b have different signs, we find $\mathrm{Re}(y) > |x|$ leading to different signs of λ_1 and λ_2. Therefore, we can conclude that the signs of the real part of the eigenvalues are not changed.

Appendix E

Pair Correlation Function in Momentum Space: Failure of Convergence of Results Obtained Based on the Tail

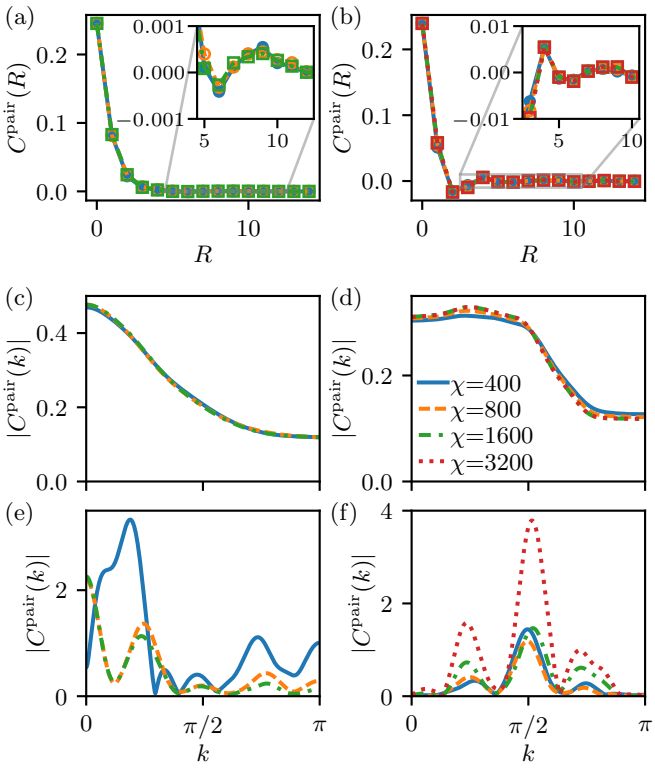

Figure E.1: Pair correlation functions in real and momentum space for $\rho = 3/8$, $t_d = 0.25$, $J = 3$, $U' = 0.4$ and (a),(c),(e) $t_c = -0.25$, (b),(d),(f) $t_c = 0.5$ with different bond dimensions. (a),(b) Real space pair correlation function with an inset zooming in on the tail. (c),(d) Fourier transform applied around $R = 0$ leading to a rather smooth pair correlation function and a significantly broadened peak. (e),(f) Fourier transform with a window applied to the tail leading to a different behavior in this regime. We note that both correlation functions are not converged but, for large enough bond dimensions, the positions of the peaks are. For (c),(e) both methods agree concerning the peak position, while in (d),(f) the phase depends on the applied method.

In Section 9.4.2, multiple approaches for performing the Fourier transform of the pair correlation function were introduced. In Fig. E.1, two parameter sets are shown, where the results obtained by applying the window within the tail of the correlation are not converged for the used bond dimensions (shown in (e),(f)). Nevertheless, the position of the maximum seems to be converged for large enough bond dimensions allowing to include these results into the phase diagrams. Here, the parameter set from (e) is associated with uniform superconductivity, while the parameter set from (f) is identified to have a 4-rung periodic PDW.
The obtained results can be compared to the momentum dependent correlation function extracted using a Fourier transform around $R = 0$. Those results are shown in Fig. E.1(c),(d). In the left column the phase obtained using the maxima, which were found using the different methods, agree, while they lead to different periodicity in the right column.
Moreover, in Fig. E.1(a),(b) the pair correlation functions in real space are shown. Here, we note that the correlation functions of both parameter sets show a oscillation at long distances. However, while the oscillation in (b) leads to the main peak obtained in (f), the oscillation in (a) only leads to an additional side peak in (e).

Appendix F

Matsubara Green's Function in Flat Band Systems

F.1 Stub Lattice

The Hamiltonian of the Stub Lattice in momentum space for $t = a = 1$ is given by $H = \sum_k \psi_k^\dagger \mathcal{H}(k) \psi_k$ with (see Eq. (10.15))

$$\mathcal{H}(k) = \begin{pmatrix} 0 & 1+e^{ik} & 1 \\ 1+e^{-ik} & 0 & 0 \\ 1 & 0 & 0 \end{pmatrix}. \tag{F.1}$$

We diagonalize this matrix and obtain

$$\mathbf{v}_1(k) = \sqrt{\frac{2+2\cos(k)}{3+2\cos(k)}} \begin{pmatrix} 0 \\ -\frac{1}{e^{ik}+1} \\ 1 \end{pmatrix}, \qquad \mathbf{v}_2(k) = \frac{1}{\sqrt{6+4\cos(k)}} \begin{pmatrix} -\sqrt{3+2\cos(k)} \\ 1+e^{-ik} \\ 1 \end{pmatrix},$$
$$\mathbf{v}_3(k) = \frac{1}{\sqrt{6+4\cos(k)}} \begin{pmatrix} \sqrt{3+2\cos(k)} \\ 1+e^{-ik} \\ 1 \end{pmatrix} \tag{F.2}$$

with eigenvalues $\varepsilon_1(k) = 0$, $\varepsilon_2(k) = -\sqrt{3+2\cos(k)}$ and $\varepsilon_3(k) = \sqrt{3+2\cos(k)}$. We define the matrix $\mathcal{H}_\mathrm{D}(k)$ as the diagonal version of $\mathcal{H}(k)$ with entries $\varepsilon_i(k)$ on the diagonal and the matrix V_k containing the eigenvectors as its columns. For the Matsubara Green's function, this leads to

$$\begin{aligned} G^{(0)}(k, i\omega) &= \frac{1}{i\omega - \mathcal{H}(k)} \\ &= V_k \frac{1}{i\omega - \mathcal{H}_D(k)} V_k^\dagger \\ &= \frac{1}{6+4\cos(k)} \cdot \\ &\begin{pmatrix} -\frac{2i\omega[3+2\cos(k)]}{\omega^2+3+2\cos(k)} & -\frac{2(1+e^{ik})[3+2\cos(k)]}{\omega^2+3+2\cos(k)} & -\frac{2[3+2\cos(k)]}{\omega^2+3+2\cos(k)} \\ -\frac{2[3+2\cos(k)](1+e^{-ik})}{\omega^2+3+2\cos(k)} & -\frac{2i\omega[2+2\cos(k)]}{\omega^2+3+2\cos(k)} + \frac{2}{i\omega} & -\frac{2i\omega(1+e^{-ik})}{\omega^2+3+2\cos(k)} - \frac{2[2+2\cos(k)]}{i\omega(e^{ik}+1)} \\ -\frac{2[3+2\cos(k)]}{\omega^2+3+2\cos(k)} & -\frac{2i\omega(1+e^{ik})}{\omega^2+3+2\cos(k)} - \frac{2(2+2\cos(k)]}{i\omega(1+e^{-ik})} & \frac{-2i\omega}{\omega^2+3+2\cos(k)} + \frac{2[2+2\cos(k)]}{i\omega} \end{pmatrix}. \end{aligned} \tag{F.3}$$

in momentum space as given in Eq. (10.18).
In order to obtain the integrals in real space, we need to apply a Fourier transform

$$G^{(0)}_{\alpha\beta}(r, i\omega) = \int_{-\pi}^{\pi} \frac{dk}{2\pi} G^{(0)}_{\alpha\beta}(k, i\omega)\, e^{ikr} \tag{F.4}$$

as already described in the main text. Here, we exploited that the Green's function only depends on the distance r of the two unit cell (and not on the indices of both of them) due to the translational symmetry of the system. We further assume $r \geq 0$ and $\omega \neq 0$.
The occurring integrals can be solved analytically using the residue theorem. We substitute $z = e^{ikx}$ and integrate over the unit circle. We need to calculate the following integrals and find:

$$\begin{aligned} I_1(x) &= \frac{1}{2\pi}\int_{-\pi}^{\pi} dk\, e^{ikx}\frac{1}{\omega^2+3+e^{ik}+e^{-ik}} = \frac{1}{2\pi}\oint dz \frac{z^x}{iz}\frac{1}{\omega^2+3+z+z^{-1}} \\ &= \frac{1}{2\pi}\oint \frac{z^x}{i}\frac{1}{(\omega^2+3)z+z^2+1} = \frac{1}{2\pi}\oint \frac{z^x}{i}\frac{1}{(z-z_1)(z-z_2)} = \frac{2\pi i}{2\pi i}z_1^x\frac{1}{z_1-z_2}+\frac{2\pi i}{2\pi i}\frac{\delta_{x,-1}}{z_1 z_2} \\ &= z_1^x \frac{1}{2\sqrt{\left(\frac{\omega^2+3}{2}\right)^2-1}} + \delta_{x,-1} \end{aligned} \tag{F.5}$$

with $z_{1/2} = -\frac{\omega^2+3}{2} \pm \sqrt{\left(\frac{\omega^2+3}{2}\right)^2-1}$ and $x \geq -1$;

$$I_2(x) = \frac{1}{2\pi}\int_{-\pi}^{\pi} dk\, e^{ikx}\frac{1}{i\omega} = \begin{cases} 0 \text{ for } x \neq 0 \\ \frac{1}{i\omega} \text{ for } x = 0 \end{cases} \quad ; \tag{F.6}$$

$$\begin{aligned} I_3(x) &= \frac{1}{2\pi}\int_{-\pi}^{\pi} dk\, e^{ikx}\frac{1}{3+e^{ik}+e^{-ik}}\frac{1}{\omega^2+3+e^{ik}+e^{-ik}} \\ &= \frac{1}{2\pi}\oint dz \frac{z^{x+1}}{i}\frac{1}{z^2+3z+1}\frac{1}{z^2+(\omega^2+3)z+1} \\ &= z_1^{x+1}\frac{1}{z_1^2+3z_1+1}\frac{1}{2\sqrt{\left(\frac{\omega^2+3}{3}\right)^2-1}} + z_3^{x+1}\frac{1}{\sqrt{5}}\frac{1}{z_3^2+(\omega^2+3)z_3+1} \end{aligned} \tag{F.7}$$

with $z_{1/2}$ as defined above and $z_{3/4} = -\frac{3}{2} \pm \frac{\sqrt{5}}{2}$; and

$$I_4(x) = \frac{1}{2\pi}\int_{-\pi}^{\pi} dk\, e^{ikx}\frac{1}{3+e^{ik}+e^{-ik}} = \frac{1}{2\pi}\oint \frac{z^x}{i}\frac{1}{z^2+3z+1} = z_3^x\frac{1}{\sqrt{5}}\,. \tag{F.8}$$

Using these integrals, we can write the Green's functions for $r \geq 0$ and $\omega \neq 0$ as

$$\begin{aligned} G_{AA}^{(0)}(r,i\omega) &= \frac{1}{2\pi}\int_{-\pi}^{\pi} dk\, e^{ikr}\frac{1}{2[3+2\cos(k)]}\frac{-2[3+2\cos(k)]i\omega}{\omega^2+3+2\cos(k)} \\ &= \frac{1}{2\pi}\int_{-\pi}^{\pi} dk\, e^{ikr}\frac{-i\omega}{\omega^2+3+e^{ik}+e^{-ik}} = -i\omega I_1(r) \end{aligned} \tag{F.9}$$

$$G_{AB}^{(0)}(r,i\omega) = \frac{1}{2\pi}\int_{-\pi}^{\pi} dk\, e^{ikr}\frac{-(1+e^{ik})}{\omega^2+3+2\cos(k)} = -\left[I_1(r)+I_1(r+1)\right] \tag{F.10}$$

$$G_{BA}^{(0)}(r,i\omega) = \frac{1}{2\pi}\int_{-\pi}^{\pi} dk\, e^{ikr}\frac{-(1+e^{-ik})}{\omega^2+3+2\cos(k)} = -\left[I_1(r)+I_1(r-1)\right] \tag{F.11}$$

$$G_{AC}^{(0)}(r,i\omega) = G_{CA}^{(0)}(k,i\omega) = \frac{1}{2\pi}\int_{-\pi}^{\pi} dk e^{ikr}\frac{-1}{\omega^2+3+2\cos(k)} = -I_1(r) \tag{F.12}$$

$$\begin{aligned} G_{BB}^{(0)}(r,i\omega) &= \frac{1}{2\pi}\int_{-\pi}^{\pi} dk e^{ikr}\frac{1}{2[3+2\cos(k)]}\left(-\frac{4i\omega[1+\cos(k)]}{\omega^2+3+2\cos(k)}+\frac{2}{i\omega}\right) \\ &= \frac{1}{2\pi}\int_{-\pi}^{\pi} dk\, e^{ikr}\left(\frac{-i\omega}{\omega^2+3+2\cos(k)}+\frac{2i\omega}{(6+4\cos(k))(\omega^2+3+2\cos(k))}+\frac{1}{i\omega[3+2\cos(k)]}\right) \end{aligned} \tag{F.13}$$

$$= -i\omega I_1(r) + i\omega I_3(r) + \frac{I_4(r)}{i\omega} \tag{F.14}$$

$$G^{(0)}_{BC}(r,i\omega) = \frac{1}{2\pi}\int_{-\pi}^{\pi} dk e^{ikr}\left(-\frac{i\omega(1+e^{-ik})}{(3+2\cos(k))(\omega^2+3+2\cos(k))} - \frac{1+e^{-ik}}{i\omega(3+2\cos(k))}\right)$$
$$= -i\omega[I_3(r)+I_3(r-1)] - \frac{I_4(r)+I_4(r-1)}{i\omega} \tag{F.15}$$
$$G^{(0)}_{CB}(r,i\omega) = \frac{1}{2\pi}\int_{-\pi}^{\pi} dk e^{ikr}\left(-\frac{i\omega(1+e^{-ik})}{(3+2\cos(k))(\omega^2+3+2\cos(k))} - \frac{1+e^{-ik}}{i\omega(3+2\cos(k))}\right)$$
$$= -i\omega[I_3(r)+I_3(r+1)] - \frac{I_4(r)+I_4(r+1)}{i\omega} = -\frac{1}{i\omega}I_1(r) - \frac{1}{i\omega}I_1(r+1) \tag{F.16}$$
$$G^{(0)}_{CC}(r,i\omega) = \frac{1}{2\pi}\int_{-\pi}^{\pi} dk e^{ikr}\left(-\frac{i\omega}{(3+2\cos(k))(\omega^2+3+2\cos(k))} + \frac{1}{i\omega} - \frac{1}{i\omega(3+2\cos(k))}\right)$$
$$= -i\omega I_3(r) + I_2(r) - \frac{1}{i\omega}I_4(r)\,. \tag{F.17}$$

To arrive at the simplified form introduced in Ref. [301], we define

$$\eta = 2\sqrt{\left(\frac{\omega^2+3}{2}\right)^2 - 1} = \sqrt{\omega^4+6\omega^2+5} = \sqrt{(\omega^2+1)(\omega^2+5)}\,. \tag{F.18}$$

We can then rewrite $z_{1/2} = \frac{-\omega^2-3\pm\eta}{2}$. This simplifies

$$I_1(x) = \frac{2^{-x}(-\omega^2-3+\eta)^x}{\eta} + \delta_{x,-1}\,. \tag{F.19}$$

Additionally, we identify

$$\begin{aligned} i\omega I_3(r) + \frac{1}{i\omega}I_4(r) &= \frac{1}{2\pi}\int_{-\pi}^{\pi} dk \frac{i\omega + \frac{1}{i\omega}\left(\omega^2+3+2\cos(k)\right)}{[3+2\cos(k)]\,[\omega^2+3+2\cos(k)]} \\ &= \frac{1}{2\pi}\int_{-\pi}^{\pi} dk \frac{3+2\cos(k)}{i\omega\,[3+2\cos(k)]\,[\omega^2+3+2\cos(k)]} \\ &= \frac{1}{2\pi}\int_{-\pi}^{\pi} dk \frac{1}{i\omega\,[\omega^2+3+2\cos(k)]} = \frac{1}{i\omega}I_1(r)\,. \end{aligned} \tag{F.20}$$

The real space Matsubara Green's functions can then be written in the more compact form

$$G^{(0)}_{AA}(r,i\omega) = -\frac{i\,2^{-r}\omega(-\omega^2-3+\eta)^r}{\eta} \tag{F.21}$$
$$\begin{aligned} G^{(0)}_{AB}(r,i\omega) &= -\frac{2^{-r}(-\omega^2-3+\eta)^r}{\eta} - \frac{2^{-(r+1)}(-\omega^2-3+\eta)^{(r+1)}}{\eta} \\ &= \frac{2^{-r-1}(-\omega^2-3+\eta)^r}{\eta}\left[-2-(-\omega^2-3+\eta)\right] \\ &= \frac{2^{-r-1}(-\omega^2-3+\eta)^r}{\eta^2}\left[(\omega^2+1)-\eta\right]\eta \\ &= \frac{2^{-r-1}(-\omega^2-3+\eta)^r}{(\omega^2+1)(\omega^2+5)}(\omega^2+1)\left[\eta-(\omega^2+5)\right] \\ &= \frac{2^{-r-1}(-\omega^2-5+\eta)(-\omega^2-3+\eta)^r}{\omega^2+5} \end{aligned} \tag{F.22}$$
$$\begin{aligned} G^{(0)}_{BA}(r,i\omega) &= -\frac{2^{-r}(-\omega^2-3+\eta)^r}{\eta} - \frac{2^{-r+1}(-\omega^2-3+\eta)^{r-1}}{\eta} - \delta_{r,0} \\ &= -\frac{2^{-r}(-\omega^2-3+\eta)^r}{\eta}\left(\frac{-\omega^2-3+\eta+2}{-\omega^2-3+\eta}\right) - \delta_{r,0} \end{aligned} \tag{F.23}$$
$$G^{(0)}_{AC}(r,i\omega) = G^{(0)}_{CA}(k,i\omega) = -\frac{2^{-r}(-\omega^2-3+\eta)^r}{\eta} \tag{F.24}$$

$$G^{(0)}_{BB}(r,i\omega) = \left(-i\omega + \frac{1}{i\omega}\right) I_1(r) = -\left(1+\frac{1}{\omega^2}\right)\frac{i\,2^{-r}\omega(-\omega^2-3+\eta)^r}{\eta} \tag{F.25}$$

$$G^{(0)}_{BC}(r,i\omega) = -\frac{1}{i\omega}I_1(r) - \frac{1}{i\omega}I_1(r-1) = \frac{2^{-r-1}\left(\omega^2+5+\eta\right)\left(-\omega^2-3+\eta\right)^r}{i\omega\left(\omega^2+5\right)} - \frac{\delta_{r,0}}{i\omega} \tag{F.26}$$

$$G^{(0)}_{CB}(r,i\omega) = -\frac{1}{i\omega}I_1(r) - \frac{1}{i\omega}I_1(r+1) = \frac{2^{-r-1}\left(-\omega^2-5+\eta\right)\left(-\omega^2-3+\eta\right)^r}{i\omega\left(\omega^2+5\right)} \tag{F.27}$$

$$G^{(0)}_{CC}(r,i\omega) = \frac{i\,2^{-r}(-\omega^2-3+\eta)^r}{\omega\eta} + \frac{\delta_{r,0}}{i\omega} \tag{F.28}$$

for the single components of the real space Matsubara Green's function of the stub lattice with $r \geq 0$ and $\omega \neq 0$.
The case $r < 0$ can be easily calculated from these results using

$$\begin{aligned} G^{(0)}_{\alpha\beta}(-r,i\omega) &= \int_{-\pi}^{\pi}\frac{dk}{2\pi}\,G^{(0)}_{\alpha\beta}(k,i\omega)\,e^{-ikr} \underset{k\to-k}{=} \int_{-\pi}^{\pi}\frac{dk}{2\pi}\,G^{(0)}_{\alpha\beta}(-k,i\omega)\,e^{ikr} \\ &\underset{G^{(0)}_{\alpha\beta}(-k,i\omega)=G^{(0)}_{\beta\alpha}(k,i\omega)}{=} \int_{-\pi}^{\pi}\frac{dk}{2\pi}\,G^{(0)}_{\beta\alpha}(k,i\omega)\,e^{ikr} = G^{(0)}_{\beta\alpha}(r,i\omega) \end{aligned} \tag{F.29}$$

F.2 Diamond Lattice

We now consider the Diamond Lattice with $t = a = 1$, which leads to an Hamiltonian of $H = \sum_k \psi_k^\dagger \mathcal{H}(k)\psi_k$ with (see Eq. (10.21))

$$\mathcal{H}(k) = \begin{pmatrix} 0 & 1+e^{ik} & 1+e^{ik} \\ 1+e^{-ik} & 0 & 0 \\ 1+e^{-ik} & 0 & 0 \end{pmatrix}. \tag{F.30}$$

The eigenvectors of this matrix are given by

$$\mathbf{v}_1(k) = \frac{1}{\sqrt{2}}\begin{pmatrix} 0 \\ -1 \\ 1 \end{pmatrix}, \qquad \mathbf{v}_2(k) = \frac{1}{2}\begin{pmatrix} -\sqrt{2}e^{ik/2} \\ 1 \\ 1 \end{pmatrix}, \qquad \mathbf{v}_3(k) = \frac{1}{2}\begin{pmatrix} \sqrt{2}e^{ik/2} \\ 1 \\ 1 \end{pmatrix} \tag{F.31}$$

with eigenvalues $\varepsilon_1(k) = 0$, $\varepsilon_2(k) = -2\sqrt{2}\cos(k/2)$ and $\varepsilon_3(k) = 2\sqrt{2}\cos(k/2)$.
We calculate the Masubara Green's function in the same way as for the Stub lattice and find

$$G^{(0)}(k,i\omega) = \frac{1}{i\omega - \mathcal{H}(k)} \tag{F.32}$$

$$= \frac{1}{4}\begin{pmatrix} \frac{-4i\omega}{\omega^2+8\cos^2(k/2)} & \frac{-8\cos(k/2)e^{ik/2}}{\omega^2+8\cos^2(k/2)} & \frac{-8\cos(k/2)e^{ik/2}}{\omega^2+8\cos^2(k/2)} \\ \frac{-8\cos(k/2)e^{-ik/2}}{\omega^2+8\cos^2(k/2)} & \frac{2}{i\omega} - \frac{2i\omega}{\omega^2+8\cos^2(k/2)} & -\frac{2}{i\omega} - \frac{2i\omega}{\omega^2+8\cos^2(k/2)} \\ \frac{-8\cos(k/2)e^{-ik/2}}{\omega^2+8\cos^2(k/2)} & -\frac{2}{i\omega} - \frac{2i\omega}{\omega^2+8\cos^2(k/2)} & \frac{2}{i\omega} - \frac{2i\omega}{\omega^2+8\cos^2(k/2)} \end{pmatrix} \tag{F.33}$$

in momentum space. For the transformation to real space (assuming again $\omega \neq 0$ and $r \geq 0$), we need $I_2(r)$ from Eq. (F.6) and

$$\begin{aligned} I_5(x) &= \frac{1}{2\pi}\int_{-\pi}^{\pi} dk\, e^{ikx}\frac{1}{\omega^2+8\cos^2(k/2)} = \frac{1}{2\pi}\int_{-\pi}^{\pi} dk\, e^{ikx}\frac{1}{\omega^2+4+2(e^{ik}+e^{-ik})} \\ &= \frac{1}{2\pi}\oint dz\frac{z^x}{2iz}\frac{1}{\frac{\omega^2}{2}+2+z+z^{-1}} = \frac{1}{2\pi}\oint\frac{z^x}{2i}\frac{1}{(\frac{\omega^2}{2}+2)z+z^2+1} = \frac{1}{2\pi}\oint\frac{z^x}{2i}\frac{1}{(z-z_5)(z-z_6)} \\ &= \frac{z_5^x}{2}\frac{1}{z_5-z_6} + \frac{\delta_{x,-1}}{z_5 z_6} = z_5^x\frac{1}{4\sqrt{\left(\frac{\omega^2}{4}+1\right)^2-1}} + \frac{1}{2}\frac{\delta_{x,-1}}{\left(\frac{\omega^2}{4}+1\right)^2-\left(\frac{\omega^2}{4}+1\right)^2+1} \\ &= z_5^x\frac{1}{4\sqrt{\left(\frac{\omega^2}{4}+1\right)^2-1}} + \frac{\delta_{x,-1}}{2} \end{aligned} \tag{F.34}$$

with $z_{5/6} = -\left(\frac{\omega^2}{4}+1\right) \pm \sqrt{\left(\frac{\omega^2}{4}+1\right)^2 - 1}$ and $x \geq -1$. Using the integrals, we can rewrite the Green's functions for $r \geq 0$ and $\omega \neq 0$ as

$$G^{(0)}_{AA}(r, i\omega) = \frac{1}{2\pi}\int_{-\pi}^{\pi} dk\, e^{ikr} \frac{-i\omega}{\omega^2 + 8\cos^2(k/2)} = -i\omega I_5(r) \tag{F.35}$$

$$G^{(0)}_{AB}(r, i\omega) = G^{(0)}_{AC}(r, i\omega) = \frac{1}{2\pi}\int_{-\pi}^{\pi} dk\, e^{ikr} \frac{-(1+e^{ik})}{\omega^2 + 8\cos^2(k/2)} = -[I_5(r) + I_5(r+1)] \tag{F.36}$$

$$G^{(0)}_{BA}(r, i\omega) = G^{(0)}_{CA}(r, i\omega) = \frac{1}{2\pi}\int_{-\pi}^{\pi} dk\, e^{ikr} \frac{-(1+e^{-ik})}{\omega^2 + 8\cos^2(k/2)} = -[I_5(r) + I_5(r-1)] \tag{F.37}$$

$$G^{(0)}_{BB}(r, i\omega) = G^{(0)}_{CC}(r, i\omega) = \frac{I_2(r)}{2} + \frac{1}{2} G^{(0)}_{AA}(r, i\omega) \tag{F.38}$$

$$G^{(0)}_{BC}(r, i\omega) = G^{(0)}_{CB}(r, i\omega) = -\frac{I_2(r)}{2} + \frac{1}{2} G^{(0)}_{AA}(r, i\omega)\,. \tag{F.39}$$

In order to find the compact form from Ref. [301], we define

$$\gamma = \frac{4}{\omega}\sqrt{\left(\frac{\omega^2}{4}+1\right)^2 - 1} = \frac{1}{\omega}\sqrt{\omega^4 + 8\omega^2} = \mathrm{sgn}(\omega)\sqrt{8+\omega^2}\,. \tag{F.40}$$

We can then rewrite $z_{5/6} = -\left(\frac{\omega^2}{4}+1\right) \pm \frac{\omega\gamma}{4} = -1 + \frac{\omega}{4}(-\omega \pm \gamma)$ and

$$I_5(x) = \frac{[-1 + \frac{\omega}{4}(-\omega+\gamma)]^x}{\omega\gamma} + \frac{\delta_{x,-1}}{2}\,. \tag{F.41}$$

For the components of the real space Matsubara Green's functions with $r \geq 0$ and $\omega \neq 0$, this leads to the compact form

$$G^{(0)}_{AA}(r, i\omega) = \frac{-i[-1 + \frac{\omega}{4}(-\omega+\gamma)]^r}{\gamma} \tag{F.42}$$

$$\begin{aligned} G^{(0)}_{AB}(r, i\omega) = G^{(0)}_{AC}(r, i\omega) &= \frac{-[-1 + \frac{\omega}{4}(-\omega+\gamma)]^r}{\omega\gamma}\left(1 + [-1 + \frac{\omega}{4}(-\omega+\gamma)]\right) \\ &= \frac{-[-1 + \frac{\omega}{4}(-\omega+\gamma)]^r}{4\gamma}(-\omega+\gamma) = \frac{4^{-1-r}[-4 + \omega(-\omega+\gamma)]^r}{\gamma}(\omega-\gamma) \end{aligned} \tag{F.43}$$

$$\begin{aligned} G^{(0)}_{BA}(r, i\omega) = G^{(0)}_{CA}(r, i\omega) &= -\frac{[-1 + \frac{\omega}{4}(-\omega+\gamma)]^r}{\omega\gamma} - \frac{[-1 + \frac{\omega}{4}(-\omega+\gamma)]^{r-1}}{\omega\gamma} - \frac{\delta_{r,0}}{2} \\ &= -\frac{[-1 + \frac{\omega}{4}(-\omega+\gamma)]^r}{\omega\gamma}\left(1 + \frac{1}{-1 + \frac{\omega}{4}(-\omega+\gamma)}\right) - \frac{\delta_{r,0}}{2} \\ &= -\frac{[-1 + \frac{\omega}{4}(-\omega+\gamma)]^r}{\gamma}\left(\frac{\frac{1}{4}(-\omega+\gamma)}{-1 + \frac{\omega}{4}(-\omega+\gamma)}\right) - \frac{\delta_{r,0}}{2} \\ &= -\frac{4^{-r}[-4 + \omega(-\omega+\gamma)]^r}{\gamma}\left(\frac{-(\omega+\gamma)}{4}\right) - \frac{\delta_{r,0}}{2} \\ &= \frac{4^{-r-1}(\omega+\gamma)[-4 + \omega(-\omega+\gamma)]^r}{\gamma} - \frac{\delta_{r,0}}{2} \end{aligned} \tag{F.44}$$

$$G^{(0)}_{BB}(r, i\omega) = G^{(0)}_{CC}(r, i\omega) = \frac{1}{2}\left(\frac{-i\left[-1 + \frac{\omega}{4}(-\omega+\gamma)\right]^r}{\gamma} + \frac{\delta_{r,0}}{i\omega}\right) \tag{F.45}$$

$$G^{(0)}_{BC}(r, i\omega) = G^{(0)}_{CB}(r, i\omega) = \frac{1}{2}\left(\frac{-i\left[-1 + \frac{\omega}{4}(-\omega+\gamma)\right]^r}{\gamma} - \frac{\delta_{r,0}}{i\omega}\right)\,. \tag{F.46}$$

Here, we used

$$\omega + \gamma = \frac{(\omega+\gamma)\left(-1 + \frac{\omega}{4}(-\omega+\gamma)\right)}{-1 + \frac{\omega}{4}(-\omega+\gamma)} = \frac{-\omega - \gamma + 2\omega}{-1 + \frac{\omega}{4}(-\omega+\gamma)} = \frac{\omega-\gamma}{-1 + \frac{\omega}{4}(-\omega+\gamma)} \tag{F.47}$$

for the simplification of $G^{(0)}_{BA}(k, i\omega) = G^{(0)}_{CA}(k, i\omega)$. The Green's functions for $r < 0$ can again be calculated using Eq. (F.29).

List of Acronyms

AFM	antiferromagnetic
BCS	Bardeen-Cooper-Schrieffer
BdG	Bogoliubov de Gennes
BHZ	Bernevig-Hughes-Zhang
DMRG	density-matrix renormalization group
ED	exact diagonalization
FF	Fulde-Ferrel
FFLO	Fulde–Ferrell–Larkin–Ovchinnikov
FM	ferromagnetic
LO	Larkin-Ovchinikov
MPS	matrix product state
MPO	matrix product operator
NTP	non-topological phase
PDW	pair density wave
PS	phase separation
RKKY	Ruderman-Kittel-Kasuya-Yosida
SOTI	second order topological insulator
SUSY	supersymmetry
SVD	singular value decomposition
TEBD	time evolved block decimation
TP	topological phase
WP	Weyl phase

Bibliography

[1] S. Kivelson and S. A. Kivelson, "Defining emergence in physics", npj Quantum Materials **1**, 16024 (2016).

[2] V. Drouin-Touchette, "Emergent quantum and classical phases from competing interactions", Ph.D. thesis (Rutgers, The State University of New Jersey, 2022).

[3] P. A. Murthy, "Emergent phenomena in two-dimensional fermi systems", Ph.D. thesis (Ruperto-Carola University of Heidelberg, 2018).

[4] P. W. Anderson, "More is different", Science **177**, 393–396 (1972).

[5] "The rise of quantum materials", Nature Physics **12**, 105–105 (2016).

[6] R. H. McKenzie, "Emergence: more is different", in *Condensed Matter Physics: A Very Short Introduction* (Oxford University Press, May 2023).

[7] D. Riegler, "Emergent phenomena in strongly correlated electron systems: auxiliary particle approach to the many-body problem", Ph.D. thesis (Universität Würzburg, 2022).

[8] E. Pavarini, E. Koch, and U. Schollwöck, eds., *Emergent Phenomena in Correlated Matter*, Vol. 3, Schriften des Forschungszentrums Jülich. Reihe modeling and simulation (Forschungszentrum Jülich GmbH Zentralbibliothek, Verlag, Jülich, Sept. 23, 2013), 520 S.

[9] J. K. Asbóth, L. Oroszlány, and A. Pályi, *A short course on topological insulators* (Springer International Publishing, 2016).

[10] X.-L. Qi and S.-C. Zhang, "Topological insulators and superconductors", Rev. Mod. Phys. **83**, 1057–1110 (2011).

[11] M. Franz and L. Molenkamp, eds., *Topological insulators*, Vol. 6, Contemporary Concepts of Condensed Matter Science (Elsevier, 2013).

[12] A. S. T. Pires, *A brief introduction to topology and differential geometry in condensed matter physics*, 2053-2571 (Morgan & Claypool Publishers, 2019).

[13] R. H. McKenzie, "Topology matters", in *Condensed Matter Physics: A Very Short Introduction* (Oxford University Press, May 2023).

[14] L. D. Landau, "On the theory of phase transitions", Zh. Eksp. Teor. Fiz. **7**, 19–32 (1937).

[15] M. Z. Hasan and C. L. Kane, "Colloquium: topological insulators", Rev. Mod. Phys. **82**, 3045–3067 (2010).

[16] M. Fruchart and D. Carpentier, "An introduction to topological insulators", Comptes Rendus. Physique **14**, 779–815 (2013).

[17] A. G. Grushin, "Introduction to topological phases in condensed matter", Lecture Notes for Les Houches doctoral school, Frontiers of Condensed Matter (2022).

[18] A. B. Khanikaev and A. Alù, "Topological photonics: robustness and beyond", Nature Communications **15**, 931 (2024).

[19] Y. Ando, "Topological insulator materials", Journal of the Physical Society of Japan **82**, 102001 (2013).

[20] Y. Ando, "Topological insulators", in *Encyclopedia of condensed matter physics (second edition)*, edited by T. Chakraborty, Second Edition (Academic Press, Oxford, 2024), pp. 690–699.

[21] H. Weng, R. Yu, X. Hu, X. Dai, and Z. Fang, "Quantum anomalous hall effect and related topological electronic states", Advances in Physics **64**, 227–282 (2015).

[22] C.-Z. Chang, C.-X. Liu, and A. H. MacDonald, "Colloquium: quantum anomalous hall effect", Rev. Mod. Phys. **95**, 011002 (2023).

[23] J. Alicea, "New directions in the pursuit of majorana fermions in solid state systems", Reports on Progress in Physics **75**, 076501 (2012).

[24] M. Leijnse and K. Flensberg, "Introduction to topological superconductivity and majorana fermions", Semiconductor Science and Technology **27**, 124003 (2012).

[25] M. Sato and Y. Ando, "Topological superconductors: a review", Reports on Progress in Physics **80**, 076501 (2017).

[26] M. M. Sharma, P. Sharma, N. K. Karn, and V. P. S. Awana, "Comprehensive review on topological superconducting materials and interfaces", Superconductor Science and Technology **35**, 083003 (2022).

[27] C. Beenakker, "Search for majorana fermions in superconductors", Annual Review of Condensed Matter Physics **4**, 113–136 (2013).

[28] B. A. Bernevig and T. L. Hughes, *Topological insulators and topological superconductors*, STU - Student edition (Princeton University Press, 2013).

[29] C. Kallin and J. Berlinsky, "Chiral superconductors", Reports on Progress in Physics **79**, 054502 (2016).

[30] A. Y. Kitaev, "Unpaired majorana fermions in quantum wires", Physics-Uspekhi **44**, 131 (2001).

[31] M. Sato and S. Fujimoto, "Majorana fermions and topology in superconductors", Journal of the Physical Society of Japan **85**, 072001 (2016).

[32] S. D. Sarma, M. Freedman, and C. Nayak, "Majorana zero modes and topological quantum computation", npj Quantum Information **1**, 15001 (2015).

[33] M. Mandal, N. C. Drucker, P. Siriviboon, T. Nguyen, A. Boonkird, T. N. Lamichhane, R. Okabe, A. Chotrattanapituk, and M. Li, "Topological superconductors from a materials perspective", Chemistry of Materials **35**, 6184–6200 (2023).

[34] S.-Q. Shen, "The family of topological phases in condensed matter†", National Science Review **1**, 49–59 (2013).

[35] M. C. Rechtsman, J. M. Zeuner, Y. Plotnik, Y. Lumer, D. Podolsky, F. Dreisow, S. Nolte, M. Segev, and A. Szameit, "Photonic floquet topological insulators", Nature **496**, 196–200 (2013).

[36] J. Cayssol, B. Dóra, F. Simon, and R. Moessner, "Floquet topological insulators", physica status solidi (RRL) – Rapid Research Letters **7**, 101–108 (2013).

[37] A. A. Burkov, "Topological semimetals", Nature Materials **15**, 1145–1148 (2016).

[38] H. Gao, J. W. Venderbos, Y. Kim, and A. M. Rappe, "Topological semimetals from first principles", Annual Review of Materials Research **49**, 153–183 (2019).

[39] Y. Hatsugai, "Topological aspects of the quantum hall effect", Journal of Physics: Condensed Matter **9**, 2507 (1997).

[40] J. E. Avron, D. Osadchy, and R. Seiler, "A Topological Look at the Quantum Hall Effect", Physics Today **56**, 38–42 (2003).

[41] Z. Wang, X. Wang, Z. Hu, D. Bongiovanni, D. Jukić, L. Tang, D. Song, R. Morandotti, Z. Chen, and H. Buljan, "Sub-symmetry-protected topological states", Nature Physics **19**, 992–998 (2023).

[42] A. Kitaev, "Periodic table for topological insulators and superconductors", AIP Conference Proceedings **1134**, 22–30 (2009).

[43] S. Ryu, A. P. Schnyder, A. Furusaki, and A. W. W. Ludwig, "Topological insulators and superconductors: tenfold way and dimensional hierarchy", New Journal of Physics **12**, 065010 (2010).

[44] A. P. Schnyder, S. Ryu, A. Furusaki, and A. W. W. Ludwig, "Classification of topological insulators and superconductors in three spatial dimensions", Phys. Rev. B **78**, 195125 (2008).

[45] X.-L. Qi, T. L. Hughes, and S.-C. Zhang, "Topological field theory of time-reversal invariant insulators", Phys. Rev. B **78**, 195424 (2008).

[46] C.-K. Chiu, J. C. Y. Teo, A. P. Schnyder, and S. Ryu, "Classification of topological quantum matter with symmetries", Rev. Mod. Phys. **88**, 035005 (2016).

[47] W. A. Benalcazar, B. A. Bernevig, and T. L. Hughes, "Quantized electric multipole insulators", Science **357**, 61–66 (2017).

[48] W. A. Benalcazar, B. A. Bernevig, and T. L. Hughes, "Electric multipole moments, topological multipole moment pumping, and chiral hinge states in crystalline insulators", Phys. Rev. B **96**, 245115 (2017).

[49] F. Schindler, A. M. Cook, M. G. Vergniory, Z. Wang, S. S. P. Parkin, B. A. Bernevig, and T. Neupert, "Higher-order topological insulators", Science Advances **4**, eaat0346 (2018).

[50] E. Khalaf, "Higher-order topological insulators and superconductors protected by inversion symmetry", Phys. Rev. B **97**, 205136 (2018).

[51] R. Chen, C.-Z. Chen, J.-H. Gao, B. Zhou, and D.-H. Xu, "Higher-order topological insulators in quasicrystals", Phys. Rev. Lett. **124**, 036803 (2020).

[52] B. Xie, H.-X. Wang, X. Zhang, P. Zhan, J.-H. Jiang, M. Lu, and Y. Chen, "Higher-order band topology", Nature Reviews Physics **3**, 520–532 (2021).

[53] Y. Xue, H. Huan, B. Zhao, Y. Luo, Z. Zhang, and Z. Yang, "Higher-order topological insulators in two-dimensional dirac materials", Phys. Rev. Res. **3**, L042044 (2021).

[54] F. Liu and K. Wakabayashi, "Higher-order topology and fractional charge in monolayer graphene", Phys. Rev. Res. **3**, 023121 (2021).

[55] S. S. Krishtopenko, "Higher-order topological insulator in cubic semiconductor quantum wells", Scientific Reports **11**, 21060 (2021).

[56] A. O. Zlotnikov, M. S. Shustin, and A. D. Fedoseev, "Aspects of topological superconductivity in 2d systems: noncollinear magnetism, skyrmions, and higher-order topology", Journal of Superconductivity and Novel Magnetism **34**, 3053–3088 (2021).

[57] Y. Zhang, J. Tang, X. Dai, and Y. Xiang, "Flexible dimensional hierarchy of higher-order topology in the stacked kagome-chain acoustic crystal", Communications Physics **6**, 130 (2023).

[58] Y. Wang, M. Lin, and T. L. Hughes, "Weak-pairing higher order topological superconductors", Phys. Rev. B **98**, 165144 (2018).

[59] J. Ahn and B.-J. Yang, "Higher-order topological superconductivity of spin-polarized fermions", Phys. Rev. Res. **2**, 012060 (2020).

[60] Y.-T. Hsu, W. S. Cole, R.-X. Zhang, and J. D. Sau, "Inversion-protected higher-order topological superconductivity in monolayer WTe_2", Phys. Rev. Lett. **125**, 097001 (2020).

[61] B. Fu, Z.-A. Hu, C.-A. Li, J. Li, and S.-Q. Shen, "Chiral majorana hinge modes in superconducting dirac materials", Phys. Rev. B **103**, L180504 (2021).

[62] K. H. Wong, M. R. Hirsbrunner, J. Gliozzi, A. Malik, B. Bradlyn, T. L. Hughes, and D. K. Morr, "Higher order topological superconductivity in magnet-superconductor hybrid systems", npj Quantum Materials **8**, 31 (2023).

[63] A. Chew, Y. Wang, B. A. Bernevig, and Z.-D. Song, "Higher-order topological superconductivity in twisted bilayer graphene", Phys. Rev. B **107**, 094512 (2023).

[64] M. Serra-Garcia, V. Peri, R. Süsstrunk, O. R. Bilal, T. Larsen, L. G. Villanueva, and S. D. Huber, "Observation of a phononic quadrupole topological insulator", Nature **555**, 342–345 (2018).

[65] J. Noh, W. A. Benalcazar, S. Huang, M. J. Collins, K. P. Chen, T. L. Hughes, and M. C. Rechtsman, "Topological protection of photonic mid-gap defect modes", Nature Photonics **12**, 408–415 (2018).

[66] S. Imhof, C. Berger, F. Bayer, J. Brehm, L. W. Molenkamp, T. Kiessling, F. Schindler, C. H. Lee, M. Greiter, T. Neupert, and R. Thomale, "Topolectrical-circuit realization of topological corner modes", Nature Physics **14**, 925–929 (2018).

[67] C. W. Peterson, W. A. Benalcazar, T. L. Hughes, and G. Bahl, "A quantized microwave quadrupole insulator with topologically protected corner states", Nature **555**, 346–350 (2018).

[68] H. Xue, Y. Ge, H.-X. Sun, Q. Wang, D. Jia, Y.-J. Guan, S.-Q. Yuan, Y. Chong, and B. Zhang, "Observation of an acoustic octupole topological insulator", Nature Communications **11**, 2442 (2020).

[69] Y. Qi, C. Qiu, M. Xiao, H. He, M. Ke, and Z. Liu, "Acoustic realization of quadrupole topological insulators", Phys. Rev. Lett. **124**, 206601 (2020).

[70] J. Wu, Y. Zhang, and B. Xiang, "Synthesis, properties and applications of topological quantum materials", JUSTC **53**, 1 (2023).

[71] O. Breunig and Y. Ando, "Opportunities in topological insulator devices", Nature Reviews Physics **4**, 184–193 (2021).

[72] L. Šmejkal, Y. Mokrousov, B. Yan, and A. H. MacDonald, "Topological antiferromagnetic spintronics", Nature Physics **14**, 242–251 (2018).

[73] M. J. Gilbert, "Topological electronics", Communications Physics **4**, 70 (2021).

[74] A. Stern and N. H. Lindner, "Topological quantum computation—from basic concepts to first experiments", Science **339**, 1179–1184 (2013).

[75] V. Lahtinen and J. K. Pachos, "A short introduction to topological quantum computation", SciPost Phys. **3**, 021 (2017).

[76] C. Zalka, "Simulating quantum systems on a quantum computer", Proceedings of the Royal Society of London. Series A: Mathematical, Physical and Engineering Sciences **454**, 313–322 (1998).

[77] S. K. Sood and Pooja, "Quantum computing review: a decade of research", IEEE Transactions on Engineering Management **71**, 6662–6676 (2024).

[78] Nandhini S, H. Singh, and Akash U N, "An extensive review on quantum computers", Advances in Engineering Software **174**, 103337 (2022).

[79] E. Chae, J. Choi, and J. Kim, "An elementary review on basic principles and developments of qubits for quantum computing", Nano Convergence **11**, 11 (2024).

[80] D. Castelvecchi, "Ibm releases first-ever 1,000-qubit quantum chip", Nature **624**, 238 (2023).

[81] L. Pause, L. Sturm, M. Mittenbühler, S. Amann, T. Preuschoff, D. Schäffner, M. Schlosser, and G. Birkl, "Supercharged two-dimensional tweezer array with more than 1000 atomic qubits", Optica **11**, 222–226 (2024).

[82] M. T. Dejpasand and M. Sasani Ghamsari, "Research trends in quantum computers by focusing on qubits as their building blocks", Quantum Reports **5**, 597–608 (2023).

[83] D. van Delft and P. Kes, "The discovery of superconductivity", Physics Today **63**, 38–43 (2010).

[84] W. Meissner and R. Ochsenfeld, "Ein neuer effekt bei eintritt der supraleitfähigkeit", Naturwissenschaften **21**, 787–788 (1933).

[85] R. G. Sharma, "The phenomenon of superconductivity and type ii superconductors", in *Superconductivity: basics and applications to magnets* (Springer International Publishing, Cham, 2021), pp. 15–72.

[86] F. London, H. London, and F. A. Lindemann, "The electromagnetic equations of the supraconductor", Proceedings of the Royal Society of London. Series A - Mathematical and Physical Sciences **149**, 71–88 (1935).

[87] M. Cyrot, "Ginzburg-landau theory for superconductors", Reports on Progress in Physics **36**, 103 (1973).

[88] V. L. Ginzburg and L. D. Landau, "On the theory of superconductivity", Zh. Eksp. Teor. Fiz. **20**, 1064–1082 (1950), [English translation in: L. D. Landau, "Collected papers," Oxford: Pergamon Press (1965), 546.]

[89] J. Bardeen, L. N. Cooper, and J. R. Schrieffer, "Microscopic theory of superconductivity", Phys. Rev. **106**, 162–164 (1957).

[90] J. Bardeen, L. N. Cooper, and J. R. Schrieffer, "Theory of superconductivity", Phys. Rev. **108**, 1175–1204 (1957).

[91] M. Sigrist, "Introduction to Unconventional Superconductivity", AIP Conference Proceedings **789**, 165–243 (2005).

[92] G. R. Stewart, "Unconventional superconductivity", Advances in Physics **66**, 75–196 (2017).

[93] Y. Maeno, S. Yonezawa, and A. Ramires, "Still mystery after all these years —unconventional superconductivity of Sr2RuO4—", Journal of the Physical Society of Japan **93**, 062001 (2024).

[94] M. R. Norman, "The challenge of unconventional superconductivity", Science **332**, 196–200 (2011).

[95] C. C. Tsuei and J. R. Kirtley, "Pairing symmetry in cuprate superconductors", Rev. Mod. Phys. **72**, 969–1016 (2000).

[96] J. Guo, Y. Zhou, C. Huang, S. Cai, Y. Sheng, G. Gu, C. Yang, G. Lin, K. Yang, A. Li, Q. Wu, T. Xiang, and L. Sun, "Crossover from two-dimensional to three-dimensional superconducting states in bismuth-based cuprate superconductor", Nature Physics **16**, 295–300 (2020).

[97] B. Keimer, S. A. Kivelson, M. R. Norman, S. Uchida, and J. Zaanen, "From quantum matter to high-temperature superconductivity in copper oxides", Nature **518**, 179–186 (2015).

[98] A. Bussmann-Holder and H. Keller, Zeitschrift für Naturforschung B **75**, 3–14 (2020).

[99] J. Nagamatsu, N. Nakagawa, T. Muranaka, Y. Zenitani, and J. Akimitsu, "Superconductivity at 39 k in magnesium diboride", Nature **410**, 63–64 (2001).

[100] C. C. Seegmiller, S. G. Baird, H. M. Sayeed, and T. D. Sparks, "Discovering chemically novel, high-temperature superconductors", Computational Materials Science **228**, 112358 (2023).

[101] W. Rogers, "Superconducting maglev: speeding toward sustainability", Global Railway Review (2022).

[102] U.S. Congress, Office of Technology Assessment, *High-temperature superconductivity in perspective*, OTA-E-440 (Washington DC: U.S. Government Printing Office, Apr. 1990).

[103] R. L. Fagaly, "Superconducting quantum interference device instruments and applications", Review of Scientific Instruments **77**, 101101 (2006).

[104] H.-L. Huang, D. Wu, D. Fan, and X. Zhu, "Superconducting quantum computing: a review", Science China Information Sciences **63**, 180501 (2020).

[105] S. M. Anlage, "The physics and applications of superconducting metamaterials", Journal of Optics **13**, 024001 (2010).

[106] H. Kaur, H. Kaur, and A. Sharma, "A review of recent advancement in superconductors", Materials Today: Proceedings **37**, International Conference on Newer Trends and Innovation in Mechanical Engineering: Materials Science, 3612–3614 (2021).

[107] C. Yao and Y. Ma, "Superconducting materials: challenges and opportunities for large-scale applications", iScience **24**, 102541 (2021).

[108] A. Weiße and H. Fehske, "Exact diagonalization techniques", in *Computational many-particle physics*, edited by H. Fehske, R. Schneider, and A. Weiße (Springer Berlin Heidelberg, Berlin, Heidelberg, 2008), pp. 529–544.

[109] E. Pavarini, E. Koch, and S. Zhang, eds., *Many-Body Methods for Real Materials*, Vol. 9, Schriften des Forschungszentrums Jülich. Modeling and Simulation, Autumn School on Correlated Electrons, Jülich (Germany), 16 Sep 2019 - 20 Sep 2019 (Forschungszentrum Jülich GmbH Zentralbibliothek, Verlag, Jülich, Sept. 16, 2019), getr. Zählung.

[110] V. Meden, "Theoretische physik iii (quantenmechanik)", Lecture Notes, RWTH Aachen University (2018).

[111] C. S. Weber, M. Pletyukhov, Z. Hou, D. M. Kennes, J. Klinovaja, D. Loss, and H. Schoeller, "Second-order topology and supersymmetry in two-dimensional topological insulators", Phys. Rev. B **107**, 235402 (2023).

[112] F. Bowman, *Introduction to bessel functions*, Dover Books on Mathematics (Dover Publications, 1958).

[113] W. Kaplan, *Advanced calculus*, Addison-Wesley higher mathematics (Addison-Wesley, 2002).

[114] M. Ashu, "Some properties of bessel functions with applications to neumann eigenvalues in the unit disc", Bachelor thesis (Lund University, 2013).

[115] M. Levitin, D. Mangoubi, and I. Polterovich, *Topics in spectral geometry*, preliminary version (2023), eprint: `https://michaellevitin.net/Book/`.

[116] U. Schollwöck, "The density-matrix renormalization group", Rev. Mod. Phys. **77**, 259–315 (2005).

[117] U. Schollwöck, "The density-matrix renormalization group in the age of matrix product states", Annals of Physics **326**, January 2011 Special Issue, 96–192 (2011).

[118] D. M. Kennes, "Dynamics in low-dimensional correlated quantum systems", Ph.D. thesis (RWTH Aachen University, 2014).

[119] C. S. Weber, "Boundary charge fluctuations", Master thesis (RWTH Aachen University, 2021).

[120] J. Hauschild and F. Pollmann, "Efficient numerical simulations with tensor networks: tensor network python (TeNPy)", SciPost Phys. Lect. Notes, 5 (2018).

[121] S. R. White, "Density matrix formulation for quantum renormalization groups", Phys. Rev. Lett. **69**, 2863–2866 (1992).

[122] S. R. White, "Density-matrix algorithms for quantum renormalization groups", Phys. Rev. B **48**, 10345–10356 (1993).

[123] G. Vidal, "Efficient classical simulation of slightly entangled quantum computations", Phys. Rev. Lett. **91**, 147902 (2003).

[124] L. Hoffman, *Calculus for business, economics and the social and life sciences, brief version* (McGraw-Hill Education, 2012).

[125] C. S. Weber, D. Kiese, D. M. Kennes, and M. Claassen, "Intertwined superconductivity and magnetism from repulsive interactions in kondo bilayers", (2024), arXiv:`2408.02847` [cond-mat.str-el].

[126] M. Dolfi, B. Bauer, S. Keller, and M. Troyer, "Pair correlations in doped hubbard ladders", Phys. Rev. B **92**, 195139 (2015).

[127] C. Hubig, J. Haegeman, and U. Schollwöck, "Error estimates for extrapolations with matrix-product states", Phys. Rev. B **97**, 045125 (2018).

[128] S. R. White, "Density matrix renormalization group algorithms with a single center site", Phys. Rev. B **72**, 180403 (2005).

[129] J. P. F. LeBlanc, A. E. Antipov, F. Becca, I. W. Bulik, G. K.-L. Chan, C.-M. Chung, Y. Deng, M. Ferrero, T. M. Henderson, C. A. Jiménez-Hoyos, E. Kozik, X.-W. Liu, A. J. Millis, N. V. Prokof'ev, M. Qin, G. E. Scuseria, H. Shi, B. V. Svistunov, L. F. Tocchio, I. S. Tupitsyn, S. R. White, S. Zhang, B.-X. Zheng, Z. Zhu, and E. Gull (Simons Collaboration on the Many-Electron Problem), "Solutions of the two-dimensional hubbard model: benchmarks and results from a wide range of numerical algorithms", Phys. Rev. X **5**, 041041 (2015).

[130] G. Ehlers, S. R. White, and R. M. Noack, "Hybrid-space density matrix renormalization group study of the doped two-dimensional hubbard model", Phys. Rev. B **95**, 125125 (2017).

[131] M. M. Rams, P. Czarnik, and L. Cincio, "Precise extrapolation of the correlation function asymptotics in uniform tensor network states with application to the bose-hubbard and xxz models", Phys. Rev. X **8**, 041033 (2018).

[132] H. Bruus and K. Flensberg, *Many-body quantum theory in condensed matter physics: an introduction*, Oxford Graduate Texts (OUP Oxford, 2004).

[133] J. W. Negele and H. Orland, *Quantum many-particle systems* (Westview Press, Nov. 1998).

[134] J. Rammer, *Quantum field theory of non-equilibrium states* (Cambridge University Press, 2007).

[135] G. Stefanucci and R. van Leeuwen, *Nonequilibrium many-body theory of quantum systems: a modern introduction* (Cambridge University Press, 2013).

[136] S. Weßel, "Quantum theory of condensed matter i", Lecture Notes, RWTH Aachen University (2019/2020).

[137] H. Schoeller, "Quantum theory of condensed matter i", Lecture Notes, RWTH Aachen University (2009/2010).

[138] H. Schoeller, "Nonequilibrium green's functions and open quantum systems", Lecture Notes on Nonequilibrium Green's functions, RWTH Aachen University (2019/2020).

[139] L. V. Keldysh, "Diagram technique for nonequilibrium processes", Zh. Eksp. Teor. Fiz. **47**, 1515–1527 (1964), [Sov. Phys. JETP **20**, 1018 (1965)].

[140] M. Pourfath, "Numerical study of quantum transport in carbon nanotube-based transistors", Ph.D. thesis (Technische Universität Wien, 2007).

[141] J. Maciejko, *An introduction to nonequilibrium many-body theory* (Springer, 2007).

[142] S. G. Jakobs, "Functional renormalization group studies of quantum transport through mesoscopic systems", Ph.D. thesis (RWTH Aachen University, 2009).

[143] C. Karrasch, "The functional renormalization group for zero-dimensional quantum systems in and out of equilibrium", Ph.D. thesis (RWTH Aachen University, 2010).

[144] M. Claassen, D. M. Kennes, M. Zingl, M. A. Sentef, and A. Rubio, "Universal optical control of chiral superconductors and majorana modes", Nature Physics **15**, 766–770 (2019).

[145] K. Laubscher, D. Chughtai, D. Loss, and J. Klinovaja, "Kramers pairs of majorana corner states in a topological insulator bilayer", Phys. Rev. B **102**, 195401 (2020).

[146] C. H. Lewenkopf and E. R. Mucciolo, "The recursive green's function method for graphene", Journal of Computational Electronics **12**, 203–231 (2013).

[147] M. M. Odashima, B. G. Prado, and E. Vernek, "Pedagogical introduction to equilibrium green's functions: condensed-matter examples with numerical implementations", Revista Brasileira de Ensino de Física **39**, e1303 (2017).

[148] N. Müller, D. M. Kennes, J. Klinovaja, D. Loss, and H. Schoeller, "Electronic transport in one-dimensional floquet topological insulators via topological and nontopological edge states", Phys. Rev. B **101**, 155417 (2020).

[149] F. Guinea, C. Tejedor, F. Flores, and E. Louis, "Effective two-dimensional hamiltonian at surfaces", Phys. Rev. B **28**, 4397–4402 (1983).

[150] M. P. L. Sancho, J. M. L. Sancho, and J. Rubio, "Highly convergent schemes for the calculation of bulk and surface green functions", Journal of Physics F: Metal Physics **15**, 851 (1985).

[151] K. S. Dy, S.-Y. Wu, and T. Spratlin, "Exact solution for the resolvent matrix of a generalized tridiagonal hamiltonian", Phys. Rev. B **20**, 4237–4243 (1979).

[152] G. Meurant, "A review on the inverse of symmetric tridiagonal and block tridiagonal matrices", SIAM Journal on Matrix Analysis and Applications **13**, 707–728 (1992).

[153] S. Andergassen, T. Enss, V. Meden, W. Metzner, U. Schollwöck, and K. Schönhammer, "Functional renormalization group for luttinger liquids with impurities", Phys. Rev. B **70**, 075102 (2004).

[154] S. Gassner, C. S. Weber, and M. Claassen, "Light-induced switching between singlet and triplet superconducting states", Nature Communications **15**, 10.1038/s41467-024-45949-x (2024).

[155] M. Sigrist and K. Ueda, "Phenomenological theory of unconventional superconductivity", Rev. Mod. Phys. **63**, 239–311 (1991).

[156] M. H. Fischer, "Gap symmetry and stability analysis in the multi-orbital fe-based superconductors", New Journal of Physics **15**, 073006 (2013).

[157] E. Pangburn, L. Haurie, A. Crépieux, O. A. Awoga, A. M. Black-Schaffer, C. Pépin, and C. Bena, "Superconductivity in monolayer and few-layer graphene. i. review of possible pairing symmetries and basic electronic properties", Phys. Rev. B **108**, 134514 (2023).

[158] M. F. Holst, M. Sigrist, and K. V. Samokhin, "Topological states of multiband superconductors with interband pairing", Phys. Rev. Res. **6**, 023105 (2024).

[159] Y. Yang, "Mathematical analysis of the multiband bcs gap equations in superconductivity", Physica D: Nonlinear Phenomena **200**, 60–74 (2005).

[160] G. Margalit, E. Berg, and Y. Oreg, "Theory of multi-orbital topological superconductivity in transition metal dichalcogenides", Annals of Physics **435**, Special issue on Philip W. Anderson, 168561 (2021).

[161] Y. Asano, A. Sasaki, and A. A. Golubov, "Dirty two-band superconductivity with interband pairing order", New Journal of Physics **20**, 043020 (2018).

[162] S. Hörhold, J. Graf, M. Marganska, and M. Grifoni, "Two-bands ising superconductivity from coulomb interactions in monolayer $NbSe_2$", 2D Materials **10**, 025008 (2023).

[163] P. Coleman, *Introduction to many-body physics* (Cambridge University Press, 2015).

[164] M. Tinkham, *Introduction to superconductivity*, 2nd ed. (Dover Publications, June 2004).

[165] A. Fetter and J. Walecka, *Quantum theory of many-particle systems*, Dover Books on Physics (Dover Publications, 2003).

[166] R. Thomale, C. Platt, W. Hanke, and B. A. Bernevig, "Mechanism for explaining differences in the order parameters of feas-based and fep-based pnictide superconductors", Phys. Rev. Lett. **106**, 187003 (2011).

[167] C. Platt, W. Hanke, and R. Thomale, "Functional renormalization group for multi-orbital fermi surface instabilities", Advances in Physics **62**, 453–562 (2013).

[168] D. M. Kennes, J. Lischner, and C. Karrasch, "Strong correlations and $d + id$ superconductivity in twisted bilayer graphene", Phys. Rev. B **98**, 241407 (2018).

[169] D. M. Kennes, *Personal communication*, 2021.

[170] T. Salamone, H. G. Hugdal, S. H. Jacobsen, and M. Amundsen, "High magnetic field superconductivity in a two-band superconductor", Phys. Rev. B **107**, 174516 (2023).

[171] V. Meden, "Theoretische physik iv: statistische physik", Lecture Notes, RWTH Aachen University (2014/2015).

[172] W. Nolting, *Grundkurs theoretische physik 6: statistische physik*, Springer-Lehrbuch (Springer Berlin Heidelberg, 2013).

[173] M. Bertolini, "Lectures on supersymmetry", Lecture Notes, SISSA (April 15, 2024).

[174] A. Gladyshev and D. Kazakov, "Is (Low Energy) SUSY still Alive?", Lectures at the European School of High-Energy Physics, June 2012, Anjou, France, 107–159 (2014), arXiv:1212.2548.

[175] S. P. Martin, "A supersymmetry primer", Adv. Ser. Direct. High Energy Phys. **18**, edited by G. L. Kane, 1–98 (1998).

[176] F. Cooper, A. Khare, and U. Sukhatme, "Supersymmetry and quantum mechanics", Physics Reports **251**, 267–385 (1995).

[177] F. Cooper, A. Khare, and U. Sukhatme, *Supersymmetry in quantum mechanics* (World Scientific, Singapore, 2001).

[178] B. K. Bagchi, *Supersymmetry in quantum and classical mechanics* (Chapman & Hall/CRC, Monographs, Surveys in Pure, and Applied Mathematics, Boca Raton, Florida, 2001).

[179] A. R. P. Rau, "Supersymmetry in quantum mechanics: an extended view", Journal of Physics A: Mathematical and General **37**, 10421 (2004).

[180] G. Junker, *Supersymmetric methods in quantum, statistical and solid state physics*, 2053-2563 (IOP Publishing, Bristol, UK, 2019).

[181] O. Pankratov, S. Pakhomov, and B. Volkov, "Supersymmetry in heterojunctions: Band-inverting contact on the basis of $Pb_{1-x}Sn_xTe$ and $Hg_1 - xCd_xTe$", Solid State Communications **61**, 93–96 (1987).

[182] M. Ezawa, "Supersymmetric structure of quantum hall effects in graphene", Physics Letters A **372**, 924–929 (2008).

[183] M. Tomka, M. Pletyukhov, and V. Gritsev, "Supersymmetry in quantum optics and in spin-orbit coupled systems", Scientific Reports **5**, 13097 (2015).

[184] T. Grover, D. N. Sheng, and A. Vishwanath, "Emergent space-time supersymmetry at the boundary of a topological phase", Science **344**, 280–283 (2014).

[185] P. Ponte and S.-S. Lee, "Emergence of supersymmetry on the surface of three-dimensional topological insulators", New Journal of Physics **16**, 013044 (2014).

[186] G. Queraltó, M. Kremer, L. J. Maczewsky, M. Heinrich, J. Mompart, V. Ahufinger, and A. Szameit, "Topological state engineering via supersymmetric transformations", Communications Physics **3**, 49 (2020).

[187] M. Geier, L. Trifunovic, M. Hoskam, and P. W. Brouwer, "Second-order topological insulators and superconductors with an order-two crystalline symmetry", Phys. Rev. B **97**, 205135 (2018).

[188] L. Trifunovic and P. W. Brouwer, "Higher-order bulk-boundary correspondence for topological crystalline phases", Phys. Rev. X **9**, 011012 (2019).

[189] B. A. Bernevig, T. L. Hughes, and S.-C. Zhang, "Quantum spin hall effect and topological phase transition in hgte quantum wells", Science **314**, 1757–1761 (2006).

[190] C. Liu, T. L. Hughes, X.-L. Qi, K. Wang, and S.-C. Zhang, "Quantum spin hall effect in inverted type-ii semiconductors", Phys. Rev. Lett. **100**, 236601 (2008).

[191] A. Manchon, H. C. Koo, J. Nitta, S. M. Frolov, and R. A. Duine, "New perspectives for rashba spin–orbit coupling", Nature Materials **14**, 871–882 (2015).

[192] G. Bihlmayer, P. Noël, D. V. Vyalikh, E. V. Chulkov, and A. Manchon, "Rashba-like physics in condensed matter", Nature Reviews Physics **4**, 642–659 (2022).

[193] G. B. Arfken, H. J. Weber, and F. E. Harris, "Chapter 14 - bessel functions", in *Mathematical methods for physicists (seventh edition)*, edited by G. B. Arfken, H. J. Weber, and F. E. Harris, Seventh Edition (Academic Press, Boston, 2013), pp. 643–713.

[194] K. Laubscher, D. Loss, and J. Klinovaja, "Fractional topological superconductivity and parafermion corner states", Phys. Rev. Res. **1**, 032017(R) (2019).

[195] K. Plekhanov, M. Thakurathi, D. Loss, and J. Klinovaja, "Floquet second-order topological superconductor driven via ferromagnetic resonance", Phys. Rev. Res. **1**, 032013(R) (2019).

[196] Y. Ren, Z. Qiao, and Q. Niu, "Engineering corner states from two-dimensional topological insulators", Phys. Rev. Lett. **124**, 166804 (2020).

[197] J. Langbehn, Y. Peng, L. Trifunovic, F. von Oppen, and P. W. Brouwer, "Reflection-symmetric second-order topological insulators and superconductors", Phys. Rev. Lett. **119**, 246401 (2017).

[198] Z. Hou, C. S. Weber, D. M. Kennes, D. Loss, H. Schoeller, J. Klinovaja, and M. Pletyukhov, "Realization of a three-dimensional quantum hall effect in a zeeman-induced second-order topological insulator on a torus", Phys. Rev. B **107**, 075437 (2023).

[199] J. Kälber, "Localisation length of second-order topological states", Bachelor thesis (RWTH Aachen University, 2022).

[200] C. S. Weber, S. Gassner, D. M. Kennes, and M. Claassen, "Metastability of subleading instabilities in superconducting materials", (unpublished).

[201] V. Vikhnin, S. Lysenko, A. Rua, F. Fernandez, and H. Liu, "The model of ultrafast light-induced insulator-metal phase transition in VO2", Solid State Communications **137**, 615–620 (2006).

[202] G. Bridoux, M. Villafuerte, J. M. Ferreyra, N. Bachi, C. A. Figueroa, and S. P. Heluani, "Light-induced metal-insulator transition in $SrTiO_3$ by photoresistance spectroscopy", Phys. Rev. B **92**, 155202 (2015).

[203] M. R. Beebe, J. M. Klopf, Y. Wang, S. Kittiwatanakul, J. Lu, S. A. Wolf, and R. A. Lukaszew, "Time-resolved light-induced insulator-metal transition in niobium dioxide and vanadium dioxide thin films", Opt. Mater. Express **7**, 213–223 (2017).

[204] L. Stojchevska, I. Vaskivskyi, T. Mertelj, P. Kusar, D. Svetin, S. Brazovskii, and D. Mihailovic, "Ultrafast switching to a stable hidden quantum state in an electronic crystal", Science **344**, 177–180 (2014).

[205] Q. Yang and Q. Tong, "Light-induced topological phases in two-dimensional gapped dirac materials", Phys. Rev. B **106**, 115406 (2022).

[206] I. Vaskivskyi, J. Gospodaric, S. Brazovskii, D. Svetin, P. Sutar, E. Goreshnik, I. A. Mihailovic, T. Mertelj, and D. Mihailovic, "Controlling the metal-to-insulator relaxation of the metastable hidden quantum state in 1T-TaS_2", Science Advances **1**, e1500168 (2015).

[207] I. Vaskivskyi, I. A. Mihailovic, S. Brazovskii, J. Gospodaric, T. Mertelj, D. Svetin, P. Sutar, and D. Mihailovic, "Fast electronic resistance switching involving hidden charge density wave states", Nature Communications **7**, 11442 (2016).

[208] A. Kogar, A. Zong, P. E. Dolgirev, X. Shen, J. Straquadine, Y.-Q. Bie, X. Wang, T. Rohwer, I.-C. Tung, Y. Yang, R. Li, J. Yang, S. Weathersby, S. Park, M. E. Kozina, E. J. Sie, H. Wen, P. Jarillo-Herrero, I. R. Fisher, X. Wang, and N. Gedik, "Light-induced charge density wave in LaTe3", Nature Physics **16**, 159–163 (2020).

[209] R. Mankowsky, A. von Hoegen, M. Först, and A. Cavalleri, "Ultrafast reversal of the ferroelectric polarization", Phys. Rev. Lett. **118**, 197601 (2017).

[210] X. Li, T. Qiu, J. Zhang, E. Baldini, J. Lu, A. M. Rappe, and K. A. Nelson, "Terahertz field–induced ferroelectricity in quantum paraelectric $SrTiO_3$", Science **364**, 1079–1082 (2019).

[211] T. F. Nova, A. S. Disa, M. Fechner, and A. Cavalleri, "Metastable ferroelectricity in optically strained $SrTiO_3$", Science **364**, 1075–1079 (2019).

[212] T. F. Nova, A. Cartella, A. Cantaluppi, M. Först, D. Bossini, R. V. Mikhaylovskiy, A. V. Kimel, R. Merlin, and A. Cavalleri, "An effective magnetic field from optically driven phonons", Nature Physics **13**, 132–136 (2017).

[213] A. S. Disa, M. Fechner, T. F. Nova, B. Liu, M. Först, D. Prabhakaran, P. G. Radaelli, and A. Cavalleri, "Polarizing an antiferromagnet by optical engineering of the crystal field", Nature Physics **16**, 937–941 (2020).

[214] D. Afanasiev, J. R. Hortensius, B. A. Ivanov, A. Sasani, E. Bousquet, Y. M. Blanter, R. V. Mikhaylovskiy, A. V. Kimel, and A. D. Caviglia, "Ultrafast control of magnetic interactions via light-driven phonons", Nature Materials **20**, 607–611 (2021).

[215] M. Mitrano, A. Cantaluppi, D. Nicoletti, S. Kaiser, A. Perucchi, S. Lupi, P. Di Pietro, D. Pontiroli, M. Riccò, S. R. Clark, D. Jaksch, and A. Cavalleri, "Possible light-induced superconductivity in K_3C_{60} at high temperature", Nature **530**, 461–464 (2016).

[216] M. Buzzi, D. Nicoletti, M. Fechner, N. Tancogne-Dejean, M. A. Sentef, A. Georges, T. Biesner, E. Uykur, M. Dressel, A. Henderson, T. Siegrist, J. A. Schlueter, K. Miyagawa, K. Kanoda, M.-S. Nam, A. Ardavan, J. Coulthard, J. Tindall, F. Schlawin, D. Jaksch, and A. Cavalleri, "Photomolecular high-temperature superconductivity", Phys. Rev. X **10**, 031028 (2020).

[217] M. Budden, T. Gebert, M. Buzzi, G. Jotzu, E. Wang, T. Matsuyama, G. Meier, Y. Laplace, D. Pontiroli, M. Riccò, F. Schlawin, D. Jaksch, and A. Cavalleri, "Evidence for metastable photo-induced superconductivity in K_3C_{60}", Nature Physics **17**, 611–618 (2021).

[218] E. Wang, J. D. Adelinia, M. Chavez-Cervantes, T. Matsuyama, M. Fechner, M. Buzzi, G. Meier, and A. Cavalleri, "Superconducting nonlinear transport in optically driven high-temperature K_3C_{60}", Nature Communications **14**, 7233 (2023).

[219] E. Rowe, B. Yuan, M. Buzzi, G. Jotzu, Y. Zhu, M. Fechner, M. Först, B. Liu, D. Pontiroli, M. Riccò, and A. Cavalleri, "Resonant enhancement of photo-induced superconductivity in K_3C_{60}", Nature Physics **19**, 1821–1826 (2023).

[220] D. Fausti, R. Tobey, N. Dean, S. Kaiser, A. Dienst, M. Hoffmann, S. Pyon, T. Takayama, H. Takagi, and A. Cavalleri, "Light-induced superconductivity in a stripe-ordered cuprate", Science (New York, N.Y.) **331**, 189–91 (2011).

[221] S. Kaiser, "Light-induced superconductivity in high-tc cuprates", Physica Scripta **92**, 103001 (2017).

[222] Z. M. Raines, V. Stanev, and V. M. Galitski, "Enhancement of superconductivity via periodic modulation in a three-dimensional model of cuprates", Phys. Rev. B **91**, 184506 (2015).

[223] A. Komnik and M. Thorwart, "Bcs theory of driven superconductivity", The European Physical Journal B **89**, 244 (2016).

[224] M. Knap, M. Babadi, G. Refael, I. Martin, and E. Demler, "Dynamical cooper pairing in nonequilibrium electron-phonon systems", Phys. Rev. B **94**, 214504 (2016).

[225] M. A. Sentef, A. F. Kemper, A. Georges, and C. Kollath, "Theory of light-enhanced phonon-mediated superconductivity", Phys. Rev. B **93**, 144506 (2016).

[226] G. Mazza and A. Georges, "Nonequilibrium superconductivity in driven alkali-doped fullerides", Phys. Rev. B **96**, 064515 (2017).

[227] D. M. Kennes, E. Y. Wilner, D. R. Reichman, and A. J. Millis, "Transient superconductivity from electronic squeezing of optically pumped phonons", Nature Physics **13**, 479–483 (2017).

[228] Z. Dai and P. A. Lee, "Superconducting-like response in driven systems near the mott transition", Phys. Rev. B **104**, L241112 (2021).

[229] C. J. Eckhardt, S. Chattopadhyay, D. M. Kennes, E. A. Demler, M. A. Sentef, and M. H. Michael, "Theory of resonantly enhanced photo-induced superconductivity", Nature Communications **15**, 2300 (2024).

[230] D. Montgomery, E. Peck, and G. Vining, *Introduction to linear regression analysis*, Wiley Series in Probability and Statistics (Wiley, 2013).

[231] C. L. Kane and E. J. Mele, "Z_2 Topological order and the quantum spin hall effect", Phys. Rev. Lett. **95**, 146802 (2005).

[232] C. L. Kane and E. J. Mele, "Quantum spin hall effect in graphene", Phys. Rev. Lett. **95**, 226801 (2005).

[233] M. Claassen, *Personal communication*, 2022.

[234] O. Vafek and A. V. Chubukov, "Hund interaction, spin-orbit coupling, and the mechanism of superconductivity in strongly hole-doped iron pnictides", Phys. Rev. Lett. **118**, 087003 (2017).

[235] A. K. C. Cheung and D. F. Agterberg, "Superconductivity in the presence of spin-orbit interactions stabilized by hund coupling", Phys. Rev. B **99**, 024516 (2019).

[236] D. J. Scalapino, E. Loh, and J. E. Hirsch, "d-wave pairing near a spin-density-wave instability", Phys. Rev. B **34**, 8190–8192 (1986).

[237] D. J. Scalapino, "Superconductivity and spin fluctuations", Journal of Low Temperature Physics **117**, 179–188 (1999).

[238] T. Moriya, "Developments of the theory of spin fluctuations and spin fluctuation-induced superconductivity", Proc Jpn Acad Ser B Phys Biol Sci **82**, 1–16 (2006).

[239] J. Chang, J. Zhao, and Y. Ding, "Hund-heisenberg model in superconducting infinite-layer nickelates", The European Physical Journal B **93**, 220 (2020).

[240] W. Kohn and J. M. Luttinger, "New mechanism for superconductivity", Phys. Rev. Lett. **15**, 524–526 (1965).

[241] S. Maiti and A. V. Chubukov, "Superconductivity from repulsive interaction", in AIP conference proceedings (2013).

[242] M. Y. Kagan, V. V. Val'kov, V. A. Mitskan, and M. M. Korovushkin, "The kohn-luttinger effect and anomalous pairing in new superconducting systems and graphene", Journal of Experimental and Theoretical Physics **118**, 995–1011 (2014).

[243] Y. Cao, Y. Zhang, Y.-B. Liu, C.-C. Liu, W.-Q. Chen, and F. Yang, "Kohn-luttinger mechanism driven exotic topological superconductivity on the penrose lattice", Phys. Rev. Lett. **125**, 017002 (2020).

[244] T. Cea, P. A. Pantaleón, V. T. Phong, and F. Guinea, "Superconductivity from repulsive interactions in rhombohedral trilayer graphene: a kohn-luttinger-like mechanism", Phys. Rev. B **105**, 075432 (2022).

[245] G. Wagner, Y. H. Kwan, N. Bultinck, S. H. Simon, and S. A. Parameswaran, "Superconductivity from repulsive interactions in bernal-stacked bilayer graphene", (2023), arXiv:2302.00682 [cond-mat.supr-con].

[246] G. Karakonstantakis, E. Berg, S. R. White, and S. A. Kivelson, "Enhanced pairing in the checkerboard hubbard ladder", Phys. Rev. B **83**, 054508 (2011).

[247] G. Ehlers, S. R. White, and R. M. Noack, "Hybrid-space density matrix renormalization group study of the doped two-dimensional hubbard model", Phys. Rev. B **95**, 125125 (2017).

[248] H.-C. Jiang and T. P. Devereaux, "Superconductivity in the doped hubbard model and its interplay with next-nearest hopping t'", Science **365**, 1424–1428 (2019).

[249] H.-C. Jiang and T. P. Devereaux, "Pair density wave and superconductivity in a kinetically frustrated doped emery model on a square lattice", Frontiers in Electronic Materials **3**, 1323404 (2023).

[250] H.-C. Jiang, "Pair density wave in the doped three-band hubbard model on two-leg square cylinders", Phys. Rev. B **107**, 214504 (2023).

[251] A. Georges, L. d. Medici, and J. Mravlje, "Strong correlations from hund's coupling", Annual Review of Condensed Matter Physics **4**, 137–178 (2013).

[252] Y. Nomura, S. Sakai, M. Capone, and R. Arita, "Unified understanding of superconductivity and mott transition in alkali-doped fullerides from first principles", Science Advances **1**, e1500568 (2015).

[253] E. Pavarini, E. Koch, R. Scalettar, and R. Martin, eds., *The Physics of Correlated Insulators, Metals, and Superconductors*, Vol. 7, Schriften des Forschungszentrums Jülich. Reihe Modeling and Simulation (Forschungszentrum Jülich GmbH Zentralbibliothek, Verlag, Jülich, Sept. 25, 2017), 450 S.

[254] L. Fanfarillo, A. Valli, and M. Capone, "Synergy between hund-driven correlations and boson-mediated superconductivity", Phys. Rev. Lett. **125**, 177001 (2020).

[255] K. Slagle and Y. B. Kim, "A simple mechanism for unconventional superconductivity in a repulsive fermion model", SciPost Phys. **6**, 016 (2019).

[256] W.-F. Tsai and S. A. Kivelson, "Superconductivity in inhomogeneous hubbard models", Phys. Rev. B **73**, 214510 (2006).

[257] V. Crépel and L. Fu, "New mechanism and exact theory of superconductivity from strong repulsive interaction", Science Advances **7**, eabh2233 (2021).

[258] V. Crépel, T. Cea, L. Fu, and F. Guinea, "Unconventional superconductivity due to interband polarization", Phys. Rev. B **105**, 094506 (2022).

[259] V. Crépel and L. Fu, "Spin-triplet superconductivity from excitonic effect in doped insulators", Proceedings of the National Academy of Sciences **119**, e2117735119 (2022).

[260] Y. He, K. Yang, J. B. Hauck, E. J. Bergholtz, and D. M. Kennes, "Superconductivity of repulsive spinless fermions with sublattice potentials", Phys. Rev. Res. **5**, L012009 (2023).

[261] O. Bodensiek, T. Pruschke, and R. Žitko, "Superconductivity in the kondo lattice model", Journal of Physics: Conference Series **200**, 012162 (2010).

[262] J. W. Lynn, V. Madhavan, and L. Jiao, "Editorial: new heavy fermion superconductors", Frontiers in Electronic Materials **2**, 1120381 (2023).

[263] G.-M. Zhang, Y.-f. Yang, and F.-C. Zhang, "Self-doped mott insulator for parent compounds of nickelate superconductors", Phys. Rev. B **101**, 020501 (2020).

[264] Y.-f. Yang and G.-M. Zhang, "Self-doping and the mott-kondo scenario for infinite-layer nickelate superconductors", Frontiers in Physics **9**, 801236 (2022).

[265] D. Chen, P. Jiang, L. Si, Y. Lu, and Z. Zhong, "Magnetism in doped infinite-layer $NdNiO_2$ studied by combined density functional theory and dynamical mean-field theory", Phys. Rev. B **106**, 045105 (2022).

[266] H. Chen, A. Hampel, J. Karp, F. Lechermann, and A. J. Millis, "Dynamical mean field studies of infinite layer nickelates: physics results and methodological implications", Frontiers in Physics **10**, 835942 (2022).

[267] J. Fowlie, M. Hadjimichael, M. M. Martins, D. Li, M. Osada, B. Y. Wang, K. Lee, Y. Lee, Z. Salman, T. Prokscha, J.-M. Triscone, H. Y. Hwang, and A. Suter, "Intrinsic magnetism in superconducting infinite-layer nickelates", Nature Physics **18**, 1043–1047 (2022).

[268] Y. Nomura and R. Arita, "Superconductivity in infinite-layer nickelates", Reports on Progress in Physics **85**, 052501 (2022).

[269] P. Fulde and R. A. Ferrell, "Superconductivity in a strong spin-exchange field", Phys. Rev. **135**, A550–A563 (1964).

[270] A. I. Larkin and Y. N. Ovchinnikov, "Nonuniform state of superconductors", Zh. Eksp. Teor. Fiz. **47**, 1136–1146 (1964), [Sov. Phys. JETP **20** (1965) 762].

[271] J. J. Kinnunen, J. E. Baarsma, J.-P. Martikainen, and P. Törmä, "The fulde-ferrell-larkin-ovchinnikov state for ultracold fermions in lattice and harmonic potentials: a review", Reports on Progress in Physics **81**, 046401 (2018).

[272] D. F. Agterberg, J. S. Davis, S. D. Edkins, E. Fradkin, D. J. Van Harlingen, S. A. Kivelson, P. A. Lee, L. Radzihovsky, J. M. Tranquada, and Y. Wang, "The physics of pair-density waves: cuprate superconductors and beyond", Annual Review of Condensed Matter Physics **11**, 231–270 (2020).

[273] P. Wan, O. Zheliuk, N. F. Q. Yuan, X. Peng, L. Zhang, M. Liang, U. Zeitler, S. Wiedmann, N. E. Hussey, T. T. M. Palstra, and J. Ye, "Orbital fulde–ferrell–larkin–ovchinnikov state in an ising superconductor", Nature **619**, 46–51 (2023).

[274] C. Setty, L. Fanfarillo, and P. J. Hirschfeld, "Mechanism for fluctuating pair density wave", Nature Communications **14**, 3181 (2023).

[275] Y. Matsuda and H. Shimahara, "Fulde–ferrell–larkin–ovchinnikov state in heavy fermion superconductors", Journal of the Physical Society of Japan **76**, 051005 (2007).

[276] W.-L. Tu and T.-K. Lee, "Evolution of pairing orders between pseudogap and superconducting phases of cuprate superconductors", Scientific Reports **9**, 1719 (2019).

[277] Y.-F. Yang, J. Chen, C. Cheng, and H.-G. Luo, "Enhanced superconductivity and various edge modes in modulated $t-J$ chains", Phys. Rev. B **105**, 165123 (2022).

[278] K. Kobayashi, M. Okumura, S. Yamada, M. Machida, and H. Aoki, "Superconductivity in repulsively interacting fermions on a diamond chain: flat-band-induced pairing", Phys. Rev. B **94**, 214501 (2016).

[279] A. Abdelwahab, G. Polat, and E. Jeckelmann, "Pair binding and enhancement of pairing correlations in asymmetric hubbard ladders", Phys. Rev. B **107**, 125117 (2023).

[280] Z. Zhu, H.-C. Jiang, D. N. Sheng, and Z.-Y. Weng, "Nature of strong hole pairing in doped mott antiferromagnets", Scientific Reports **4**, 5419 (2014).

[281] S. Chatterjee, M. Ippoliti, and M. P. Zaletel, "Skyrmion superconductivity: dmrg evidence for a topological route to superconductivity", Phys. Rev. B **106**, 035421 (2022).

[282] T. Giamarchi, *Quantum physics in one dimension*, International Series of Monographs on Physics (Oxford University Press, Oxford, 2003).

[283] N. D. Patel, A. Nocera, G. Alvarez, A. Moreo, and E. Dagotto, "Pairing tendencies in a two-orbital hubbard model in one dimension", Phys. Rev. B **96**, 024520 (2017).

[284] A. Nocera, Y. Wang, N. D. Patel, G. Alvarez, T. A. Maier, E. Dagotto, and S. Johnston, "Doping evolution of charge and spin excitations in two-leg hubbard ladders: comparing dmrg and flex results", Phys. Rev. B **97**, 195156 (2018).

[285] M. Qin, C.-M. Chung, H. Shi, E. Vitali, C. Hubig, U. Schollwöck, S. R. White, and S. Zhang (Simons Collaboration on the Many-Electron Problem), "Absence of superconductivity in the pure two-dimensional hubbard model", Phys. Rev. X **10**, 031016 (2020).

[286] J. E. Baarsma and P. Törmä, "Larkin-ovchinnikov phases in two-dimensional square lattices", Journal of Modern Optics **63**, 1795–1804 (2016).

[287] J. E. Baarsma and H. T. C. Stoof, "Inhomogeneous superfluid phases in ^{6}Li-^{40}K mixtures at unitarity", Phys. Rev. A **87**, 063612 (2013).

[288] C. Mora and R. Combescot, "Transition to fulde-ferrell-larkin-ovchinnikov phases in three dimensions: a quasiclassical investigation at low temperature with fourier expansion", Phys. Rev. B **71**, 214504 (2005).

[289] N. Yoshida and S.-K. Yip, "Larkin-ovchinnikov state in resonant fermi gas", Phys. Rev. A **75**, 063601 (2007).

[290] N. D. Mermin and H. Wagner, "Absence of ferromagnetism or antiferromagnetism in one- or two-dimensional isotropic heisenberg models", Phys. Rev. Lett. **17**, 1133–1136 (1966).

[291] C. Mora, N. Regnault, and B. A. Bernevig, "Flatbands and perfect metal in trilayer moiré graphene", Phys. Rev. Lett. **123**, 026402 (2019).

[292] E. Khalaf, A. J. Kruchkov, G. Tarnopolsky, and A. Vishwanath, "Magic angle hierarchy in twisted graphene multilayers", Phys. Rev. B **100**, 085109 (2019).

[293] S. Carr, C. Li, Z. Zhu, E. Kaxiras, S. Sachdev, and A. Kruchkov, "Ultraheavy and ultrarelativistic dirac quasiparticles in sandwiched graphenes", Nano Letters **20**, PMID: 32208724, 3030–3038 (2020).

[294] C. Lei, L. Linhart, W. Qin, F. Libisch, and A. H. MacDonald, "Mirror symmetry breaking and lateral stacking shifts in twisted trilayer graphene", Phys. Rev. B **104**, 035139 (2021).

[295] D. C ălug ăru, F. Xie, Z.-D. Song, B. Lian, N. Regnault, and B. A. Bernevig, "Twisted symmetric trilayer graphene: single-particle and many-body hamiltonians and hidden nonlocal symmetries of trilayer moiré systems with and without displacement field", Phys. Rev. B **103**, 195411 (2021).

[296] J. Shin, B. L. Chittari, and J. Jung, "Stacking and gate-tunable topological flat bands, gaps, and anisotropic strip patterns in twisted trilayer graphene", Phys. Rev. B **104**, 045413 (2021).

[297] J. M. Park, Y. Cao, K. Watanabe, T. Taniguchi, and P. Jarillo-Herrero, "Tunable strongly coupled superconductivity in magic-angle twisted trilayer graphene", Nature **590**, 249–255 (2021).

[298] Z. Hao, A. M. Zimmerman, P. Ledwith, E. Khalaf, D. H. Najafabadi, K. Watanabe, T. Taniguchi, A. Vishwanath, and P. Kim, "Electric field–tunable superconductivity in alternating-twist magic-angle trilayer graphene", Science **371**, 1133–1138 (2021).

[299] M. Christos, S. Sachdev, and M. S. Scheurer, "Correlated insulators, semimetals, and superconductivity in twisted trilayer graphene", Phys. Rev. X **12**, 021018 (2022).

[300] A. Fischer, Z. A. H. Goodwin, A. A. Mostofi, J. Lischner, D. M. Kennes, and L. Klebl, "Unconventional superconductivity in magic-angle twisted trilayer graphene", npj Quantum Materials **7**, 5 (2022).

[301] K. Laubscher, C. S. Weber, M. Hünenberger, H. Schoeller, D. M. Kennes, D. Loss, and J. Klinovaja, "Rkky interaction in one-dimensional flat-band lattices", Phys. Rev. B **108**, 155429 (2023).

[302] S. A. Parameswaran, R. Roy, and S. L. Sondhi, "Fractional quantum hall physics in topological flat bands", Comptes Rendus. Physique **14**, 816–839 (2013).

[303] E. J. Bergholtz and Z. Liu, "Topological flat band models and fractional chern insulators", International Journal of Modern Physics B **27**, 1330017 (2013).

[304] Z. Liu, F. Liu, and Y.-S. Wu, "Exotic electronic states in the world of flat bands: from theory to material", Chinese Physics B **23**, 077308 (2014).

[305] O. Derzhko, J. Richter, and M. Maksymenko, "Strongly correlated flat-band systems: the route from heisenberg spins to hubbard electrons", International Journal of Modern Physics B **29**, 1530007 (2015).

[306] D. Leykam and S. Flach, "Perspective: Photonic flatbands", APL Photonics **3**, 070901 (2018).

[307] D. Leykam, A. Andreanov, and S. Flach, "Artificial flat band systems: from lattice models to experiments", Advances in Physics: X **3**, 1473052 (2018).

[308] L. Balents, C. R. Dean, D. K. Efetov, and A. F. Young, "Superconductivity and strong correlations in moiré flat bands", Nature Physics **16**, 725–733 (2020).

[309] P. Törmä, S. Peotta, and B. A. Bernevig, "Superconductivity, superfluidity and quantum geometry in twisted multilayer systems", Nature Reviews Physics **4**, 528–542 (2022).

[310] D. Leykam, "Flat bands, sharp physics", AAPPS Bulletin **34**, 2 (2024).

[311] N. B. Kopnin, T. T. Heikkilä, and G. E. Volovik, "High-temperature surface superconductivity in topological flat-band systems", Phys. Rev. B **83**, 220503 (2011).

[312] T. T. Heikkilä, N. B. Kopnin, and G. E. Volovik, "Flat bands in topological media", JETP Letters **94**, 233–239 (2011).

[313] S. Peotta and P. Törmä, "Superfluidity in topologically nontrivial flat bands", Nature Communications **6**, 8944 (2015).

[314] A. Julku, S. Peotta, T. I. Vanhala, D.-H. Kim, and P. Törmä, "Geometric origin of superfluidity in the lieb-lattice flat band", Phys. Rev. Lett. **117**, 045303 (2016).

[315] L. Liang, T. I. Vanhala, S. Peotta, T. Siro, A. Harju, and P. Törmä, "Band geometry, berry curvature, and superfluid weight", Phys. Rev. B **95**, 024515 (2017).

[316] V. Khodel, V. Shaginyan, and V. Khodel, "New approach in the microscopic fermi systems theory", Physics Reports **249**, 1–134 (1994).

[317] H. Tasaki, "From Nagaoka's Ferromagnetism to Flat-Band Ferromagnetism and Beyond: An Introduction to Ferromagnetism in the Hubbard Model", Progress of Theoretical Physics **99**, 489–548 (1998).

[318] A. Mielke, "Exact ground states for the hubbard model on the kagome lattice", Journal of Physics A: Mathematical and General **25**, 4335 (1992).

[319] H. Tasaki, "Ferromagnetism in the hubbard models with degenerate single-electron ground states", Phys. Rev. Lett. **69**, 1608–1611 (1992).

[320] A. Mielke and H. Tasaki, "Ferromagnetism in the hubbard model", Communications in Mathematical Physics **158**, 341–371 (1993).

[321] M. Tylutki and P. Törmä, "Spin-imbalanced fermi superfluidity in a hubbard model on a lieb lattice", Phys. Rev. B **98**, 094513 (2018).

[322] K.-E. Huhtinen, M. Tylutki, P. Kumar, T. I. Vanhala, S. Peotta, and P. Törmä, "Spin-imbalanced pairing and fermi surface deformation in flat bands", Phys. Rev. B **97**, 214503 (2018).

[323] K.-E. Huhtinen, "Superconductivity and normal state properties in flat bands", PhD thesis (Aalto University, 2023).

[324] R. Bistritzer and A. H. MacDonald, "Moiré bands in twisted double-layer graphene", Proceedings of the National Academy of Sciences **108**, 12233–12237 (2011).

[325] Y. Cao, V. Fatemi, S. Fang, K. Watanabe, T. Taniguchi, E. Kaxiras, and P. Jarillo-Herrero, "Unconventional superconductivity in magic-angle graphene superlattices", Nature **556**, 43–50 (2018).

[326] Y. Cao, V. Fatemi, A. Demir, S. Fang, S. L. Tomarken, J. Y. Luo, J. D. Sanchez-Yamagishi, K. Watanabe, T. Taniguchi, E. Kaxiras, R. C. Ashoori, and P. Jarillo-Herrero, "Correlated insulator behaviour at half-filling in magic-angle graphene superlattices", Nature **556**, 80–84 (2018).

[327] Y. Xie, B. Lian, B. Jäck, X. Liu, C.-L. Chiu, K. Watanabe, T. Taniguchi, B. A. Bernevig, and A. Yazdani, "Spectroscopic signatures of many-body correlations in magic-angle twisted bilayer graphene", Nature **572**, 101–105 (2019).

[328] A. Kerelsky, L. J. McGilly, D. M. Kennes, L. Xian, M. Yankowitz, S. Chen, K. Watanabe, T. Taniguchi, J. Hone, C. Dean, A. Rubio, and A. N. Pasupathy, "Maximized electron interactions at the magic angle in twisted bilayer graphene", Nature **572**, 95–100 (2019).

[329] Y. Jiang, X. Lai, K. Watanabe, T. Taniguchi, K. Haule, J. Mao, and E. Y. Andrei, "Charge order and broken rotational symmetry in magic-angle twisted bilayer graphene", Nature **573**, 91–95 (2019).

[330] E. Y. Andrei and A. H. MacDonald, "Graphene bilayers with a twist", Nature Materials **19**, 1265–1275 (2020).

[331] M. A. Ruderman and C. Kittel, "Indirect exchange coupling of nuclear magnetic moments by conduction electrons", Phys. Rev. **96**, 99–102 (1954).

[332] T. Kasuya, "A Theory of Metallic Ferro- and Antiferromagnetism on Zener's Model", Progress of Theoretical Physics **16**, 45–57 (1956).

[333] K. Yosida, "Magnetic properties of Cu-Mn alloys", Phys. Rev. **106**, 893–898 (1957).

[334] A. M. Black-Schaffer, "Rkky coupling in graphene", Phys. Rev. B **81**, 205416 (2010).

[335] S. R. Power and M. S. Ferreira, "Indirect exchange and ruderman–kittel–kasuya–yosida (rkky) interactions in magnetically-doped graphene", Crystals **3**, 49–78 (2013).

[336] H.-R. Chang, J. Zhou, S.-X. Wang, W.-Y. Shan, and D. Xiao, "Rkky interaction of magnetic impurities in dirac and weyl semimetals", Phys. Rev. B **92**, 241103 (2015).

[337] S.-X. Wang, H.-R. Chang, and J. Zhou, "Rkky interaction in three-dimensional electron gases with linear spin-orbit coupling", Phys. Rev. B **96**, 115204 (2017).

[338] J. A. Ouassou, T. Yokoyama, and J. Linder, "Rkky interaction in triplet superconductors: dzyaloshinskii-moriya-type interaction mediated by spin-polarized cooper pairs", Phys. Rev. B **109**, 174506 (2024).

[339] D. N. Aristov, S. V. Maleyev, and A. G. Yashenkin, "Rkky interaction in layered superconductors with anisotropic pairing", Zeitschrift für Physik B Condensed Matter **102**, 467–471 (1997).

[340] K. Laubscher, D. Miserev, V. Kaladzhyan, D. Loss, and J. Klinovaja, "Rkky interaction at helical edges of topological superconductors", Phys. Rev. B **107**, 115421 (2023).

[341] F. Pientka, L. I. Glazman, and F. von Oppen, "Topological superconducting phase in helical shiba chains", Phys. Rev. B **88**, 155420 (2013).

[342] J. Klinovaja, P. Stano, A. Yazdani, and D. Loss, "Topological superconductivity and majorana fermions in rkky systems", Phys. Rev. Lett. **111**, 186805 (2013).

[343] B. Braunecker and P. Simon, "Interplay between classical magnetic moments and superconductivity in quantum one-dimensional conductors: toward a self-sustained topological majorana phase", Phys. Rev. Lett. **111**, 147202 (2013).

[344] B. Braunecker and P. Simon, "Self-stabilizing temperature-driven crossover between topological and nontopological ordered phases in one-dimensional conductors", Phys. Rev. B **92**, 241410 (2015).

[345] "Observation of flat band, rkky plateau, and magnetization jump in quasi-one-dimensional triangular kagome lattice model", Journal of Applied Physics **128**, 163903 (2020).

[346] D. O. Oriekhov and V. P. Gusynin, "Rkky interaction in a doped pseudospin-1 fermion system at finite temperature", Phys. Rev. B **101**, 235162 (2020).

[347] G. Bouzerar, "Rkky couplings in the lieb lattice: flat-band induced frustration", Phys. Rev. B **104**, 155151 (2021).

[348] G. Bouzerar, "Flat band induced room-temperature ferromagnetism in two-dimensional systems", Phys. Rev. B **107**, 184441 (2023).

[349] U. Larsen, "The rkky indirect exchange interaction in metals in arbitrary continuous dimension", Physics Letters A **85**, 471–473 (1981).

[350] M. M. Valizadeh and S. Satpathy, "Rkky interaction for the spin-polarized electron gas", International Journal of Modern Physics B **29**, 1550219 (2015).

[351] R. R. Gimaev, A. S. Komlev, A. S. Davydov, B. B. Kovalev, and V. I. Zverev, "Magnetic and electronic properties of heavy lanthanides (Gd, Tb, Dy, Er, Ho, Tm)", Crystals **11**, 82 (2021).

[352] N. Bloembergen and T. J. Rowland, "Nuclear spin exchange in solids: Tl^{203} and Tl^{205} magnetic resonance in thallium and thallic oxide", Phys. Rev. **97**, 1679–1698 (1955).

[353] N. F. Schwabe, R. J. Elliott, and N. S. Wingreen, "Ruderman-kittel-kasuya-yosida interaction across a tunneling junction out of equilibrium", Phys. Rev. B **54**, 12953–12968 (1996).

[354] H.-H. Lai, W.-M. Huang, and H.-H. Lin, "Spatial trends of noncollinear exchange coupling mediated by itinerant carriers with different fermi surfaces", Phys. Rev. B **79**, 045315 (2009).

[355] H. Imamura, P. Bruno, and Y. Utsumi, "Twisted exchange interaction between localized spins embedded in a one- or two-dimensional electron gas with rashba spin-orbit coupling", Phys. Rev. B **69**, 121303 (2004).

[356] J. Gao, W. Chen, X. C. Xie, and F.-c. Zhang, "In-plane noncollinear exchange coupling mediated by helical edge states in quantum spin hall systems", Phys. Rev. B **80**, 241302 (2009).

[357] D. M. Deaven, D. S. Rokhsar, and M. Johnson, "Simple theory of exchange coupling in transition-metal magnetic multilayers", Phys. Rev. B **44**, 5977–5980 (1991).

[358] E. H. Lieb, "Two theorems on the hubbard model", Phys. Rev. Lett. **62**, 1201–1204 (1989).

[359] B. Sutherland, "Localization of electronic wave functions due to local topology", Phys. Rev. B **34**, 5208–5211 (1986).

[360] M. N. Huda, S. Kezilebieke, and P. Liljeroth, "Designer flat bands in quasi-one-dimensional atomic lattices", Phys. Rev. Res. **2**, 043426 (2020).

[361] L. Morales-Inostroza and R. A. Vicencio, "Simple method to construct flat-band lattices", Phys. Rev. A **94**, 043831 (2016).

[362] J.-H. Bae, T. Sedrakyan, and S. Maiti, "Isolated flat bands in 2d lattices based on a novel path-exchange symmetry", SciPost Phys. **15**, 139 (2023).

[363] H. Schoeller, "Topology in condensed matter systems", Lecture Notes, RWTH Aachen University (2019/2020).

[364] D. Wanisch, "The anderson-holstein model with coulomb interaction", Master thesis (RWTH Aachen University, 2019).

[365] S. Saremi, "Rkky in half-filled bipartite lattices: graphene as an example", Phys. Rev. B **76**, 184430 (2007).

[366] A. Kruchkov, "Quantum geometry, flat chern bands, and wannier orbital quantization", Phys. Rev. B **105**, L241102 (2022).

[367] H. C. Po, L. Zou, T. Senthil, and A. Vishwanath, "Faithful tight-binding models and fragile topology of magic-angle bilayer graphene", Phys. Rev. B **99**, 195455 (2019).

[368] J. Ahn, S. Park, and B.-J. Yang, "Failure of nielsen-ninomiya theorem and fragile topology in two-dimensional systems with space-time inversion symmetry: application to twisted bilayer graphene at magic angle", Phys. Rev. X **9**, 021013 (2019).

[369] A. Skurativska, S. S. Tsirkin, F. D. Natterer, T. Neupert, and M. H. Fischer, "Flat bands with fragile topology through superlattice engineering on single-layer graphene", Phys. Rev. Res. **3**, L032003 (2021).

[370] H. C. Po, H. Watanabe, and A. Vishwanath, "Fragile topology and wannier obstructions", Phys. Rev. Lett. **121**, 126402 (2018).

[371] P. Kopietz, L. Bartosch, and F. Schütz, *Introduction to the functional renormalization group* (Springer Berlin Heidelberg, 2010).

[372] W. Metzner, M. Salmhofer, C. Honerkamp, V. Meden, and K. Schönhammer, "Functional renormalization group approach to correlated fermion systems", Rev. Mod. Phys. **84**, 299–352 (2012).

[373] N. Dupuis, L. Canet, A. Eichhorn, W. Metzner, J. Pawlowski, M. Tissier, and N. Wschebor, "The nonperturbative functional renormalization group and its applications", Physics Reports **910**, 1–114 (2021).

[374] G. Camacho, C. Klöckner, D. M. Kennes, and C. Karrasch, "Review of recent developments of the functional renormalization group for systems out of equilibrium", The European Physical Journal B **95**, 195 (2022).

[375] J. B. Profe, D. M. Kennes, and L. Klebl, "Diverge implements various exact renormalization group examples", SciPost Phys. Codebases, 26 (2024).

[376] J. B. Profe, C. Honerkamp, S. Achilles, and D. M. Kennes, "Electronic instabilities in penrose quasicrystals: competition, coexistence, and collaboration of order", Phys. Rev. Res. **3**, 023180 (2021).

[377] G. Carleo and M. Troyer, "Solving the quantum many-body problem with artificial neural networks", Science **355**, 602–606 (2017).

[378] D.-L. Deng, X. Li, and S. Das Sarma, "Machine learning topological states", Phys. Rev. B **96**, 195145 (2017).

[379] G. Carleo, K. Choo, D. Hofmann, J. E. Smith, T. Westerhout, F. Alet, E. J. Davis, S. Efthymiou, I. Glasser, S.-H. Lin, M. Mauri, G. Mazzola, C. B. Mendl, E. van Nieuwenburg, O. O'Reilly, H. Théveniaut, G. Torlai, F. Vicentini, and A. Wietek, "Netket: a machine learning toolkit for many-body quantum systems", SoftwareX **10**, 100311 (2019).

[380] M. J. Hartmann and G. Carleo, "Neural-network approach to dissipative quantum many-body dynamics", Phys. Rev. Lett. **122**, 250502 (2019).

[381] J. Stokes, J. R. Moreno, E. A. Pnevmatikakis, and G. Carleo, "Phases of two-dimensional spinless lattice fermions with first-quantized deep neural-network quantum states", Phys. Rev. B **102**, 205122 (2020).

[382] J. Carrasquilla and G. Torlai, "How to use neural networks to investigate quantum many-body physics", PRX Quantum **2**, 040201 (2021).

[383] G. Passetti, D. Hofmann, P. Neitemeier, L. Grunwald, M. A. Sentef, and D. M. Kennes, "Can neural quantum states learn volume-law ground states?", Phys. Rev. Lett. **131**, 036502 (2023).

[384] J. B. Profe, *Personal communication*, 2023.

[385] Jülich Supercomputing Centre, "JURECA: Data centric and booster modules implementing the modular supercomputing architecture at jülich supercomputing centre", Journal of large-scale research facilities **7**, A182 (2021).

Publications and Preprints

1. D. M. Kennes, N. Müller, M. Pletyukhov, C. Weber, C. Bruder, F. Hassler, J. Klinovaja, D. Loss, and H. Schoeller, *Chiral 1D Floquet topological insulators beyond rotating wave approximation*, Phys. Rev. B **100**, 041103(R) (2019)

2. Y.-T. Lin, D. M. Kennes, M. Pletyukhov, C. S. Weber, H. Schoeller, and V. Meden, *The interacting Rice-Mele model – bulk and boundaries*, Phys. Rev. B **102**, 085122 (2020)

3. Y.-T. Lin, C. S. Weber, D. M. Kennes, M. Pletyukhov, H. Schoeller, and V. Meden, *Quantitative analysis of interaction effects in generalized Aubry-André-Harper models*, Phys. Rev. B **103**, 195119 (2021)

4. C. S. Weber, K. Piasotski, M. Pletyukhov, J. Klinovaja, D. Loss, H. Schoeller, D. M. Kennes, *Universality of Boundary Charge Fluctuations*, Phys. Rev. Lett. 126, 016803 (2021)

5. K. Laubscher, C. S. Weber, D. M. Kennes, M. Pletyukhov, H. Schoeller, D. Loss, J. Klinovaja, *Fractional boundary charges with quantized slopes in interacting one- and two-dimensional systems*, Phys. Rev. B **104**, 035432 (2021)

6. K. Piasotski, M. Pletyukhov, C. S. Weber, J. Klinovaja, D. M. Kennes, H. Schoeller, *Universality of Abelian and non-Abelian Wannier functions in one dimension*, Phys. Rev. Research **3**, 033167 (2021)

7. Z. Hou, C. S. Weber, D. M. Kennes, D. Loss, H. Schoeller, J. Klinovaja, M. Pletyukhov, *Realization of a three-dimensional quantum Hall effect in a Zeeman-induced second-order topological insulator on a torus*, Phys. Rev. B **107**, 075437 (2023)

8. C. S. Weber, M. Pletyukhov, Z. Hou, D. M. Kennes, J. Klinovaja, D. Loss, H. Schoeller, *Second-order topology and supersymmetry in two-dimensional topological insulators*, Phys. Rev. B **107**, 235402 (2023) [1]

9. K. Laubscher, C. S. Weber, M. Hünenberger, H. Schoeller, D. M. Kennes, D. Loss, J. Klinovaja, *RKKY interaction in one-dimensional flat band lattices*, Phys. Rev. B **108**, 155429 (2023) [1]

10. S. Gassner, C. S. Weber, M. Claassen, *Light-induced switching between singlet and triplet superconducting states*, Nat Commun **15**, 1776 (2024)

11. L. Wang, L. Wei, Z.-L. Gu, A. Fischer, Y. He, Q. Xu, A. Ghiotto, C. Weber, K. Watanabe, T. Taniguchi, M. Claassen, A. Rubio, A. Millis, A. Pasupathy, L. Xian, D. Rhodes, D. Kennes, J.-X. Li, *Mapping the Mottness under Magnetic Field*, doi:10.21203/rs.3.rs-3385782/v1. (2023), submitted to Nature in Sep. 2023

12. C. S. Weber, D. Kiese, D. M. Kennes, M. Claassen, *Intertwined Superconductivity and Magnetism from Repulsive Interactions in Kondo Bilayers*, arXiv:2408.02847 (2024) [1]

[1] Publications used for this thesis.

Acknowledgment

First of all, I would like to thank Dante Kennes for giving me the opportunity to do this PhD and for supervising me during this time. I especially want to thank him for all the advice I received and also for connecting me with researchers from all over world. He created the opportunity for me to spend a year of my PhD at the University of Pennsylvania. Additionally, I want to thank Herbert Schoeller for co-supervising this thesis and for his delightful insights on the many projects that we have been working on together. Thanks to both of you for guiding me through all this time from my bachelor thesis to the end of my PhD!
Furthermore, I want to thank Martin Claassen and the University of Pennsylvania for hosting me for one year of my PhD. I thoroughly enjoyed the time in Philadelphia and all the collaborations that I made during this time. Martin Claassen taught me a lot about physics and I enjoyed the countless discussions we had.

Additionally, I want to thank my collaborators. Thanks to Denitsa Baykusheva, Zhe Hou, Maximilian Hünenberger, Dominik Kiese, I-Te Lu, Matteo Mitrano, Kiryl Piasotski, Mikhail Pletyukhov. Moreover, a special thank you to Jelena Klinovaja and Daniel Loss for numerous collaborations and for inviting me to Basel twice; and to Katharina Laubscher and Steven Gassner for beeing such great collaborators and friends.

Moreover, I want to thank all my friends and colleagues at RWTH Aachen University. Thanks for the numerous discussions and the help that I received during my PhD. And thanks for making the institute such a pleasant place and for all the fun that we had outside of work. Thank you Jacob Beyer, Matthew Bunney, Nils Çaçi, Mara Caltapanides, Fabian Engelhardt, Ammon Fischer, Francesco Grandi, Jan Herre, Florian Kischel, Lennart Klebl, Martin Maurer, Niclas Müller, Robert Nolte, Takuya Okugawa, Giacomo Passetti, Jonas Profe, Jonas Reimann, Alexander Sushchyev, Anna Stollenwerk and many more!
Additionally, I want to thank all my colleagues and friends from Philadelphia for the discussions and all the fun that we had. Thanks to Christophe de Beule, Ben Kass, Suman Kulkarni, Yue (Cathy) Li, Clara Marty, Ben Pisanty, Felipe Rodrigues Martins, Wai Ting (Terrence) Tai, Pok Man Tam, and many more! I also want to thank Randall Kamien for all his advice and support! All of you guys made this time one of the best years in my life that I will never forget!

Furthermore, I would like to thank all of my friends from outside of the institute, especially Johanna, Kathi, Lukas and Sebastian. Moreover, I want to thank Hannah for her support especially in the last few months. Thanks for always being understanding and patient whenever I was worried or stressed about this thesis. Finally, I would like to thank my wonderful family. Thanks to my parents, Beate and Michael, for always having my back and for being so supportive. I also want to thank my brother Felix and my grandparents Doris and Richard. I would not have been able to achieve all of this without your help.

The author gratefully acknowledges computing time on the supercomputer JURECA [385] at Forschungszentrum Jülich under grant no. enhancerg. Further computations were performed with computing resources granted by RWTH Aachen University, mostly under projects rwth0752, rwth0841 and rwth 1258, and by the University of Pennsylvania. I was supported by the Deutsche Forschungsgemeinschaft (DFG, German Research Foundation) via RTG 1995.

Eidesstattliche Erklärung

Ich, Clara Stephanie Weber, erkläre hiermit, dass diese Dissertation und die darin dargelegten Inhalte die eigenen sind und selbstständig, als Ergebnis der eigenen originären Forschung, generiert wurden.

Hiermit erkläre ich an Eides statt

1. Diese Arbeit wurde vollständig oder größtenteils in der Phase als Doktorand dieser Fakultät und Universität angefertigt;
2. Sofern irgendein Bestandteil dieser Dissertation zuvor für einen akademischen Abschluss oder eine andere Qualifikation an dieser oder einer anderen Institution verwendet wurde, wurde dies klar angezeigt;
3. Wenn immer andere eigene oder Veröffentlichungen Dritter herangezogen wurden, wurden diese klar benannt;
4. Wenn aus anderen eigenen oder Veröffentlichungen Dritter zitiert wurde, wurde stets die Quelle hierfür angegeben. Diese Dissertation ist vollständig meine eigene Arbeit, mit der Ausnahme solcher Zitate;
5. Alle wesentlichen Quellen von Unterstützung wurden benannt;
6. Wenn immer ein Teil dieser Dissertation auf der Zusammenarbeit mit anderen basiert, wurde von mir klar gekennzeichnet, was von anderen und was von mir selbst erarbeitet wurde;
7. Teile dieser Arbeit wurden zuvor veröffentlicht, und zwar in Referenzen [111, 125, 301].

Aachen, February 4, 2025
Clara Stephanie Weber